Mondragon Unibertsitatea

DOCTORAL THESIS

MODULAR CONVERTER STRUCTURES FOR STATCOM APPLICATION UNDER UNBALANCED CONDITIONS

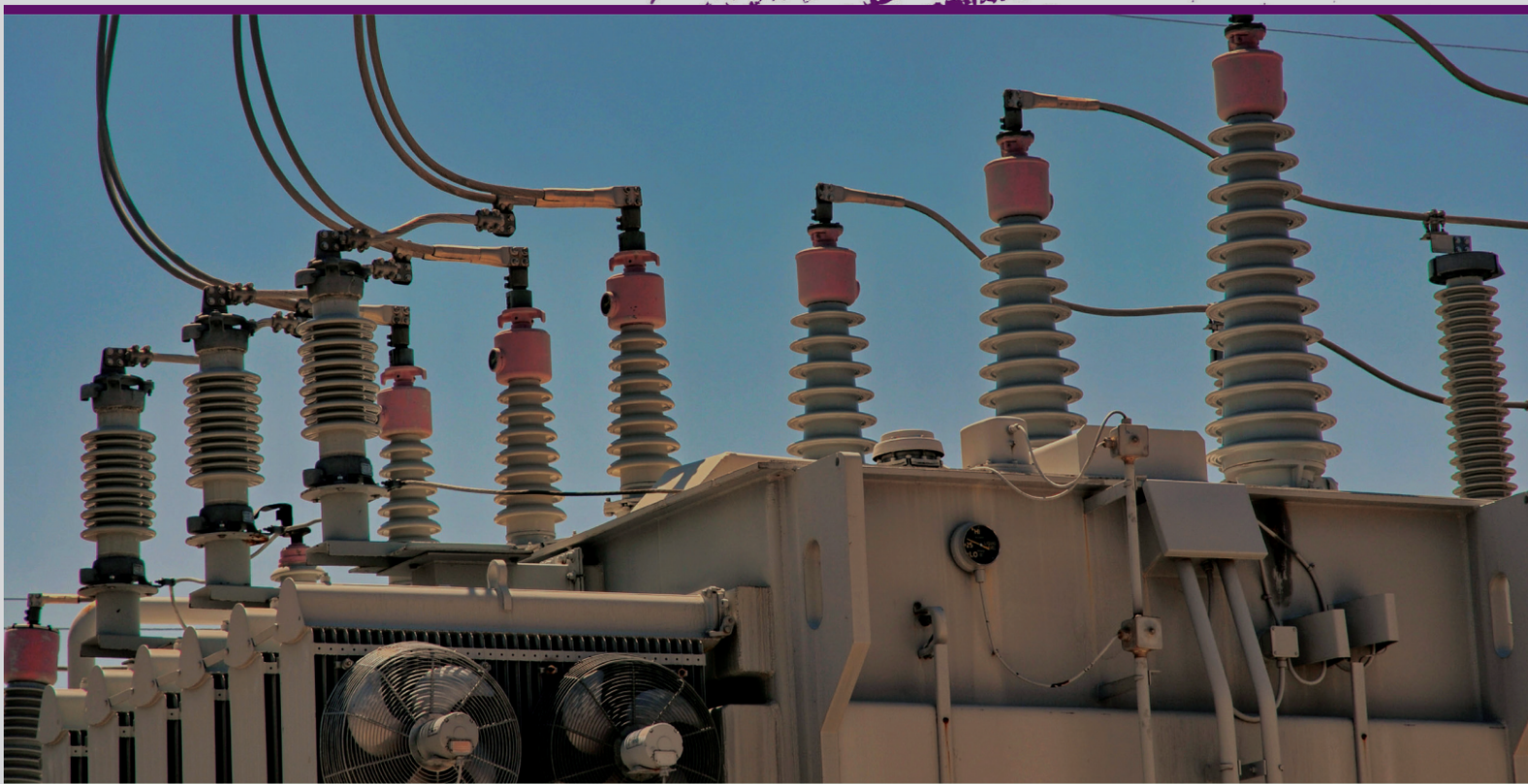

IOSU MARZO ELGUERO | Arrasate-Mondragón, 2022

IOSU MARZO ELGUERO | Modular Converter Structures for STATCOM Application under Unbalanced Conditions

DOCTORAL DISSERTATION

Modular Converter Structures for STATCOM Application under Unbalanced Conditions

IOSU MARZO ELGUERO
Electronics and Computer Science Department
Mondragon Unibertsitatea

Supervised by
DR. JON ANDONI BARRENA
Electronics and Computer Science Department
Mondragon Unibertsitatea

Co-supervised by
DR. ALAIN SANCHEZ RUIZ
Ingeteam R&D Europe

In ARRASATE, 20th May 2022

Submitted in partial fulfillment of the requirements for the
PHD PROGRAM IN APPLIED ENGINEERING

Mondragon Unibertsitatea Faculty of Engineering

Ingeteam

Modular Converter Structures for STATCOM Application under Unbalanced Conditions

IOSU MARZO ELGUERO
Electronics and Computer Science Department
Mondragon Unibertsitatea

Supervised by
DR. JON ANDONI BARRENA
Electronics and Computer Science Department
Mondragon Unibertsitatea

Co-supervised by
DR. ALAIN SANCHEZ RUIZ
Ingeteam R&D Europe

Submitted in partial fulfillment of the requirements
for the degree of Doctor of Philosophy under the program:
APPLIED ENGINEERING

Thesis Committee:
President: Dr. Remus Teodorescu *(Aalborg Universitet)*
Vocal: Dr. Oriol Gomis-Bellmunt *(Universitat Politècnica de Catalunya)*
Vocal: Dr. Salvador Ceballos *(Tecnalia Research and Innovation)*
Vocal: Dr. Juan José Valera-García *(Ingeteam R&D Europe)*
Secretary: Dr. Aritz Milikua *(Mondragon Unibertsitatea)*

In ARRASATE, 20th May 2022

Dedicated to my parents

Dedicated to Maialen

Here I leave you a quote, which I have been lucky enough to read every day of the last four years before facing the tasks of the thesis.

"Above all, don't fear difficult moments.
The best comes from them."

— Rita Levi-Montalcini

STATEMENT OF ORIGINALITY

Hereby I declare, that this dissertation is my original authorial work, which I have worked out by my own. All sources, references and literature used or excerpted during elaboration of this work are properly cited and listed in complete reference to the due source.

As author and holder of the intellectual property rights of this doctoral thesis, I authorize *Mondragon Unibertsitatea*, free of charge and exclusively for research and academic purposes, the rights of reproduction and public communication of this document, in part or in its entirety, as long as the original author is cited, the use made of the work is not commercial, and a derivative work is not created from the original one.

Iosu Marzo Elguero
In Arrasate, 20th May 2022

ABSTRACT

The current society is facing several challenges in terms of energy, such as the high dependency on fossil fuels, the high rate of reliance on imported energy, the constant increment in the energy consumption, and the environmental problems caused by these factors. The integration of distributed generation systems, mainly based on renewable energy sources (RES), is the most interesting solution to address these issues.

However, the penetration of RES into the power grid implies certain challenges due to their non-dispatchable nature compared to conventional generation systems. Such systems often use power electronic converters for grid connection instead of synchronous generators, making power systems become converter-dominated. As the power electronic converter-based grid makes it increasingly necessary to employ power equipment with higher voltage and power rating, since their scalable attributes, multilevel Voltage Source Converters (VSCs) based on modular structures are envisioned as the most promising alternatives for that purpose.

In this framework, Flexible AC Transmission System (FACTS) devices, and in particular Static Synchronous Compensators (STATCOMs), play a key role in the evolution of the modern power grids to the future smart grids. The STATCOM, especially the one which employs multilevel VSCs based on modular structures, is applied in an increasingly wider variety of scenarios in which the operation under negative-sequence voltage and/or current conditions stands out.

From the power converter manufacturer point of view, it is not obvious which VSC topology should be used. That is why the purpose of the thesis is to contribute to the body of knowledge in the field of the design of VSCs, with the aim of facilitating the manufacturer to compare and select the most appropriate topology, to design it properly, or to adapt it in order to face the demanding operating requirements that a converter-dominated power grid implies. Among these, this work is mainly focused on the STATCOM application of multilevel VSCs based on modular structures operating under unbalanced voltage and/or current conditions.

To achieve this goal, the operation of the most commonly used high power – MV VSC topologies and their main modulation strategies are first reviewed. Secondly, a methodology which provides valuable information that allows the converter manufacturer to compare and select the most suitable VSC topology for any required application is proposed. Then, a comprehensive review about the operation of multilevel VSCs based on modular structures for different and equivalent unbalanced operating scenarios is presented, in which the STATCOM functionality is included. Having identified the research gap, the reactive power limits of different VSC topologies for STATCOM application operating under unbalanced voltage and/or current conditions are studied and compared. Finally, the control implementation of one of the most interesting topologies for the application under study is evaluated, comparing the performance of different regulators that could be employed. Experimental results obtained from a real-scale 100 kVA prototype in a MV laboratory validate the carried out studies.

RESUMEN

La sociedad actual se enfrenta a varios retos importantes en materia energética, entre los que destacan la gran dependencia de los combustibles fósiles y de la energía importada, el constante aumento del consumo energético, o los problemas medioambientales que estos factores conllevan. La integración de sistemas de generación distribuida, principalmente de origen renovable, se presenta como la solución más interesante para hacer frente a estos desafios.

No obstante, la penetración de generación renovable en la red eléctrica trae consigo ciertos retos debido a su naturaleza no gestionable en comparación con los sistemas de generación convencionales. Los sistemas de origen renovable utilizan a menudo convertidores electrónicos de potencia para su conexión a la red en lugar de generadores síncronos, lo que hace que los sistemas eléctricos hayan pasado a estar dominados por convertidores. Dado que una red eléctrica dominada por convertidores electrónicos de potencia hace cada vez más necesario contar con dispositivos de mayor tensión y potencia, los convertidores multinivel de fuente de tensión (VSC) basados en estructuras modulares se perfilan como una de las alternativas más prometedoras para tal fin.

En este contexto, los sistemas flexibles de transmisión de corriente alterna (FACTS), y en particular los compensadores síncronos estáticos (STATCOM), desempeñan un papel fundamental en la evolución de las redes eléctricas modernas hacia las futuras redes inteligentes. Los STATCOM-s, especialmente los que se basan en convertidores VSC multinivel basados en estructuras modulares, se utilizan en una variedad cada vez más amplia de escenarios en los que destaca el funcionamiento en condiciones desequilibradas de tensión y/o corriente.

Desde el punto de vista del fabricante del convertidor, no es tan evidente qué topología VSC debe utilizarse para cada caso. Es por ello que el propósito de esta tesis doctoral es contribuir al conocimiento en el campo del diseño de VSC-s, con el objetivo de facilitar al fabricante la comparación y selección de la topología más adecuada, su correcto diseño, o su adaptación para hacer frente a los exigentes requisitos de operación que una red eléctrica dominada por convertidores implica. Entre estos requisitos, este tesis doctoral se centra principalmente en la aplicación STATCOM de los convertidores VSC multinivel basados en estructuras modulares que operan ante tensiones y/o corrientes desequilibradas.

Con el fin de cumplir este objetivo, en primera instancia, se desarrolla un estudio sobre el funcionamiento de las topologías VSC de alta potencia más utilizadas y sus principales estrategias de modulación. En segundo lugar, se propone una metodología que proporciona información útil que permitirá al fabricante de convertidores comparar y seleccionar la topología VSC más adecuada para cualquier aplicación requerida. A continuación, se presenta una revisión del estado del arte sobre el funcionamiento de los VSC multinivel basados en estructuras modulares para diferentes escenarios de funcionamiento desequilibrado, en los que se incluye la funcionalidad STATCOM. Una vez identificado el vacío de conocimiento, se estudian y comparan los límites de potencia reactiva de diferentes topologías VSC para la aplicación STATCOM operando en condiciones de tensión y/o corriente desequilibradas. Finalmente, se analiza la implementación de control de una de las topologías más interesantes para la aplicación objeto de estudio, evaluando y comparando el comportamiento de diferentes reguladores que podrían emplearse. Los estudios teóricos realizados se validan mediante resultados experimentales obtenidos a partir de un convertidor a escala real de 100 kVA en un laboratorio de media tensión.

LABURPENA

Gaur egungo gizartea energiaren arloko hainbat erronka garrantzitsuren aurrean aurkitzen da, besteak beste, erregai fosilekiko menpekotasun handia, inportatutako energiarekiko dependentzia, kontsumo energetikoaren etengabeko gorakada, edota faktore hauek eragiten dituzten ingurumen arazoak. Sorkuntza banatuko sistemen integrazioa, bereziki iturri berriztagarrietan oinarritutakoa, arazo horiei aurre egiteko aukera interesgarriena da.

Hala ere, bere izaera kudeaezina dela eta, sorkuntza berriztagarria sare elektrikoan integratzeak zenbait erronka dakartza ohiko sorkuntza sistemekin alderatuta. Gainera, iturri berriztagarrien sistemek, sorgailu sinkronoen ordez, potentzia bihurgailu elektronikoak erabiltzen dituzte sarera konektatzeko. Bihurgailuak nagusi diren sare elektrikoak tentsio eta potentzia handiagoko gailuak erabiltzea eskatzen du, eta horretarako, tentsio iturridun bihurgailu (VSC) multinibel modularrak alternatiba erakargarrienetariko bat dira.

Testuinguru honetan, "FACTS" bezala ezagutzen diren korronte alternoko transmisio gailuek, eta bereziki konpentsatzaile sinkrono estatikoek (STATCOM), funtsezko eginkizuna dute sare elektriko modernoen eboluzioan etorkizuneko sare adimendunerantz. STATCOM-ak, batez ere VSC bihurgailu multinibel modularretan oinarrituta daudenak, gero eta aplikazio ugariagoetan erabiltzen dira, non tentsio eta/edo korronte desorekatuen aurrean funtzionatzea nabarmandu daitekeen.

Bihurgailu fabrikatzailearen ikuspuntutik, ez da hain agerikoa zein VSC topologia erabili behar den. Hori dela eta, doktorego tesi honen helburua VSC diseinuaren alorreko ezagutzan laguntzea da, fabrikatzaileari topologiak konparatu eta egokiena hautatzen errazteko, era egokian diseinatzeko, edota egokitzapenak egiten laguntzeko helburuarekin, bihurgailuek dituzten eskakizun zorrotzei aurre egiteko. Eskakizun horien artean, tesi hau VSC bihurgailu multinibel modularrez eraikitako STATCOM-en tentsio zein korronte desorekatuen funtzionamenduan zentratzen da.

Helburu hori betetzeko, lehenik eta behin, potentzia handiko erdi-tentsioko VSC topologien eta haien modulazio estrategia nagusien funtzionamenduari buruzko ikerketa bat garatzen da. Bigarrenik, metodologia bat proposatzen da, bihurgailu fabrikatzaileri behar duen edozein aplikaziorako VSC topologia egokiena konparatu eta hautatzeko informazio baliagarria eskaintzen diona. Jarraian, VSC bihurgailu modular multinibelen funtzionamendu desorekatu desberdinei buruzko literatura zientifikoaren errebisio bat egiten da, STATCOM-aren funtzionalitatea barne. Ezagutza hutsunea identifikatu ondoren, tentsio eta/edo korronte desoreken aurrean funtzionatzen duen STATCOM aplikaziorako VSC topologia desberdinen potentzia erreaktiboaren mugak aztertu eta konparatzen dira. Azkenik, aztergai dugun aplikaziorako topologia interesgarrienetariko baten kontrol inplementazioa ebaluatzen da, erabil daitezkeen kontroladore desberdinen portaera aztertu eta konparatzen delarik. Erdi-tentsioko laborategi batean, 100 kVA-ko eskala errealeko bihurgailu batetik lortutako emaitza esperimentalek egindako azterketa teorikoak balioztatuko dituzte.

ACKNOWLEDGEMENTS

Nire ingurukoengatik ez balitz, ez zinateke errusiar mendi bat izan den tesi hau irakurtzen egongo. Horregatik, nahiz eta ezinezkoa den paragrafo gutxi batzutan nigan eragina izan duten, edota azken urte hauek eramangarriagoak izaten lagundu duten guzti haiek aipatzea, lerro hauen bitartez batzuk nabarmendu nahiko nituzke.

Lehenik eta behin, *Mondragon Unibertsitatea*-ri eta *Ingeteam* enpresari doktoretza tesi hau egiteko aukera eskertu behar diet, baita azken egunerarte eman didaten babesa ere. Plazer hutsa izan da bi erakunde hauekin lan egitea. Espainiako *Hezkuntza eta Lanbide Hezikeeta Ministerioa*-ri ere eskerrak; bai tesi hau burutu ahal izateko emandako dirulaguntzarengatik, eta baita irakaskuntzan lehen urratsak ematen hasteko bultzadagatik.

Bereziki, tesi honen zuzendari baino gehiago izan ditudan bi horiei eskerrak. Jonan, Alain, ezingo dizuet inoiz eskertu proiektu honetan eman didazuen guztia. Eskerrik asko ikerkuntzaren mundu hau deskubritzeko parada emateagatik, eta sarri, behar izan dudan sostengua izateagatik. Eskerrik asko zuen jakintza eta esperientzia oparitzeagatik, lanarekiko zuen pasioa trasmititzeagatik, eta baita ekaitz egunetan barealdia aurkitzen laguntzeagatik.

Gonzalo Abad ere modu berezian eskertu nahiko nuke, lehenengo egunetik proiektu honetan jarritako interesarengatik. Teknikoki egindako ekarpen guztiez gain, zurekin partekatutako gogoetak oso aberasgarriak izan dira. Ignacio Muguruzari ere eskerrak, zorte handia izan dut zu bezalako laguntzaile bat alboan izateaz. Ez ginateke iritsi garen lekura iritsiko zure ekarpenengatik ez balitz. Aritz Milikuari ere eskertu behar diot emandako laguntza guztia. Baita *Elektronika* departamentuko lankide guztiei.

Ezin naiz *Ingeteam*-eko kideetaz ahaztu. Batez ere Joseba Arzari eskerrak, lehenengo egunetik nigan jarritako konfiantza guztiagatik, eta proiektu honetan sinisteagatik. Juanjo Valera, Eneko Olea eta Iñigo Rebollo ere eskertu nahiko nituzke. Emaitza esperimentalak aurrera eramatea posible egin duen Hector Fernandez-Rebolledari ere esker bereziak.

Hainbeste bazkari, merienda zein bulego ordu partekatu ditugun Kepa Iribar, Jose Luis Abellán, Carlos Ruiz, Aitor Bilbao, Xabi Sinde eta *Ingeteam gela*-ko beste lankide guztiei ere eskerrak eman behar dizkiet lanegunak eramangarriago egiteagatik. Aipamen berezia ere Ander Udabe, Julen Paniagua, Imanol Eguren eta Jon Santisori. Tesiak lagun onak ere eman dizkidalako. Eskerrik zintzoenak azken lau urteetan alboan izan ditudan lankideei, haien hitzetan aurkitu baitut behin baino gehiagotan aurrera jarraitzeko kemena.

Kuadrillakoei eta lagun minei ere bihotzez eskerrik asko, bizikletan, gimnasioan, mendian, soziedadean, zein ordu txikitan ihesbide izateagatik. Eta nola ez, nire eskerrik sentikorrenak etxekoei. Aita, ama, eskerrik asko guztiagatik. Hau guztia posible egiteagatik, emandako maitasunagatik, eta inoiz ez dela nahikoa irakasteagatik. Gertu zein urrun, babesleku izateagatik. Zuek zaretelako naiz gaur naizena. Ez dakit zer egingo nukeen zuek gabe. Eta zuek, zuek bai egin duzuela tesi bat nirekin!

Azkenik zuri, Maialen, eskua eman eta sekula ez askatzeagatik. Nola diren gauzak, tesiaren abentura hau hasi nuenean ez genuen elkar ezagutzen, eta begira orain. Eskerrak eman behar dizkizut eskainitako maitasunagatik, izateagatik, eta egoteagatik. Ezin izango dizkizut sekula nahikoa eskertu tesiak iraun duen denboran nire egunerokotasuna errazteko egin dituzun esfortzu titanikoak, ezta nire marmar zein pozak jasateko izan duzun pazientzia amaigabea ere. Onenetan eta txarrenetan hor egoteagatik. Zin dagizut datozen urteak lasaiagoak izango direla, merezi duzu eta!

Guztioi, mila esker!

CONTENTS

LIST OF FIGURES

LIST OF TABLES

ABBREVIATIONS

3L NPC	**3**-**L**evel **N**eutral **P**oint **C**lamped
5L NPC/HB	**5**-**L**evel **N**eutral **P**oint **C**lamped **H**-**B**ridge
AC	**A**lternating **C**urrent
APOD	**A**lternative **P**hase **O**pposite **D**isposition
BESS	**B**attery **E**nergy **S**torage **S**ystem
CHB	**C**ascaded **H**-**B**ridge
DC	**D**irect **C**urrent
DCHB	**D**elta-connected **C**ascaded **H**-**B**ridge
DFE	**D**iode **F**ront **E**nd
DMM	**D**ouble **M**in-**M**ax
DSC	**D**elayed **S**ignal **C**ancellation
DTHI	**D**ouble **T**hird-**H**armonic **I**njection
FACTS	**F**lexible **AC** **T**ransmission **S**ystem
FFR	**F**ast **F**requency **R**esponse
FFZSI	**F**undamental-**F**requency **Z**ero-**S**equence **I**njection
HB	**H**-**B**ridge
HVDC	**H**igh **V**oltage **D**irect **C**urrent
IGBT	**I**nsulated **G**ate **B**ipolar **T**ransistor
IGCT	**I**ntegrated **G**ate **C**ommutated **T**hyristor
IPD	**I**n-**P**hase **D**isposition
LCC	**L**ine-**C**ommutated **C**onverter
LSC-PWM	**L**evel-**S**hifted **C**arrier **P**ulse **W**idth **M**odulation
LVRT	**L**ow-**V**oltage **R**ide-**T**hrough
MMC	**M**odular **M**ultilevel **C**onverter
MPPT	**M**aximum **P**ower **P**oint **T**racking
MV	**M**edium **V**oltage
OZSI	**O**ptimal **Z**ero-**S**equence **I**njection
PCC	**P**oint of **C**ommon **C**oupling
PEBB	**P**ower **E**lectronics **B**uilding **B**lock
PI	**P**roportional-**I**ntegral
PLL	**P**hase **L**ocked-**L**oop
POD	**P**hase **O**pposite **D**isposition
PR	**P**roportional-**R**esonant
PR_d	**P**roportional-**R**esonant with **d**elay compensation
PSC-PWM	**P**hase-**S**hifted **C**arrier **P**ulse **W**idth **M**odulation
PV	**P**hotovoltaic
PWM	**P**ulse **W**idth **M**odulation

RES	**R**enewable **E**nergy **S**ources
RMS	**R**oot **M**ain **S**quare
RTHI	**R**educed **T**hird-**H**armonic **I**njection
SHE	**S**elective **H**armonic **E**limination
SOC	**S**tate-**O**f-**C**harge
STATCOM	**S**tatic **S**ynchronous **C**ompensator
SVM	**S**pace **V**ector **M**odulation
SWZSI	**S**quare-**W**ave **Z**ero-**S**equence **I**njection
THD	**T**otal **H**armonic **D**istortion
THD_i	Current **T**otal **H**armonic **D**istortion
THD_v	Voltage **T**otal **H**armonic **D**istortion
THI	**T**hird-**H**armonic **I**njection
THSWI	**T**hird-**H**armonic **S**quare-**W**ave **I**njection
VPI	**V**ector **P**roportional-**I**ntegral
VSC	**V**oltage **S**ource **C**onverter
WMM	**W**eighted **M**in-**M**ax
WPP	**W**ind **P**ower **P**lant
YCHB	Star-connected (**Y**) **C**ascaded **H**-**B**ridge

Chapter 1

INTRODUCTION

This first chapter gives a general perspective of the framework and the aspects that motivate the formulation and realization of this PhD thesis. The context of the work and the topic of the investigation are introduced, and the objectives of the thesis are also identified. Then, the articles that have been published, and those that are currently being reviewed are listed, as well as their main contributions. Additionally, an outline of the document is given.

1.1 FRAMEWORK

The greenhouse gas emissions generated by the supply of energy services have contributed significantly to the historic increase in the concentration of these gases in the atmosphere. For more than a century, the use of fossil fuels has augmented to become the predominant energy supply, a situation that has led to a rapid increase in carbon dioxide (CO_2) emissions [1]. The dependency on fossil fuel-based conventional generation, and the high rate of reliance on imported energy —especially in Europe—, among others, have led to an unsustainable energy system. The high energy dependence on other countries results in energy supply instability, as well as in the continuous impact on the economy, consequences that we are experiencing recently. Note that in last years, more than a half of the European Union energy needs were met by net imports [2]. Besides, over the last decades, the global energy demand is increasing at an accelerating rate, with a few exceptions, due to the modernization of underdeveloped countries and a strong global economy [3].

The aforementioned rapid increment in the energy consumption, the concern about climate change, and the high energy dependency [1]–[3] have motivated great research effort to develop alternative generation systems [4] and technology solutions for their integration in the power system [5], [6]. The ongoing energy transition is transforming the fossil fuel-based energy system of today into a more sustainable future energy system [7]. This transition is accelerated by the *Paris Agreement*, which aims to significantly reduce the global CO_2 emission levels [8].

The necessity to reduce the power sector carbon footprint has made generating electricity by using renewable energy sources (RES) become an important topic. These non-conventional sources can actively contribute to decrease greenhouse gas emissions, increase the grid power capacity, reduce the energy dependency, prevent the saturation of power grid lines, reduce electricity prices, and improve the overall efficiency [9].

However, generating energy from RES also has its disadvantages. Their non-dispatchable nature results in many generation plants requiring greater flexibility to accommodate the changes in generation [10]. Conventional generators, such as coal and gas plants, are considered dispatchable because they can change their power output to meet changes in load. In contrast, RES such as the solar photovoltaic (PV) and Wind Power Plants (WPPs) are different from most thermal generators, mainly because of their variable and uncertain power output determined by local weather conditions [11], [12].

Apart from grids continuous growth due to power consumption increment, traditional power systems are evolving due to the progressive integration of distributed RES, which has changed electrical power system functioning, emphasizing on system regulation and control. Generally, RES use inverters to connect to the grid instead of synchronous generators. Thus, as more RES are added into power systems, the grid requires more power electronic converter-based generators, becoming much more distributed than the current power system, which is dominated by centralized synchronous generation units (see Fig. 1.1). In other words, as non-conventional variable generation sources are introduced in the system, actual transmission and distribution grids become converter-dominated [4]–[6], [9]–[12].

Moving towards a future electricity system dominated by power electronic converters involves significant changes in power system dynamics. Specifically, as new converter-based sources replace synchronous machines, the amount of rotational inertia in power systems decreases, accompanied with the loss of stabilizing control mechanisms that are present in conventional generators [13]. In this sense, frequency regulation is an essential control mechanism for the correct operation of the grid. Besides, when integrating RES into the grid there are a number of additional challenges associated with large power electronic converter penetration, such as power quality issues [14].

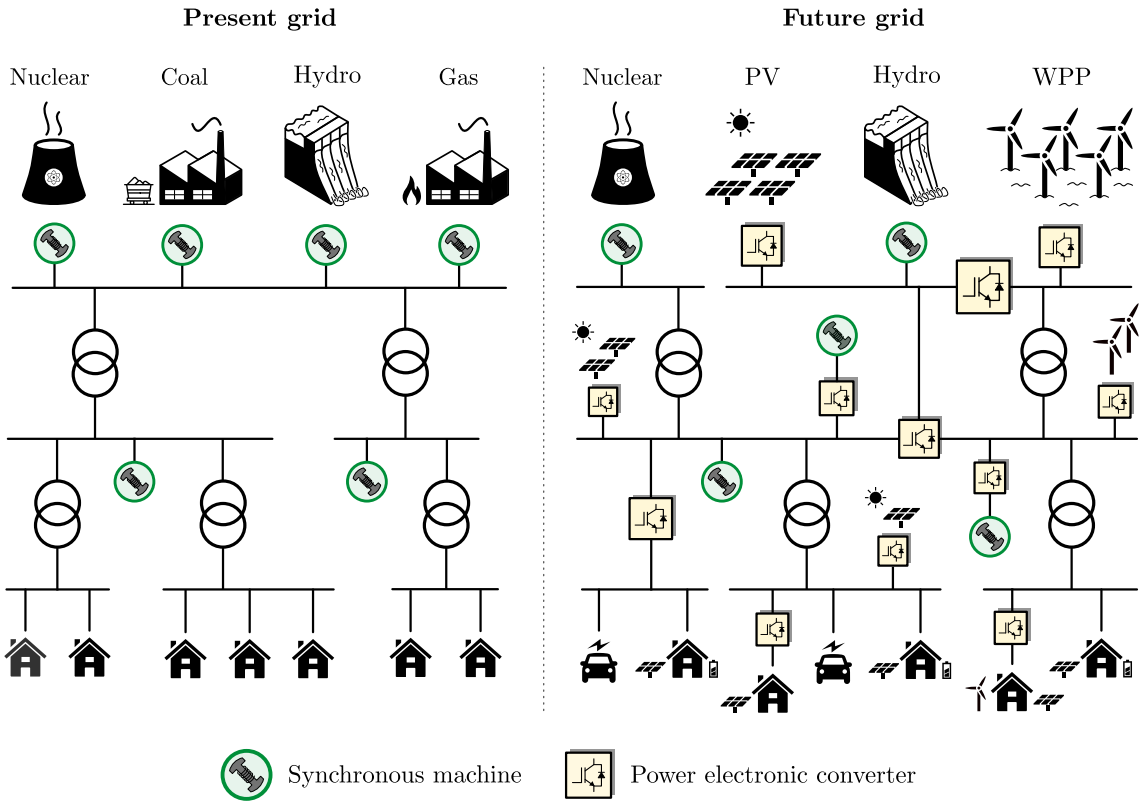

Fig. 1.1. Scheme of the present grid dominated by large synchronous machines, and the future grid dominated by power electronic converters.

Battery Energy Storage Systems (BESS) are of vital importance in order to handle with the variability of RES and facilitate their integration in the grid [15]. It is a technology that enables power system operators and utilities to store energy for later use. A BESS is an electrochemical device that collects energy when there is an excess of generation, and then discharges it at a later time to provide electricity when there is not enough energy to meet demand —e.g., during moments without wind or sun, peak demands or power outages. In addition, BESS can also provide grid services that conventional fossil fuel-based sources would no longer provide with a high RES penetration —such as Fast Frequency Response (FFR), inertia emulation, or voltage regulation [16].

Flexible AC Transmission System (FACTS) devices also play a key role in the evolution of the modern power grids to the future smart grids. These devices increase the reliability of ac grids and reduce power delivery costs, improving the transmission quality and efficiency by supplying inductive or reactive power to the grid [17]–[24]. Foremost among FACTS, the Static Synchronous Compensator (STATCOM) is nowadays an essential device in both industry and power grid applications, since facilitates the integration of large power consuming industrial loads or RES, by fulfilling the requirements imposed by grid codes.

The aforementioned RES, BESS and FACTS devices generally use Voltage Source Converters (VSCs) to connect to the grid. The development of self-commutated semiconductor devices [25] (i.e., cost reduction, higher switching frequencies, larger current rating, higher insulation voltage tolerance, etc.), and fast digital controllers [26] have accelerated the introduction of VSCs in industrial motor driven processes [27], and in utility applications such as the integration of RES, FACTS, and High Voltage Direct Current (HVDC) connections worldwide [5]. Therefore, as Fig. 1.1 shows, the concept of a power electronic converter-dominated grid takes shape as the number of grid-connected VSCs increase in today's electric power system.

Within VSCs, the two-level (2L) structure has been the most pioneering. However, the limited voltage and power rating and the supply quality issues that 2L configurations offer makes it difficult the use of these in high power – Medium Voltage (MV) scenarios such as utility applications, arc-furnace loads, or railway traction drives. The emergence of new multilevel VSC topologies [28]–[36], accompanied with the evolution of existing semiconductor switches [25], have allowed to increase the power and voltage ratings of power electronic converters. This means that the converter could be connected directly to MV levels without the need of a bulky step-up transformer. Moreover, this has permitted to face the demanding operating requirements that massive RES integration imply [37].

Multilevel VSCs have received widespread attention because of their attractive features such as output currents with low harmonic distortion or lower switching losses [28]–[30], [32]–[36]. Besides the mentioned advantages of multilevel VSCs, since their scalable attributes which facilitate the connection to MV levels, those based on modular structures are envisioned as some of the most prominent topologies available for grid and industry applications [34], [38]–[40]. These structures are very well suited for high power – MV FACTS devices, large-scale PV power integration, or BESS. Connecting them to different power cells, modular structures allow to separate PV module strings to maximize the solar power generation [41]–[43]. Likewise, connecting each battery unit independently to separate power cells, the power can be distributed unequaly depending on the state-of-charge (SOC) of each one [44].

The requirements that the VSCs connected to the grid must fulfill are becoming more and more demanding. Among these challenging operating scenarios, the unbalanced operation should be highlighted. Just to give some examples, dealing with the unbalanced power generation of large-scale PV plants [41]–[43], or with the unequal power distribution in BESS [44]–[46], suppose a challenge when delivering balanced currents to the grid. Requirements from grid codes have started to demand negative-sequence voltage and/or current injection and withstanding capability to the VSCs connected to their power grid [37], [47]–[52];

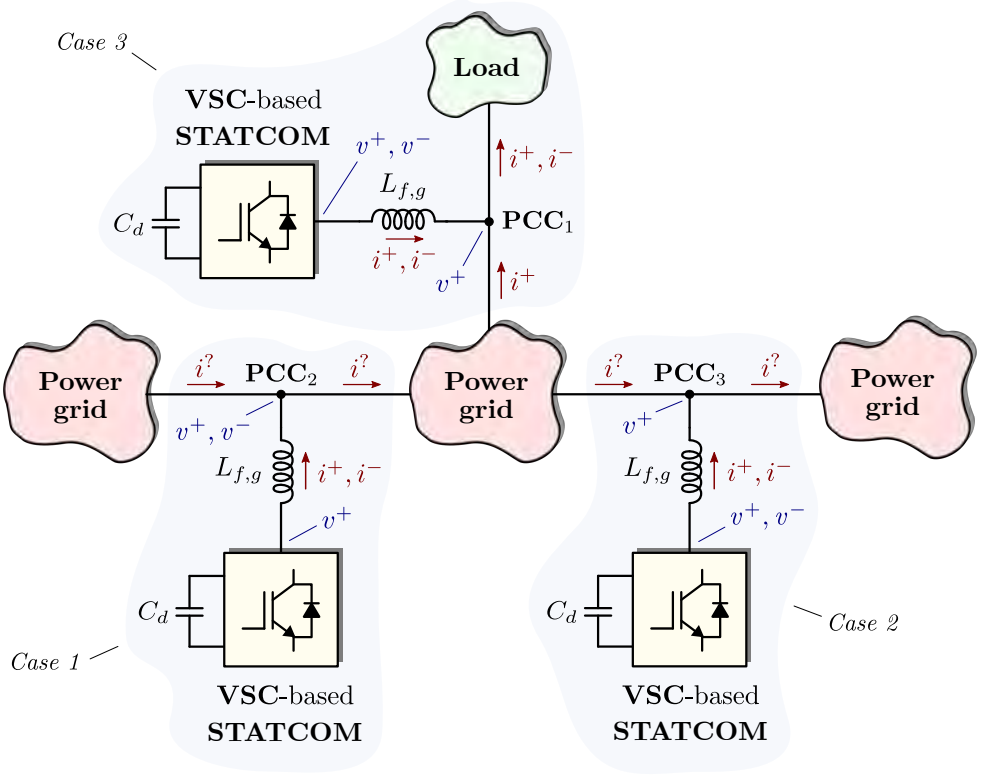

Fig. 1.2. Possible unbalanced scenarios that the VSC-based STATCOM might face.

especially to STATCOMs. The STATCOM, particularly the one which employs multilevel VSCs based on modular structures, is applied in an increasingly wider variety of scenarios in which the operation under unbalanced voltage and/or current conditions stands out [53], [54]. These conditions might appear under asymmetrical faults, or connected to unbalanced loads such as railway traction drives, adjustable speed drives, or arc-furnaces [29]. Even, unbalanced conditions can occur in steady-state operation [49], [50].

Fig. 1.2 shows some examples of the unbalanced power grid scenarios that the VSC-based STATCOM might face. Until recently, when an unbalanced voltage appeared in the Point of Common Coupling (PCC), the VSC was normally disconnected. As *case 1* shows, nowadays, it might be demanded by the corresponding grid code to withstand a small amount of negative-sequence voltage in the power grid [49], [50]. In this case, the VSC can operate with a classical controller, generating only positive-sequence voltage in its output terminals, and withstanding the generated negative-sequence current circulation. Or, as in *case 2*, the technical requirement might even demand the VSC-based STATCOM to compensate the grid asymmetry, by means of generating also a negative-sequence voltage in its output and cancelling it in the PCC [51]. In *case 3*, the STATCOM is used to completely compensate the unbalanced current due to the presence of an unbalanced load [54]. The operation under all these conditions might involve certain problems for different VSC topologies, which could limit the maximum power that the STATCOM could deliver to the power grid.

In this grid paradigm, from the power converter manufacturer point of view, it is not obvious which VSC topology should be used; configurations which behave properly under balanced conditions, might cease to be so interesting depending on the application demands. As grid codes did not demand power converters to face these operating conditions before, deeper analyses are necessary in order to select the most suitable VSC topology, and to design it properly in order to face the aforementioned unbalanced operating conditions.

1.2 OBJECTIVES

This work is mainly focused on high power – MV grid-connected VSCs, with special focus on the STATCOM application of multilevel VSCs based on modular structures operating under unbalanced voltage and/or current conditions. The main goal of this doctoral thesis is to facilitate the power converter manufacturer to compare and select the most appropriate topology for each operating requirement that will be demanded to the converter, as well as to adequately control the mentioned modular VSC topologies under unbalanced conditions. In order to reach this target, the following specific objectives were defined:

[O1] Develop a methodology which provides valuable information that allows the converter manufacturer to compare and select the most appropriate VSC topology for any required application.

[O2] Study and compare the limitations of Cascaded H-Bridge STATCOMs in star and delta configurations to withstand negative-sequence current (*case 1* of Fig. 1.2).

[O3] Study and compare the limitations of single-phase dc-link and three-phase dc-link VSC topologies for STATCOM application operating under unbalanced voltage and/or current conditions.

[O4] Analyze the control implementation of star- and delta-connected Cascaded H-Bridge configurations to operate under unbalanced conditions.

1.3 LIST OF PUBLICATIONS

The most relevant technical contributions of this PhD thesis have been published in the form of journal articles and conference proceedings. Below there is a summary of these publications.

Journal Articles

PUBLICATION 1: Ref. [55]

[J1] I. Marzo, A. Sanchez-Ruiz, J. A. Barrena, G. Abad, and I. Muguruza, "Power balancing in cascaded H-bridge and modular multilevel converters under unbalanced operation: a review", *IEEE Access*, vol. 9, pp. 110525-110543, 2021.

This paper provides a literature review about the operation and the solutions for multilevel VSCs based on modular structures under unbalanced conditions. The paper identifies, classifies, and analyzes the intercluster active power balancing strategies for the adequate operation of the Cascaded H-Bridge (CHB) and the Modular Multilevel Converter (MMC) in some typical unbalanced operating scenarios: the STATCOM under unbalanced voltage and/or current conditions, the unequal power generation in large-scale PV power plants, and the uneven power distribution in a BESS. Each of the applications is independently studied so as to provide a comprehensive analysis of the alternative techniques found in the specialized literature, clearly explaining their respective strengths and drawbacks. Several future challenges are identified during the study, which will involve greater research effort in this key research topic.

PUBLICATION 2: Ref. [56]

[J2] I. Marzo, J. A. Barrena, A. Sanchez-Ruiz, G. Abad, H. Fernandez-Rebolleda, and I. Muguruza, "Reactive power limits of cascaded H-bridge STATCOMs in star and delta configuration under negative-sequence current withstanding", *International Journal of Electrical Power and Energy Systems*, vol. 142, p. 108267, 2022.

This paper investigates and compares the reactive power limits of CHB STATCOMs in star (YCHB) and delta (DCHB) configuration to withstand negative-sequence current (*case 1* of Fig. 1.2). Zero-sequence voltage for the YCHB and zero-sequence current for the DCHB are injected in order to correct the intercluster uneven active power distribution and thus to preserve dc-link voltage balancing. Both solutions will have an impact on the power rating of the converter. This work clearly quantifies the reactive power limits of each CHB STATCOM configuration depending on the current unbalance at converter terminals, by means of a systematic procedure. Improved explicit expressions of the zero-sequence current in the DCHB are also provided. Experimental results obtained from a real-scale set-up in a MV laboratory validate the theoretical analysis.

PUBLICATION 3 (*under review*): Ref. [57]

[J3] I. Marzo, I. Muguruza, J. A. Barrena, A. Sanchez-Ruiz, G. Abad, and H. Fernandez-Rebolleda, "Zero-sequence controller requirements and comparison for a delta-CHB STATCOM under unbalanced conditions", submitted to *International Journal of Electrical Power and Energy Systems*, July 2022.

The control loop of the zero-sequence current injected in the DCHB STATCOM to guarantee dc-link capacitor voltage balancing under unbalanced voltage and/or current

conditions is analyzed in this paper. The particularities of the system are identified in order to determine the requirements that the implemented controller must fulfill. Considering these requirements, appropriate transient response and stability margin indicators are defined to quantify and evaluate the performance of different controllers that could be employed —Proportional-Resonant controller (PR), PR controller with delay compensation (PR_d), and Vector Proportional-Integral controller (VPI) are proposed in this paper. Based on the defined indicators a comparison of the controllers is presented, where the VPI is the most appropriate among the studied control techniques. Experimental results validate the analytical model of the controllers and their performance.

Conference Proceedings

PUBLICATION 4: Ref. [58]

[C1] I. Marzo, J. A. Barrena, and A. Sanchez-Ruiz, "Methodology to evaluate converter structures based on 3L NPC PEBBs", in *IECON 2020 – The 46th Annual Conference of the IEEE Industrial Electronics Society*, Singapore, 2020, pp. 4107-4114.

A methodology to evaluate different multilevel VSC structures working under any operating scenario is presented in this conference paper. The methodology is integrated into a software-based tool. This tool enables to obtain valuable information to compare, select and design the converter Power Electronics Building Block (PEBB) combination that better suits certain operating requirements. In order to evaluate its potential, the proposed methodology is applied to compare some multilevel VSC structures based on the interconnection of three-level Neutral Point Clamped (3L NPC) PEBBs in two operating case studies.

PUBLICATION 5: Ref. [59]

[C2] I. Marzo, J. A. Barrena, A. Sanchez-Ruiz, G. Abad, and I. Muguruza, "Reactive power limits of single-phase and three-phase dc-link VSC STATCOMs under negative-sequence voltage and current", in *IECON 2021 – The 47th Annual Conference of the IEEE Industrial Electronics Society*, Toronto, 2021, pp. 1-8.

This last conference paper analyzes and compares the reactive power limits of single- and three-phase configured dc-link VSC structures for STATCOM to operate with negative-sequence voltage and current. While the 3L NPC is used as an example of a three-phase dc-link topology, the CHB is used as a single-phase dc-link case, in both star and delta configurations. The MMC is also considered as a combination of both dc-link configurations. The conclusions drawn are generic whichever the PEBB used in each VSC structure.

1.4 OUTLINE OF THE DOCUMENT

The following lines contain a short summary of each of the upcoming chapters. Fig. 1.3 depicts the structure of the thesis showing how the proposed partial objectives and contributions relate to each chapter.

CHAPTER 2

This chapter describes the high power multilevel VSC topologies studied throughout the document, and proposes a methodology to compare and select the most appropriate among them. Firstly, a general overview about the multilevel VSC topologies and their main modulation strategies is given. Then, a methodology to evaluate different converter structures is presented, and it is applied to compare some multilevel VSC structures based

on the interconnection of 3L NPC PEBBs in two case studies. The proposed methodology resulted in the first publication of the thesis [C1].

CHAPTER 3

The conclusions of the previous chapter motivate the research project around this doctoral thesis to further study multilevel VSCs based on modular structures, especially for those high power – MV applications where the power converter is required to operate under unbalanced conditions. Previous investigations regarding the operation and the solutions for modular structures under unbalanced conditions have already addressed this topic, but information is dispersed over a wide number of sources. That is why this chapter identifies, classifies, and analyzes the intercluster active power balancing strategies for the adequate operation of the CHB and the MMC in some typical unbalanced operating scenarios: the STATCOM under unbalanced voltage and/or current conditions, the unequal power generation in large-scale PV power plants, and the uneven power distribution in BESS. Each of the applications is independently studied so as to provide a comprehensive analysis of the alternative techniques found in the specialized literature, clearly explaining their respective strengths and drawbacks. Several future challenges are identified during the study, and a research gap is identified. The literature review provided in this chapter resulted in publication [J1].

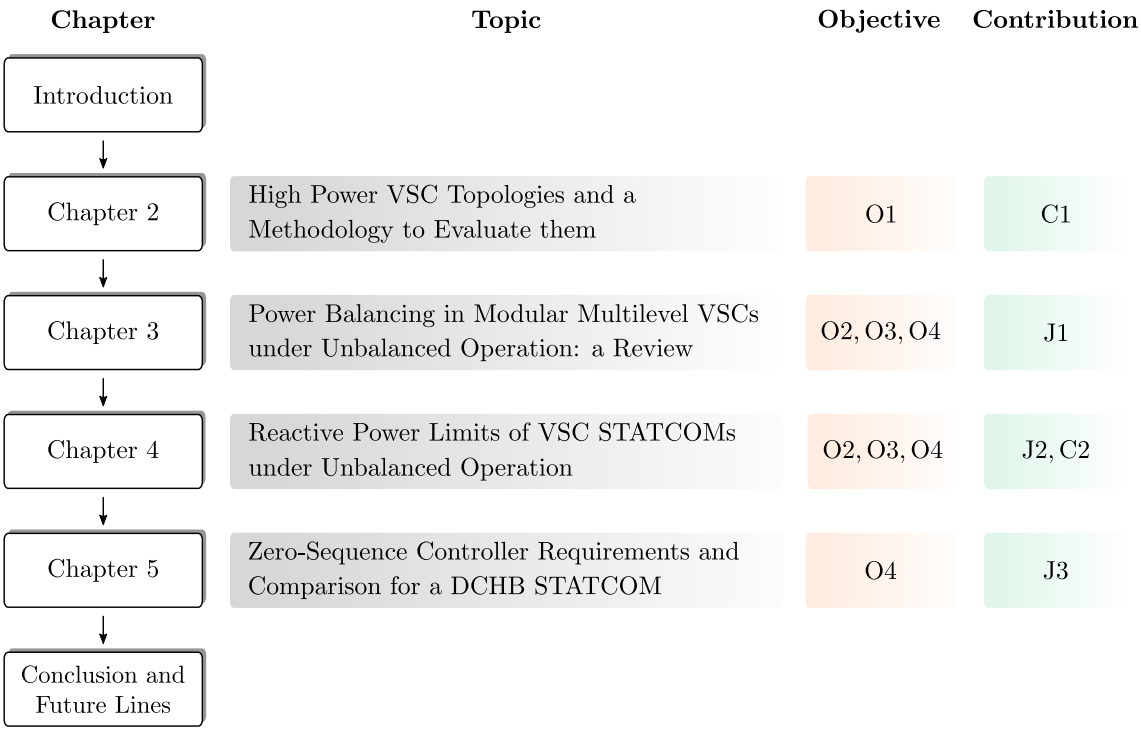

Fig. 1.3. Structure of the chapters and their relation to the specific objectives and main contributions.

CHAPTER 4

Based on the knowledge gap identified, the fourth chapter analyzes the operation of the YCHB, DCHB, MMC, and 3L NPC structures for STATCOM application operating under unbalanced voltage and/or current conditions. The limitations that these VSC structures present in the application under study are further investigated, with the aim of quantifying the reactive power limits and thus be able to compare them with each other. First of all, the YCHB and the DCHB are compared in a negative-sequence current withstanding scenario (*case 1* of Fig. 1.2), study which is validated by experimental results. Secondly,

the MMC and 3L NPC topology are added to the analysis, extending the study to include also the negative-sequence voltage in the comparison of the reactive power limits. The first study resulted in publication [J2], and the second in publication [C2].

CHAPTER 5

The fifth chapter, which led to publication [J3], addresses the analysis of the zero-sequence current control loop of the DCHB STATCOM to operate under unbalanced voltage and/or current conditions. Firstly, the particularities of the system are identified in order to determine the requirements that the implemented controller must fulfill. Then, considering these requirements, appropriate transient response and stability margin indicators are defined to quantify and evaluate the performance of different controllers that could be employed —PR, PR_d and VPI. Based on the defined indicators a comparison of the controllers is presented, and finally, experimental results validate the analytical model of the controllers and their performance.

CHAPTER 6

This chapter closes the dissertation of the PhD thesis, listing the main conclusions of the project, discussing the degree of accomplishment of the specific objectives defined, and suggesting some challenges and opportunities for further research, which could be the continuation of this work.

Chapter 2

HIGH POWER VOLTAGE SOURCE CONVERTERS AND AN EVALUATION METHODOLOGY

This chapter provides a general overview about multilevel Voltage Source Converter (VSC) topologies, and their main modulation strategies, especially those that have been studied in the course of the PhD thesis. A methodology to evaluate different converter structures is presented, and it is applied to compare some multilevel VSC structures based on the interconnection of three-level Neutral Point Clampled (3L NPC) Power Electronics Building Blocks (PEBBs) in two case studies. The latter work resulted in publication [C1].

2.1 INTRODUCTION

As a result of technology advancements in self-commutated semiconductor devices, such as Insulated Gate Bipolar Transistors (IGBTs) or Integrated Gate Commutated Thyristors (IGCTs) [25], hard-switched multilevel Voltage Source Converters (VSCs) have been recommended for high power – MV applications. These converter structures present very attractive characteristics such as waveform quality, lower switching frequencies (lower switching losses), output currents with low harmonic distortion, small common-mode voltage, and small electromagnetic interference noise [28]–[36]. They are increasingly used both grid-connected or motor-connected, in RES integration, other power grid applications, petrochemical, mining, steel and metals, railway traction, and marine propulsion [5], [27]. This chapter provides a description of the multilevel VSCs studied in this PhD dissertation, as well as the main modulation strategies employed.

As multilevel VSC topology-based equipment prevails in MV applications, the operating range of these converters is getting increasingly wider. A common choice to increase the power rating is to combine basic Power Electronics Building Blocks (PEBBs) in modular structures. PEBBs are well known power electronic stacks which are interconnected forming a converter with increased power capability. By doing so, the reliability and the robustness are increased whereas the total cost of the overall power equipment design is decreased. Nowadays, PEBB-based multilevel VSC structures prevail in high power – MV applications [60]–[62].

Since there is a demand of new operating requirements, such as unbalances in the grid or asymmetrical fault operation, the way PEBBs are interconnected is not obvious and a deep analysis needs to be carried out to define the most suitable VSC structure. Accordingly, this chapter also presents a methodology to evaluate different MV multilevel VSC structures working under any operating scenario. The methodology is integrated into a software-based tool. This tool enables to obtain valuable information to compare, select, and design the converter PEBB combination that better suits certain operating requirements. In order to evaluate the potential, the proposed methodology is applied in two case studies to compare four particular VSC structures. However, this methodology can be applied for any VSC topology and PEBB connection structure, and can be extended to any operating point.

2.2 MODULATION TECHNIQUES FOR VSC-S

Although the study of modulation strategies is out of the scope of this doctoral thesis, this section gives a general overview of the most popular modulation techniques employed in two-level (2L) and multilevel VSCs, which are used throughout the dissertation. What this section describes is mainly based on references [36] and [63].

2.2.1 Pulse Width Modulation for 2L VSC-s

First of all, even its utilization in the aforementioned high power – MV applications is quite limited due to the reduced power and insufficient output power quality, it is necessary to understand the operation of the simplest VSC structure; the *two-level converter*. Then, through the 2L VSC, the fundamental modulation strategies, and more advanced multilevel VSC topologies can be studied.

The main function of VSCs is to convert a fixed dc voltage to a three-phase ac voltage with variable amplitude and frequency. The 2L VSC is composed of six active switches (S_1 to S_6) with a free-wheeling diode in anti-parallel with each switch. Depending on the dc-link operating voltage of the converter (V_{dc}), each group of switches consists of two

or more IGBT or IGCT semiconductor devices connected in series [64]. It is known as "two-level" converter because the waveform of the terminal voltage v_{aN} has only two levels, $+V_{dc}$ and 0. Fig. 2.1 shows the simplified scheme of a 2L VSC.

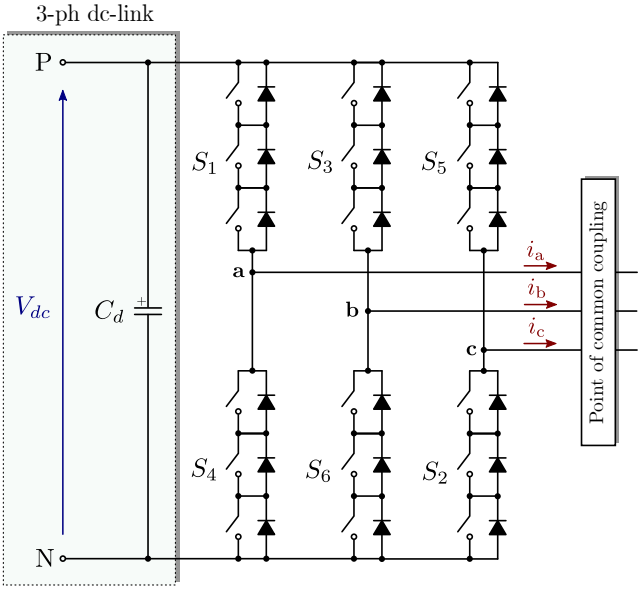

Fig. 2.1. Simplified circuit diagram of the 2L VSC.

The principle of the sinusoidal *Pulse Width Modulation* (PWM) is based on the comparison between three-phase sinusoidal modulating waves ($v_{m\text{-a}}, v_{m\text{-b}}, v_{m\text{-c}}$) and a triangular carrier wave (v_{cr}), which determines the operation of the switches [65]. Fig. 2.2 illustrates the principle of the sinusoidal PWM scheme for a 2L VSC.

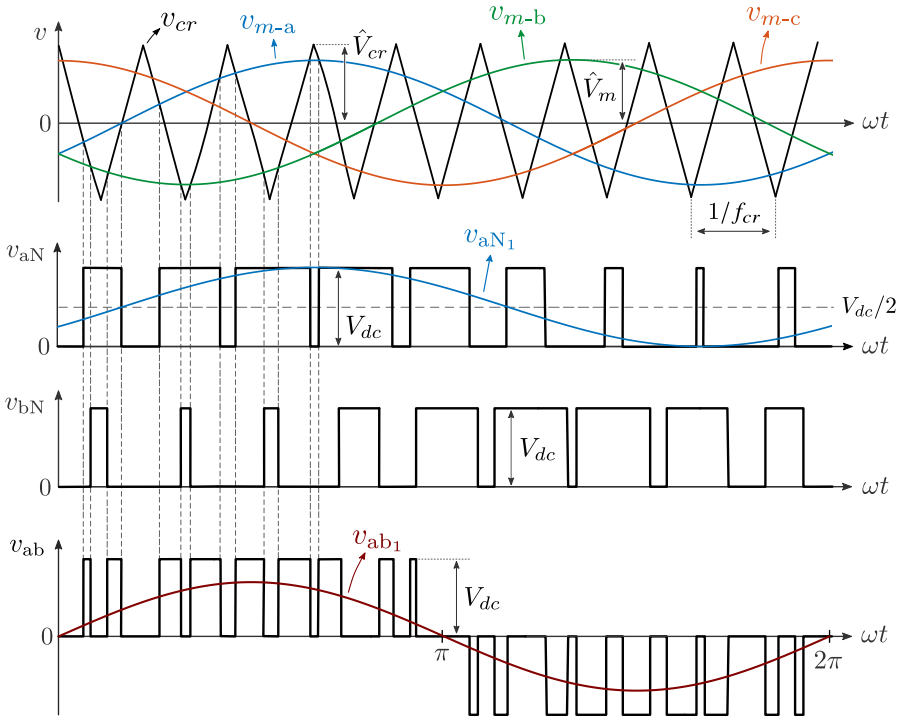

Fig. 2.2. Switching pattern generation with the sinusoidal PWM.

When $v_{m\text{-a}} > v_{cr}$, the upper switch S_1 in the converter leg "a" is turned ON. The lower switch S_4 operates in a complementary manner and thus is switched OFF. The resultant

converter terminal voltage v_{aN}, which is the voltage at the phase "a" terminal with respect to the dc-link negative terminal "N", is equal to the dc voltage (V_{dc}). When $v_{m\text{-a}} < v_{cr}$, S_4 is ON and S_1 OFF, leading to $v_{\mathrm{aN}} = 0$, as shown in Fig. 2.2. The converter line-to-line voltage can be determined by $v_{\mathrm{ab}} = v_{\mathrm{aN}} - v_{\mathrm{bN}}$. Note that to avoid possible short circuits during switching transients of the upper and lower devices in the converter leg, a dead time should be introduced, during which both switches are turned OFF.

As shown in Fig. 2.2, the fundamental-frequency output voltage $v_{\mathrm{aN_1}}$ follows the reference of that phase ($v_{m\text{-a}}$). The magnitude $\hat{V}_{\mathrm{aN_1}}$ is controlled by the *amplitude modulation index* (m_a), which is defined as

$$m_a = \frac{\hat{V}_m}{\hat{V}_{cr}} \tag{2.1}$$

where $\hat{V}_m$ and $\hat{V}_{cr}$ are the peak values of the modulating and carrier waves, respectively. m_a is usually adjusted by varying $\hat{V}_m$ while keeping $\hat{V}_{cr}$ fixed. $\hat{V}_{\mathrm{aN_1}}$ is determined by the following equation, where the modulation index should go from 0 to 1:

$$\hat{V}_{out_1} = \hat{V}_{\mathrm{aN_1}} = m_a \frac{V_{dc}}{2} \tag{2.2}$$

The *frequency modulation index* is defined as

$$m_f = \frac{f_{cr}}{f_m} \tag{2.3}$$

being f_m and f_{cr} the frequencies of the modulating and carrier waves, respectively. The switching frequency (f_{sw}) of the active switches in the 2L converter is equal to f_{cr}.

As can be seen from (2.2), without overmodulation (which occurs when $m_a > 1$), $\hat{V}_{\mathrm{aN_1}}$ is limited to $\pm V_{dc}/2$. When overmodulation occurs, v_m is greater than v_{cr} during peaks, so the output voltage remains constant at $v_{\mathrm{aN}} = V_{dc}$ or at $v_{\mathrm{aN}} = 0$ during these peaks. This has certain drawbacks such as the non-linearity of $\hat{V}_{\mathrm{aN_1}}$ with m_a, or the appearance of low-order harmonics at the output. The converter output voltage $\hat{V}_{\mathrm{aN_1}}$ can be increased without overmodulation by adding a third-harmonic component to the three-phase sinusoidal modulating wave; this is known as *Third-Harmonic Injection* (THI) PWM. In this case, the modulating wave v_m is calculated by the sum of a fundamental-frequency component v_{m_1} and a third-harmonic component v_{m_3}, making v_m slightly flattened on the top, as it is represented in Fig. 2.3. In this manner, the magnitude of the fundamental-frequency component ($\hat{V}_{m_1}$) can be higher than the carrier wave magnitude ($\hat{V}_{cr}$) without overmodulation. As this third-harmonic component is injected in phase in the three phases,

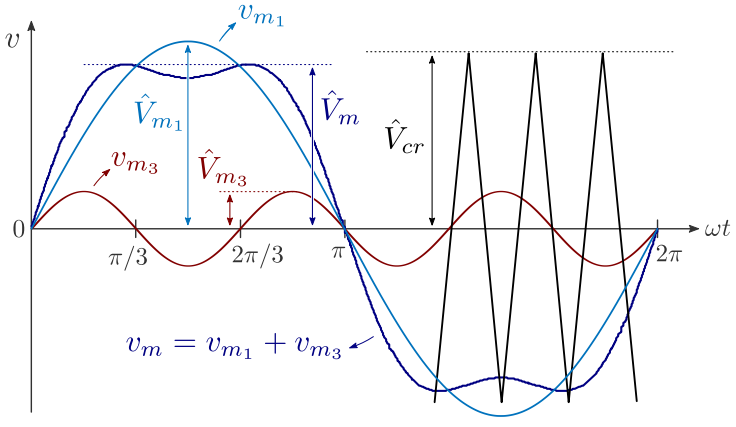

Fig. 2.3. PWM with third-harmonic injection.

it is a zero-sequence component, and hence it does not appear in the three-phase system —if the zero-sequence impedance is high enough.

Holmes and Lipo demonstrated analytically that the maximum increase of $\hat{V}_{\mathrm{aN_1}}$ that can be achieved with this scheme is 15.5% $(2/\sqrt{3})$, which is obtained by injecting a 1/6 third-harmonic component into the fundamental-frequency reference waveform $(\hat{V}_{m_3} = \hat{V}_{m_1}/6)$ [63]. Commonly, a THI of a one-quarter $(\hat{V}_{m_3} = \hat{V}_{m_1}/4)$ is also used. In this way, $\hat{V}_{\mathrm{aN_1}}$ can be increased up to 12%. It should be noted that by injecting a third-harmonic component, the output voltage ($\mathrm{THD_v}$) and current total harmonic distortions ($\mathrm{THD_i}$) can be reduced, improving the output waveform quality.

2.2.2 Carrier-based Pulse Width Modulation for Multilevel VSC-s

Carrier-based PWM schemes could be employed in VSCs with more than two levels, also called *multilevel* VSCs (described in *section 2.3*). These schemes can be classified into two categories: phase- and level-shifted schemes.

2.2.2.1 *Phase-Shifted Multicarrier PWM*

Generally, a multilevel converter with m voltage levels requires $(m-1)$ triangular carriers. In the *phase-shifted multicarrier* PWM (PSC-PWM) scheme, all the triangular carriers have the same frequency (f_{cr}) and the same peak amplitude $(\hat{V}_{cr})$, but there is a phase displacement between any two adjacent carrier waves, given by

$$\phi_{cr} = 360^\circ/(m-1) \tag{2.4}$$

The modulating signal is usually a three-phase sinusoidal wave $(v_{m\text{-a}}, v_{m\text{-b}}, v_{m\text{-c}})$ with adjustable frequency (f_m) and amplitude $(\hat{V}_m)$. The gate signals are generated by comparing the modulating wave with the carrier waves $(v_m > v_{cr})$.

To implement a PSC-PWM strategy in a five-level (5L) VSC, four triangular carriers are needed with a 90° phase shift between any two adjacent of them. For example, Fig. 2.4 shows a PSC-PWM strategy applied to a 5L Cascaded H-Bridge (CHB) converter, like the one that will be described in *subsection 2.3.3.1*. For simplicity, only the reference wave of one phase is plotted (v_m). The carrier waves v_{cr_1} and v_{cr_2} are used to generate gate orders for the upper switches S_{11} and S_{12} in the left legs of power cells H_1 and H_2, respectively.

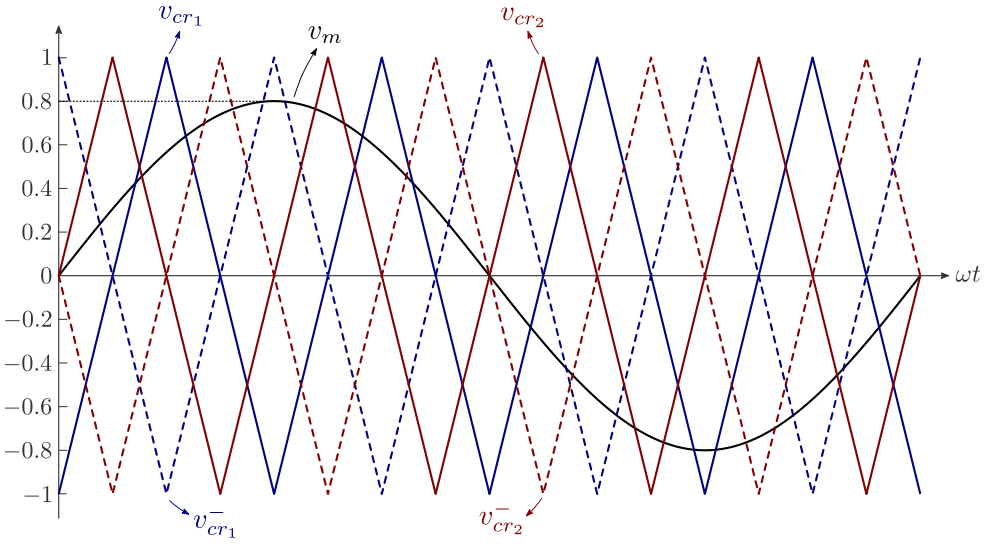

Fig. 2.4. PSC-PWM modulating and carrier waves for a 5L CHB converter ($m_f = 4$ and $m_a = 0.8$).

Furthermore, the other two carrier waves, $v_{cr_1}^-$ and $v_{cr_2}^-$, which are 180° out of phase with v_{cr_1} and v_{cr_2}, respectively, produce the gatings for the bottom switches S_{21} and S_{22} in the right legs of the HB cells. The gate signals of the rest of the switches in the HB legs are not shown since these switches operate in a complementary way with respect to their corresponding upper and lower switches.

Regarding the voltage, the power cell output voltages v_{H_1} and v_{H_2} are almost identical except a small phase displacement among them. That is because all the devices operate with the same switching frequency (f_{sw}) and conduction time. The waveform of v_{aN} is composed of five voltage levels with a peak value of $2V_{dc}$, and the line-to-line voltage v_{ab} contains nine voltage levels with an amplitude of $4V_{dc}$.

The device switching frequency can be calculated by $f_{sw,dev} = f_{cr} = f_m\, m_f$. The switching frequency of the converter using the phase-shifted modulation is related to the device switching frequency by

$$f_{sw,conv} = 2n f_{sw,dev} = f_{sw,dev}(m-1) \tag{2.5}$$

being n the number of power cells per phase cluster, and $m = 2n+1$.

The PSC-PWM can also be applied in the Flying Capacitor topology (described in *subsection 2.3.2*), in the same way as in CHBs, respecting the complementarities of switches. Nevertheless, this scheme cannot be implemented in the Diode Clamped topology (studied in *subsection 2.3.1*), since prohibited switching states would be set.

2.2.2.2 *Level-Shifted Multicarrier PWM*

The *level-shifted multicarrier* PWM (LSC-PWM) is especifically designed for being used in Diode Clamped topologies, although it can be employed in any multilevel VSC topology. Similar to the PSC-PWM, an m-level VSC using the LSC-PWM scheme requires $(m-1)$ triangular carriers, all having the same amplitude and frequency. However, these triangular carriers are vertically disposed such that the bands they occupy are contiguous (avoiding the application of forbidden states in the Diode Clamped topology). The frequency modulation index is also given by $m_f = f_{cr}/f_m$, which remains the same as that for the PSC-PWM scheme, whereas the amplitude modulation index is defined as

$$m_a = \frac{\hat{V}_m}{\hat{V}_{cr}(m-1)} \tag{2.6}$$

The implementation of the LSC-PWM in multilevel converters can be carried out through several schemes which are presented in Fig. 2.5: (a) in-phase disposition (IPD), where all carriers are in phase; (b) alternative phase opposite disposition (APOD), where all carriers are alternatively in opposite disposition; and (c) phase opposite disposition (POD), where all carriers above the zero reference are in phase but in opposition with those below the zero reference. Ref. [63] demonstrated that the IPD scheme provides the best harmonic profile.

In the PSC-PWM, the device switching frequency ($f_{sw,dev}$) is equal to the carrier frequency f_{cr}. This relationship, however, is not fulfilled in the LSC-PWM. In other words, the switching frequencies corresponding to the comparison between the modulating wave and each carrier wave are not equal. In a CHB converter, for instance, the switching frequency is not the same for the devices in different HB power cells. Accordingly, the switching frequency of the converter using the level-shifted modulation is equal to the carrier frequency, that is,

$$f_{sw,conv} = f_{cr} \tag{2.7}$$

while the average device switching frequency is

$$f_{sw,dev} = f_{cr}/(m-1) \tag{2.8}$$

As a result of the unequal device switching frequencies, the conduction time of the devices is not equitably distributed either. Thus, the switching pattern should rotate among the converter to equally distribute the switching and conduction losses (if the topology permits it). This is not a problem in the PSC-PWM, since all the semiconductor devices will have a balanced conduction time per period, regardless of the m_a using.

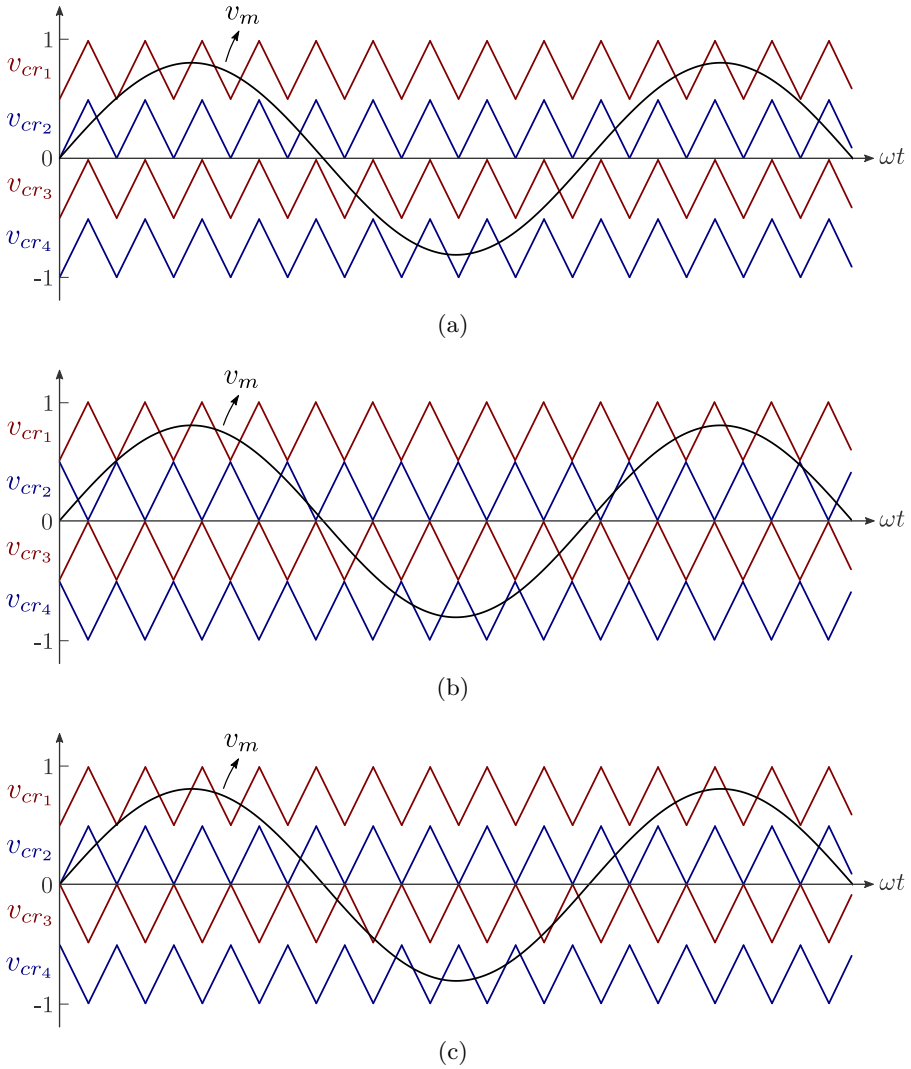

Fig. 2.5. LSC-PWM schemes for 5L VSCs. (a) In-phase disposition (IPD), (b) alternative phase opposite disposition (APOD), and (c) phase opposite disposition (POD).

A detail to mention is that an equivalent output voltage waveform obtained with the PSC-PWM could be obtained also with the level-shifted APOD scheme, if $(m-1)$ times greater carrier wave frequency (f_{cr}) than in the PSC-PWM is used for APOD modulation; i.e., the same equivalent or average device switching frequency $(f_{sw,dev})$. Ref. [36] compared the THD_v of the line-to-line voltage modulated by the PSC-PWM and level-shifted IPD schemes applied in a 7L CHB converter, concluding that the PSC-PWM achieves the best output voltage quality.

2.2.3 Space Vector Modulation

While the PWM aims to independently modulate the amplitude of the voltage of each of the three phases, the philosophy of the *Space Vector Modulation* (SVM) is to modulate the output three-phase voltage (as a whole) [63], [65]. For this, the output three-phase voltage is analyzed as space vector. In a 2L VSC there are eight possible combinations of switching states. "P" denotes that the upper switch in the 2L VSC leg is ON and the converter terminal voltage ($V_{\mathrm{aN}}, V_{\mathrm{bN}}, V_{\mathrm{cN}}$) is positive ($+V_{dc}$), while "N" denotes that the converter terminal voltage is zero due to the conduction of the lower switch (see Table 2.1). The switching state [NPN], for instance, corresponds to the conduction of S_4, S_3, and S_2 in the converter legs "a", "b", and "c", respectively.

Table 2.1. Definition of switching states in the 2L VSC.

Switching state	**Leg "a"**			**Leg "b"**			**Leg "c"**		
	S_1	S_4	v_{aN}	S_3	S_6	v_{bN}	S_5	S_2	v_{cN}
P	ON	OFF	V_{dc}	ON	OFF	V_{dc}	ON	OFF	V_{dc}
N	OFF	ON	0	OFF	ON	0	OFF	ON	0

Fig. 2.6 shows a typical space vector diagram for the 2L VSC. Each state can be defined as a stationary space vector, distinguishing six active vectors ($\vec{V}_1$ to $\vec{V}_6$), and a zero one ($\vec{V}_0$); i.e., seven voltage vectors and eight switching states. The first six form a regular hexagon with six equal sectors (I to VI), while de zero vector lies on the center of the hexagon. The vector $\vec{V}_0$ has two switching states [PPP] and [NNN], one of which is redundant. Redundant switching states provide great flexibility for switching pattern design.

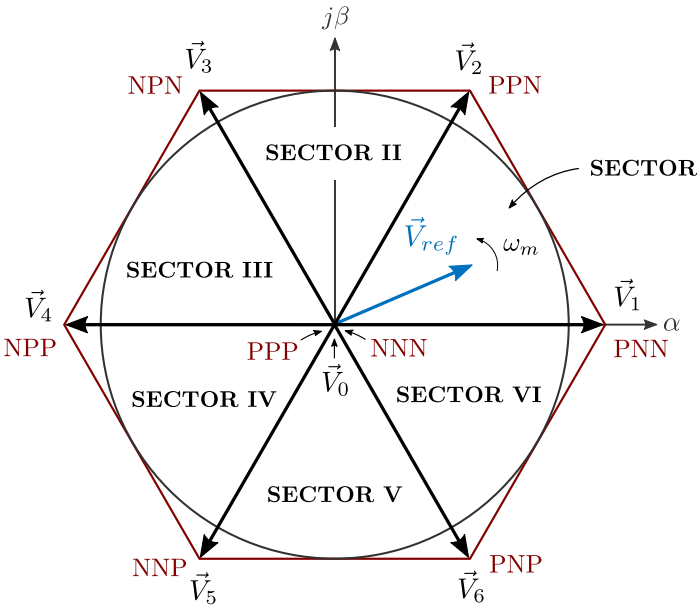

Fig. 2.6. SVM diagram for a 2L VSC.

Having identified the stationary vectors, at any point in time, an arbitrary target output voltage vector $\vec{V}_{ref}$, which rotates at a frequency equal to that of the converter output f_m, can be formed. For a given module and position, the average $\vec{V}_{ref}$ during one sampling period can be synthesized by applying the three adjacent stationary vectors. These vectors represent different switching states of the converter, generating corresponding

gate signals for the active switches. This strategy is applied whichever the sector, phase and magnitude of the reference vector are. The dwell times for the stationary vectors represent the duty-cycle time (ON-state or OFF-state time) of the chosen switches during the sampling period of the modulation scheme. Note that this strategy generates a similar output quality to the PWM when applying it in a 2L VSC.

As the number of levels increases, the SVM becomes more complex since the number of voltage vectors and switching states increase. For instance, in the case of a 3L VSC, as shown in Fig. 2.7, there are 19 voltage vectors and 27 switching states [66]–[68]. Moving to a 5L, its space vector diagram has 61 voltage vectors and 125 switching states. However, as the number of levels increases, the number of vectors with redundant states increases as well, so the number of degrees of freedom increases exponentially. As mentioned, the switching state redundancy provides great flexibility to reduce the switching frequency, balance dc-link voltages, reduce common-mode voltage/current, etc.

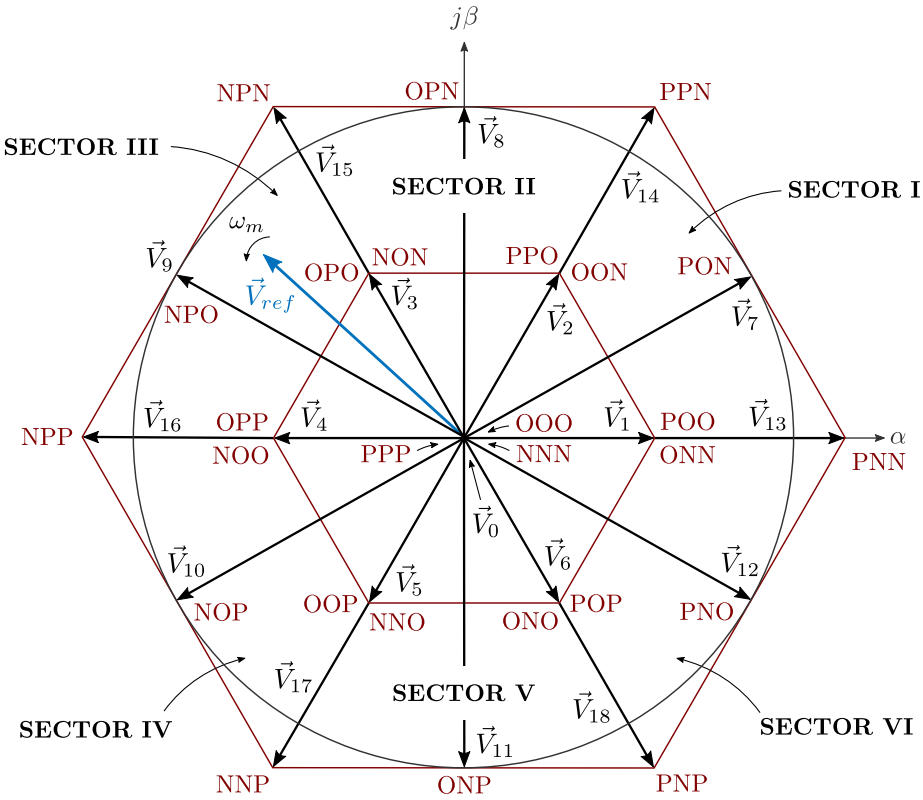

Fig. 2.7. SVM diagram for a 3L VSC.

2.3 MULTILEVEL VSC TOPOLOGIES

Multilevel VSCs allow to increase the voltage and power of the power equipment, and have a variety of configurations [28]–[36]. The following lines cover the description of those considered most typical in the specialized literature.

2.3.1 Diode Clamped Multilevel Converter

The *Diode Clamped* multilevel converter, initially proposed in 1981 by Nabae *et al.* in a 3L version [69], was the first multilevel VSC topology employed in large scale. The converter can be generally configured as a 3L, 4L, or 5L topology, but only the 3L one, commonly known as *Neutral Point Clamped* (NPC), has found wide application in high power – MV

scenarios. The main features of the NPC topology include reduced dv/dt and THD in its ac output voltages in comparison to the aforementioned 2L VSC. The 3L NPC topology is presented in Fig. 2.8.

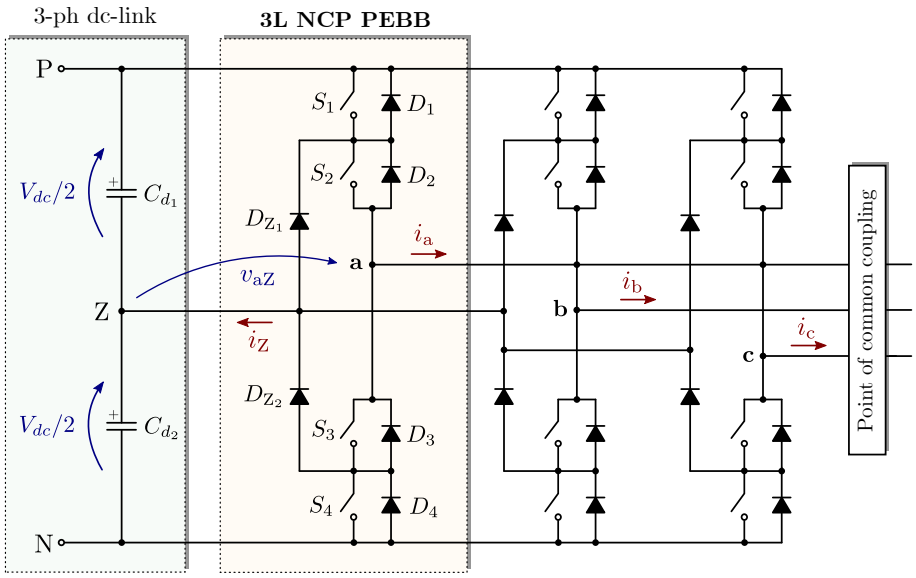

Fig. 2.8. Simplified circuit diagram of the 3L NPC converter.

The converter phase leg "a" is composed of four active switches (S_1 to S_4) with four anti-parallel diodes (D_1 to D_4). The dc input voltage of the converter is split by two equal cascaded dc-link capacitors ($C_{d_1} = C_{d_2}$), providing a floating neutral point "Z". The diodes connected to this neutral point are known as clamping diodes (D_{Z_1} and D_{Z_2}). The voltage across each of the dc capacitors is the half of the total three-phase dc-link voltage; in this manner, $+V_{dc}/2$ and $-V_{dc}/2$ voltages can be synthesized (three levels). With a finite value for C_{d_1} and C_{d_2}, the capacitors can be charged or discharged by the neutral current i_Z, causing neutral point voltage deviation. The control and regulation of this dc-link midpoint voltage is an important drawback of this topology.

The switching states shown in Table 2.2 represent the operating status of the switches in the 3L NPC converter. On the one hand, switching state "P" denotes that the upper two switches in the phase leg "a" are ON and the converter terminal voltage v_{aZ}, which is the voltage at terminal "a" with respect to the neutral point "Z", is $+V_{dc}/2$. Note that each of the switches in the 3L NPC converter withstands only half of the total dc voltage during commutation. For its part, "N" indicates that the lower two switches conduct, leading to $v_{aZ} = -V_{dc}/2$. On the other hand, switching state "O" means that the inner two switches S_2 and S_3 are ON, and v_{aZ} is clamped to zero through the clamping diodes. Depending on the direction of the output current i_a, one of the two clamping diodes is turned ON. For instance, a positive output current ($i_a > 0$) forces D_{Z_1} to turn ON, and

Table 2.2. Switching states of the 3L NPC converter.

Switching state	**Device switching status (leg "a")**				**Converter voltage (v_{aZ})**
	S_1	S_2	S_3	S_4	
P	ON	ON	OFF	OFF	$V_{dc}/2$
O	OFF	ON	ON	OFF	0
N	OFF	OFF	ON	ON	$-V_{dc}/2$
Forbidden state	ON	OFF	OFF	ON	*Depends on i_a direction*

the terminal "a" is connected to the neutral point "Z" through the conduction of D_{Z_1} and S_2. The line-to-line voltage v_{ab} can be found from $v_{ab} = v_{aZ} - v_{bZ}$, which contains five voltage levels ($+V_{dc}, +V_{dc}/2, 0, -V_{dc}/2$, and $-V_{dc}$). It is very common to generate the gate signals of this topology with the SVM scheme shown in Fig. 2.7.

Switches S_1 and S_3 operate in a complementary manner, as Table 2.2 indicates. With one switched ON, the other must be OFF. Similarly, S_2 and S_4 are also a complementary pair. Nevertheless, unlike the rest of multilevel VSCs studied below, the 3L NPC presents a switching state that must be avoided: the state in which S_1 and S_4 conduct belongs to a forbidden state. In this switching state, the voltage v_{aZ} depends on the current direction. If the output current is positive ($i_a > 0$), v_{aZ} is $-V_{dc}/2$, whereas if it is negative takes the value of $+V_{dc}/2$.

As the current power grid makes it increasingly necessary to count on power equipment with higher voltage and power rating, the interconnection of 3L NPC Power Electronics Building Blocks (PEBBs) is also a common practice [58]. In fact, this is nowadays the commercially available standard switching branch for MV levels (3.3 kV to 6.6 kV). That is why *Ingeteam*'s simplest multilevel VSC stacks for those voltage levels are based on these switching branches. These structures are usually used in order to increase the power capability when the semiconductor voltage limit is achieved (see Fig. 2.8).

To increase the voltage rating and improve the waveform quality, higher-level Diode Clamped converters can be employed. Fig. 2.9 shows the per-phase diagram of the 5L version, while Table 2.3 summarizes the switching states and the terminal voltage v_{aN}. As can be seen, to obtain each of the five levels of this topology there is only one possible switching state; the others are forbidden. This is the reason why the PSC-PWM technique cannot be applied in Diode Clamped topologies. In contrast, in the other multilevel VSC topologies that will be studied below, some voltage levels can be obtained with several redundant switching states. Another problem of higher-level topologies is that the number of clamping diodes increases dramatically with the voltage level; while the 3L only requires

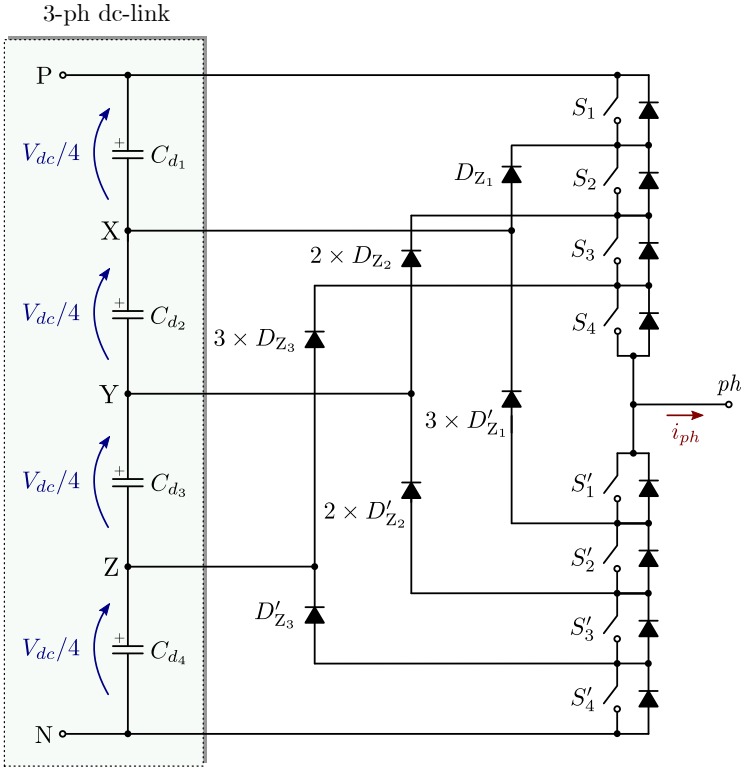

Fig. 2.9. Simplified per-phase circuit diagram of the 5L Diode Clamped converter.

six clamping diodes, the 5L needs 36. Besides, as the number of levels increases, the number of neutral points does as well, whose voltage deviations must be controlled. These are, in fact, the main reasons why the 4L and 5L topologies are seldom found.

Table 2.3. Voltage levels and switching states of the 5L Diode Clamped converter.

Converter voltage (v_{aN})	**Switching state**			
	S_1	S_2	S_3	S_4
V_{dc}	1	1	1	1
$3V_{dc}/4$	0	1	1	1
$V_{dc}/2$	0	0	1	1
$V_{dc}/4$	0	0	0	1
0	0	0	0	0

2.3.2 Flying Capacitor Multilevel Converter

Meynard *et al.* introduced the *Flying Capacitor* multilevel converter in 1992. Fig. 2.10 shows the typical configuration of this topology in a 5L version. There are four complementary switch pairs in each of the converter legs. For instance, the switch pairs in leg "a" are (S_1, S_1'), (S_2, S_2'), (S_3, S_3'), and (S_4, S_4'). Therefore, only four independent gate signals are required for each phase. The converter in Fig. 2.10 can produce a converter phase voltage v_{aN} with five voltage levels. When switches S_1, S_2, S_3, and S_4 conduct, the converter phase voltage v_{aN} is $+V_{dc}$, which is the voltage at the terminal "a" with respect to the dc-link negative terminal "N". Similarly, with S_1, S_2, and S_3 switched ON, $v_{aN} = 3V_{dc}/4$.

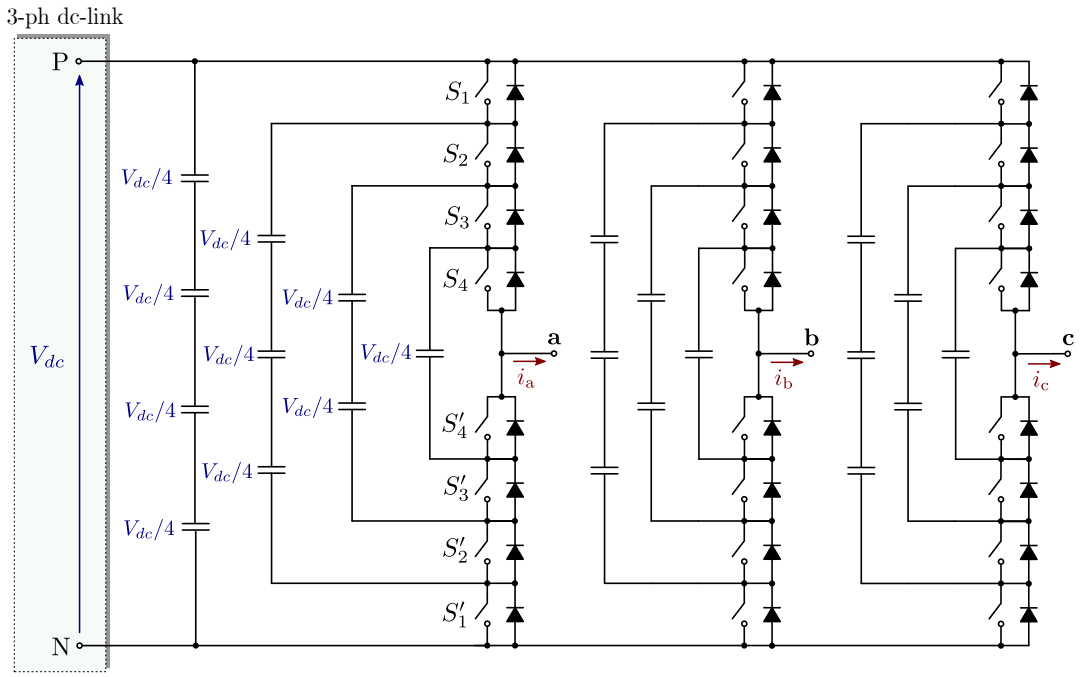

Fig. 2.10. Simplified circuit diagram of the 5L Flying Capacitor converter.

Table 2.4 summarizes all the voltage levels of the 5L Flying Capacitor converter and their corresponding switching states. Some voltage levels can be obtained by more than one switching state. The voltage level $+V_{dc}/2$, for instance, can be produced by six sets of different (redundant) switching states.

Table 2.4. Voltage levels and switching states of the 5L Flying Capacitor converter.

Converter voltage (v_{aN})	**Switching state**			
	S_1	S_2	S_3	S_4
V_{dc}	1	1	1	1
$3V_{dc}/4$	1	1	1	0
	0	1	1	1
	1	0	1	1
	1	1	0	1
$V_{dc}/2$	1	1	0	0
	0	0	1	1
	1	0	0	1
	0	1	1	0
	1	0	1	0
	0	1	0	1
$V_{dc}/4$	1	0	0	0
	0	1	0	0
	0	0	1	0
	0	0	0	1
0	0	0	0	0

2.3.3 Modular Multilevel VSC Topologies

The current power grid makes it increasingly necessary to count on power equipment with higher voltage and power ratings. Since their scalable features, multilevel VSC topologies based on modular structures are interesting solutions for that purpose [39], [40].

2.3.3.1 *Cascaded H-Bridge Multilevel Converter*

In 1997, *Halmar Robicon Corporation* brought to the industry a high power – MV motor drive multilevel inverter with a PWM strategy [70], [71]; the emergence of what nowadays is known as *Cascaded H-Bridge* (CHB) multilevel converter [33], [39], [40]. In order to deliver energy to all the cascaded power cells, the presented ac-dc converter required a multiwinding line-frequency transformer. The CHB is composed of a multiple units of single-phase full-bridge (or HB) power cells, connected in cascade on their ac side. As the ac voltage is proportional to the number of power cells, these structures are scalable, and direct power grid connection is often feasible without a bulky step-up transformer. It allows high voltage operation without switching devices in series. This topology requires isolated dc energy sources to feed each power cell, which is not a drawback when the energy source is also modular, but may require a multiwinding transformer with diode rectifier if it is not the case. Fig. 2.11 shows the simplified circuit diagram of a 5L CHB converter, composed by two HB power cells per converter phase cluster.

The converter configuration served in Fig. 2.11 can produce a phase cluster voltage $(v_{\mathrm{aN}}, v_{\mathrm{bN}}, v_{\mathrm{cN}})$ with five voltage levels, which is the voltage at the converter terminal with respect to the neutral point "N" (the union of the phase clusters). The switches in each 2L branch of the HB are complementary (e.g., S_{11} and S_{41}). When switches S_{11}, S_{21}, S_{12}, and S_{22} conduct, the output voltage of the power cells H_1 and H_2 is $v_{H_1} = v_{H_2} = V_{dc}$, and the resultant converter phase cluster voltage is $v_{\mathrm{aN}} = v_{H_1} + v_{H_2} = 2V_{dc}$. In the same way, with S_{31}, S_{41}, S_{32}, and S_{42} switched ON, $v_{\mathrm{aN}} = -2V_{dc}$. The other three voltage levels are $+V_{dc}$, 0, and $-V_{dc}$, which correspond to various switching states summarized in Table 2.5.

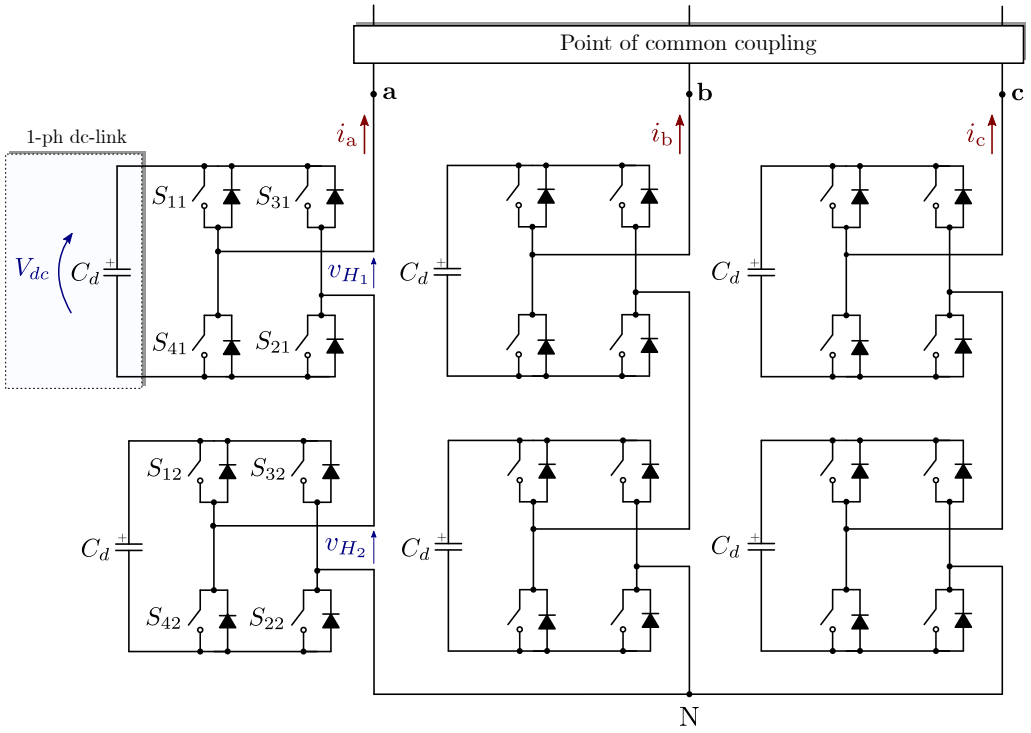

Fig. 2.11. Simplified circuit diagram of the 5L CHB converter.

Table 2.5. Voltage levels and switching states of the 5L CHB converter.

Converter voltage (v_{aN})	**Switching state**					
	S_{11}	S_{31}	S_{12}	S_{32}	v_{H_1}	v_{H_2}
$2V_{dc}$	1	0	1	0	V_{dc}	V_{dc}
V_{dc}	1	0	1	1	V_{dc}	0
	1	0	0	0	V_{dc}	0
	1	1	1	0	0	V_{dc}
	0	0	1	0	0	V_{dc}
0	0	0	0	0	0	0
	0	0	1	1	0	0
	1	1	0	0	0	0
	1	1	1	1	0	0
	1	0	0	1	V_{dc}	$-V_{dc}$
	0	1	1	0	$-V_{dc}$	V_{dc}
$-V_{dc}$	0	1	1	1	$-V_{dc}$	0
	0	1	0	0	$-V_{dc}$	0
	1	1	0	1	0	$-V_{dc}$
	0	0	0	1	0	$-V_{dc}$
$-2V_{dc}$	0	1	0	1	$-V_{dc}$	$-V_{dc}$

It can be observed from Table 2.5 that some voltage levels can be obtained by more than one switching state. The voltage level V_{dc}, for instance, can be produced by four sets of different (redundant) switching states. The switching state redundancy is a common phenomenon in multilevel converters. It provides a great flexibility for switching pattern design, especially for SVM schemes.

The dc supply voltages of the power cells introduced in the previous converter are commonly all the same. Alternatively, unequal dc voltages may be selected for the power

cells, achieving an increase of the number of voltage levels without necessarily increasing the number of cascaded power cells. This allows more voltage steps in the converter output voltage waveform for a given number of power cells.

Phase clusters of the CHB can be connected either in star (YCHB) or in delta (DCHB). The circuit diagrams of both configurations are depicted in Figs. 2.12 (a) and (b). When employing the YCHB, the phase cluster voltage is the line-to-neutral voltage ($v_{ph\text{-}\mathrm{N}}$). Thus, when compared with the DCHB, where the phase cluster voltage is the line-to-line voltage ($v_{ph\text{-}ph}$), either the switching devices can be sized at lower blocking voltage rating, or the number of the cascaded power cells can be reduced to obtain the same output ac voltage level. Opposite behavior can be found in terms of current. Another important feature to consider is that the DCHB requires a solution to minimize the circulating current inside the delta; e.g., control loops and/or magnetic elements (L_f).

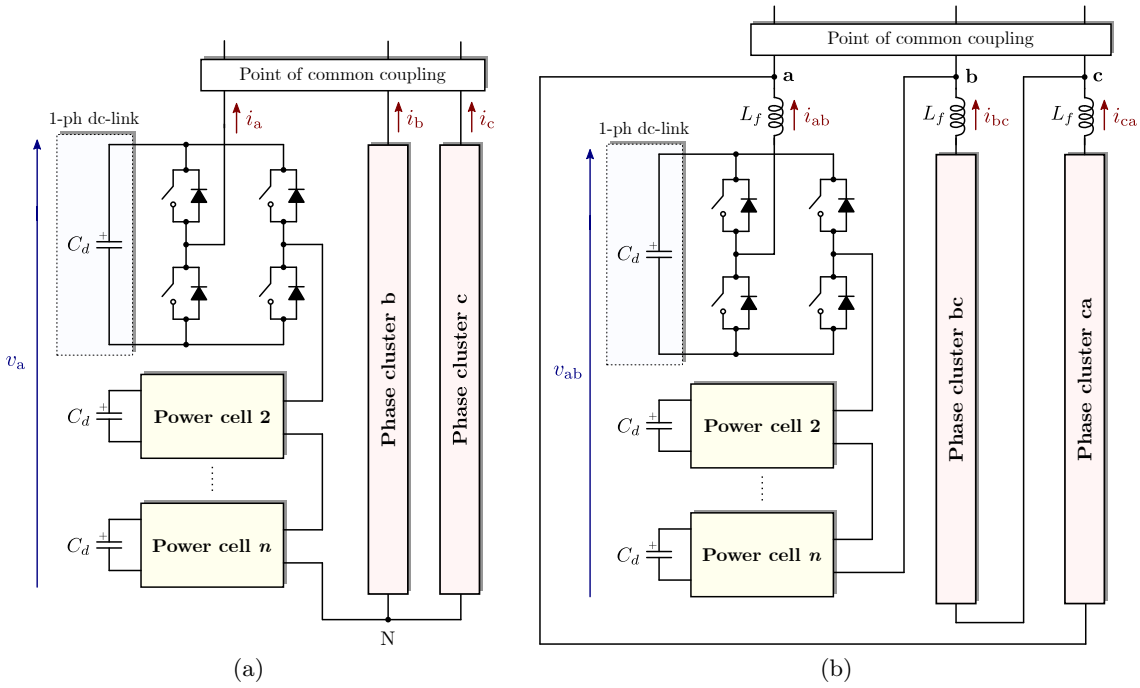

Fig. 2.12. Simplified circuit diagrams of CHB configurations. (a) YCHB, and (b) DCHB.

2.3.3.2 *Five-Level NPC/HB Converter*

To increase the power and voltage levels, on the basis of the above CHB topology, instead of increasing the number of power cells, 3L branches can be used (instead of 2L), such as 3L NPC PEBBs. As mentioned, these switching branches are employed by *Ingeteam*. The 5L NPC/HB power cell is composed of two 3L NPC PEBBs in an HB form. This topology presents some unique features that have promoted its use in high power – MV applications. The output voltage and power of a 3L NPC converter discussed in *subsection 2.3.1* can be doubled by using 24 active switches, replacing one of the switches for two in series connection. The 5L NPC/HB converter shown in Fig. 2.13 also uses 24 active switches to achieve the same voltage and power ratings as the 24-switch 3L NPC converter.

The 5L NPC/HB converter offers some advantages over the 3L NPC. Each 5L NPC/HB power cell achieves a three-level voltage waveform with respect to its dc-link neutral point "Z", while the converter output voltages ($v_{\mathrm{aN}}, v_{\mathrm{bN}}, v_{\mathrm{cN}}$) contain five voltage levels, leading to a lower dv/dt and better waveform quality (lower THD). Nine levels are attained in the line-to-line output voltage ($v_{\mathrm{ab}}, v_{\mathrm{bc}}, v_{\mathrm{ca}}$). Furthermore, if the number of output voltage

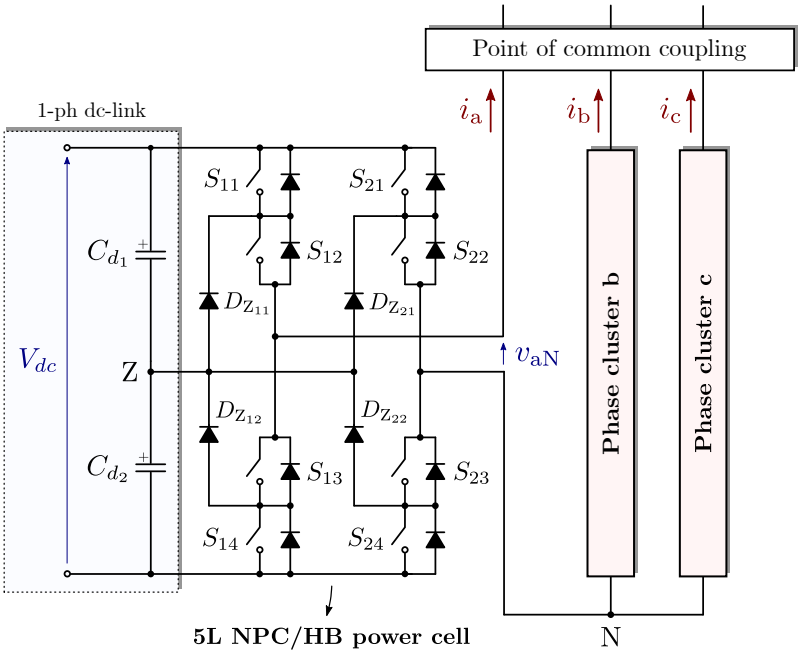

Fig. 2.13. Simplified circuit diagram of the star-connected 5L NPC/HB converter.

levels is desired to be augmented, the serialization of more power cell per phase can be assumed by this modular design.

Series-connection of switching devices is also avoided with the 5L NPC/HB topology, which eliminates the device dynamic and static voltage sharing problems. Nevertheless, the converter requires isolated dc-links (one per 5L NPC/HB power cell), which increases the complexity and cost of the dc energy source. As in CHBs, phases clusters can be connected either in star or in delta (see Fig. 2.12).

2.3.3.3 *Modular Multilevel Converter*

Marquardt and his group introduced a novel power conversion structure called *Modular Multilevel Converter* (MMC) [72], which was based on the series-connection of single-phase 2L VSC-based power cells (also known as half-bridge cells). In this converter configuration, the phase cluster is separated into two equal parts (upper and lower arms) to be able to generate positive and negative voltage levels at the ac side. The MMC has received increased attention since early 2000s, particularly for High Voltage Direct Current (HVDC) transmission systems [73]–[75].

The MMC is composed of two sets of star-connected converters in which the ac sides of multiple cascaded power cells are interconnected to constitute each phase cluster [76], [77]. The power cell topology can have a number of different designs (e.g., 3L NPC, Flying Capacitor, full-bridge, 5L NPC/HB, etc.), but the half-bridge power cell is widely used. It is also known as "double-star-configured MMC" [40]. Fig. 2.14 shows the circuit configuration of the classical MMC. If the same power cell voltage is used, to achieve the same voltage rating in the PCC, the MMC needs twice as many power cells per phase cluster than an equivalent CHB. However, the MMC can be built with half-bridge power cells, while the CHB needs full-bridge ones [77].

Unlike CHB configurations, the power cells constituting each phase cluster of the MMC share a common three-phase dc energy source. This configuration gives the currents a way to recirculate; being the control of these currents a specific issue to consider in the MMC. Both the upper and the lower arms have an inductor L_{arm}, which is used to limit the circulating current in steady-state operation.

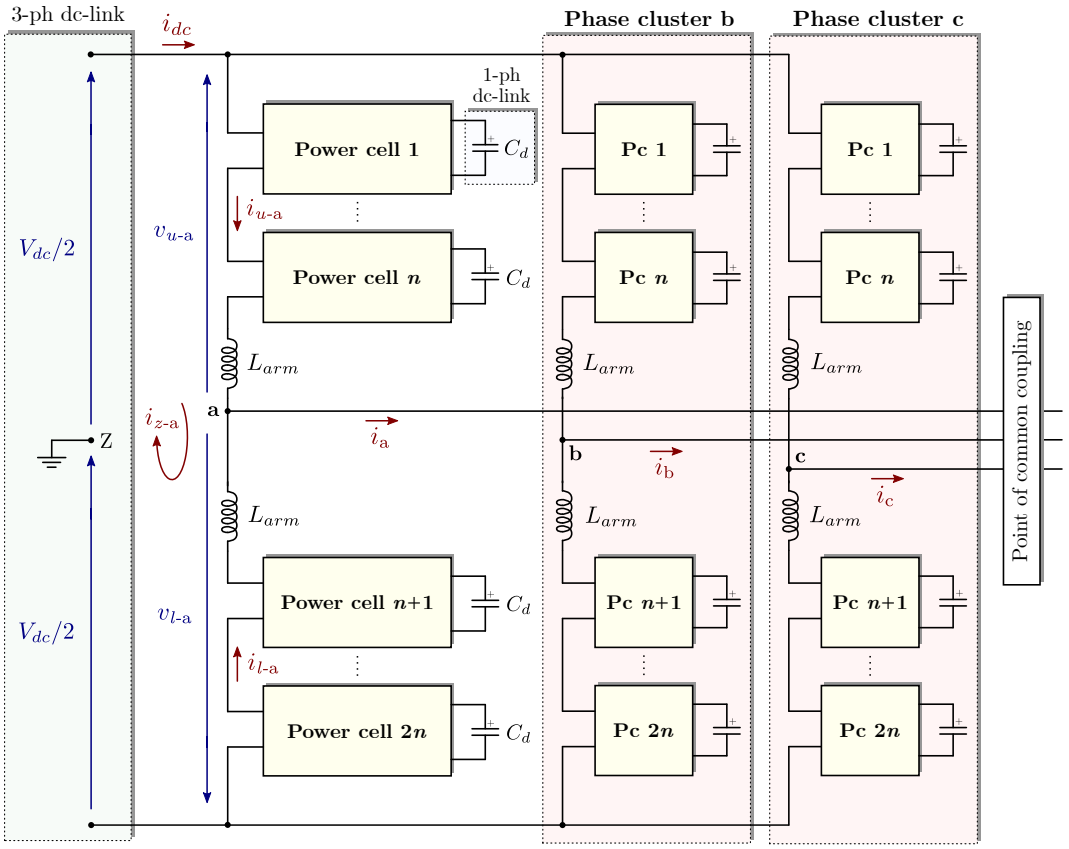

Fig. 2.14. Simplified circuit diagram of the MMC.

2.4 METHODOLOGY TO EVALUATE CONVERTER STRUCTURES BASED ON 3L NPC PEBB-S

Together with the increase in the installation of MV converters, there is a demand of new operating point requirements, such as unbalanced voltage and/or current conditions [55]. Power converters had not been asked by grid codes to face these working conditions before, and thus, specific designs need to be carried out in order to adapt the PEBB topology and the connection structure to these new scenarios. This fact might involve that configurations which behave properly under design or balanced conditions, cease to be so interesting in these new operating scenarios.

Multilevel VSC topologies have been deeply analyzed and reviewed by several authors [19], [28], [30]–[36], [78]–[80]. Several references also cover comparisons of the basic multilevel VSC topologies [19], [78]–[80]. Some of the latter compare configurations in terms of the supply quality, considering the output current and voltage total harmonic distortions (THD_i and THD_v). Some of these references compare also multilevel VSC topologies focusing on the reliability, the number of semiconductor devices, and passive components. Additionally, thermal constraints are common to be analyzed when comparing converter topologies. However, with the new considered operating points other indicators may define the behavior and the limits of a power converter.

MV PEBBs are normally designed considering objective operating scenarios. The increase of new scenarios makes it difficult to define which configuration fits better with all the demanded operating points. For instance, unbalanced conditions may suppose new working conditions that power converters have not dealt with before, or were not taken into account in the design stage. Therefore, design simulations and indicators to compare converter topologies and connection structures may not be representative.

Desired converter structures in the required operating scenario need to be analyzed, usually by means of simulations of specific operating points. In order to study the converter performance under different operating requirements, simulations considering those requirements need to be performed again.

This section, which led to publication [C1], presents a methodology that provides relevant information to study and compare converter topologies and connection structures. A database is generated, which contemplates all possible operating points of the converter, regardless of the application. After identifying the operating scenarios of a requested application, the designer can analyze the results without the need of extra simulations. The results analysis tool may give the information to determine which configuration is the most interesting, or which is the one that better suits the specific operating requirements.

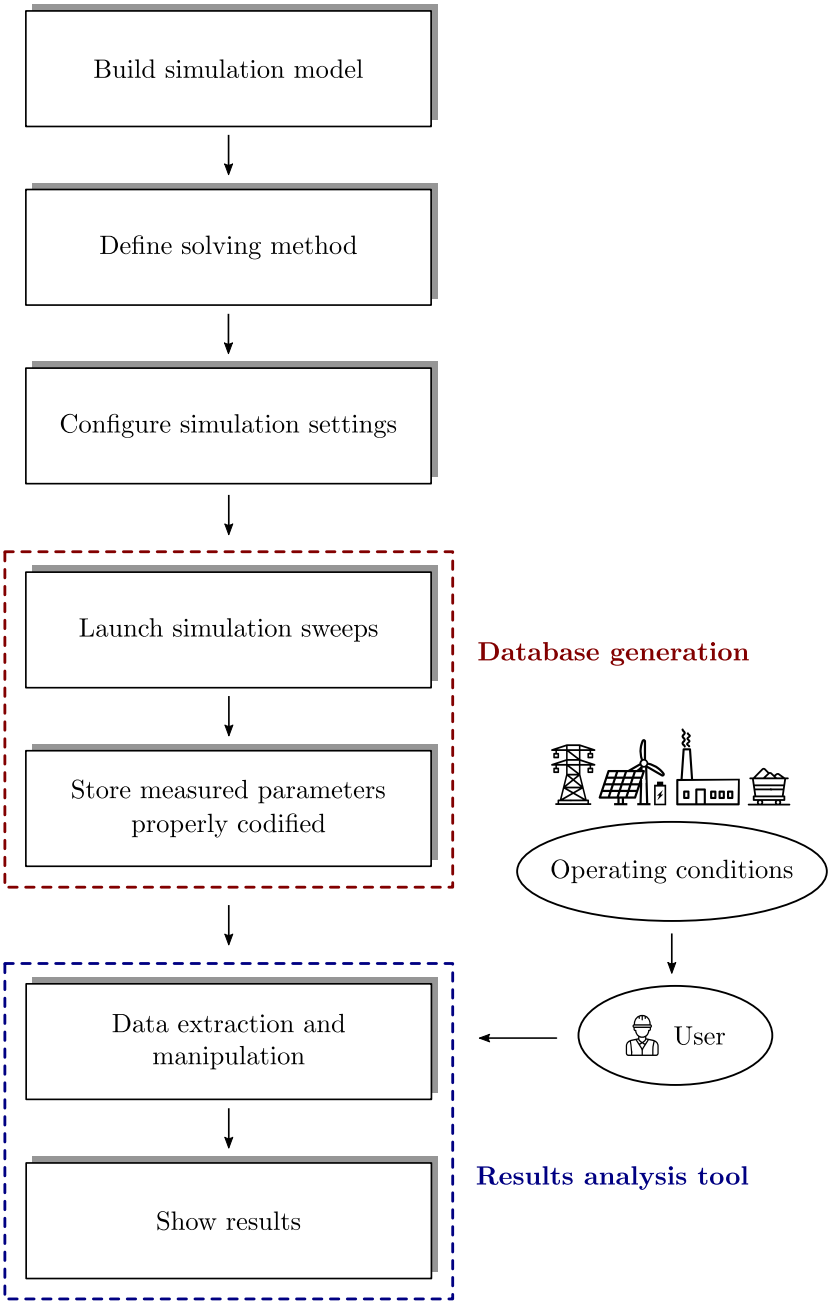

Fig. 2.15. Block diagram of the proposed methodology.

2.4.1 Proposed Methodology

Some converter topologies or converter PEBB connection structures might present certain limitations and advantages for specific operating requirements or application demands. This fact may mean that one converter configuration can be more appropriate than others for a given scenario. The proposed methodology provides valuable information to analyze these limitations, compare, choose, and design the most suitable conversion structure. It could be applied from the design stage till the analysis of new operating scenarios in already installed converters. Although it is oriented to the study of specific VSC configurations, it is applicable to any conversion structure. The methodology is integrated into a software-based tool, developed in *MATLAB/Simulink*® environment.

The philosophy of this proposed methodology is to generate an n-dimensional database (being n the number of variables which define the converter operating point). This database is created by launching simulation sweeps of the variables, and collects measurements of all possible operating points of the converter, whatever the application. That is, simulations performed for the database generation are independent of the characteristics of the power grid, the output filter, or the load to which the power converter is connected.

After that, the results analysis tool, which is integrated in the methodology, accesses the database searching for the operating requirements requested by the user. It extracts measured parameters in these operating conditions, and after data post-processing, provides the values of the indicators that reflect the performance of each converter structure. If the operating point varies, the user does not need to repeat the simulations; just by asking the results analysis tool for the new operating condition is sufficient. Fig. 2.15 summarizes the proposed methodology.

2.4.1.1 *Database generation*

The first step to create the database is to identify the variables that define all the possible operating points of the converter. Secondly, the range of values for each variable needs to be defined, in order to limit the magnitude of each dimension. Fig. 2.16 illustrates an example of a three-dimensional database, where the operating point is established with three variables —three-dimension figures will be served for the sake of simplicity. This space covers all the possible operating points of the power converter. Within the generated database, different scenarios exist where one of the variables can be fixed, where, in this example, would be delimited by a plane of operating points. This example could easily be extended to generic n dimensions.

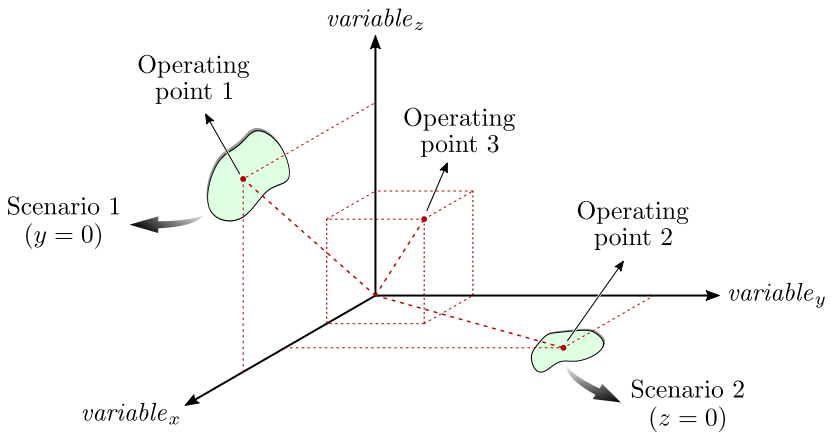

Fig. 2.16. Example of a three-dimensional operating conditions database.

These are possible input variables of the n-dimensional space for which the output measures are done:

- PEBB converter topology.
- VSC PEBBs connection structure. Sometimes common dc-link or independent can be considered.
- Modulation scheme. For instance, PWM, PWM with third-harmonic injection (THI), SVM, or Selective Harmonic Elimination (SHE) [36], [63], [65].
- f: Output fundamental frequency ($f = f_m$).
- f_{sw}: Equivalent switching frequency in converter output terminals.
- m_a: Amplitude modulation index. In this dissertation it is defined as the amplitude of the sine used in the converter modulator reference, as explained in *subsection 2.2.1.*
- V_{dc}: DC-link voltage.
- V^+, V^-: Positive- and negative-sequence converter voltage phasor amplitudes.
- δ_v^+, δ_v^-: Positive- and negative-sequence converter voltage phasor angles.
- δ_{vpn}: Phase shift between V^- and V^+; i.e., $\delta_{vpn} = \delta_v^- - \delta_v^+$.
- I^+, I^-: Positive- and negative-sequence converter current phasor amplitudes.
- θ_i^+, θ_i^-: Positive- and negative-sequence converter current phasor angles.
- θ_{ipn}: Phase shift between I^- and I^+; i.e., $\theta_{ipn} = \theta_i^- - \theta_i^+$.
- ϕ^+: Phase shift between I^+ and V^+; i.e., $\phi^+ = \theta_i^+ - \delta_v^+$. This angle defines the positive-sequence power factor ($\cos\phi^+$). The *generator agreement* is taken, assuming that the current flows from the converter to the application, and considering a positive phase difference ($\phi^+ > 0$) when I^+ is ahead of V^+. Note that the latter phasor is normally taken as a reference; i.e., $\delta_v^+ = 0°$.

Each of the presented points could represent a dimension in the different operating points of the converter. However, there are some scenarios where the number of variables is reduced or the dimension of some variables is limited, as illustrated in Fig. 2.16. These scenarios represent different applications within the generated database. For example, when the converter operates with a classical controller without including negative-sequence current control loops (without dual control), and it is only able to operate generating positive-sequence voltage, $V^- = 0$ and $\delta_{vpn} = 0°$ can be stated. If this same converter is working with a balanced load, $I^- = 0$ and $\theta_{ipn} = 0°$ can also be considered.

In order to analyze and compare the limitations of different converter structures, the proposed methodology is based on studying the converter internal indicators. For each simulated operating point, different parameters are measured and stored. The considered output parameters are measured in steady state. Fig. 2.17 shows the generation of the data of one operation point of the three-dimensional database. Output data of each operating point is created by launching simulation sweeps of each dimension; for instance, the variables x, y, and z in Fig. 2.16.

The case studies discussed in *subsection 2.4.2* are based on the analysis of dc-link indicators. As Fig. 2.17 shows, the dc-link is simulated with constant voltage sources (V_{dc}). In this manner, voltage ripples produced by dc-link capacitors do not affect the obtained results, and hence, all measured parameters are only dependent on the operating point

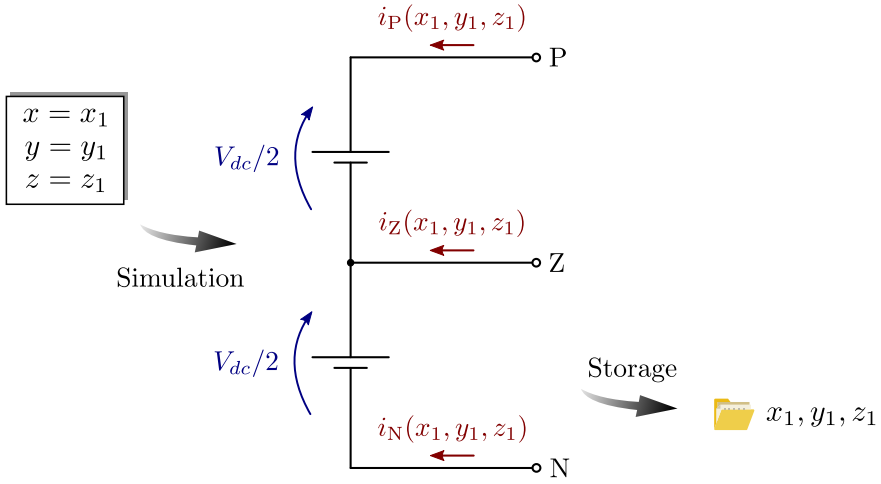

Fig. 2.17. Example of the generation of the operating point (x_1, y_1, z_1) data in the three-dimensional database. In this example, the dc-link currents i_P, i_Z, and i_N corresponding to the operating point (x_1, y_1, z_1) are measured and stored properly codified.

of the converter structure. As case studies evaluate 3L NPC PEBB-based structures, a dc-link neutral point "Z" is considered [69] (see *subsection 2.3.1*). Therefore, two $V_{dc}/2$ dc voltage sources are considered, and the currents i_P, i_Z, and i_N are measured. This could be generically extended to higher number of dc-link levels.

2.4.1.2 *Data extraction and results analysis*

After generating the database, the measured parameters need to be transformed into a post-processing stage in order to analyze the results. The first step, in order to analyze the measured data for a certain application, is to identify the dimensions of the n-dimensional space that need to be studied. That is, to recognize the operating scenario of the demanded application (Fig. 2.16). Once this is done, the results analysis tool extracts from the database the corresponding measured parameters (e.g., dc-link currents) stored previously for the identified operating points. Finally, the tool carries out a data post-processing, where several indicators are calculated (e.g., voltage ripples produced by dc-link capacitors). These are graphically illustrated as a function of the desired operating variable(s). Note that these indicators could be whichever the user considers important to be analyzed.

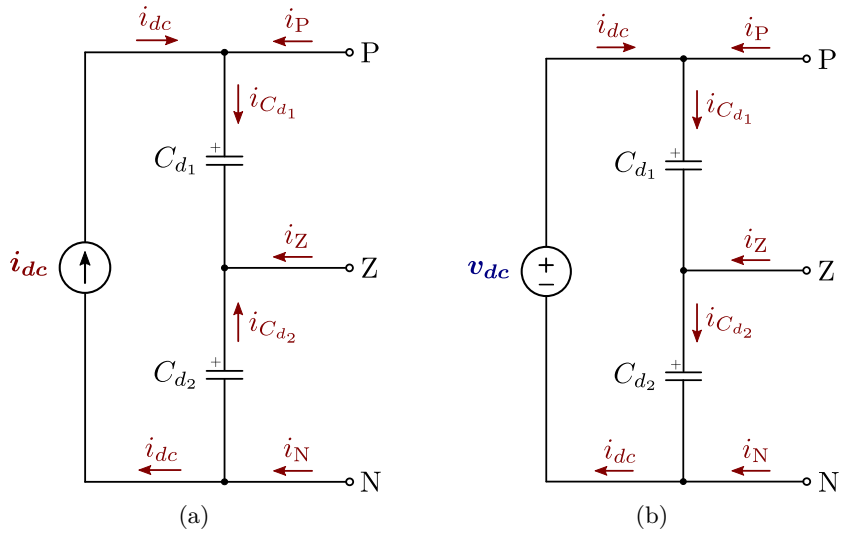

Fig. 2.18. Schemes of (a) current source and (b) voltage source dc-links of a 3L NPC converter.

Depending on the dc energy source type of the analyzed application, the dc-link can be treated differently in the post-processing stage. Fig. 2.18 shows two common cases covered in the case studies of *subsection 2.4.2*, applied to a 3L NPC converter. On the one hand, applications where the dc-link is supplied by far batteries or by a Diode Front End (DFE) rectifier with dc-link inductance can be considered as a dc current source (Fig. 2.18 (a)). On the other hand, a dc-link supplied by a nearby power source installed in the converter equipment itself, a back-to-back converter, a PV installation, or nearby installed batteries can be treated as a voltage source dc-link (Fig. 2.18 (b)).

From the dc-link currents measured (i_{P}, i_{Z}, and i_{N}) in the example database generation, the currents through dc capacitors (i_{C_d}) can be calculated, depending on the dc-link source type. The following indicators are proposed: dc-link current RMS values, amplitudes of the dc-link current low-order harmonics, dc capacitor voltage ripple (Δv_{C_d}), entire dc-link voltage ripple (Δv_{dc}), and neutral point voltage oscillation (Δv_{Z}). For that purpose, the user has to define the capcitance values of dc-link capacitors (C_{d_1} and C_{d_2}).

2.4.2 Case Studies

With the aim of validating the proposed methodology and demonstrating the potential of the tool, a comparison of various converter structures based on the connection of 3L NPC PEBBs is carried out. As mentioned, this is nowadays the standard VSC-based switching branc for MV levels. Considering a specific comparison scenario with certain operating variables, the database of the selected converter structures is created. Two particular operating scenarios included in the generated database are analyzed as case studies: a converter that operates as an ac power source connected to a balanced load, and a Static Synchronous Compensator (STATCOM) application with an unbalanced load.

2.4.2.1 *Fundamental PEBB and selected connection structures*

As mentioned, although wide variety of multilevel VSC topologies can be found in the specialized literature [28]–[36], one of the most commercially available and analyzed fundamental switching branch for MV levels (3.3 kV to 6.6 kV) is the 3L NPC [69] (see *subsection 2.3.1*). MV applications such as grid supporting, RES integration, metal processing, mining, marine or railway traction, demand electronic converter equipment of increased power. To obtain the required high power ratings, it is very common to interconnect 3L NPC PEBBs [60]–[62]. The way they are interconnected is not obvious and a deep analysis needs to be carried out to define the most suitable structure. That is why the proposed methodology is applied to compare structures based on the interconnection of these fundamental blocks.

Interconnecting 3L NPC PEBBs, large amount of combinations are possible. Depending on how PEBBs are interconnected, different voltage and current levels can be obtained in converter terminals. The possible 3L NPC PEBB combinations can be distinguished in two main groups, depending on the dc-link connection configuration [80]:

- Connecting three 3L NPC PEBBs, a three-phase 3L NPC VSC as the one studied in *subsection 2.3.1* is obtained. These converter structures can be parallelized, with a common dc-link for the three phases of each one of converters. Each converter dc-link can be independent, or all parallelized converters can share a common dc-link.

- As analyzed in *subsection 2.3.3.2*, if two 3L NPC PEBBs are connected forming an HB, a single-phase 5L NPC/HB power cell is obtained [81]. These cells can be connected either in star or in delta, forming three-phase VSC structures. Then, three-phase

converters can be parallelized, or more power cells can be connected in cascade, as a solution to increase the power rating.

It is not evident which PEBB interconnection structure suits better for a particular operating requirement. Especially, which one is more appropriate for new operating conditions that power converters did not have to deal with before.

Equivalent 3L NPC PEBB interconnection-based structures are selected, in order to reach the conclusions solely dependent on structural criteria. Four structures are considered, composed by 18 fundamental PEBBs: the first two are based on the 3L NPC VSC, and the other two on the 5L NPC/HB VSC. In this manner, all converter structures contain the same amount of PEBBs; thus, the same amount and type of switching semiconductor devices (formed by, for instance, IGBTs and diodes). Due to this fact, equal thermal limit of all the analyzed alternatives can be considered, as well as equal switching and conduction losses [82]. As 3L NPC PEBB voltage and currents are the same in all the configurations, output voltage and current ratings are different in each, but always maintaining the same output power for all the configurations.

– Fig. 2.19 (a) illustrates six 3L NPC three-phase VSCs parallelized, where each converter has its isolated three-phase dc-link. By contrast, in the structure showed in Fig. 2.19 (b), the six parallelized converters share a common three-phase dc-link.

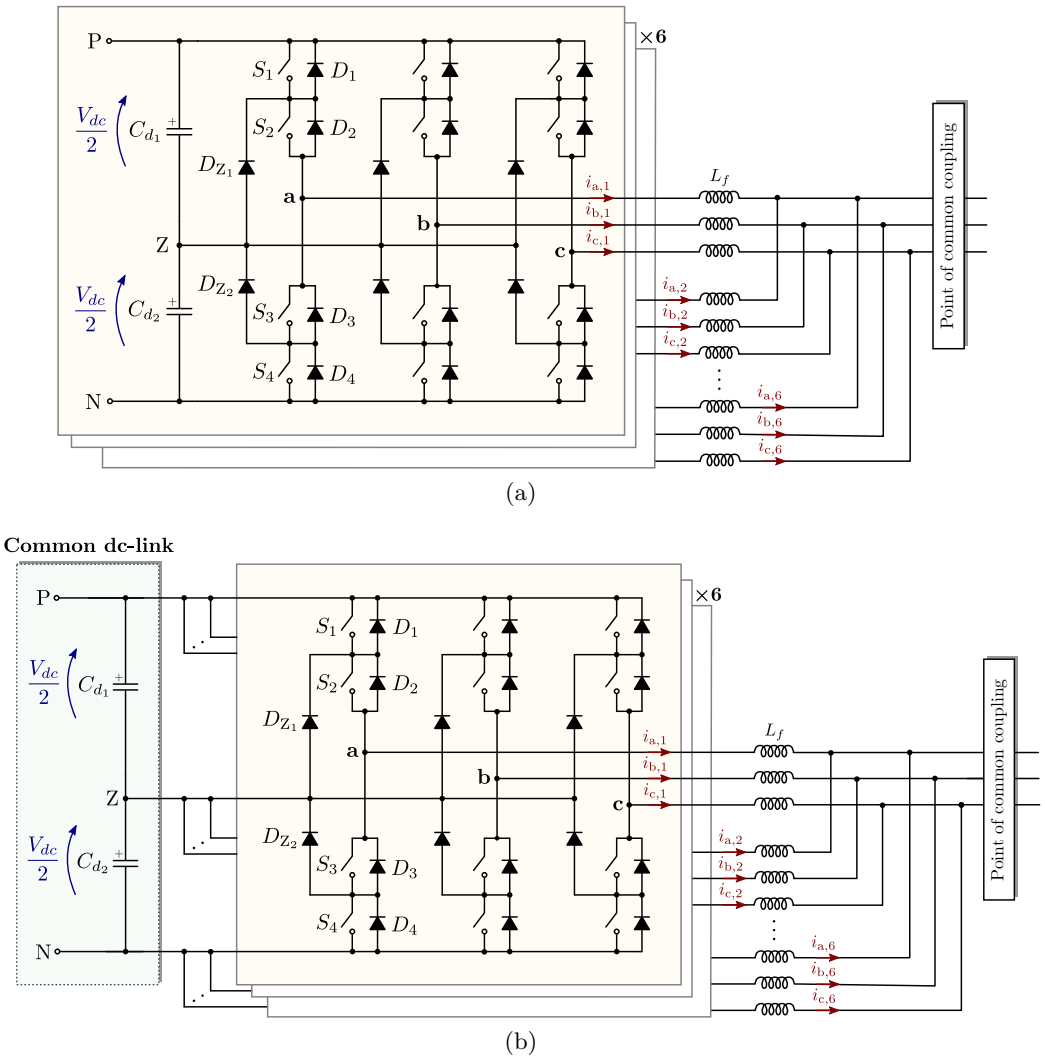

Fig. 2.19. Simplified schemes of three-phase 3L NPC VSCs. (a) Independent dc-links, and (b) common dc-link.

– 5L NPC/HB power cells of Fig. 2.13 with single-phase dc-links are interconnected to achieve three-phase VSCs. Converters are also parallelized in order to have the same number of semiconductors in all the structures (18 PEBBs). The structure represented in Fig. 2.20 (a) is based on the star-connection of 5L NPC/HB power cells and on the parallelization of three converters. Delta-connection is used for the other VSC structure, showed in Fig. 2.20 (b).

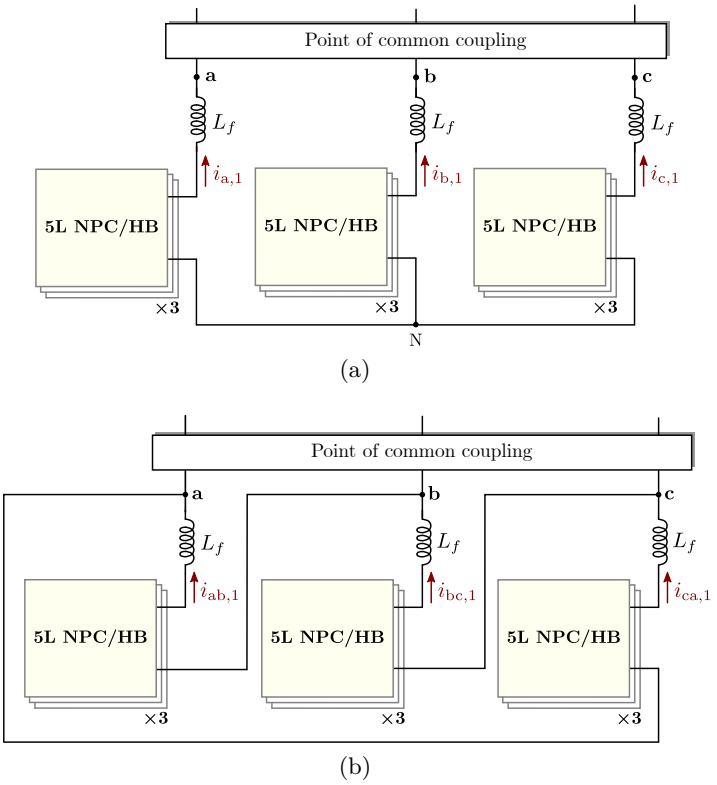

Fig. 2.20. Simplified schemes of three-phase 5L NPC/HB VSCs. (a) Star connection (YCHB), and (b) delta connection (DCHB).

2.4.2.2 *Database generation of the comparison scenario*

Once the converter structures are selected, the next step is to generate the database. For that, the n-dimensional space database needs to be defined. The first step is to define the dimensions to be covered. After, the range of each dimension should be clearly defined.

In the proposed database, only fundamental-frequency current is considered in converter terminals. Thus, the dimensions of the output current harmonics (magnitude and phase) are not contemplated. With this assumption, wave quality issues are not relevant since the selected converter structures contain almost identical output current total harmonic distortions (THD_i). This consideration cannot be assumed, for instance, to study harmonic active filtering applications, where the output current harmonics take some value.

The peak value of the fundamental-frequency phase current ($|\bar{I}_{ph}|$) considered at the converter output correspond to the nominal current of the 3L NPC PEBB used by a power converter manufacturer [80]. This current might be balanced (only i^+), or unbalanced (i^+ and/or i^-). In order to quantify the degree of current unbalance, the ratio k_{ipn} is defined in this dissertation, which allows to quantify unbalances where I^- exceeds I^+:

$$\text{for } I^+ \geq I^- \rightarrow \; k_{ipn} = \frac{I^-}{I^+} \; \rightarrow \; 0 \leq k_{ipn} \leq 1 \tag{2.9}$$

$$\text{for } I^+ \leq I^- \rightarrow \; k_{ipn} = 2 - \frac{I^+}{I^-} \; \rightarrow \; 1 \leq k_{ipn} \leq 2 \tag{2.10}$$

Equation (2.9) is applied when i^+ predominates, and (2.10) when i^- does. $k_{ipn} = 0$ states that the current sequence is only positive (balanced condition); $k_{ipn} = 1$ that both components exist and are of equal magnitude; and $k_{ipn} = 2$ expresses that the converter is only supplying negative-sequence current. Fig. 2.21 shows the evolution of the positive- and negative-sequence current phasor amplitudes (I^+, I^-) as a function of the ratio k_{ipn} and the phase shift between both sequences $(\theta_{ipn} = \theta_i^- - \theta_i^+)$.

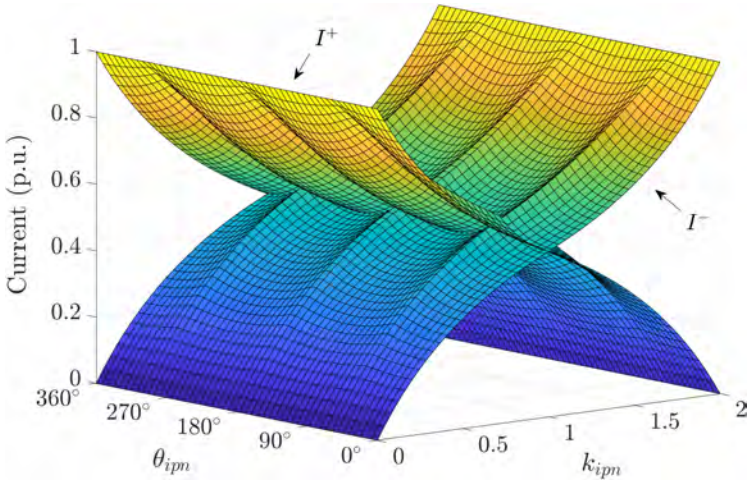

Fig. 2.21. Positive- and negative-sequence current amplitudes (I^+, I^-) at nominal phase current, as a function of k_{ipn} and θ_{ipn}. The same could be applied to the voltage.

Likewise, the ratio of voltage unbalance (k_{vpn}) can also be defined [55]:

$$\text{for } V^+ \geq V^- \rightarrow \; k_{vpn} = \frac{V^-}{V^+} \; \rightarrow \; 0 \leq k_{vpn} \leq 1 \tag{2.11}$$

$$\text{for } V^+ \leq V^- \rightarrow \; k_{vpn} = 2 - \frac{V^+}{V^-} \; \rightarrow \; 1 \leq k_{vpn} \leq 2 \tag{2.12}$$

Regarding the modulation strategy, the LSC-PWM IPD scheme is applied (see *subsection 2.2.2.2*). This PWM scheme is considered with or without THI. If the THI is applied, its amplitude is considered 1/6 of the fundamental-frequency component (see *subsection 2.2.1*). The carrier wave frequency (f_{cr}) is another variable that needs to be defined. When VSCs are parallelized or connected in cascade, interleaved carrier-based PWM is carried out [65]; i.e., phase shifting the carrier signals associated to each parallelized converter.

In the scenarios analyzed in the following case studies, a classical controller is used; that means that the VSC does not have negative-sequence current regulators and incorporates only positive-sequence voltage control loops, i.e., the VSC is not able to generate v^- $(k_{vpn} = 0)$. If v^- is not considered, the magnitude of v^+ in each single VSC is defined as

$$|\bar{V}_{ph}| = V^+ = m_a \frac{V_{dc}}{2} \tag{2.13}$$

for 3L NPC-based connection structures, and as

$$|\bar{V}_{ph}| = V^+ = m_a V_{dc} \tag{2.14}$$

for 5L NPC/HB-based connection structures. Table 2.6 lists the operating variables and the simulated values of each one for database generation. Once the variables are defined, the

database is generated performing simulation sweeps of different values of these variables. After this, each case study is analyzed in the results analysis stage, without the need of extra simulations.

Table 2.6. Operating variables for database generation.

Operating variable	**Simulated values**
PEBB converter topology	3L NPC switching branch
VSC PEBBs connection structure	$6 \times$ 3L NPC/HB $6 \times$ 3L NPC/HB with common dc-link $3 \times$ Y-connected 5L NPC/HB $3 \times \Delta$-connected 5L NPC/HB
DC-link voltage (V_{dc})	6500 V
DC-link capacitance ($C_{d_1} = C_{d_2}$)	1 mF per PEBB
Modulation scheme	LSC-PWM (IPD) LSC-PWM (IPD) + 1/6 THI
Output fundamental-frequency (f)	50 Hz
Carrier wave frequency (f_{cr})	900 Hz
Amplitude modulation index (m_a)	$0 \dots 2\sqrt{3}$
Positive-sequence power factor (ϕ^+)	$0° \dots 360°$
Nominal phase current ($\lvert\bar{I}_{ph}\rvert$)	400 A
Ratio of current unbalance (k_{ipn})	$0 \dots 2$
Phase shift between I^- and I^+ (θ_{ipn})	$0° \dots 360°$

2.4.2.3 *Case study I: ac power source connected to a balanced load*

In this operating scenario, the converter operates as an ac active power source, supplying the active (P) and the required reactive power (Q) to the load. Depending on the PQ required by the load, the positive-sequence power factor ($\cos\phi^+$) of the application varies. This could be a drive application, where the load demands the active power and the

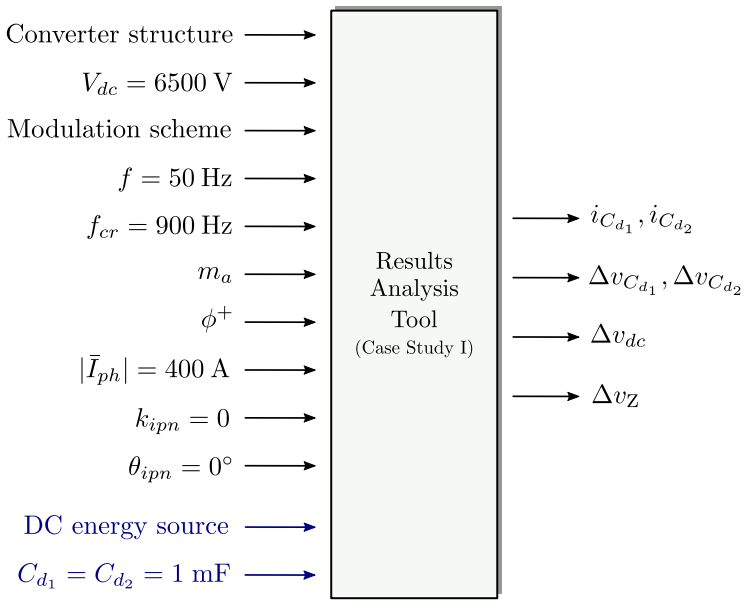

Fig. 2.22. Input operating variables and output dc-link indicators of *case study I* results analysis (blue inputs are defined for the post-processing).

magnetizing current represents the reactive power. Since the load is balanced, the converter exchanges only positive-sequence current ($k_{ipn} = 0$).

In order to convert dc-link currents into voltage, same dc-link capacitance per fundamental PEBB branch is assumed ($C_{d_1} = C_{d_2} = 1\,\text{mF}$). In such way, the selected four structures are equivalent, and the conclusions drawn depend only on structural criteria. Operating variables taking part in *case study I* are shown in Fig. 2.22, as well as the output dc-link indicators obtained by the results analysis tool. The dc-link energy source type and the values of the dc-link capacitors (C_{d_1}, C_{d_2}) are defined by the user for the post-processing. The presented tool can illustrate the evolution of calculated dc-link indicators as a function of some operating variables within the operating scenario.

On the one hand, Fig. 2.23 shows the evolution of the dc-link neutral point voltage oscillation (Δv_Z) of each converter structure, as a function of the phase shift between the converter positive-sequence voltage and current (ϕ^+); that is, as a function of the operating point positive-sequence power factor ($\cos\phi^+$).

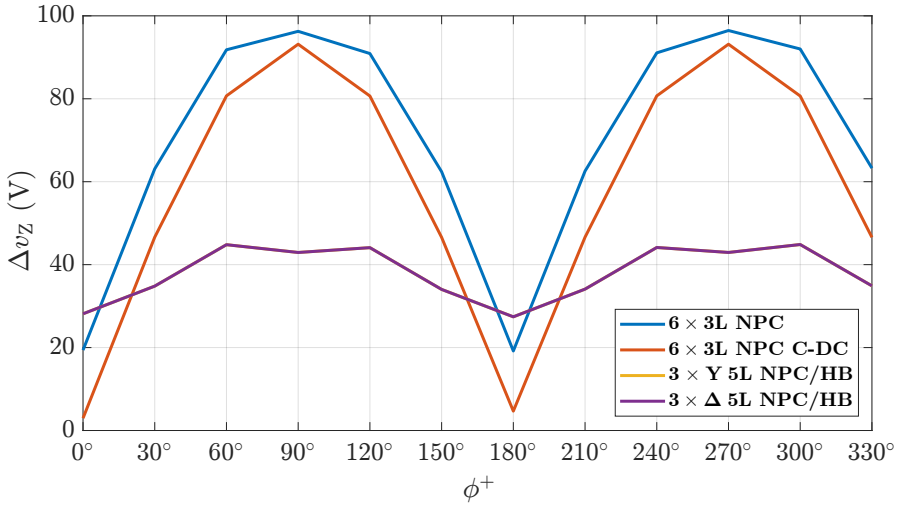

Fig. 2.23. DC-link neutral point voltage oscillation as a function of ϕ^+ (voltage source dc-link, LSC-PWM + 1/6 THI, and $m_a = 1$).

Voltage source dc-link case enables to analyze the dc-link neutral point ("Z") voltage oscillation. It can be seen that topologies based on 5L NPC/HB structures are equivalent. 3L NPC converters with common dc-link show smaller voltage oscillation whichever the power factor is, compared to 3L NPC with isolated dc-link configuration; this fact happens since the interleaving is also applied in the dc side when the dc-link is commonly connected. Besides, all the analyzed converter structures show the smallest neutral point oscillations in $\cos\phi^+ = 1$ applications, especially in three-phase dc-link converter structures.

On the other hand, current source dc-link case is interesting to study the entire dc-link voltage ripple, as well as voltage ripples in dc capacitors. Fig. 2.24 illustrates the voltage ripple of the bottom dc-link capacitor ($\Delta v_{C_{d_2}}$) as a function of the amplitude modulation index (m_a). The 3L NPC structure with a common dc-link presents less voltage ripple than with isolated dc-links. The two 5L NPC/HB-based structures show the same behavior and present more dc capacitor voltage ripple. This voltage ripple increases with the amplitude modulation index in all the analyzed converter alternatives.

2.4.2.4 *Case study II: STATCOM connected to an unbalanced load*

The use of the Static Synchronous Compensator (STATCOM) connected in parallel to the power grid is also frequent. The aim of the STATCOM is to give only reactive power (Q), with no energy source in the dc-link; thus, $\cos\phi^+ = 0$. These shunt type Flexible

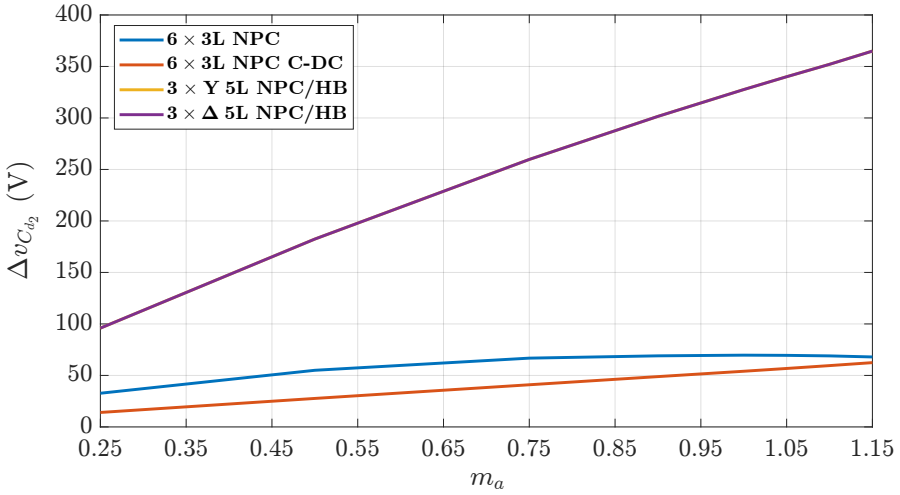

Fig. 2.24. Bottom dc capacitor voltage ripple as a function of m_a (current source dc-link, LSC-PWM + 1/6 THI, and $\phi^+ = 30°$.

AC Transmission System (FACTS) controllers are used for power quality improvements since provide/absorb Q in order to regulate the voltage, correct the power factor, eliminate harmonics in the supply currents, or balance supply currents when the load currents are unbalanced [17]–[24], [53], [54]. Note that the STATCOM application is discussed in more detail in the following chapters —as it is the main subject of study of this work.

In this last case study, the STATCOM is connected to an unbalanced load, exchanging unbalanced currents (i^+, i^-). Therefore, unlike *case study I*, the ratio k_{ipn} and the angle θ_{ipn} take different values. The values of the operating variables that define this scenario are outlined in Fig. 2.25. It is assumed that converter dc-links are powered by dc current sources (the case in Fig. 2.18 (a)).

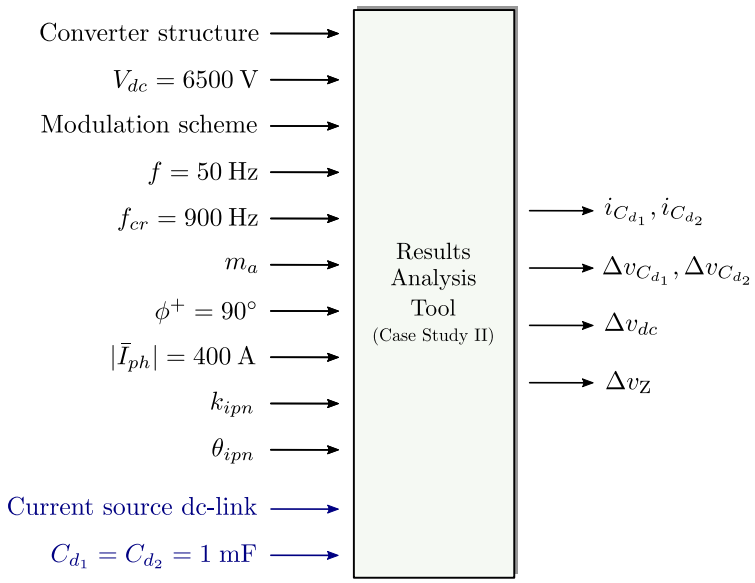

Fig. 2.25. Input operating variables and output dc-link indicators of *case study II* results analysis (blue inputs are defined for the post-processing).

Fig. 2.26 illustrates the evolution of the voltage ripple (Δv_{dc}) of the most restrictive dc-link as a function of the ratio of current unbalance (k_{ipn}) and the phase shift between the negative- and positive-sequence current components (θ_{ipn}). A repetitiveness of 120°

and a symmetry of 60° is detected in θ_{ipn}. Due to this reason, a range between 0° and 60° is only shown.

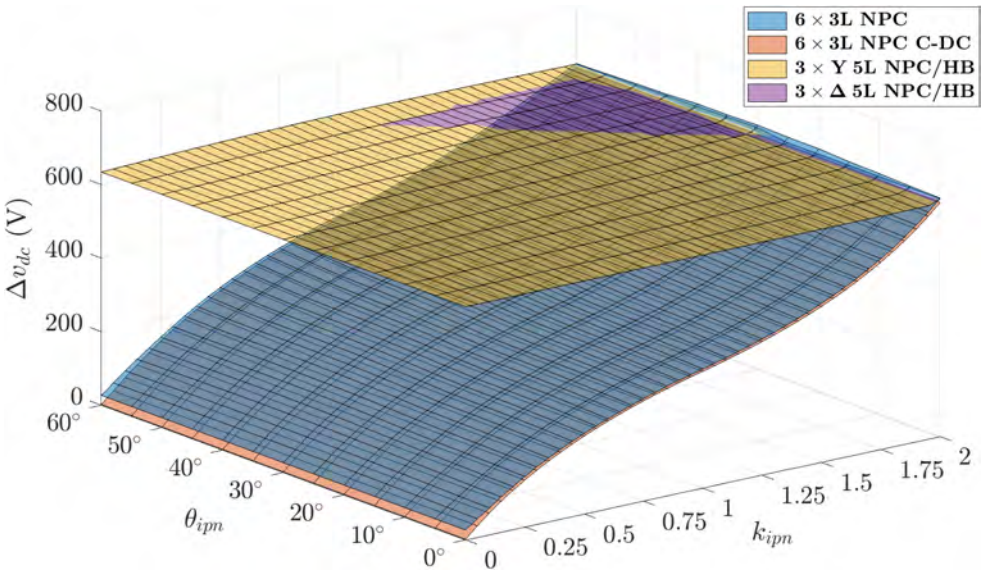

Fig. 2.26. DC-link voltage ripple in STATCOM application as a function of k_{ipn} and θ_{ipn} (LSC-PWM and $m_a = 1$).

It can be appreciated that 3L NPC-based structures present less voltage ripple than 5L NPC/HB-based ones. Either connected in star or delta, 5L NPC/HB-based structures present an equal and almost constant dc-link voltage ripples, regardless of k_{ipn}. On the contrary, 3L NPC-based structures increase their voltage ripple as k_{ipn} increases. Added to this, as in the balanced scenario analyzed in *case study I*, when all the 3L NPC converters share the same dc-link, less voltage ripple is always achieved.

One converter design dimensioning criterion could be to consider the worst dc-link voltage ripple case for each ratio of current unbalance. Due to this fact, Fig. 2.27 illustrates the maximum dc-link voltage ripple for each k_{ipn}; that is, the dc-link voltage ripple for the most restrictive θ_{ipn}, and for the most charged dc-link (in case of 5L NPC/HB single-phase dc-link structures).

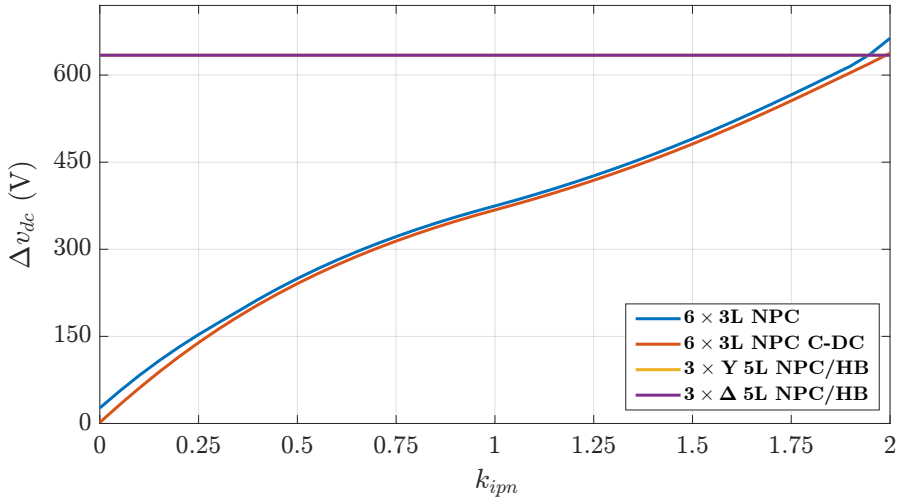

Fig. 2.27. Maximum dc-link voltage ripple in STATCOM application for each k_{ipn} (LSC-PWM and $m_a = 1$).

The above example clearly shows that 3L NPC-based parallelized converters with common dc-link present smaller voltage ripple than with independent dc-links. As mentioned, this indicator gets bigger as k_{ipn} increases in this type of structures. On the contrary, 5L NPC/HB-based structures (CHBs) are interesting to operate as STATCOM under unbalanced current conditions, since the maximum dc voltage ripple is equal regardless of k_{ipn} in output terminals. Therefore, it can be concluded that if a 5L NPC/HB converter is dimensioned for balanced conditions ($k_{ipn} = 0$), the dc-link will withstand any unbalanced current condition in terms of dc voltage ripple. In contrast, the 3L NPC converter needs to be over-rated if it is required to operate with both positive- and negative-sequence currents. That is, the 3L NPC converter must be correctly sized for the current unbalance where it is expected to work; otherwise, it will have to be disconnected.

2.5 CONCLUSIONS

Power electronic converter-based grid demands power equipment with higher voltage and power rating. From the overview provided in this chapter about multilevel VSC topologies, it can be concluded that, since their scalable attributes, those based on modular structures are the most promising alternatives for grid and industry applications. These include principally the CHB and the MMC. To increase the power, voltage increasing means less power losses than current increasing, and thus, from this point of view, it is more feasible to connect single-phase power cells in cascade than to parallelize three-phase VSCs such as the 3L NPC. Multilevel VSCs based on modular structures even make the transformerless grid connection possible.

Nevertheless, modular structures require single-phase dc-links which are isolated from each other, and hence, for applications where active power (P) is exchanged, it is also necessary for all energy sources to be isolated from each other. In applications where only reactive power (Q) is exchanged, such as the STATCOM, the mentioned drawback does not exist; energy sources are not necessary since there is no net energy transfer ($P = 0$). This makes multilevel VSCs based on modular structures attractive for STATCOM application.

The methodology presented in this chapter allows the power electronic converter designer to evaluate different VSC structures. The proposed methodology provides valuable information to study the converter features and limitations under any operating requirement, enabling the user to compare, select, or develop the most suitable configuration. An n-dimensional database is generated, which incorporates all possible operating points of the converter, independent from the application. The presented tool extracts from the database the measured parameters, and following a data post-processing, provides information to determine which conversion structure is the most appropriate, or which suits better the specific operating requirement. After identifying the operating scenario of a demanded application, the designer can analyze the results in a simple way without carrying out any extra simulation.

In order to demonstrate the potential of the methodology and the results analysis tool, various converter structures based on the interconnection of 3L NPC PEBBs have been compared under two operating scenarios. However, this methodology can be applied for any converter topology or PEBB connection structure; even for structures other than VSC-based. The study can also be extended with more operating point dimensions and more indicators that the user considers important to be analyzed. For instance, if different type of switching semiconductor devices are considered, the number of switches needed, or conduction and switching losses could be analyzed. Just to give another example, if different cooling systems need to be examined, other indicators such as the maximum current ($|\bar{I}_{ph}|$) could also be studied [80] (see example of Fig. 2.28).

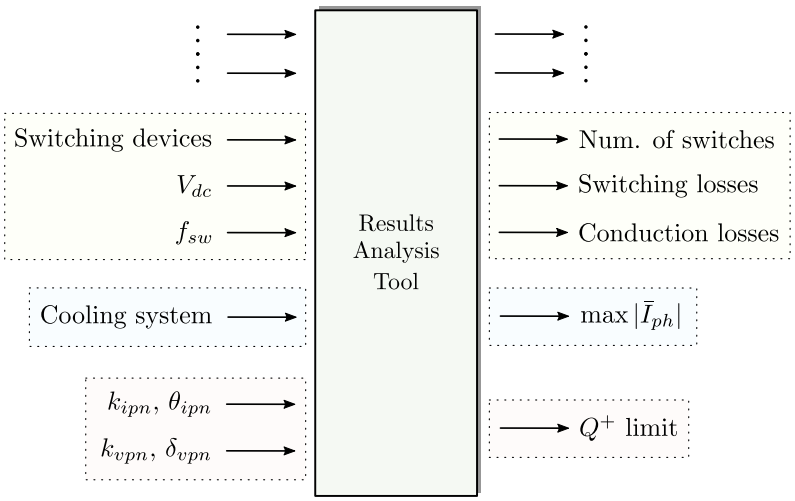

Fig. 2.28. Results analysis with possible input variables and output indicators for further studies.

In the last scenario analyzed in *subsection 2.4.2.4 (case study II)*, it is concluded that, for STATCOM application, the CHB presents higher dc-link voltage ripple than the 3L NPC under unbalanced current conditions. Nevertheless, contrary to the 3L NPC, the maximum dc voltage ripple of the CHB is the same regardless of the ratio of current unbalance (k_{ipn}) in output terminals. This means that CHBs dimensioned to operate under balanced conditions can operate also with unbalanced currents; at least in terms of dc-link voltage ripple. Anyway, in order to analyze the behavior of VSCs in the face of unbalanced conditions, in addition to the dc-link voltage ripple, more indicators should be added to the results analysis tool. Since normally the aim of the STATCOM is to provide positive-sequence reactive power (Q^+), the limit of this indicator is, from the manufacturer point of view, the indicative parameter to compare and select the most suitable VSC structure to operate under unbalanced voltage and/or current conditions (see Fig. 2.28).

To sum up, the aforementioned conclusions have motivated the research project around this doctoral thesis to further study multilevel VSCs based on modular structures, especially for those high power – MV applications where the power converter is required to operate under unbalanced conditions. Although these VSC structures are very well suited for STATCOM, they are also attractive for large-scale PV power integration and Battery Energy Storage Systems (BESS). However, it has been observed that they present certain drawbacks under unbalanced operation, which might limit the maximum power that the converter could deliver. That is why the next chapter provides a comprehensive literature overview of the operation and the solutions for the adequate operation of the most commonly used multilevel VSCs based on modular structures in some typical unbalanced operating scenarios.

Chapter 3

POWER BALANCING IN MODULAR VOLTAGE SOURCE CONVERTERS UNDER UNBALANCED OPERATION: A REVIEW

Multilevel VSCs based on modular structures are envisioned as a prominent alternative for high power – MV grid and industry applications, in which the unbalanced conditions stand out. This chapter provides a comprehensive literature review about the operation and the solutions of the CHB and the MMC for that purpose, identifying, classifying, and analyzing the intercluster active power balancing strategies for their adequate operation in some typical unbalanced operating scenarios: the STATCOM under unbalanced voltage and/or current conditions, the unequal power generation in large-scale PV power plants, and the uneven power distribution in BESS. Several future challenges are identified during the study, and the research gap is identified. The literature review provided in this chapter resulted in publication [J1].

3.1 INTRODUCTION

As mentioned, power electronic converter-based grid makes it increasingly necessary to count on power equipment with higher voltage and power rating [58]. Since their scalable attributes, multilevel VSCs based on modular structures are nowadays the most promising alternatives commercially available for that purpose (see *subsection 2.3.3*). As the ac voltage is proportional to the number of power cells, direct power grid connection is often feasible without a bulky step-up transformer [33], [39], [40], [83]. Furthermore, due to the multilevel waveform, the power quality is improved compared to non-modular VSC topologies [84].

Since multilevel VSCs based on modular structures were proposed in the technical literature, there has been confusion regarding terminology within this family. Because both circuit configurations stand out due to their *modular* and *multilevel* features, Akagi classified the Cascaded H-Bridge (CHB) converter and its connection configurations within the Modular Multilevel Converter (MMC) family [40]. After this publication, many authors have used this criterion to distinguish and classify modular converter structures. Nevertheless, the author of this PhD dissertation understands the MMC as the particular converter topology presented by Marquardt *et al.* [72]. Hence, modular converter structures are grouped separately in this work: on the one hand, the CHB multilevel converter, in both star (YCHB) and delta (DCHB) configurations (see Fig. 2.12); on the other hand, the MMC (see Fig. 2.14). In both converter groups, any VSC-based power cell topology is considered (e.g., half-bridge, full-bridge, or 5L NPC/HB power cells). Fig. 3.1 shows the simplified classification of the multilevel VSCs based on modular structures discussed.

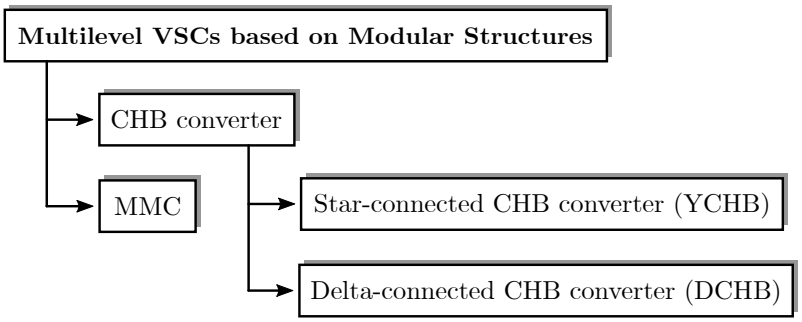

Fig. 3.1. Classification of multilevel VSCs based on modular structures.

Table 3.1 collects the main per-unit (p.u.) electrical characteristics of the structures considered in this chapter, which provides a general idea of the number of power cells and/or the transformer conversion ratio that need to be used for each one. As mentioned, if the same power cell voltage is used, to achieve the same voltage rating in ac terminals, the MMC needs twice as many power cells per phase cluster than the CHB. However, the MMC can be built with half-bridge power cells, while the CHB needs full-bridge ones [77]. In this manner, the number of switching devices is the same for the three structures.

Modular structures are frequently used as Static Synchronous Compensator (STATCOM) to facilitate the RES integration into the power grid [9], by helping to meet the requirements imposed by transmission and distribution system operators. The STATCOM provides fast dynamic reactive power support and improves the supply quality [24]. It is also used to compensate unbalanced loads in large industry applications such as mining or metal processing [40]. When the STATCOM was proposed, first thyristor-based [85], and later VSC-based [86], it was defined as a converter connected in parallel to the power grid which delivers or absorbs ac reactive power [17]. Today, the specialized literature calls "STATCOM" the power equipment that provides a wide variety of functionalities [47]. The

author of this PhD dissertation considers the STATCOM as the regulating static device which does not exchange net energy (active power) with the power grid.

Table 3.1. Electrical characteristics of the multilevel VSCs based on modular structures under study. All the values are normalized with reference to the YCHB configuration.

	YCHB	**DCHB**	**MMC**
PCC voltage	1 p.u.	$1/\sqrt{3}$ p.u.	1 p.u.
PCC current	1 p.u.	$\sqrt{3}$ p.u.	1 p.u.
Rated power	1 p.u.	1 p.u.	1 p.u.
Number of power cells	n	n	$2n$
Number of switches	S_x	S_x	S_x

Due to its modular configuration, modular structures are also the most interesting solutions for large-scale photovoltaic (PV) integration [41]–[43]. Connecting them to different power cells, modular structures allow to separate PV module strings, controlling each one separately and maximizing the PV power generation. Similarly, modular converters are also very suitable for Battery Energy Storage Systems (BESS) [45], [46]. Each battery unit is connected independently to separate power cells, and depending on the state-of-charge (SOC) of each one, an unequal active power distribution is enabled, where some battery units can be consuming and others delivering energy [44].

Among the challenging operating scenarios that a converter-dominated power system implies, the unbalanced operation should be highlighted; a new scenario that converters had not been asked to deal with before. On the one hand, dealing with the unbalanced generation of RES supposes a challenge when delivering balanced currents into the power grid [87]. On the other hand, requirements from grid codes are changing and start to demand negative-sequence injection capability from the converters connected to their power grid [37], [47]–[51]. The unbalanced operation is an issue that the converter must face, either in transmission or in distribution systems. Single-phase loads such as traction drives, arc-furnaces, or adjustable speed drives are one of the causes of an unbalanced current scenario [40]. The voltage unbalance may arise, for instance, from asymmetric grid faults or unbalanced loads [29]. The unbalance may ask the converter to give negative-sequence current and/or voltage to balance the current and/or the voltage at the PCC.

In the case of unbalanced operation, the main disadvantage of CHBs is the lack of a common three-phase dc-link, and thereby the difficulty in exchanging energy among phase clusters [54]. Consequently, countermeasures must be taken in order to preserve the balancing of dc-link capacitors. Different intercluster balancing methods have been proposed in the specialized literature, depending on whether it is a YCHB or a DCHB, and the application. These solutions will have an impact on the overall rating of the converter, especially in terms of voltage and current requirements.

The circulating current between the upper and lower arms of each phase cluster might also have an impact on the ac output current of the MMC under unbalanced conditions [88], [89], assuming that the converter has been dimensioned for balanced operation (where circulating currents of different harmonic orders also exist).

The unbalanced operation is a trending issue, and it will have a large impact in the future electrical system. Despite their advantages, multilevel VSCs based on modular structures present some drawbacks under unbalanced conditions. In order to overcome these, different control solutions have been proposed in the specialized literature. However, the information around the operation and the solutions for modular structures under unbalanced conditions is very disperse, and has not been previously reviewed or classified.

Therefore, the aim of this chapter is to perform a comprehensive review of the problems that the unbalanced operation suppose for multilevel VSCs based on modular structures, to classify the proposed solutions, and to identify challenges.

3.2 PROBLEM OF THE UNBALANCED OPERATION IN MODULAR VSC STRUCTURES

The instantaneous active power in each phase cluster of the power converter $(p_{\mathrm{a}}, p_{\mathrm{b}}, p_{\mathrm{c}})$ can be calculated by the inner product of the phase cluster voltage and current [90]:

$$p_{ph}(t) = v_{ph}(t) \cdot i_{ph}(t) \tag{3.1}$$

Assuming unbalanced voltage and current scenarios, the time-domain converter phase cluster voltage can be expressed as

$$v_{ph}(t) = V^{+} \sin\left(\omega t + \delta_v^{+} + k\frac{2\pi}{3}\right) + V^{-} \sin\left(\omega t + \delta_v^{-} - k\frac{2\pi}{3}\right) \tag{3.2}$$

and the current as

$$i_{ph}(t) = I^{+} \sin\left(\omega t + \theta_i^{+} + k\frac{2\pi}{3}\right) + I^{-} \sin\left(\omega t + \theta_i^{-} - k\frac{2\pi}{3}\right) \tag{3.3}$$

being $k = 0, -1, 1$ for $ph = \mathrm{a}, \mathrm{b}, \mathrm{c}$, respectively. The phase cluster voltage and current can also be expressed as stationary space phasors:

$$\bar{V}_{ph} = V^{+} e^{j(\delta_v^{+} + 2\pi k/3)} + V^{+} e^{j(\delta_v^{-} - 2\pi k/3)} \tag{3.4}$$

$$\bar{I}_{ph} = I^{+} e^{j(\theta_i^{+} + 2\pi k/3)} + I^{-} e^{j(\theta_i^{-} - 2\pi k/3)} \tag{3.5}$$

Applying the following trigonometric identity,

$$\sin\alpha \sin\beta = \frac{\cos(\alpha - \beta) - \cos(\alpha + \beta)}{2} \tag{3.6}$$

expression (3.1) can be developed to:

$$\begin{aligned} p_{ph}(t) = {} & \underbrace{\frac{V^{+}I^{+}}{2}\cos\left(\delta_v^{+} - \theta_i^{+}\right)}_{\bar{P}_{ph}^{++}} + \underbrace{\frac{V^{+}I^{-}}{2}\cos\left(\delta_v^{+} - \theta_i^{-} + k\frac{4\pi}{3}\right)}_{\bar{P}_{ph}^{+-}} \\ & + \underbrace{\frac{V^{-}I^{+}}{2}\cos\left(\delta_v^{-} - \theta_i^{+} - k\frac{4\pi}{3}\right)}_{\bar{P}_{ph}^{-+}} + \underbrace{\frac{V^{-}I^{-}}{2}\cos\left(\delta_v^{-} - \theta_i^{-}\right)}_{\bar{P}_{ph}^{--}} \\ & - \underbrace{\frac{V^{+}I^{+}}{2}\cos\left(2\omega t + \delta_v^{+} + \theta_i^{+} + k\frac{4\pi}{3}\right)}_{\tilde{p}_{ph}^{++}} - \underbrace{\frac{V^{+}I^{-}}{2}\cos\left(2\omega t + \delta_v^{+} + \theta_i^{-}\right)}_{\tilde{p}_{ph}^{+-}} \\ & - \underbrace{\frac{V^{-}I^{+}}{2}\cos\left(2\omega t + \delta_v^{-} + \theta_i^{+}\right)}_{\tilde{p}_{ph}^{-+}} - \underbrace{\frac{V^{-}I^{-}}{2}\cos\left(2\omega t + \delta_v^{-} + \theta_i^{-} - k\frac{4\pi}{3}\right)}_{\tilde{p}_{ph}^{--}} \end{aligned} \tag{3.7}$$

As can be seen in (3.7), the per-phase instantaneous active power contains both an average ($\bar{P}_{\mathrm{a}}$, $\bar{P}_{\mathrm{b}}$, $\bar{P}_{\mathrm{c}}$) and an oscillating ($\tilde{p}_{\mathrm{a}}$, $\tilde{p}_{\mathrm{b}}$, $\tilde{p}_{\mathrm{c}}$) term:

– The oscillating term ($\tilde{p}$) is generated due to the single-phase nature of power converters. This term oscillates at twice the power grid frequency (2ω) with a zero average value. From (3.7) different expressions can be distinguished. Terms $\tilde{p}_{ph}^{+,+}$ and $\tilde{p}_{ph}^{-,-}$ correspond to the positive- and negative-sequence oscillating active power expressions, while terms $\tilde{p}_{ph}^{+,-}$ and $\tilde{p}_{ph}^{-,+}$ represent the oscillating active power due to the cross-interaction between positive- and negative-sequence voltage and current components. Note that $\tilde{p}_{ph}^{+,-}$ and $\tilde{p}_{ph}^{-,+}$ are common in the three phases.

– The average active power ($\bar{P}$) corresponds to the exchanged energy. Terms $\bar{P}_{ph}^{+,+}$ and $\bar{P}_{ph}^{-,-}$ represent the positive- and negative-sequence average active power expressions, which are common in the three phases. For its part, terms $\bar{P}_{ph}^{+,-}$ and $\bar{P}_{ph}^{-,+}$ correspond to the average active power due to the cross-interaction between positive- and negative-sequence voltage and current components.

As it will be explained in more detail in *section 4.3*, the oscillating active power terms generated due to the cross-interaction between positive- and negative-sequence components ($\tilde{p}_{ph}^{+,-}$ and $\tilde{p}_{ph}^{-,+}$) will not affect single-phase dc-link topologies such as the multilevel VSCs based on modular structures analyzed in this chapter. It is this 2ω oscillating term which mainly has an effect on the dc-link voltage ripple (Δv_{dc}), and *subsection 2.4.2.4* concludes that this ripple is independent of the unbalance in single-phase dc-link configured VSCs such as the CHB. That is why this chapter only focuses on the distribution of the average active power under unbalanced conditions. Moreover, this chapter reviews the state of the art, where the effect of the oscillating active power in both single- and three-phase dc-link VSC structures under unbalanced conditions has not been previously analyzed nor quantified.

3.2.1 STATCOM Scenario

The STATCOM using multilevel VSCs is finding increased utilization in transmission and distribution grids [18]–[23]. The most typical applications of the STATCOM could be the improvement of the power system stability, power factor ($\cos\phi$) correction, regulation of line voltages, active power filtering (APF), mitigation of voltage flicker, unbalanced load compensation, and low-voltage ride-through (LVRT) [24]. The main characteristic of the STATCOM application is that both the positive- ($\cos\phi^{+}$) and negative-sequence power factors ($\cos\phi^{-}$) are zero (i.e., $\delta_v^{+} \perp \theta_i^{+}$, and $\delta_v^{-} \perp \theta_i^{-}$). That is, there is no need of any energy source [17], since, neglecting losses, the net active power (energy) transfer between the power converter and the application is zero ($\bar{P}_{\mathrm{a}} + \bar{P}_{\mathrm{b}} + \bar{P}_{\mathrm{c}} = 0$).

When there is no interaction between positive- (v^{+}, i^{+}) and negative-sequence (v^{-}, i^{-}) components (i.e., only term $\bar{P}_{ph}^{+,+}$ or $\bar{P}_{ph}^{-,-}$ exists), the average active power which flows into each phase cluster of the STATCOM is zero. In contrast, when the STATCOM operates under unbalanced voltage and/or current conditions, terms $\bar{P}_{ph}^{+,-}$ and/or $\bar{P}_{ph}^{-,+}$ appear in (3.7), which are also different in each phase cluster. These new terms cancel out in the ac side, but may appear in the single-phase dc side. Thus, each phase cluster might give or absorb active power different from zero ($\bar{P}_{\mathrm{a}} \neq \bar{P}_{\mathrm{b}} \neq \bar{P}_{\mathrm{c}} \neq 0$).

On the one hand, in the case of CHB configurations (see Figs. 2.12 (a) and (b)), where each power cell of the converter has its own single-phase dc-link, an external dc energy source is required. In STATCOM application, where there is no need of any dc energy supply for each cascaded power cell, dc-link capacitor balancing cannot be guaranteed under unbalanced conditions, and hence, dc-link voltage drift appears. Fig. 3.2 shows an example of the impact of an unbalance on the phase cluster instantaneous active powers (p_{a}, p_{b}, p_{c}), and on dc-link capacitor voltages ($v_{dc\text{-}\mathrm{a}}$, $v_{dc\text{-}\mathrm{b}}$, $v_{dc\text{-}\mathrm{c}}$) of a YCHB STATCOM.

For clarity of the illustration, the plotted voltages are low-pass filtered in order to remove the double-frequency component (2ω). Each phase cluster is composed of a single power cell for the sake of simplicity ($n = 1$). It can be appreciated that when the current becomes unbalanced, non-zero average active powers appear in each phase cluster, which lead to the drifting of dc-side voltages. The effect in the DCHB is almost identical.

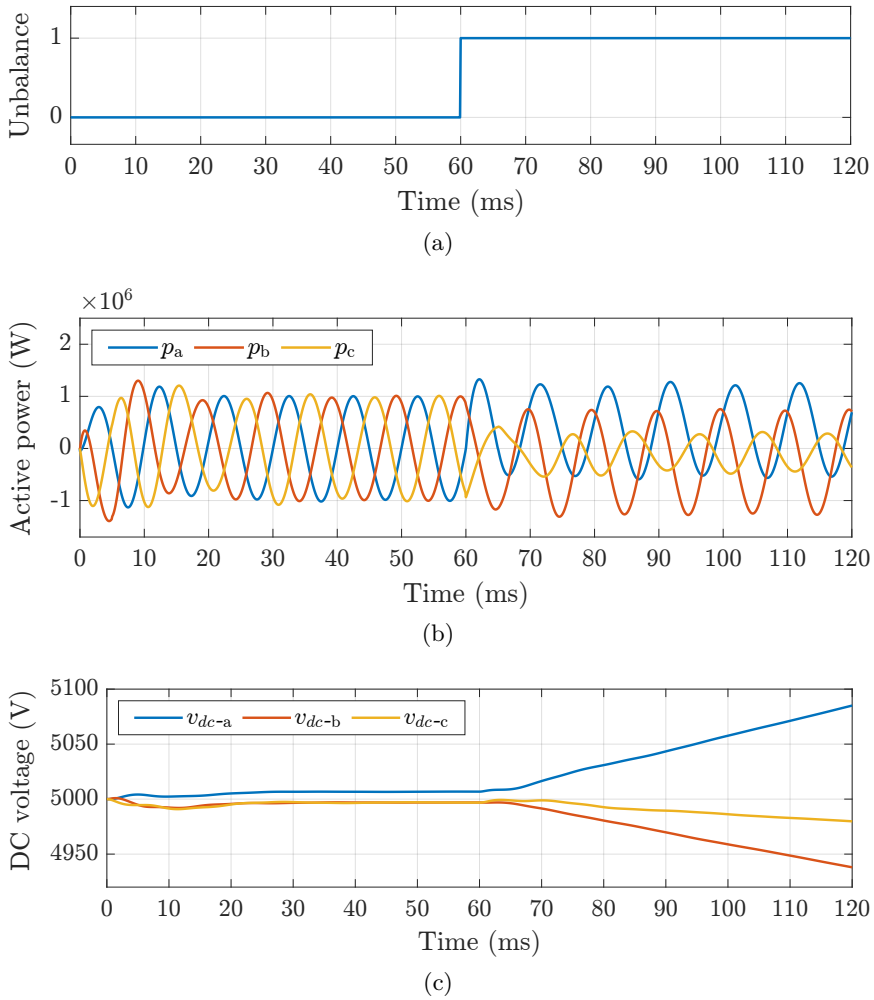

Fig. 3.2. Impact of an unbalance on the YCHB STATCOM. (a) Unbalance, (b) phase cluster active power, and (c) phase cluster dc-link capacitor voltage.

Consequently, countermeasures must be taken in order to correct this uneven active power distribution among the phase clusters of the CHB. The unbalance of the dc voltage may cause higher semiconductor stress, isolation failures or increase in total harmonic distortion (THD) at ac voltage and currents [91], or even can make the converter exceed its operating limits. In this case, the control strategy has to keep dc-link capacitor voltages in each phase cluster adjusted to the reference. This solution might suppose a de-rating in the converter output power.

On the other hand, VSC structures with a common dc-link for three phase clusters (e.g., 3L NPC) do not need any energy source connected to this dc-link in STATCOM application, whatever the unbalance is. That is, the sum of terms $\bar{P}_{ph}^{+-}$ and $\bar{P}_{ph}^{-+}$ of (3.7) in the three phase clusters is zero ($\bar{P}_a + \bar{P}_b + \bar{P}_c = 0$). This is the case of the MMC (see Fig. 2.14). However, as the phase cluster active power still differs from zero ($\bar{P}_a \neq \bar{P}_b \neq \bar{P}_c \neq 0$), different dc circulating currents appear in each phase cluster of the MMC; as a result of the potential difference between the neutral points of each set of star-connected converters forming the MMC [92].

3.2.2 Large-Scale PV Power Plant Scenario

Multilevel VSCs based on modular structures may be required to operate with active power. This can be the case of large-scale PV power plants, where the active power flows unidirectionally from the PV modules to the power grid.

Among all practical multilevel VSC topologies, the CHB converter is considered as one of the most suitable structures for large PV integration. In this case the active power is supplied directly by the PV modules with no need of extra energy sources. The separate low voltage PV strings can be modularly connected to each cascaded power cell. This allows easy extension to reach higher voltage and power levels, thus making it feasible to connect a large-scale PV power plant to a MV grid with a single converter. The main reasons for choosing the CHB structure for large-scale PV integration are: 1) individual maximum power point tracking (MPPT) algorithm alternatives; 2) improved high-power quality; 3) power cell fault redundancy; and even 4) the transformerless direct grid connection [41], [42]. Some of these characteristics cannot be achieved with the MMC.

The CHB converter is typically designed considering that equal amount of active power is delivered to each phase cluster. Nevertheless, this assumption does not hold for large-scale PV applications. Even if the number of PV modules connected to each power cell is the same, and they are of the same characteristics, the active power supplied to each power cell will differ ($\bar{P}_{\mathrm{a}} \neq \bar{P}_{\mathrm{b}} \neq \bar{P}_{\mathrm{c}}$). This unequal power distribution occurs as a result of the dependence of the PV string generation on local weather conditions, or other causes such as partial shading due to near objects or cloud movement, unequal module temperature, manufacturing tolerances, dirt, or inhomogeneous module degradation [93].

As a consequence of the unequal power generation in large-scale PV power plants, the three-phase grid currents will become unbalanced if countermeasures are not taken [87]. As grid standards demand balanced grid current injection [37], [94], the control strategy has to redistribute equally the active power among phase clusters.

3.2.3 BESS Scenario

Another application where an active power is needed is the BESS. These systems play a key role in order to handle with the non-dispatchable nature of RES and facilitate their grid integration. They can even provide Fast Frequency Response (FFR), inertia emulation, or voltage regulation services to the grid. In this case, the active power can flow bidirectionally, either from the batteries to the application or vice versa.

Modular VSCs are the most interesting alternatives for BESS [45], [46]. The isolated dc-links of each power cell are connected to separate battery strings, and thus, an independent management of each battery unit forming the BESS installation is achieved. Due to this reason, each of the converter phase clusters can absorb or deliver an unequal active power ($\bar{P}_{\mathrm{a}} \neq \bar{P}_{\mathrm{b}} \neq \bar{P}_{\mathrm{c}}$) [44]. As well as PV plants, in order to absorb/deliver only positive-sequence average active power from/to the ac or dc source, a control strategy needs to be added.

Although the aim of the application differs, the operation principle under unbalanced conditions is the same, either a STATCOM application, large-scale PV power plant, or BESS: to maintain the dc-link capacitor voltages balanced, or to supply/absorb balanced currents. That is, to set the average active power of each phase cluster to the reference value. *Section 3.3* deals with the techniques used for that purpose.

3.3 INTERCLUSTER ACTIVE POWER BALANCING IN MODULAR VSC STRUCTURES

The unbalanced operation of multilevel VSCs based on modular structures involves some drawbacks to be addressed. The countermeasures adopted depend on the converter structure and the application.

3.3.1 STATCOM under Unbalanced Voltage and/or Current Conditions

As (3.7) shows, different average active power is derived in each phase cluster due to the cross-interaction between positive- and negative-sequence voltage and/or current components. This involves a non-zero average active power in each phase cluster of the STATCOM ($\bar{P}_a \neq \bar{P}_b \neq \bar{P}_c \neq 0$).

Three main unbalanced scenarios can be distinguished that the VSC-based STATCOM might have to deal with:

– *Negative-sequence current withstanding.* Sometimes, the STATCOM is only used for dynamic power factor correction or regulation of line voltages (usually in weak grids). In this scenario, the STATCOM must not be disconnected from the power grid. However, the converter can be demanded by the corresponding grid code to withstand a small amount of v^- in the PCC, even in steady-state (e.g., $0.02 - 0.03$ p.u.) [49], [50]. If the VSC-based STATCOM employs a classical controller and does not include negative-sequence current regulators, it is not able to generate v^- in output terminals. As Fig. 3.3 shows, if the VSC only provides v^+, the v^- in the PCC generates i^- circulation through the STATCOM, which should be capable of copping with it [95], [96]. This scenario, which is very common, is discussed in more depth in *section 4.2*.

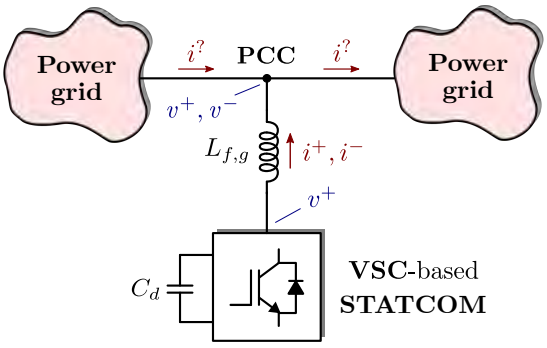

Fig. 3.3. Negative-sequence current withstanding scenario.

– *Unbalanced load compensation.* The STATCOM might be required to compensate also unbalanced loads, such as arc-furnaces, single-phase loads, etc. In this scenario, the load absorbs unbalanced current (i^+, i^-), and the VSC-based STATCOM needs to provide i^- so the grid is only required of i^+. If in addition to this, the STATCOM is also providing other functionalities, such as the positive-sequence power factor ($\cos\phi^+$) fine adjustment, also will provide i^+ (see Fig. 3.4) [54], [97], [98].

– *Low-voltage ride-through (LVRT).* As Fig. 3.5 depicts, when a voltage sag or an unbalanced fault occurs, in the worst case, both v^+ and v^- might appear in the PCC [52], [99]–[101]. Thus, the STATCOM needs to provide positive- and negative-sequence voltage (v^+, v^-) and current (i^+, i^-) in order to compensate the power grid

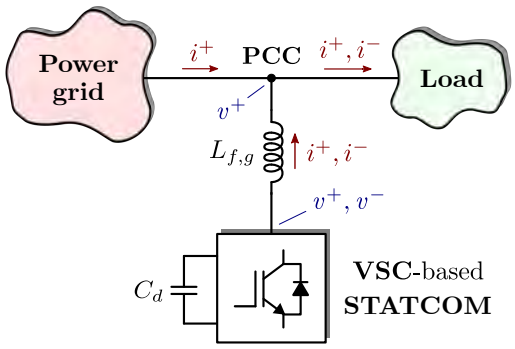

Fig. 3.4. Unbalanced load compensation scenario.

asymmetry. In Germany, for example, the technical requirement imposes i^- injection so as to reduce v^- during a fault [51].

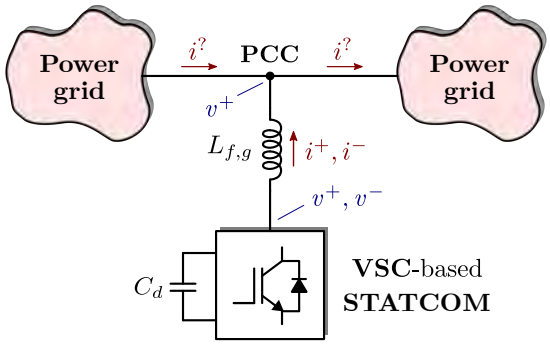

Fig. 3.5. Low-voltage ride-through (LVRT) scenario.

3.3.1.1 *Phase cluster average active power cancellation in the CHB STATCOM*

When CHB configurations with single-phase dc-links are used for the STATCOM and operating under unbalanced voltage ($k_{vpn} > 0$) and/or current ($k_{ipn} > 0$) conditions, the derived average active power term in each power cell and each phase cluster must be cancelled ($\bar{P}_\mathrm{a} = \bar{P}_\mathrm{b} = \bar{P}_\mathrm{c} = 0$). The adopted power balancing strategy needs to guarantee constant dc capacitor voltages. This means that apart from ensuring an equal active power distribution among phase clusters *(intercluster balancing)*, power cells forming each phase cluster need to be balanced from their dc voltage point of view *(intracluster balancing)*.

It should be made clear that this doctoral thesis deals with the *intercluster active power balancing* [96], which aims to redistribute the active power equally among the three phase clusters so as to preserve the dc-link voltages adjusted to the reference value. The *intracluster active power balancing* needs to be addressed in CHBs regardless of whether it is an unbalanced scenario or not [91], [93], [102]; therefore, it is not covered in this dissertation.

The CHB converter topology was introduced by Peng and Lai at the end of the 90's as a promising converter structure for STATCOM application [103], [104]. It was expected to be the best alternative suitable for MV applications, due to its modular structure, a transformerless grid connection, and output filter size reduction. These first designs were based on the YCHB configuration, composed of full-bridge power cells [105]–[107].

The use of the STATCOM for rebalancing issues was well established [108]–[114]. However, most of the papers published previously addressed the unbalanced operation of non-modular converter structures. In 2004, Peng proposed the DCHB converter as the

alternative to the YCHB for STATCOM application under unbalanced conditions [97]. In contrast to the star, the delta configuration allowed to compensate unbalanced loads while compensating also the reactive power (Q). The author proposed an "admittance compensation theorya", an active solution to force the phase cluster average active powers to zero. This technique was based on calculating the converter current magnitude and phase by means of an analogous YCHB converter. References [115], [116] analyzed the possibility of controlling the circulating current flowing inside the DCHB. An intercluster active power balancing solution was addressed for the DCHB STATCOM [97], [115], [116], but not yet for the star structure.

Akagi and coauthors presented a transformerless YCHB STATCOM with PWM [53], handling the dc capacitor voltage unbalance by independently cancelling the average active power of each individual phase cluster. However, this paper does not contemplate any unbalanced situation. Reference [117] presented a control method based on the injection of i^- to operate under unbalanced grid voltage conditions.

Betz and Summers proposed a pioneering intercluster active power balancing control concept based on the injection of fundamental-frequency zero-sequence voltage (YCHB), and zero-sequence current (DCHB) [118]–[120]. The aim was to cancel the terms $\bar{P}_{ph}^{+-}$ and $\bar{P}_{ph}^{-+}$ of (3.7), by means of an additional zero-sequence term ($\bar{P}_{0\text{-}ph}^{\text{YCHB}}$ in case of the YCHB, and $\bar{P}_{0\text{-}ph}^{\text{DCHB}}$ in case of the DCHB):

$$\begin{aligned}\bar{P}_{ph} = &\underbrace{\frac{V^+I^+}{2}\cos\left(\delta_v^+ - \theta_i^+\right)}_{\bar{P}_{ph}^{++}} + \underbrace{\frac{V^-I^-}{2}\cos\left(\delta_v^- - \theta_i^-\right)}_{\bar{P}_{ph}^{--}} \\ &+ \underbrace{\frac{V^+I^-}{2}\cos\left(\delta_v^+ - \theta_i^- + k\frac{4\pi}{3}\right)}_{\bar{P}_{ph}^{+-}} + \underbrace{\frac{V^-I^+}{2}\cos\left(\delta_v^- - \theta_i^+ - k\frac{4\pi}{3}\right)}_{\bar{P}_{ph}^{-+}} \\ &+ \bar{P}_{0\text{-}ph}^{\text{YCHB}} + \bar{P}_{0\text{-}ph}^{\text{DCHB}}\end{aligned} \tag{3.8}$$

When the YCHB operates under unbalanced voltage and/or current conditions, a fundamental-frequency zero-sequence voltage (v_0^{Y}) is added to the converter star point N. The addition of this component does not affect the three-phase voltages and currents at the converter output (see Fig. 3.6), and allows two degrees of freedom; its amplitude (V_0^{Y}), and angle ($\delta_{v_0^{\text{Y}}}$):

$$v_0^{\text{Y}}(t) = V_0^{\text{Y}}\sin(\omega t + \delta_{v_0^{\text{Y}}}) \tag{3.9}$$

The aim is to find an appropriate V_0^{Y} and $\delta_{v_0^{\text{Y}}}$ so as to generate an average common active power ($\bar{P}_{0\text{-}ph}^{\text{YCHB}}$). This term will cancel out the effect of the non-zero average active power at each phase cluster due to the cross-interaction between positive- and negative-sequence components (terms $\bar{P}_{ph}^{+-}$ and $\bar{P}_{ph}^{-+}$), as well as it will compensate for any type of power disturbance caused by non-idealities ($\bar{P}_{dis\text{-}ph}$):

$$\begin{aligned}\bar{P}_{0\text{-}ph}^{\text{YCHB}} = &\frac{V_0^{\text{Y}}I^+}{2}\cos\left(\delta_{v_0^{\text{Y}}} - \theta_i^+ - k\frac{2\pi}{3}\right) \\ &+ \frac{V_0^{\text{Y}}I^-}{2}\cos\left(\delta_{v_0^{\text{Y}}} - \theta_i^- + k\frac{2\pi}{3}\right) = -\bar{P}_{ph}^{+-} - \bar{P}_{ph}^{-+} + \bar{P}_{dis\text{-}ph}\end{aligned} \tag{3.10}$$

It is worth noting that as terms $\bar{P}_{ph}^{++}$ and $\bar{P}_{ph}^{--}$ are common in the three phase clusters, they are controlled through the overall dc-link voltage control, as it will be explained in

subsection 4.2.2. In order to isolate the terms derived by the injection of v_0^{Y}, the following trigonometric indentity is applied to expand the cosine terms in (3.10):

$$\cos(\alpha \pm \beta) = \cos\alpha\cos\beta \mp \sin\alpha\sin\beta \tag{3.11}$$

In this manner, (3.10) can be developed to

$$V_0^{\mathrm{Y}}(K_2^{ph}\cos\delta_{v_0^{\mathrm{Y}}} + K_3^{ph}\sin\delta_{v_0^{\mathrm{Y}}}) = -K_1^{ph} + \bar{P}_{dis\text{-}ph} \tag{3.12}$$

where the following constant terms are defined:

$$\begin{aligned} K_1^{ph} &= V^+I^-\cos\left(\delta_v^+ - \theta_i^- + k\frac{4\pi}{3}\right) + V^-I^+\cos\left(\delta_v^- - \theta_i^+ - k\frac{4\pi}{3}\right) \\ K_2^{ph} &= I^+\cos\left(\theta_i^+ + k\frac{2\pi}{3}\right) + I^-\cos\left(\theta_i^- - k\frac{2\pi}{3}\right) \\ K_3^{ph} &= I^+\sin\left(\theta_i^+ + k\frac{2\pi}{3}\right) + I^-\sin\left(\theta_i^- - k\frac{2\pi}{3}\right) \end{aligned} \tag{3.13}$$

Any two of the three active power equations in (3.12) can be used to determine the explicit expression of the angle $\delta_{v_0^{\mathrm{Y}}}$. Thus, equalizing the expressions of phase clusters "a" and "b":

$$\tan\delta_{v_0^{\mathrm{Y}}} = \frac{(\bar{P}_{dis\text{-b}} - K_1^{\mathrm{b}})K_2^{\mathrm{a}} - (\bar{P}_{dis\text{-a}} - K_1^{\mathrm{a}})K_2^{\mathrm{b}}}{(\bar{P}_{dis\text{-a}} - K_1^{\mathrm{a}})K_3^{\mathrm{b}} - (\bar{P}_{dis\text{-b}} - K_1^{\mathrm{b}})K_3^{\mathrm{a}}} \tag{3.14}$$

Solving (3.14), and substituting the calculated $\delta_{v_0^{\mathrm{Y}}}$ in any of the active power equations in (3.12), the amplitude V_0^{Y} can be derived [95], [121]:

$$V_0^{\mathrm{Y}} = \frac{\bar{P}_{dis\text{-}ph} - K_1^{ph}}{K_2^{ph}\cos\delta_{v_0^{\mathrm{Y}}} + K_3^{ph}\sin\delta_{v_0^{\mathrm{Y}}}} \tag{3.15}$$

Fig. 3.7 shows how the injected zero-sequence voltage component (v_0^{Y}) in the YCHB STATCOM corrects the effect of a current unbalance, making the average active power zero in each of the phase clusters. However, depending on the ratios k_{vpn} and/or k_{ipn}, the injection of v_0^{Y} could lead the converter voltage exceeding its rated level, resulting in the converter achieving its voltage limits or in dc-link voltages drifting away. As a consequence, the YCHB must be over-rated in terms of voltage in order to let a wide voltage margin to guarantee the nominal ac voltage at the PCC; otherwise, the STATCOM should be

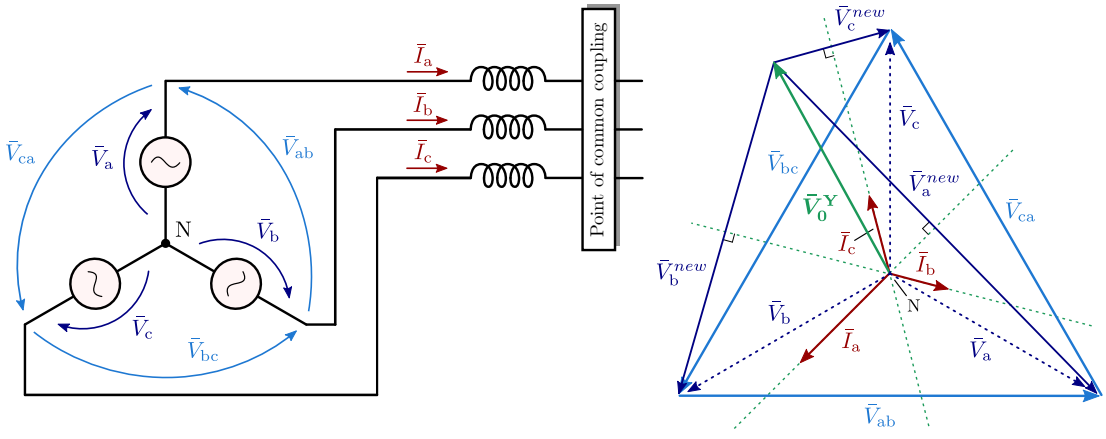

Fig. 3.6. Phasor diagram of the v_0^{Y} injection in the YCHB STATCOM under unbalanced current conditions ($k_{vpn} = 0$, $k_{ipn} > 0$).

disconnected from the power grid. The voltage over-rating can be achieved either serializing more power cells, or increasing the power cell dc-link voltage.

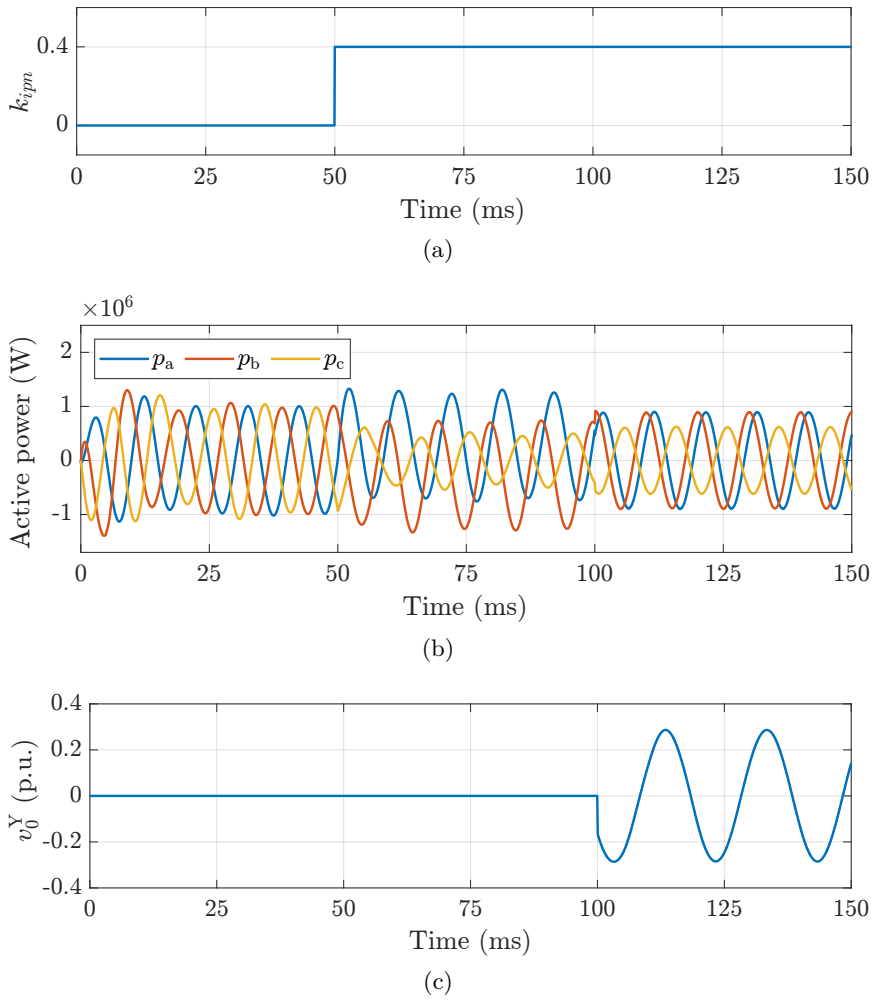

Fig. 3.7. Phase cluster average active power cancellation in the YCHB STATCOM using the v_0^{Y} injection ($k_{vpn} = 0$). The current becomes unbalanced at $t = 50$ ms, and the intercluster active power balancing is activated at $t = 100$ ms. (a) Ratio of current unbalance, (b) phase cluster active power, and (c) injected zero-sequence voltage.

Regarding the DCHB, the intercluster active power balancing can be addressed by injecting a fundamental-frequency zero-sequence current (i_0) inside the delta (see Fig. 3.8). Analogous to the v_0^{Y} injection in the star, the injected i_0 circulates only inside the delta, without affecting three-phase voltages and currents at the converter ac side. It also allows two degrees of freedom in terms of its amplitude (I_0), and angle (θ_{i_0}):

$$i_0(t) = I_0 \sin(\omega t + \theta_{i_0}) \tag{3.16}$$

The required i_0 will generate an average active power term ($\bar{P}_{0\text{-}ph}^{\mathrm{DCHB}}$) which will guarantee that the active power is equally distributed among delta-connected clusters, while it preserves the dc-link voltages in each phase cluster adjusted to the reference value:

$$\begin{aligned} \bar{P}_{0\text{-}ph}^{\mathrm{DCHB}} &= \frac{V^+ I_0}{2} \cos\left(\delta_v^+ - \theta_{i_0} + k\frac{2\pi}{3}\right) \\ &+ \frac{V^- I_0}{2} \cos\left(\delta_v^- - \theta_{i_0} - k\frac{2\pi}{3}\right) = -\bar{P}_{ph}^{+-} - \bar{P}_{ph}^{-+} + \bar{P}_{dis\text{-}ph} \end{aligned} \tag{3.17}$$

where $k = 0, -1, 1$ for $ph = \text{ab}, \text{bc}, \text{ca}$ (delta case). Following the same procedure adopted for the YCHB, θ_{i_0} and I_0 are calculated as [95], [121]

$$\tan\theta_{i_0} = \frac{(\bar{P}_{dis\text{-bc}} - K_1^{\text{bc}})K_2^{\text{ab}} - (\bar{P}_{dis\text{-ab}} - K_1^{\text{ab}})K_2^{\text{bc}}}{(\bar{P}_{dis\text{-ab}} - K_1^{\text{ab}})K_3^{\text{bc}} - (\bar{P}_{dis\text{-bc}} - K_1^{\text{bc}})K_3^{\text{ab}}} \tag{3.18}$$

$$I_0 = \frac{\bar{P}_{dis\text{-}ph} - K_1^{ph}}{K_2^{ph}\cos\theta_{i_0} + K_3^{ph}\sin\theta_{i_0}} \tag{3.19}$$

defining the following constant terms:

$$\begin{aligned} K_1^{ph} &= V^+ I^- \cos\left(\delta_v^+ - \theta_i^- + k\frac{4\pi}{3}\right) + V^- I^+ \cos\left(\delta_v^- - \theta_i^+ - k\frac{4\pi}{3}\right) \\ K_2^{ph} &= V^+ \cos\left(\delta_v^+ + k\frac{2\pi}{3}\right) + V^- \cos\left(\delta_v^- - k\frac{2\pi}{3}\right) \\ K_3^{ph} &= V^+ \sin\left(\delta_v^+ + k\frac{2\pi}{3}\right) + V^- \sin\left(\delta_v^- - k\frac{2\pi}{3}\right) \end{aligned} \tag{3.20}$$

Analogously to the YCHB, the injected i_0 will involve a current de-rating in the DCHB, which will limit the available power that the STATCOM could deliver.

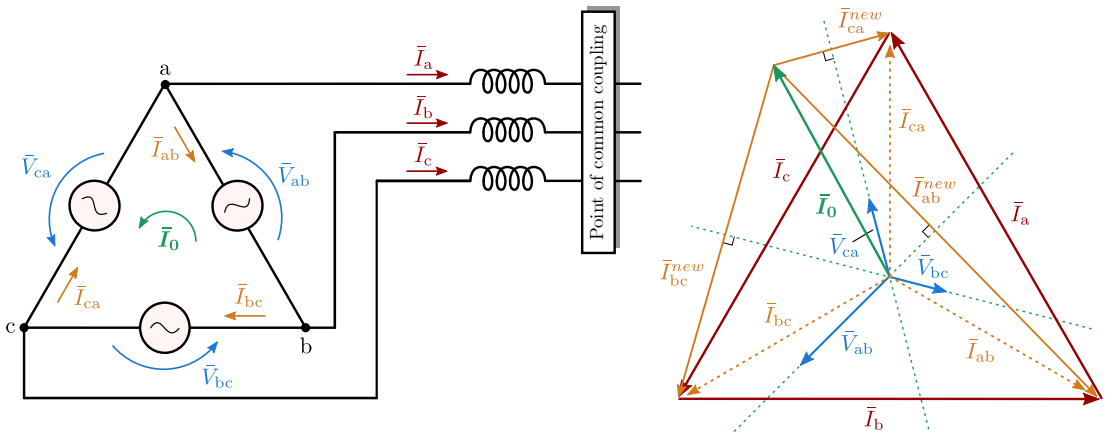

Fig. 3.8. Phasor diagram of the i_0 injection in the DCHB STATCOM under unbalanced voltage conditions ($k_{ipn} = 0$, $k_{vpn} > 0$).

In the first approach, Betz and Summers developed the zero-sequence injection expressions and discussed the technique under unbalanced current conditions, assuming terminal voltages of the STATCOM to be balanced [118] ($k_{vpn} = 0,\ k_{ipn} > 0$). Later, they studied the same solution when the output voltages were unbalanced [119] ($k_{vpn} > 0,\ k_{ipn} > 0$). These papers concluded that a duality exists between the YCHB voltage rating and DCHB current rating under unbalanced operation [118], [119]. The method was integrated in a novel control strategy in [120].

The previously proposed i^- injection method for the YCHB STATCOM [117] was compared with the fundamental-frequency v_0^{Y} injection, considering the latter as the best technique for LVRT (see Fig. 3.5) [122]. Both methods can be combined together depending on the unbalanced voltage sag depth [122]–[124]. However, the negative-sequence currents for voltage balance purpose will be injected into the power grid inevitably, which is not preferred from the power quality point of view [125]. Accordingly, the scientific literature shows that the fundamental-frequency v_0^{Y} injection is the most widespread technique to address any unbalanced operating point with the YCHB STATCOM [54], [125]–[135].

Several authors have studied the technique of injecting a circulating fundamental-frequency i_0 for the unbalanced operation of the DCHB STATCOM. In [97], a control

method is presented for intercluster active power balancing, but no feedback loop is formed to control the circulating current among the delta-connected clusters. References [136]–[141] present a control strategy for the DCHB STATCOM considering both unbalanced operation and circulating zero-sequence current control.

3.3.1.2 *Comparison of YCHB and DCHB STATCOMs*

CHB structures are interesting for STATCOM applications under unbalanced operation. This has led many authors to individually analyze and compare the limitations and the operating ranges of the YCHB and DCHB.

Behrouzian *et al.* [95], [142] investigated the capabilities of the YCHB and DCHB STATCOMs under unbalanced current ($k_{vpn} = 0$, $k_{ipn} > 0$) and voltage conditions ($k_{ipn} = 0$, $k_{vpn} > 0$), respectively. For that purpose, analytical expressions of the injected fundamental-frequency zero-sequence voltage (in case of YCHB) and current (in case of DCHB) were developed. The authors concluded that the utilization of these STATCOM configurations for negative-sequence injection presents some limitations. That is, due to a singularity that exists in the solution for the calculation of the zero-sequence components, there are special operating points for both YCHB and DCHB STATCOMs, where v_0^{Y} and i_0 are unable to set the average active power in each phase cluster to zero. These operating points are $k_{ipn} = 1$ for the star, and $k_{vpn} = 1$ for the delta. These two singular points demand infinite V_0^{Y} for the YCHB, and infinite I_0 for the DCHB in order to reach the dc-link capacitor voltage balancing. The authors identified that the phase shift between current components ($\theta_{ipn} = \theta_i^- - \theta_i^+$) in the YCHB, and the phase shift between voltage components ($\delta_{vpn} = \delta_v^- - \delta_v^+$) in the DCHB have also an impact in the zero-sequence components to be injected. The results presented confirm the mentioned duality between the two configurations; the impact of k_{ipn} in the YCHB (when $k_{vpn} = 0$) is equivalent to the impact of k_{vpn} in the DCHB (when $k_{ipn} = 0$). Other authors led to similar conclusions [143], [144].

Even the duality between both configurations is interesting, comparing the YCHB and the DCHB STATCOMs in the same operating scenario is a fair approach. References [96], [121], [144] compared the two CHB-based circuit configurations under balanced voltage and unbalanced current conditions ($k_{vpn} = 0$, $k_{ipn} > 0$), which is a negative-sequence current withstanding scenario (see Fig. 3.3). In this application, the duality between the two configurations exposed previously is lost: the DCHB requires less I_0 than the V_0^{Y} demanded by an equivalent YCHB STATCOM for a certain ratio of current unbalance (k_{ipn}). This conclusion has motivated several authors to investigate the delta configuration for unbalanced load compensation [98], [145]. Some researchers also analyzed the DCHB STATCOM for LVRT purposes [99], [100], [146].

3.3.1.3 *MMC STATCOM under unbalanced operating conditions*

Apart from CHB configurations, the MMC is also considered an interesting alternative to operate in unbalanced scenarios as STATCOM [40]. Although the MMC needs twice as many power cells than CHB configurations to reach the same output voltage, it presents more degrees of freedom in its circulating current control strategy [92].

As with CHB structures, this dissertation deals with the intercluster active power unbalance. Since both the intracluster active power unbalance [147] and the active power unbalance between the upper and lower arms of the MMC need to be addressed regardless of whether it is an unbalanced scenario or not [148], they are not analyzed.

The average active power terms $\bar{P}_{ph}^{+-}$ and $\bar{P}_{ph}^{-+}$ are cancelled out also when added together in the three phase clusters of the MMC; that is, there is no net energy exchange between the ac and dc sides. Therefore, the physical energy source connected to the

common three-phase dc-link is also not needed in the MMC STATCOM to operate under v^- and/or i^-. However, as CHBs, the phase cluster active power still differs from zero due to the cross-interaction between positive- and negative-sequence components (terms $\bar{P}_{ph}^{+-}$ and $\bar{P}_{ph}^{-+}$). Due to the potential difference between the two sets of star-connected converters (V_{dc}), a dc current circulates across each phase cluster of the MMC ($i_{z\text{-}ph}$), which redistributes the active power among the phase clusters, and hence the charge of dc-link capacitors remains adjusted to the reference value in each phase cluster:

$$\bar{P}_{ph}^{+-} + \bar{P}_{ph}^{-+} = V_{dc} \cdot i_{z\text{-}ph} \tag{3.21}$$

The sum of these circulating dc currents in the three phase clusters naturally sums up to zero in STATCOM application ($i_{dc} = i_{z\text{-a}} + i_{z\text{-b}} + i_{z\text{-c}} = 0$) (see Fig. 2.14). This current ($i_{z\text{-}ph}$) is not injected like the zero-sequence voltage or current in CHBs, but appears because it has a path to recirculate. Under balanced conditions $i_{z\text{-}ph}$ is zero, so the power cells are sized only considering the output ac current. But the appearance of this circulating dc current might imply an output power de-rating.

Hagiwara and Akagi proposed a control method for the MMC STATCOM under unbalanced conditions [149]–[151], both theoretically and experimentally. In this approach, the circulating current control of the MMC introduces a internal dc voltage in each phase cluster ($v_{z\text{-}ph}$), which controlls the circulating dc current ($i_{z\text{-}ph}$) [152]–[161].

Some technical papers can be found which compare CHB and MMC configurations for STATCOM application under unbalanced conditions. In [152], the authors analyze the capability of the YCHB, DCHB and MMC for compensating unbalanced loads or LVRT operation (see Fig. 3.5). The paper concludes that the MMC is the preferable option in the above mentioned scenarios. References [156], [161] compare the negative-sequence compensation capability between the MMC and the DCHB configuration in LVRT application. The authors concluded that the compensation capability of the MMC is higher than the DCHB, considering that both are rated for the same output power (double total energy storage for the MMC). Finally, [52] compares the performances of the YCHB, DCHB and MMC for STATCOM in large-scale offshore WPPs, with special focus on LVRT capability under asymmetrical grid faults. This publication concludes that the full-bridge MMC is the most attractive structure for that purpose (with similar total cost and volume). Table 3.2 presents a classification of the most relevant references analyzed in *subsection 3.3.1* for STATCOM application.

3.3.2 Large-Scale PV Power Plants under Unbalanced Power Generation

As mentioned in *subsection 3.2.2*, the CHB converter is one of the most attractive structures for large-scale PV integration [162]. The MMC is not commonly used in this type of applications. Fig. 3.9 illustrates the scheme of a single-phase CHB power cell connected to a PV string by a dc-dc converter. The dc-dc stage allows independent MPPT in order to maximize the power extraction from the PV string. CHB power cells can be cascaded, and then the three phase clusters can be connected either in star (Fig. 2.12 (a)), or in delta (Fig. 2.12 (b)).

During balanced operation, the PV power delivered to each CHB power cell is equal; thus, the active power in each of the three phase clusters of the converter is equal to the other two ($\bar{P}_{\text{a}} = \bar{P}_{\text{b}} = \bar{P}_{\text{c}}$). In this scenario, the three-phase currents injected to the PCC will be balanced ($k_{ipn} = 0$). The converter is controlled to generate balanced phase cluster voltages ($k_{vpn} = 0$). As the aim of a PV power plant is to maximize the active power extraction, it operates with a power factor as close to the unity as possible ($\cos\phi \approx 1$).

Table 3.2. Classification of multilevel VSCs based on modular structures for STATCOM application and typical unbalanced operating scenarios. The crosses (×) indicate which converter structure and scenario are discussed in each reference.*

Reference	VSC structure			Operating scenario		
	YCHB	DCHB	MMC	I^- withstanding	Unbalanced load compensation	LVRT
[54], [125], [126], [128]	×				×	
[117], [122]–[124], [127], [130]–[135]	×					×
[136], [140]		×		×		
[97], [98], [137]–[139], [145]		×			×	
[99], [100], [146]		×				×
[95], [96], [118], [120], [121], [142], [144]	×	×		×		
[143]	×	×		×	×	
[119]	×	×				×
[153]–[155], [157]–[160]			×			×
[152]	×	×	×		×	
[156], [161]		×	×			×
[52]	×	×	×			×

Authors of the papers may not necessarily use this terminology.

However, the PV power generation levels in each power cell are unlikely to be equal, especially in a large geographically-dispersed power plant. Hence, the PV power delivered to each phase cluster of the CHB converter can become unequal ($\bar{P}_a \neq \bar{P}_b \neq \bar{P}_c$). This uneven power generation in large-scale PV power plants involves an unbalanced current injection into the PCC ($k_{ipn} > 0$) [87]. Specific control strategies are thus needed so as to supply balanced three-phase currents to the power grid [37], [94]. This problem is analogous to the one recognized in the unbalanced operation of the STATCOM application, as seen in *subsection 3.3.1.*

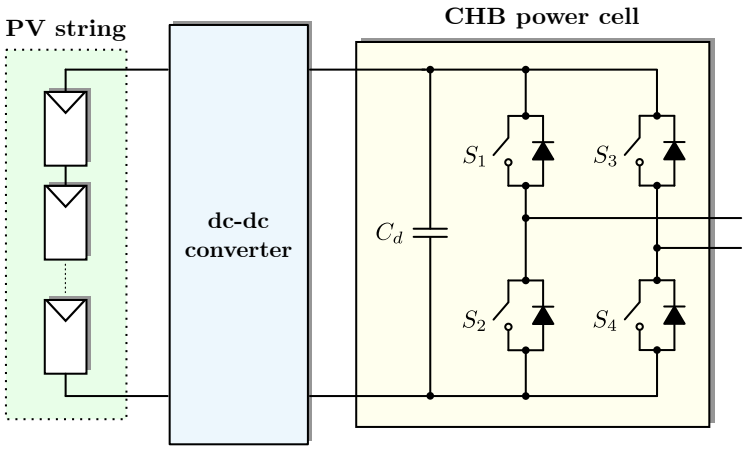

Fig. 3.9. Scheme of a single-phase cascaded power cell connected to a PV string by a dc-dc converter.

3.3.2.1 *Intercluster active power balancing in large-scale PV power plants*

The objective of the power balancing in large-scale PV power plants consists of delivering three-phase balanced currents to the power grid ($k_{ipn} = 0$), even with unbalanced PV power generation in each power cell. The required control is applied at two levels: 1) intercluster active power balancing, which is used when each phase cluster delivers a different amount of power; and 2) individual or intracluster active power balancing, which is applied when each power cell in the same phase cluster delivers a different amount of power [93]. This review covers the first one.

References [41], [42], [163] presented an intracluster power balancing technique of a CHB power cell-based single-phase converter for PV integration. These first approaches did not face the intercluster balancing. In 2012, Townsend [164] proposed the utilization of the technique introduced by Betz and Summers for dc capacitor voltage balancing in a STATCOM [118]–[120] for PV applications: the *Fundamental-Frequency Zero-Sequence Injection*. This technique was called FFZSI by [165] for PV integration, and it is the same technique analyzed in *subsection 3.3.1.1*.

The injected fundamental-frequency zero-sequence voltage in the YCHB, expressed in (3.9), is able to rebalance the three-phase grid currents [37], even with an unbalanced three-phase PV power generation [164]–[168]. However, the FFZSI involves the increasing of the resultant converter output voltage, which can easily exceed the limit set by the dc side as the power unbalance increases. Once the voltage limit is reached, the converter saturates, and three-phase balanced grid currents cannot be guaranteed. The available dc voltage can be increased by means of voltage over-rating, which should not be the preferable option. Reference [169] proposes a converter topology that can avoid the zero-sequence injection by adjusting the active power that parallel connected dc-dc converters feed into each phase cluster. Henceforth, the references that followed this one tried to achieve both the maximum output ac voltage, and the intercluster active power balancing.

The *Weighted Min-Max* (WMM) zero-sequence voltage injection was proposed for the YCHB in [87], and implemented in [170]. The zero-sequence voltage is generated by using simple comparisons of weighted positive-sequence voltage references [171]. Nevertheless, in references [166], [172] it is stated that the WMM zero-sequence injection is not able to provide sufficiently accurate results since it synthesizes an incorrect fundamental-frequency zero-sequence component. Due to this fact, the system dynamic performance is reduced.

An effective method to improve the dc voltage utilization in a three-phase VSC is the *Third-Harmonic Injection* (THI). As analyzed in *subsection 2.2.1*, Holmes and Lipo [63] deduced that a THI of 1/6 of the fundamental-frequency component achieves the highest ac output voltage without overmodulation (when $k_{vpn} = 0$). Based on this, Yu *et al.* [173] proposed to combine the optimal injection of the positive-sequence voltage with the optimal one of the zero-sequence:

$$v_0^{\mathrm{DTHI}}(t) = \underbrace{V_0 \sin(\omega t + \delta_{v_0})}_{v_0} + \underbrace{\frac{V_0}{6} \sin(3\omega t + 3\delta_{v_0})}_{v_{0_3}} + \underbrace{\frac{V^+}{6} \sin(3\omega t + 3\delta_v^+)}_{v_3^+} \tag{3.22}$$

The method is called *Double Third-Harmonic Injection* (DTHI). As (3.22) shows, in addition to the fundamental-frequency zero-sequence component (v_0) of (3.9), its third-harmonic component (v_{0_3}) and the third-harmonic component of the phase cluster positive-sequence voltage (v_3^+) are also injected. These two third-harmonic terms reduce the peak value of the resultant phase voltages without affecting the injected fundamental-frequency zero-sequence. In this manner, the power balancing capabilities are improved in comparison to the FFZSI [93], [166], [173]. The DTHI was also applied to extend the operating ranges of CHB STATCOMs under unbalanced current conditions [96].

The DTHI is derived considering that the overall optimal THI is equal to the sum of the optimal THI of its positive-sequence and its fundamental-frequency components ($v_{ph_3} \neq v_{0_3} + v_3^+$). However, this superposition principle does not apply in this situation. From this conclusion, an improvement of the DTHI was proposed: the *Reduced Third-Harmonic Injection* (RTHI) [93]. With this injection, the third-harmonic terms (v_{0_3} and v_3^+) are injected to the most vulnerable phase cluster so as to reduce its maximum voltage. If this injection increases the voltage of another phase cluster, the injection level is reduced from 1/6; this is why it is called RTHI.

Very similar to WMM zero-sequence injection, the *Double Min-Max* (DMM) zero-sequence injection was proposed [93], [166] as another improvement of the DTHI. This method consists of injecting the derived min-max sequence of the positive-sequence as well as that of the required fundamental-frequency zero-sequence. Since the superposition principle can be applied by this injection, the separation of both min-max sequences is allowed [93].

Reference [171] proposed the *Square-Wave Zero-Sequence Injection* (SWZI) [63] for PV power balancing: an injection of a fundamental zero-sequence square wave $4/\pi$ times larger than its peak value. A combination of third-harmonic and square-wave was also proposed under the name *Third-Harmonic Square-Wave Injection* (THSWI) to further reduce the phase cluster peak reference voltage [171].

As [172] states, all the zero-sequence injection methods proposed by Yu *et al.* lacked of satisfying both conditions for the injection technique to be optimal: 1) its fundamental-frequency component should be equal to that of FFZSI; and 2) its harmonic component should make the converter output voltage peak as low as possible to avoid saturation. Thus, they proposed the method that would satisfy both conditions; the *Optimal Zero-Sequence Injection* (OZSI) [165], [166], [172]. This method extends the power balancing capabilities of the converter by making full use of the available voltage [172].

Comparative studies of the power balancing capabilities of zero-sequence injection methods proposed for large-scale PV integration by CHB structures are also a novel approach [93], [166], [171]. Table 3.3 classifies the zero-sequence injection methods analyzed.

Table 3.3. Classification of CHB configurations and zero-sequence injection methods for large-scale PV integration.

	VSC structure		**Zero-sequence injection method**							
Reference	YCHB	DCHB	FFZSI	SWZSI	WMM	DTHI	THSWI	RTHI	DMM	OSZI
[164], [167], [168]	×		×							
[174]–[176]	×	×	×							
[87], [170]	×				×					
[173]	×		×			×				
[93]	×					×		×	×	
[165], [172]	×									×
[166]	×		×		×	×			×	×
[171]	×	×	×	×	×	×	×			×

3.3.2.2 *Comparison of YCHB and DCHB for PV integration*

In order to address the phase cluster PV power balancing in a CHB converter, a zero-sequence voltage (YCHB) or a zero-sequence current (DCHB) must be added. Both of them are expected to increase as the power unbalance among phase clusters becomes more severe. This fact involves a converter over-rating in terms of voltage for the star case, and in terms of current for the delta one [174]. As in the field of STATCOM application, this has motivated some authors to individually analyze and compare the power balancing capabilities of the YCHB and DCHB.

Most of the references focused on the FFZSI of the YCHB. The main drawback of this method is that the power balancing capability is limited by the available dc voltage in each phase cluster. Due to this fact, as seen in *subsection 3.3.2.1*, some studies have extended slightly the operating range of the YCHB by means of injecting a wide variety of non-sinusoidal zero-sequence voltage components (see Table 3.3).

The DCHB configuration started to draw attention as a promising alternative for PV integration [171], [174]–[176]. As these references identify, the limiting factor in the delta case is the maximum phase cluster current that flows through each cascaded power cell. The p.u. zero-sequence current asked to the DCHB is smaller than the p.u. zero-sequence voltage asked to the YCHB for the same power unbalance scenario. This fact makes the DCHB superior to the YCHB. In the worst case-scenario (when zero power is delivered to one phase cluster while the other two generate the rated power), the DCHB converter needs around 15% of current over-rating so as to supply balanced currents. A bit of extra current rating on the phase cluster allows the DCHB to tolerate any level of power unbalance among phase clusters.

3.3.3 Unequal Active Power Distribution in BESS

Multilevel VSCs based on modular structures are a promising family for BESS [40], [46], [84], [177]–[182]. These structures are modular, and thus scalable to MV levels, necessary for the high power rating demanded by grid applications. Modular structures allow the distribution of energy storage units among the converter power cells. Fig. 3.10 shows the scheme of a single-phase power cell connected to a battery unit by a dc-dc converter.

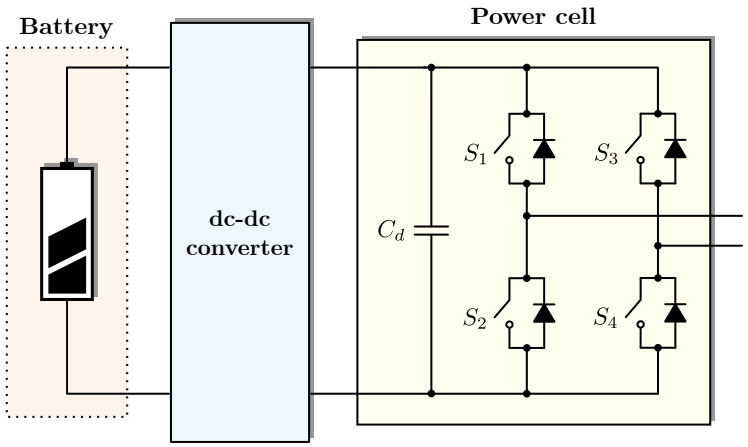

Fig. 3.10. Scheme of a single-phase cascaded power cell connected to a battery by a dc-dc converter.

Very similar to large-scale PV power plants, during balanced operation, all battery units absorb/deliver an equal active power. Thus, the active power is distributed equally among the three phase clusters ($\bar{P}_\mathrm{a} = \bar{P}_\mathrm{b} = \bar{P}_\mathrm{c}$). This means that the three-phase current absorbed/delivered from/to the PCC will be balanced ($k_{ipn} = 0$).

In the practical use of a BESS, an uneven active power distribution among multiple battery units and phase clusters is more usual ($\bar{P}_\mathrm{a} \neq \bar{P}_\mathrm{b} \neq \bar{P}_\mathrm{c}$), as a result of manufacturing tolerances, uneven temperature conditions or differences in ageing [183]. The intercluster active power balancing allows each of the three clusters to absorb or deliver an unequal active power without exchanging negative-sequence currents with the PCC [44]. This time the zero-sequence voltage or current has to be calculated in order to achieve the desired active power distribution among the phase clusters. This issue is also analogous to the unbalanced operation identified for STATCOM (see *subsection 3.3.1*) and large-scale PV power (see *subsection 3.3.2*) applications.

Maharjan and Akagi proposed the utilization of the YCHB converter for BESS [44], [183]–[185]. As these references state, the star configuration is preferable to the delta in this applications, so as to minimize the number of power cells connected in cascade. For phase cluster active power balancing, these papers applied the technique introduced

by Betz and Summers for dc capacitor voltage balancing in the unbalanced operation of the STATCOM [118]–[120]. The authors add a fundamental-frequency zero-sequence voltage expressed in (3.9), in such a way as to absorb/deliver three-phase balanced current in spite of operating all the power cells at different power levels. Two philosophies are distinguished: 1) phase cluster voltage balancing control [183]–[185], which has the function of balancing the three mean dc voltages of the three phase clusters; and 2) phase cluster state-of-charge (SOC) balancing [44], which has the function of balancing the three mean SOC values of the three phase clusters. The latter provides more effective utilization of battery energy. But still, both methods allow unequal power distribution among the three phase clusters, without causing any change in the line-to-line voltages; thus, balanced currents are absorbed/delivered. Reference [186] describes a SOC balancing-based real-scale YCHB BESS.

The dc circulating current between the phase clusters and the three-phase dc-link of the MCC is able to exchange active power among phase clusters. This current can be used to compensate the unequal power distribution in a MMC BESS. Hence, without affecting the converter output, the phase cluster SOC balancing can also be reached [187], [188]. That is, a dc portion of the circulating current can guarantee that all phase clusters present the same average SOC. Some references can be found which also face asymmetrical grid faults by the MMC BESS [189], [190]. Reference [191] proposed to integrate a RES with a BESS by a MMC. In this application, the circulating dc current facilitates the active power transfer between phase clusters and the three-phase dc-link, being able to cope with the fluctuating power generated by RES.

3.4 CONCLUSIONS

Multilevel VSCs based on modular structures are positioned as essential components of the future power grid. Due to their modular and scalable features, enable high output ac voltage with low dc voltage inputs. As seen, unbalanced condition is a mandatory scenario in which these structures must operate in different applications such as STATCOM, large-scale PV power plants, or BESS.

This chapter has performed a comprehensive review of the problems that the unbalanced operation in different applications suppose for multilevel VSCs based on modular structures, classifying the proposed intercluster active power balancing strategies. As main conclusion, an equivalency between the three analyzed applications can be arisen. In the same way, an equivalency between the intercluster active power balancing applied to the YCHB, DCHB, and MMC can be found. This chapter provides a proposal for researchers to develop further studies.

Although several works focus on the operation of multilevel VSCs based on modular structures under unbalanced conditions, there still are some future challenges that have not been covered in depth:

– Either grid-connected or industry applications, STATCOMs are being asked for new operating scenarios which demand negative-sequence operation and/or injection capability. Different converter structures have been proposed for that purpose, analyzing them mostly independently. As far as the author knows, there is no source that clearly evaluates and fairly compares the capabilities of the multilevel VSCs based on modular structures discussed for STATCOM application operating under v^- and/or i^-. Besides, it has been observed that the mathematical expressions of the required v_0^{Y} in the YCHB and i_0 in the DCHB are treated and explained differently among several references. Also, the unbalanced operating scenarios identified in some references do not correspond each other in the nomenclature. The injection of novel zero-sequence

components proposed for PV integration in order to increase the STATCOM power rating can be considered another open point.

– Regarding large-scale PV integration, only CHB configurations have been analyzed in the specialized literature. The possible extension to the MMC structure has not been analyzed in depth, which might be a promising research topic. Moreover, new grid codes may demand unbalanced voltage and/or currents in the PCC, in order to support an asymmetrical grid fault or LVRT. The analysis of unbalanced PV power generation during unbalanced PCC conditions is a key research topic for the future power grid. Also, the hybridization of PV and BESS for that purpose.

– The utilization of multilevel VSCs based on modular structures for BESS has not been so widely covered as STATCOM or PV applications. While large-scale PV integration aims to maximize the active power extraction, BESS need to supply/absorb active power depending on the application demands. It is remarkable that the DCHB configuration, which is a competitive solution for other unbalanced scenarios, has not been examined in BESS applications. Besides, even some references about the MMC have been found, the utilization of this structure has not been completely justified in the specialized literature.

Focusing on the unbalanced operation of the STATCOM, which is the main topic of this doctoral thesis, many papers have compared the intercluster balancing capabilities of both CHB configurations by means of quantifying the required v_0^{Y} injection in the YCHB, and i_0 in the DCHB. The presence of v^- and/or i^-, as well as the required v_0^{Y} or i_0, will reduce the available positive-sequence reactive power (Q^+) that the CHB-based STATCOM could deliver to the power grid. As far as the author knows, the Q^+ limits applied to each configuration as a result of the intercluster active power balancing have not been quantified nor fairly compared. And that is, from the STATCOM manufacturer point of view, the indicative parameter to compare and select the most suitable converter structure.

Likewise, the circulating dc current in the MMC due the cross-interaction between positive- and negative-sequence components will also limit the output ac current, and hence the available Q^+ that the STATCOM could provide; a quantification that has not yet been reported either. Apart from modular structures, there is also no reference which evaluates the operation of three-phase dc-link VSC structures such as the 3L NPC for STATCOM application operating with v^- and/or i^-. This would allow to compare the 3L NPC with CHBs and the MMC for this particular application, with the aim of selecting the most appropriate PEBB interconnection configuration.

Taking all these conclusions into consideration, the following chapter analyzes the operation of the YCHB, DCHB, MMC, and 3L NPC structures for STATCOM application operating under unbalanced voltage and/or current conditions. The limitations that these VSC structures present in the application under study are further studied, with the aim of quantifying the Q^+ limits and thus be able to compare them fairly with each other.

Chapter 4

REACTIVE POWER LIMITS OF VSC STATCOM-S UNDER UNBALANCED OPERATION

Unbalanced voltage and/or current operation is an increasingly frequent requirement that the VSC-based STATCOM must face. This chapter studies the operation of YCHB, DCHB, MMC, and 3L NPC structures under these conditions, quantifies the positive-sequence reactive power limits of each one, and compares them with each other. Firstly, the YCHB and the DCHB are compared in a negative-sequence current withstanding scenario, and the theoretical study is experimentally validated. Then, the MMC and the 3L NPC are added to the analysis, including also the negative-sequence voltage in the comparison of the power limits. The studies performed in this chapter resulted in publications [J2] and [C2].

4.1 INTRODUCTION

As it has been concluded from the literature review provided in *Chapter 3*, the evaluation of the limitations that different multilevel VSC structures present for the application under study would allow comparing them with each other, in order to be able to select and design the most suitable solution. This would be a novel approach for the STATCOM manufacturer. For this reason, this chapter analyzes and compares the positive-sequence reactive power (Q^+) limits of YCHB, DCHB, MMC, and 3L NPC topologies for STATCOM application operating with negative-sequence voltage and/or current. The chapter is divided into two main parts, starting with a very specific scenario with two configurations, and extending the study to a generic case with more multilevel VSC structures:

- *Section 4.2* analyzes and compares the Q^+ limits of YCHB and DCHB STATCOMs to withstand negative-sequence current (i^-). As seen in *subsection 3.3.1.1*, zero-sequence voltage for the YCHB (v_0^{Y}) and zero-sequence current (i_0) for the DCHB are injected in order to correct the intercluster uneven average active power distribution, and thus to preserve the dc-link voltage balancing. However, both solutions will have an impact on the power rating of the converter. So, by means of a systematic procedure proposed, the Q^+ of each CHB STATCOM configuration is quantified depending on the current unbalance at converter terminals. Experimental results obtained from a real-scale set-up in a MV laboratory validate this theoretical analysis. The analysis carried out in *section 4.2* resulted in publication [J2].

- *Section 4.3* extends the analysis by including also the MMC and the 3L NPC to the study, as well as by adding also the negative-sequence voltage (v^-) in converter terminals. As v^- and/or i^- in the ac side have an influence on the dc side of the converter, especially in STATCOM application, VSC structures are classified according to whether they have a single- or three-phase configured dc-link. In this manner, the effect of both the average active power ($\bar{P}$) and the 2ω oscillating active power ($\tilde{p}$) terms as a result of negative-sequences is evaluated in both groups of VSCs, and Q^+ limits are quantified. The study provided in *section 4.3* resulted in publication [C2].

4.2 YCHB AND DCHB UNDER NEGATIVE-SEQUENCE CURRENT WITHSTANDING

As analyzed in *Chapter 3*, due to their attractive features such as the scalability and the possibility of direct grid connection, multilevel VSCs based on modular structures are today the industrial standard for high power – MV applications. Foremost among these is the CHB topology, which its employment in STATCOM applications has been receiving growing attention, in both star (YCHB) and delta (DCHB) configurations (see Fig. 2.12).

Nowadays, the STATCOM is used for reactive power support in different grid applications. In most cases, the aim of the STATCOM is to provide Q^+, by means of generating positive-sequence voltage (v^+) and current (i^+). However, a negative-sequence voltage (v^-) will appear in the PCC under unbalanced conditions. For instance, as seen, grid codes permit a small amount of v^- even in steady-state [49], [50]. However, in many cases, the STATCOM must operate connected to loads with much severe unbalanced conditions in metal processing (e.g., arc-furnace loads), mining, or railway traction applications. One alternative to cope with this unbalance could be to generate v^- at the VSC output so the negative-sequence current (i^-) is zero in steady-state, but this increases the digital control burden. Thus, a common choice is to use a classical controller and withstand the generated i^-. This specific scenario, also discussed in *subsection 3.3.1*, is referred to as

negative-sequence current withstanding. If the VSC only provides v^+ and the grid gets unbalanced, i^- will circulate through the device, which should be capable of copping with it in order to remain connected [55].

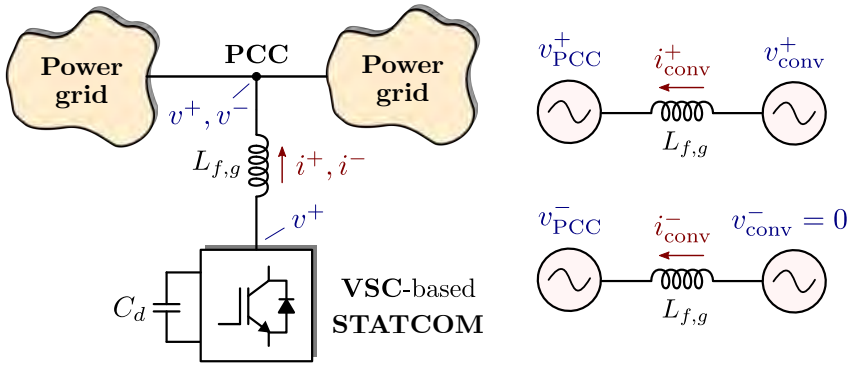

Fig. 4.1. Negative-sequence current withstanding scenario of a VSC-based STATCOM. Both positive- and negative-sequence simplified electric diagrams are also shown.

As Fig. 4.1 shows, if the VSC-based STATCOM is not designed to control v^- (since it is required only to provide Q^+), and the PCC gets unbalanced, i^- is generated and circulates through the converter [55]. Even if the amount of v^- in the PCC is not large ($0.02-0.03$ p.u. as [49], [50] state), the amplitude of i^- could be significant ($0.2-0.3$ p.u.), considering typical MV connection filter ($L_{f,g}$) impendance values ($0.1-0.2$ p.u.). Furthermore, in the applications in which it is required to provide only reactive power, the STATCOM is normally on standby situation and no providing any Q^+ ($i^+=0$). In this scenario, the appearance of any minimum v^- in the PCC will induce a i^- and the converter will start its operation with $k_{ipn}=2$. That is why this analysis is extended also to operating points where i^- exceeds i^+ ($k_{ipn}>1$), which is not found in the specialized literature.

In this scenario, as explained in *subsection 3.3.1.1*, although there is no net energy exchange between the STATCOM and the application, an active power different from zero might appear in each phase of the converter. The CHB presents a major drawback under unbalanced conditions: the incapacity to exchange active power among phase clusters due to the lack of a common three-phase dc-link. Consequently, dc-link voltages may drift away from their reference values (see Fig. 3.2). The adopted power balancing strategy needs to guarantee constant dc-link capacitor voltages. First of all, an equal active power distribution among phase clusters needs to be ensured *(intercluster active power balancing)* [118]. Secondly, dc voltages of the power cells forming each phase cluster need to be balanced *(intracluster active power balancing)* [53], [91], [102]. This work deals with the first one, since the intracluster balancing needs to be addressed in CHBs regardless of whether it is i^- or not.

The intercluster active power balancing in the YCHB can be addressed by adding a fundamental-frequency zero-sequence voltage (v_0^{Y}) [54], [125], [135]. That is why the operating range of the star during unbalanced conditions is limited by the available dc-side voltage. Regarding the DCHB, a fundamental-frequency zero-sequence current (i_0) can be injected inside the delta to correct the uneven active power distribution among phase clusters [136], [140], [145], [146].

Several references have compared the intercluster balancing capabilities of both CHB STATCOM configurations by means of quantifying the required v_0^{Y} in the YCHB, and i_0 in the DCHB [95], [96], [121], [143], [171]. Both the presence of i^-, and the injection of v_0^{Y} or i_0 will limit the maximum power that the STATCOM could deliver to the grid. From the STATCOM manufacturer point of view, the reactive power limit is the indicative

parameter to quantify the impact of v_0^{Y} and i_0 injections on the power rating of the device, as well as to compare and select the most appropriate CHB configuration. To the best knowledge of the author, the quantification of this limit cannot be found in the specialized literature. So, the main contribution of this section is to quantify the Q^+ limits of the YCHB and DCHB STATCOMs as a function of the current unbalance (k_{ipn}).

Also, some of the aforementioned references compare the YCHB and the DCHB in an analogous but different scenario; e.g., the authors of [95] investigated and compared the power balancing capabilities of the YCHB under unbalanced current conditions, and the DCHB under unbalanced voltage. This approach concluded that a duality exists in the voltage and current ratings of the star and the delta, respectively. In this dissertation both YCHB and DCHB configurations are fairly compared in the same operating scenario. Moreover, most of these references validate their comparisons in a reduced power rating experimental set-up. The results provided in this dissertation are validated in a real-scale prototype in a MV laboratory. Additionally, the presence of the filters inside the delta (L_f) has not been considered before in the calculation of i_0 in the DCHB, so these explicit expressions are derived considering also that filters.

Summarizing, this section aims to analyze and compare the reactive power limits of CHB-based STATCOMs in star and delta configuration for i^- withstanding, by means of the following contributions:

- The Q^+ limits of the YCHB and DCHB STATCOMs for i^- withstanding are generically quantified. To do so, a systematic procedure is proposed. These limits allow comparing both configurations and concluding which one is more suitable for a certain scenario. This is one of the main contributions of this PhD thesis.
- Both YCHB and DCHB configurations are fairly compared in the same operating scenario. Besides, this section extends the analysis to operating points where i^- exceeds i^+, which is not found in the specialized literature.
- Derivation of the explicit expressions of the required i_0 in the DCHB considering the zero-sequence voltage drop across the filters inside the delta (L_f). It is demonstrated that this assumption is crucial in order to be precise in the calculation of i_0, which has not been considered before.
- Experimental validation in a 100 kVA real-scale prototype.

4.2.1 Intercluster Active Power Balancing

The intercluster active power balancing control must guarantee that the active power is equally distributed among phase clusters, compensating for the system losses as well as maintaining the charge of the dc-link capacitors adjusted. The adopted intercluster active power balancing strategy depends on the CHB circuit configuration.

4.2.1.1 *Solution for the YCHB*

The issue of withstanding i^- in the YCHB STATCOM is addressed by injecting a fundamental-frequency common zero-sequence voltage (v_0^{Y}). Considering v_0^{Y}, and assuming that the converter is not able to synthesize v^-, the stationary space phasors of the YCHB phase cluster voltage and current are defined:

$$\bar{V}_{ph} = V^+ e^{j(\delta_v^+ + 2\pi k/3)} + V_0^{\mathrm{Y}} e^{j\delta_{v_0^{\mathrm{Y}}}} \tag{4.1}$$

$$\bar{I}_{ph} = I^+ e^{j(\theta_i^+ + 2\pi k/3)} + I^- e^{j(\theta_i^- - 2\pi k/3)} \tag{4.2}$$

being $k = 0, -1, 1$ for $ph = \mathrm{a}, \mathrm{b}, \mathrm{c}$ (star case), respectively. The aim is to find a suitable V_0^{Y} and $\delta_{v_0^{\mathrm{Y}}}$ which will cancel out the effect of the non-zero average active power at each phase cluster due to the interaction between v^+ and i^-, as well as it will compensate for any type of power disturbance caused by non-idealities ($\bar{P}_{dis}$). The expressions of $\delta_{v_0^{\mathrm{Y}}}$ and V_0^{Y} are derived in *subsection 3.3.1.1*, solved in (3.14) and (3.15), respectively.

Fig. 4.2 (a) shows the evolution of the required zero-sequence voltage amplitude (V_0^{Y}) as a function of the ratio k_{ipn} and the phase angle between the current sequences ($\theta_{ipn} = \theta_i^- - \theta_i^+$) in a YCHB STATCOM. Note that the required V_0^{Y} is equal regardless of whether the converter is operating as capacitive or inductive power factor ($\phi^+ = \pm 90°$). For the simulated ideal case, $\bar{P}_{dis}$ has been neglected, and the most restrictive phase cluster current is set to the rated one. It can be observed that V_0^{Y} tends to infinity when $I^+ = I^-$ [95]. That is, if $k_{ipn} = 1$, theoretically infinity voltage is required to keep dc-link voltages balanced. Normally, the ratio of current unbalance is the operating requirement for which the converter is dimensioned, regardless of the angle θ_{ipn}. Fig. 4.2 (b) illustrates the maximum and minimum V_0^{Y} for each k_{ipn}.

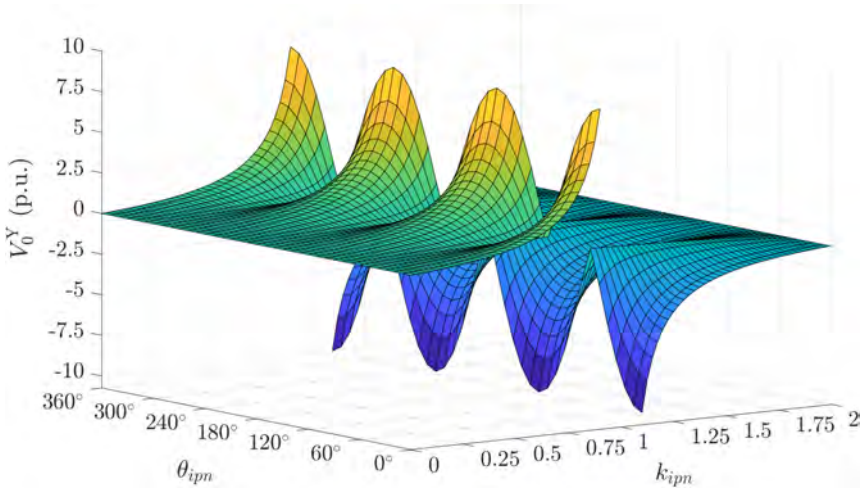

(a)

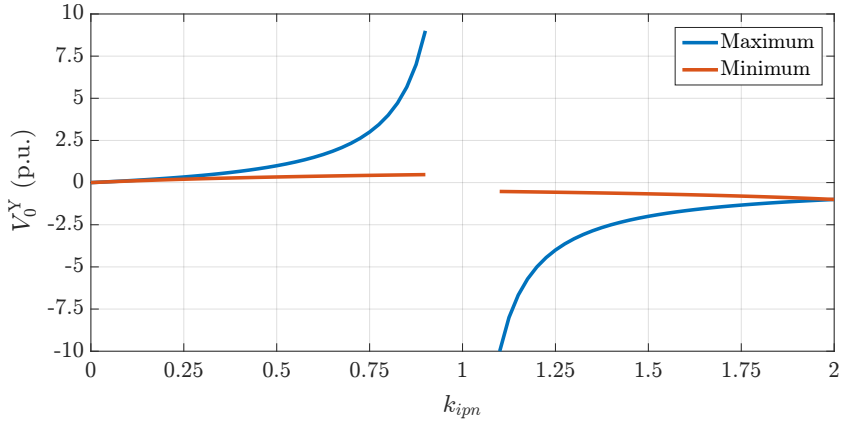

(b)

Fig. 4.2. Required zero-sequence voltage amplitude in the YCHB STATCOM ($V^+ = 1$ p.u., and $\max(|\bar{I}_{ph}|) = 1$ p.u.). (a) As a function of k_{ipn} and θ_{ipn}, and (b) max. and min. V_0^{Y} for each k_{ipn}.

In a real application, as mentioned above, the injection of v_0^{Y} could lead the converter voltage exceeding its rated level, and thus resulting in the YCHB operating in overmodulation or even becoming uncontrollable. That is, the zero-sequence voltage can be injected until the maximum attainable output voltage is reached. The amplitude modulation index

(m_a) will determine the maximum i^- (and thus k_{ipn}) that the converter could withstand without losing the controllability of dc-link capacitor voltages. Fig. 4.3 depicts the theoretical operation area of the YCHB STATCOM. If the voltage limit is reached, the converter can be over-rated either serializing more power cells or increasing the dc-link voltage of power cells.

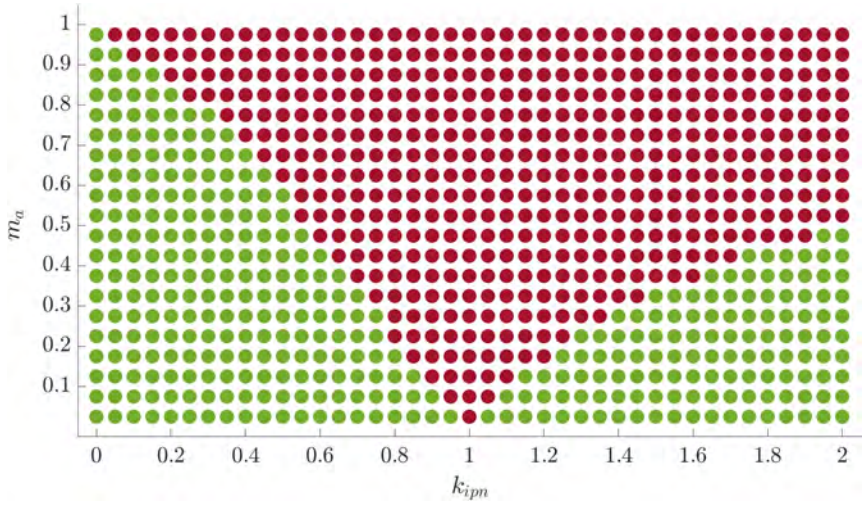

Fig. 4.3. k_{ipn} operation area of the YCHB STATCOM as function of m_a. Points which the converter can operate are illustrated in green, while the voltage limit is reached in those drawn in red.

4.2.1.2 *Solution for the DCHB*

For the DCHB STATCOM a fundamental-frequency zero-sequence current (i_0) can be injected to guarantee a uniform active power distribution among phase clusters. Assuming that the converter does not include v^- control loops as in the YCHB, the stationary space phasors of the converter phase cluster voltage and current are expressed in (4.3) and (4.4); being $k = 0, -1, 1$ for $ph = \text{ab}, \text{bc}, \text{ca}$ (delta case), respectively.

$$\bar{V}_{ph} = V^+ e^{j(\delta_v^+ + 2\pi k/3)} + V_0^\Delta e^{j\delta_{v_0}^\Delta} \tag{4.3}$$

$$\bar{I}_{ph} = I^+ e^{j(\theta_i^+ + 2\pi k/3)} + I^- e^{j(\theta_i^- - 2\pi k/3)} + I_0 e^{j\theta_{i_0}} \tag{4.4}$$

The injected i_0 will generate a zero-sequence voltage drop across the filters inside the delta (L_f). Thus, the converter must generate also a zero-sequence voltage (v_0^Δ) to compensate for this term so that it does not affect the grid-side ac voltage, as seen in (4.3). In this sense, the intercluster active power balancing control needs to generate this zero-sequence voltage, which will lead to the calculated i_0 (see *subsection 4.2.2*). Note that v_0^Δ is much smaller than v_0^Y, since in the DCHB the zero-sequence voltage is only responsible for creating the zero-sequence current rather than distributing the active power among phase clusters.

Analogously to the star, the required i_0 will generate an average active power term which will guarantee that the active power is equally distributed among delta-connected clusters, while it preserves the dc-link voltages in each phase cluster adjusted to the reference value. Following the same procedure adopted for the YCHB in *subsection 3.3.1.1*, and considering the filters inside the delta purely inductive to facilitate the calculation, the explicit expressions of θ_{i_0} and I_0 are also given by (3.18) and (3.19), being $X_f = \omega L_f$, and the constant terms the following:

$$
\begin{aligned}
K_1^{ph} &= \underbrace{V^+ I^- \cos\left(\delta_v^+ - \theta_i^- + k\frac{4\pi}{3}\right)}_{\bar{P}_{ph}^{+-}} \\
K_2^{ph} &= K_4^{ph} + X_f K_7^{ph} \\
K_3^{ph} &= K_5^{ph} + X_f K_6^{ph} \\
K_4^{ph} &= V^+ \cos\left(\delta_v^+ + k\frac{2\pi}{3}\right) \\
K_5^{ph} &= V^+ \sin\left(\delta_v^+ + k\frac{2\pi}{3}\right) \\
K_6^{ph} &= I^+ \cos\left(\theta_i^+ + k\frac{2\pi}{3}\right) + I^- \cos\left(\theta_i^- - k\frac{2\pi}{3}\right) \\
K_7^{ph} &= I^+ \sin\left(\theta_i^+ + k\frac{2\pi}{3}\right) + I^- \sin\left(\theta_i^- - k\frac{2\pi}{3}\right)
\end{aligned}
\tag{4.5}
$$

It should be noted that by this resolution method, modifying the values of the constants, the same equations are obtained for v_0^{Y} in the YCHB, i_0 in the DCHB, and i_0 in the DCHB considering the zero-sequence voltage drop inside the delta (v_0^{Δ}).

The evolution of the required zero-sequence current amplitude (I_0) in the DCHB STATCOM is shown in Fig. 4.4. Note that the maximum I_0 is demanded when $k_{ipn} = 1.5$; i.e., when $I^- = 2I^+$. The injected i_0 involves a current de-rating so as not to exceed the

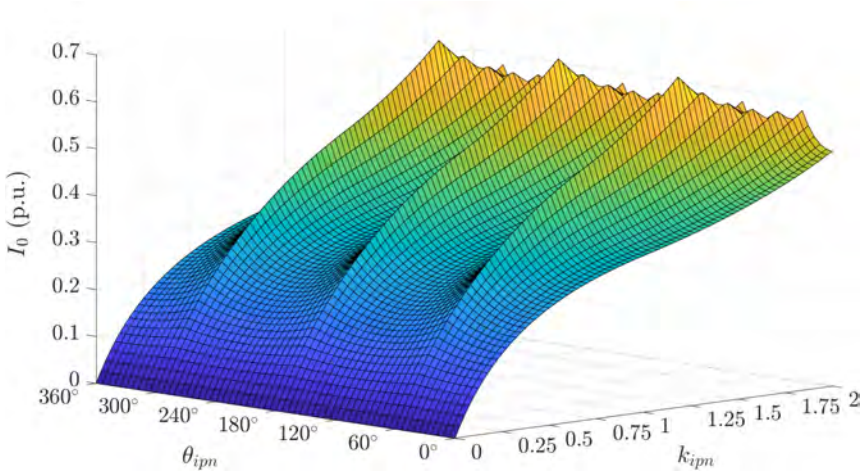

(a)

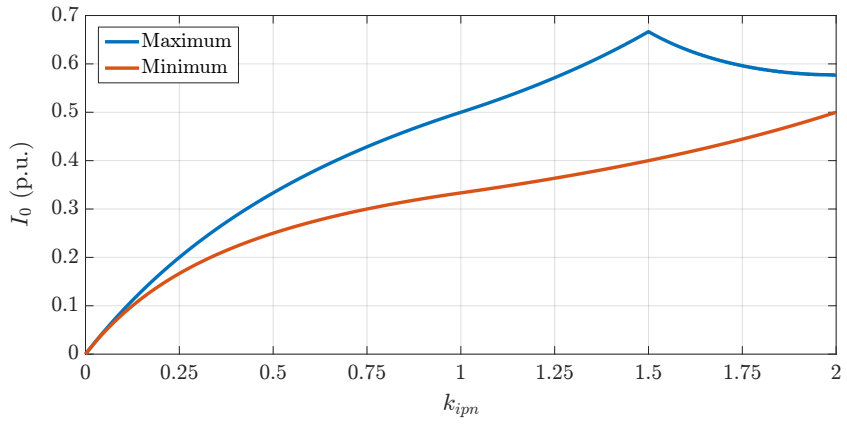

(b)

Fig. 4.4. Required zero-sequence current amplitude in the DCHB STATCOM ($V^+ = 1$ p.u., and $\max(|\bar{I}_{ph}|) = 1$ p.u.). (a) As a function of k_{ipn} and θ_{ipn}, and (b) max. and min. I_0 for each k_{ipn}.

rated value of switching devices, which forces to reduce the converter i^+ (and thus the available Q^+). However, in contrast to the YCHB, the DCHB converter can stay connected to that PCC maintaining its nominal ac voltage up to 100% current de-rating, without the necessity of changing m_a. Besides, although the calculation of the required i_0 in the DCHB presents a singular point where the converter cannot operate in other scenarios (e.g., when $V^+ = V^-$ [95]), it does not present any in this i^- withstanding scenario. As Fig. 4.5 also shows, it is essential to consider v_0^{Δ} and the value of L_f in the expressions of i_0 in order to be accurate in the calculation; a fact that has not been contemplated in previous investigations.

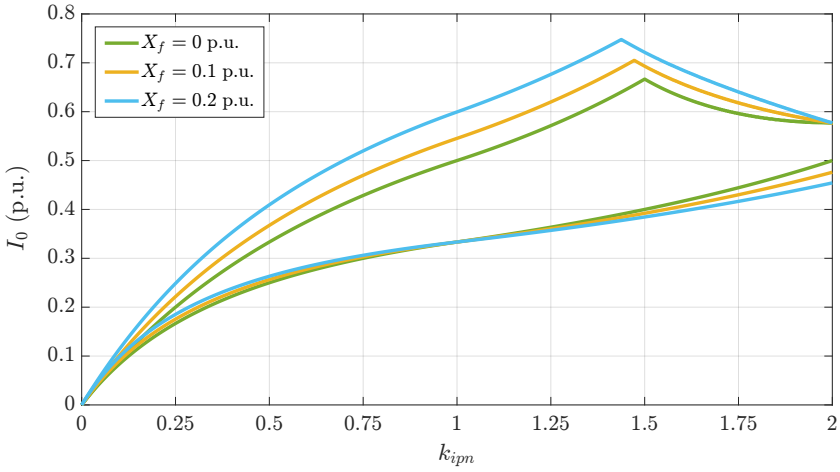

Fig. 4.5. Required zero-sequence current max. and min. amplitude in the DCHB STATCOM for each k_{ipn} and for different inductive filter values inside the delta ($V^+ = 1$ p.u., and max $(|\bar{I}_{ph}|) = 1$ p.u.).

4.2.2 Overall Control Design

The operation of CHB converters for STATCOM application and i^- withstanding requires controllers in order to address both the overall dc-link voltage unbalance and the intercluster active power unbalance. Fig. 4.6 shows the overall control structure of the STATCOM, which can be applied either to the YCHB or the DCHB configurations. This is composed of three main parts: the *dual vector control*, the *overall dc-link voltage control*, and the *intercluster active power balancing control*. However, dual vector control is sometimes simplified to the positive control loop.

Three-phase grid currents ($i_{g,\text{abc}}$) are decomposed into positive- and negative-sequences, and are transformed to the dq-reference frame using the transformation angle ($\theta = \omega t$) provided by the Phase-Locked Loop (PLL), which synchronizes the converter with the positive-sequence grid voltage (v_g^+). The positive- and negative-sequence dq components of the measured current are estimated using the Delayed Signal Cancellation (DSC) technique, and the dual vector control allows to control both sequences independently (tuned as [192]). The obtained converter reference voltages are then transformed to three-phase quantities (v_{ph}^{+*}), and the converter switching pattern is obtained by the modulator; in this case, through a Pulse Width Modulation (PWM). It should be remembered that in the scenario under study, negative-sequence current loops do not exist, and that is why the converter only generates positive-sequence voltage (v_{ph}^{+*}). The control design described in Fig. 4.6 corresponds to a general case.

The overall dc-link voltage controller is required to absorb the sufficient three-phase active power from the power grid ($\bar{P}_g^*$) to compensate for power losses and non-idealities

across the converter. It generates the necessary d-component positive-sequence current (i_d^{+*}) for maintaining the average dc-link voltage adjusted at the reference value ($v^*_{dc\text{-}ph}$).

The equality of the three-phase dc-link voltages is guaranteed by the intercluster active power balancing control. When using the YCHB, the required v_0^{Y*} is calculated according the i^- to withstand, and the power disturbances in each phase cluster ($\bar{P}^*_{dis\text{-}ph}$) generated by the intercluster dc voltage control, from (3.14) and (3.15). Analogously, the required i_0^* in the DCHB is calculated from (3.18) and (3.19). As mentioned, power disturbance references of two phase clusters are enough for calculating the phase angles $\delta_{v_0^Y}$ in (3.14) and θ_{i_0} in (3.18). Note that while the calculated v_0^{Y*} in the YCHB can be directly added to the output reference voltages of the dual vector control (v_{ph}^{+*}), when using the DCHB configuration, a controller G is necessary to generate the $v_0^{\Delta*}$ that will lead to the calculated i_0^* [95], [96], [136], [141], [161], [174], [193]. The requirements that this regulator needs to fulfill and its design are discussed in *Chapter 5*.

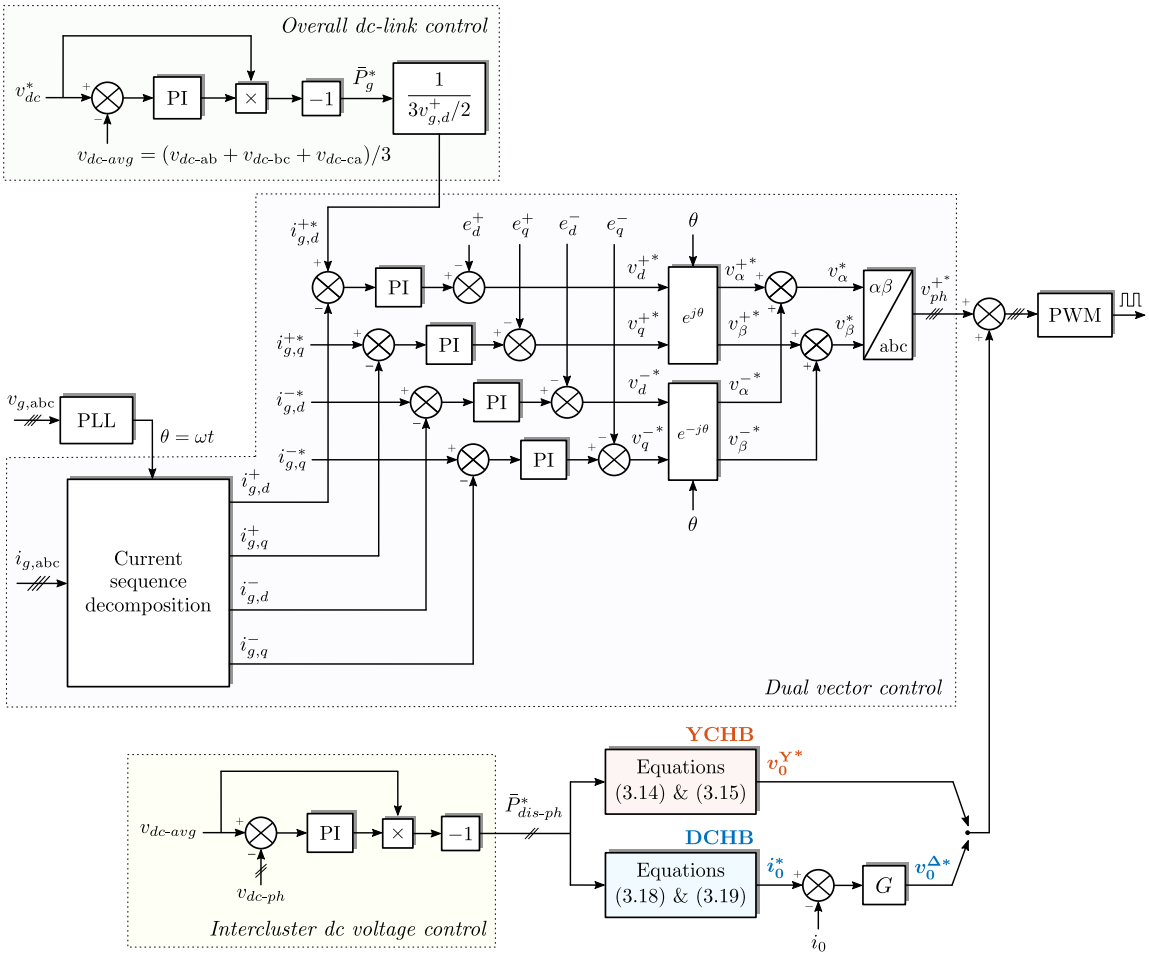

Fig. 4.6. Simplified block diagram of the overall control design for both YCHB and DCHB STATCOMs to operate with i^-.

4.2.3 Reactive Power Limits

As mathematically demonstrated, additional fundamental-frequency zero-sequence voltage (YCHB) or current (DCHB) can be injected to deal with i^-, both of which vary depending on k_{ipn} and θ_{ipn}. In this context, the converter will be limited in terms of voltage and/or current for STATCOM application. That is, both the presence of i^-, and the required v_0^Y or i_0 injections will limit the maximum power that the STATCOM could deliver to the

grid. However, the values of v_0^{Y} and i_0 are not significant to compare and select which CHB configuration is the most appropriate for this scenario. As in the scenario under study the aim of the STATCOM is to provide positive-sequence reactive power (Q^+), the limit of this is, from a dimensioning point of view, the indicative parameter to define the most suitable configuration. The quantification of this limit cannot be found in the specialized literature.

Fig. 4.7 shows the proposed systematic procedure to quantify Q^+ in each CHB STATCOM configuration, and Fig. 4.8 shows the Q^+ limits for i^- withstanding; i.e., the limit for each k_{ipn}, for the most restrictive θ_{ipn} angle. The theoretical maximum attainable Q^+ is also provided. This is one of the main contributions of this PhD dissertation.

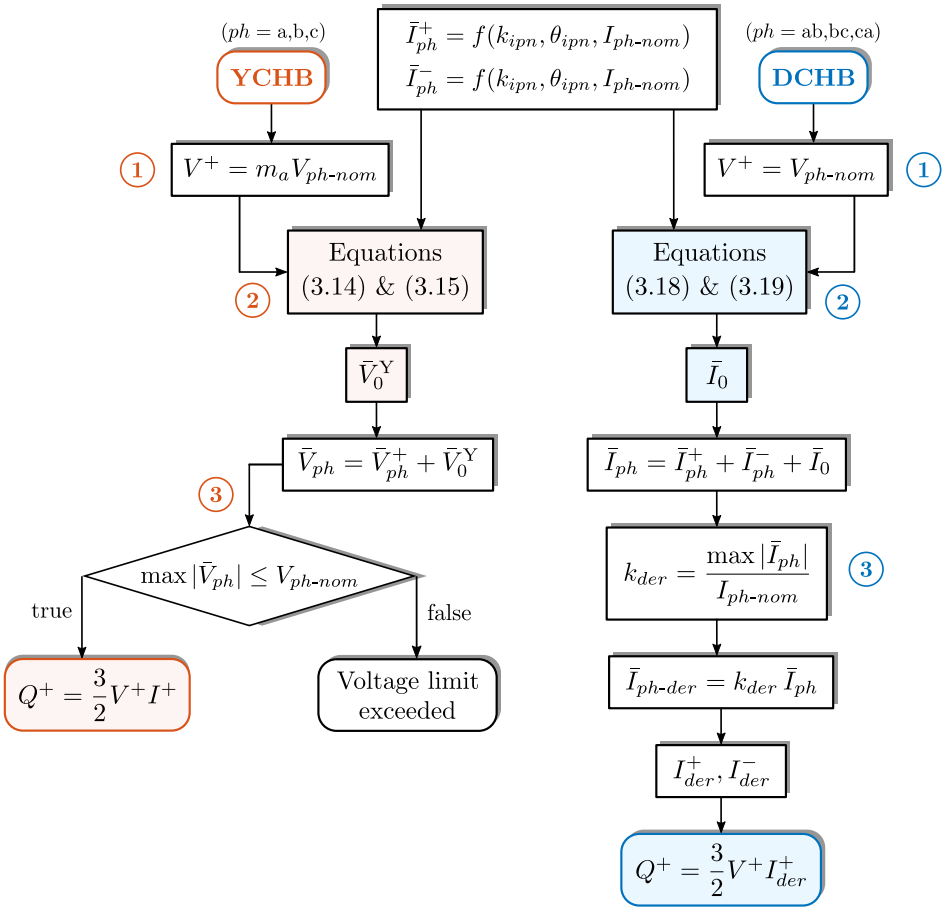

Fig. 4.7. Flow chart of the procedure to quantify Q^+ in each CHB STATCOM configuration.

It is worth noting that the 2ω dc-link capacitor voltage fluctuation has negligible effect on the Q^+ limits of single-phase dc-link VSC topologies [59], such as the YCHB and the DCHB, as it will be concluded in *section 4.3*.

4.2.3.1 Q^+ *limits of the YCHB STATCOM*

The Q^+ limits of the YCHB STATCOM are calculated as follows, summarized in Fig. 4.7:

- *Step 1.* The positive-sequence voltage amplitude (V^+) generated in the YCHB depends on the amplitude modulation index (m_a) using.
- *Step 2.* Then, for each ratio k_{ipn} and angle θ_{ipn}, the required $\bar{V}_0^{\mathrm{Y}}$ is calculated from (3.14) and (3.15).
- *Step 3.* As mentioned, the YCHB topology cannot operate when the converter phase cluster voltage exceeds its rated level; i.e., when $\max|\bar{V}_{ph}| \leq V_{ph\text{-}nom}$. That is why

voltage over-rating is sometimes required so as to increase the available dc-side voltage. This can be achieved either increasing the dc-link voltage, or serializing more cascaded power cells.

The plotted line in Fig. 4.8 illustrates the theoretical Q^+ limit of the correctly voltage over-rated YCHB for each k_{ipn}. This means that the converter is supposed to be able to give the reference voltage. As this voltage over-rating is not feasible in practice, limits for the YCHB configuration with practical voltage ratings are also served (different m_a values); dashed lines represent k_{ipn} operating points where the voltage limit is reached and the converter is not able to work. For instance, it can be seen that with $m_a = 0.9$ (which can be case of a grid-connected STATCOM), the YCHB cannot withstand a negative-sequence current up to $k_{ipn} = 0.1$. In this configuration, the power de-rating is due to the i^+ decreasing as k_{ipn} increases. An important drawback is that as infinity V_0^{Y} is required in the operating point $k_{ipn} = 1$ [95], beyond this singular point, the YCHB becomes uncontrollable in practical applications. Thus, it can be concluded that the capability of the YCHB STATCOM to withstand i^- is strongly limited by the voltage rating of its phase clusters; in other words, by the available dc-side voltage.

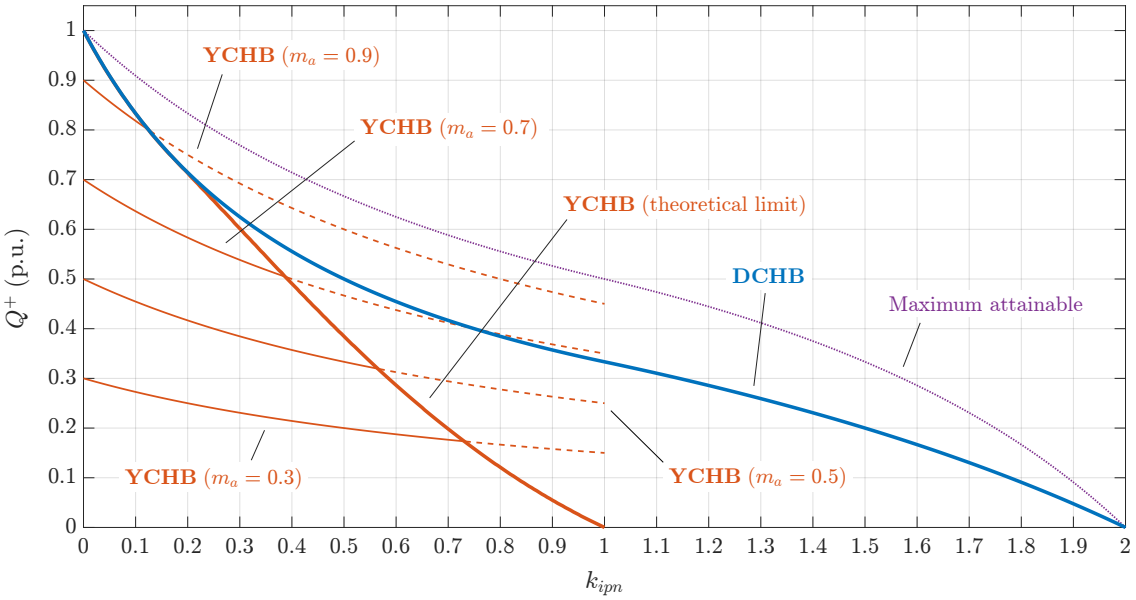

Fig. 4.8. Positive-sequence reactive power (Q^+) limits of YCHB and DCHB configurations for STATCOM application under i^- withstanding.

4.2.3.2 *Q^+ limits of the DCHB STATCOM*

Fig. 4.7 also shows the procedure to obtain the Q^+ limits of the DCHB STATCOM:

- *Step 1.* In contrast with the YCHB, the delta configuration does not present any limitation in terms of exceeding the rated voltage; as long as it has a few margin to compensate for the zero-sequence voltage drop across the filters inside the delta (v_0^{Δ}). In other words, the amplitude modulation index (m_a) used does not imply any limitation for the DCHB topology. That is why, in this negative-sequence current withstanding scenario, it can remain connected to the PCC guaranteeing the nominal ac voltage up to 100% de-rating of i^+ ($Q^+ = 0$), as the grid code might demand.
- *Step 2.* The required $\bar{I}_0$ is calculated from (3.18) and (3.19), depending on the ratio k_{ipn} and the angle θ_{ipn}.

– *Step 3.* The i^+ limit (I^+_{der}) is calculated by making the most charged phase cluster have the rated value ($I_{ph\text{-}nom}$).

Therefore, the line plotted in Fig. 4.8 decreases when k_{ipn} increases either as a result of the phase cluster i^+ de-rating due to the increasing of i_0, and/or the decreasing of i^+ as i^- increases. In this scenario the Q^+ p.u. limit is equal to the I^+ p.u. limit. The major advantage over the star is that the DCHB can deal with severe intercluster active power unbalances guaranteeing the controllability of dc-link capacitor voltages; even at $k_{ipn} >> 1$. In other words, while the YCHB is strongly limited by the available dc-side voltage, the DCHB can stay connected to the PCC regardless of the i^- to withstand. Besides, note that the delta configuration does not present any singular point which might cause the STATCOM to lose controllability, as long as there is no v^- at the converter terminals. These conclusions confirm the DCHB as the preferable option to the YCHB for STATCOM application dealing with severe unbalanced current conditions.

4.2.4 Experimental Results

Experimental results obtained from a 500 V – 100 kVA three-phase 5L NPC/HB converter prototype are provided to demonstrate the intercluster active power balancing capabilities and Q^+ limits of both YCHB and DCHB STATCOMs when withstanding i^-. As analyzed in *subsection 2.3.3.2*, the 5L NPC/HB power cell is commonly employed in the CHB topology in order to increase the power rating [58]. Note that the conclusions drawn are valid regardless of the topology used in the power cell. To calculate the required v_0^{Y} (YCHB) or i_0 (DCHB), the fundamental-frequency component of the converter output voltage needs to be only considered, and the topology of the power cell does not influence in this variable (it only affects in the harmonic content of this voltage).

The layout of the experimental set-up built in the *Medium Voltage Laboratory* of *Ingeteam Power Technology S.A.* (*Bizkaia Science and Technology Park*, Zamudio, Spain), as well as the simplified circuit diagrams corresponding to the YCHB and the DCHB configurations for the scenario under study are shown in Figs. 4.9 and 4.10, respectively.

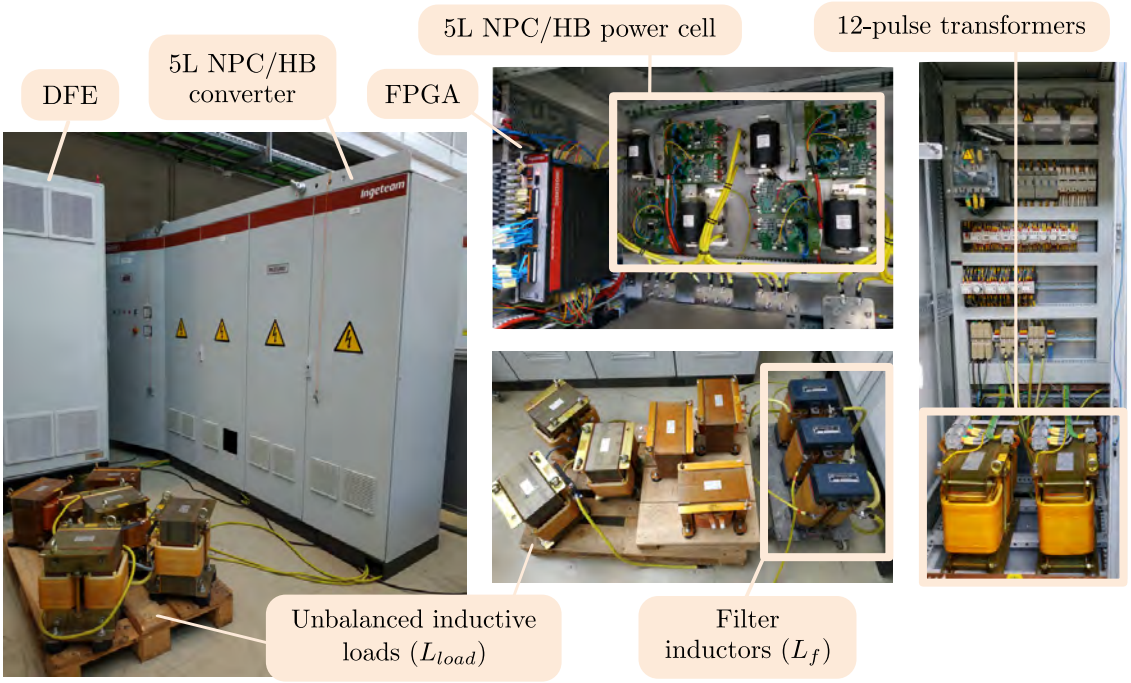

Fig. 4.9. Layout of the experimental set-up.

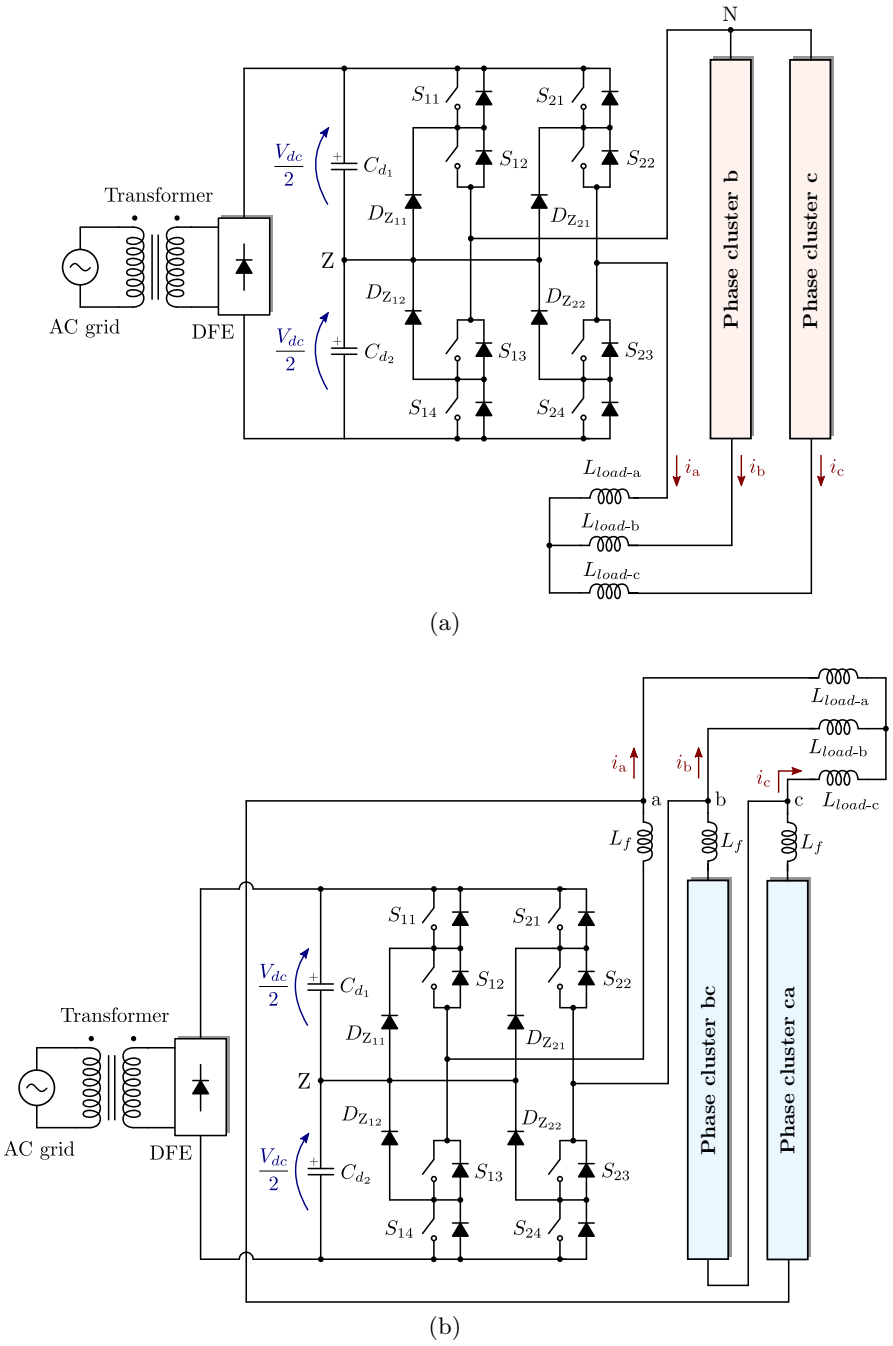

Fig. 4.10. Simplified circuit diagrams of the experimental set-up. (a) YCHB, and (b) DCHB.

With the aim of isolating the analyzed intercluster active power balancing control, each phase cluster is composed of a single 5L NPC/HB power cell ($n = 1$); this allows avoiding the intracluster power balancing. The switching scheme used is the multilevel SVM with a switching frequency of 1 kHz. In order to reach the voltage limit and demonstrate the power limits, the converter nominal voltage of the YCHB has been limited to its half; hence, $Q^+ = 1$ p.u. and $m_a = 1$ correspond to the Q^+ and m_a achieved with this voltage. Similarly, the nominal current in the DCHB has also been limited to its half.

By a common scalar voltage/frequency regulation (thus, the dual vector control of Fig. 4.6 is not used), the 5L NPC/HB converter synthesizes positive-sequence voltage (v^+), and connected to single-phase unbalanced inductive loads ($L_{load\text{-}ph}$), i^- circulation is generated through the converter phase clusters. For these tests, 3.2 mH and 7.5 mH loads are combined so as to generate different k_{ipn} and θ_{ipn} operating points. It should be

remarked that using different combinations of single-phase passive inductive loads, it is not possible to generate operating points where I^- exceeds I^+; that is why the ratio k_{ipn} is less than the unity in the carried out experiments.

Since the VSC is not connected to the grid, and is feeding passive loads, it is necessary to have an energy source connected to the dc-links. That is why these experiments are performed using a 12-pulse Diode Front End (DFE) rectifier connected to each power cell. For the results that this work aims to validate these experiments are valid. If the intercluster active power balancing strategy does not regulate properly, the dc-link capacitor voltages will remain unbalanced, and even some of the dc-link voltages could continuously increase above the dc voltage set by the DFE rectifier. Therefore, the overall dc-link control of Fig. 4.6 is not needed for these experiments.

Assuming that the DFE rectifier will provide the active power consumed by all the resistive components of the prototype, this experimental set-up emulates the i^- withstanding scenario of a STATCOM application. Note that although in the following experiments the STATCOM is operating with capacitive power factor (connected to inductive loads), the results with inductive power factor are the same (since $\bar{V}_0^{\mathrm{Y}}$ and $\bar{I}_0$ are equal in both power factor cases). For the DCHB, 2.5 mH single-phase passive inductive loads are used as a filter inside the delta (L_f). The parameters of the set-up and the experiments are given in Table 4.1.

Table 4.1. Experimental set-up parameters.

Parameter	**Value**
Rated power (S_n)	100 kVA
Rated voltage ($V_{ll\text{-}rms}$)	500 V
Power cell dc-link voltage (V_{dc})	430 V
Power cell dc-link capacitor ($C_d = C_{d_1}/2 = C_{d_2}/2$)	0.825 mF
Power cell topology	5L NPC/HB
Number of power cells per phase cluster (n)	1
Output nominal fundamental-frequency (f)	50 Hz
Switching frequency (f_{sw})	1 kHz
Filter inductor in the DCHB (L_f)	2.5 mH

All the experimental tests performed for both YCHB and DCHB configurations are constituted of three main stages:

1. Firstly, the converter withstands i^- without activating the intercluster active power balancing control. During this interval, dc-link voltages ($v_{dc\text{-}ph}$) drift from their reference values. Without the DFE rectifier, at least one of the dc capacitors would discharge.

2. When the intercluster balancing control is activated, dc-link voltages in each phase cluster are equaled. At this point, the converter operates within its limits. Note that dc-link voltages vary from one experiment to another, because they depend on the loads connected to the MV laboratory ac grid.

3. Finally, the voltage reference is increased and the converter limits are reached. As a consequence, dc-link capacitor voltages begin to drift away.

Figs. 4.11 and 4.12 show the experimental results of the YCHB under two i^- withstanding scenarios. In the first experiment of Fig. 4.11 $L_{load\text{-a}}$ and $L_{load\text{-b}}$ are 7.5 mH, while $L_{load\text{-c}}$ is 10.7 mH; this generates a current unbalance of $k_{ipn} = 0.12$ and $\theta_{ipn} = 60°$. For its

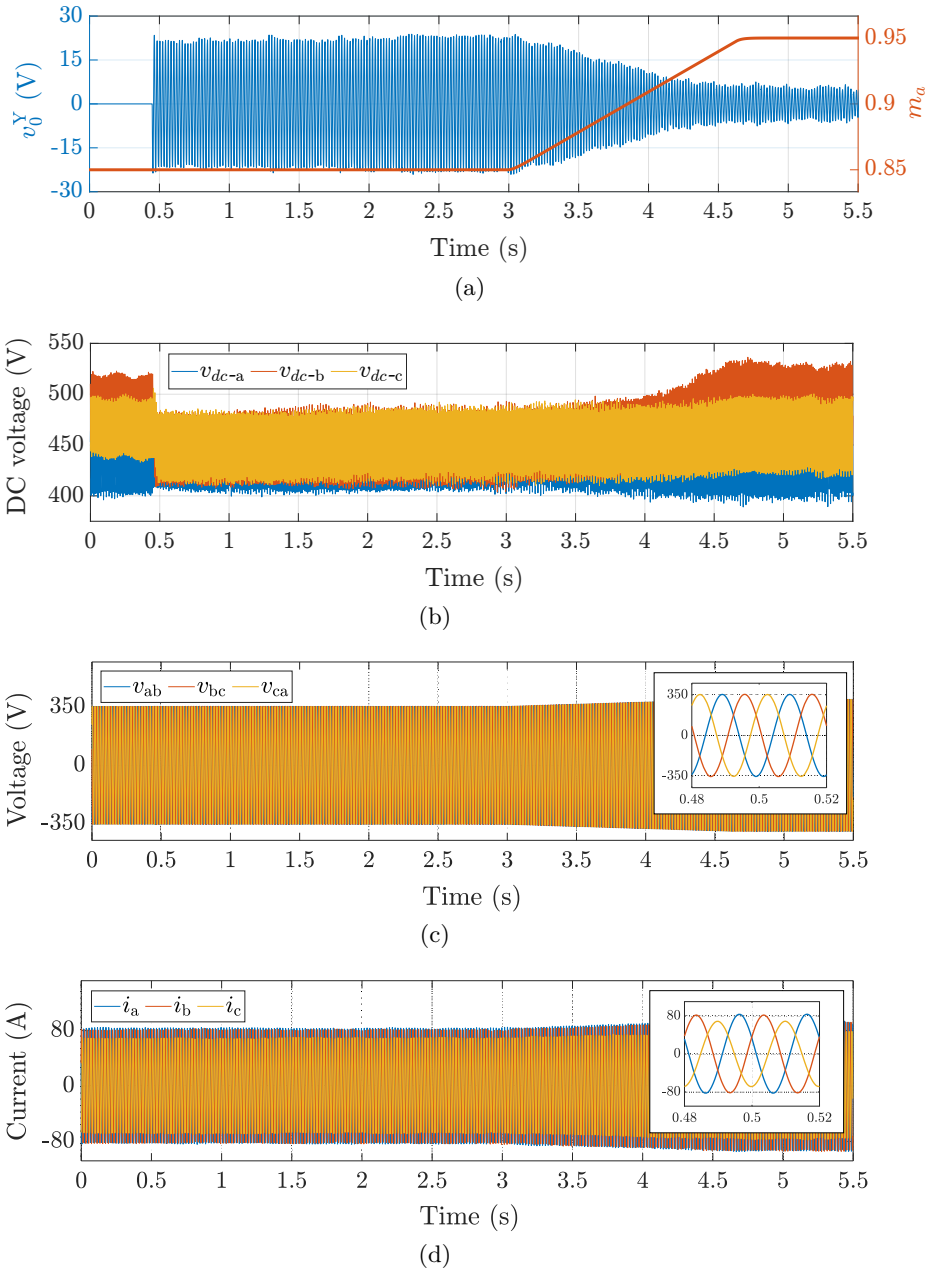

Fig. 4.11. Experimental Q^+ limits of the YCHB with $L_{load\text{-a}} = L_{load\text{-b}} = 7.5$ mH and $L_{load\text{-c}} = 10.7$ mH ($k_{ipn} = 0.12$, $\theta_{ipn} = 60°$).

part, $k_{ipn} = 0.31$ and $\theta_{ipn} = 60°$ are achieved in the experiment of Fig. 4.12 with $L_{load\text{-a}} = L_{load\text{-b}} = 3.2$ mH, and $L_{load\text{-c}} = 7.5$ mH.

In Figs. 4.11 (a) and 4.12 (a) the injected zero-sequence voltage (v_0^Y) and the amplitude modulation index (m_a) are plotted. It can be seen that in Fig. 4.11 (a) m_a goes from 0.85 to 0.95; likewise, in Fig. 4.12 (a) m_a goes from 0.75 to 0.85. Figs. 4.11 (b) and 4.12 (b) depict the dc-link voltages of each phase cluster. As expected, these dc voltages contain both an average and a double-frequency component (2ω) value. The injected v_0^Y acts over the average one, which is generated by the average active power component. Figs. 4.11 (c) and 4.12 (c) show the line-to-line voltages of each experiment, which are not modified when injecting v_0^Y. The load currents are also served in Figs. 4.11 (d) and 4.12 (d), which are clearly unbalanced but are not altered by injecting v_0^Y.

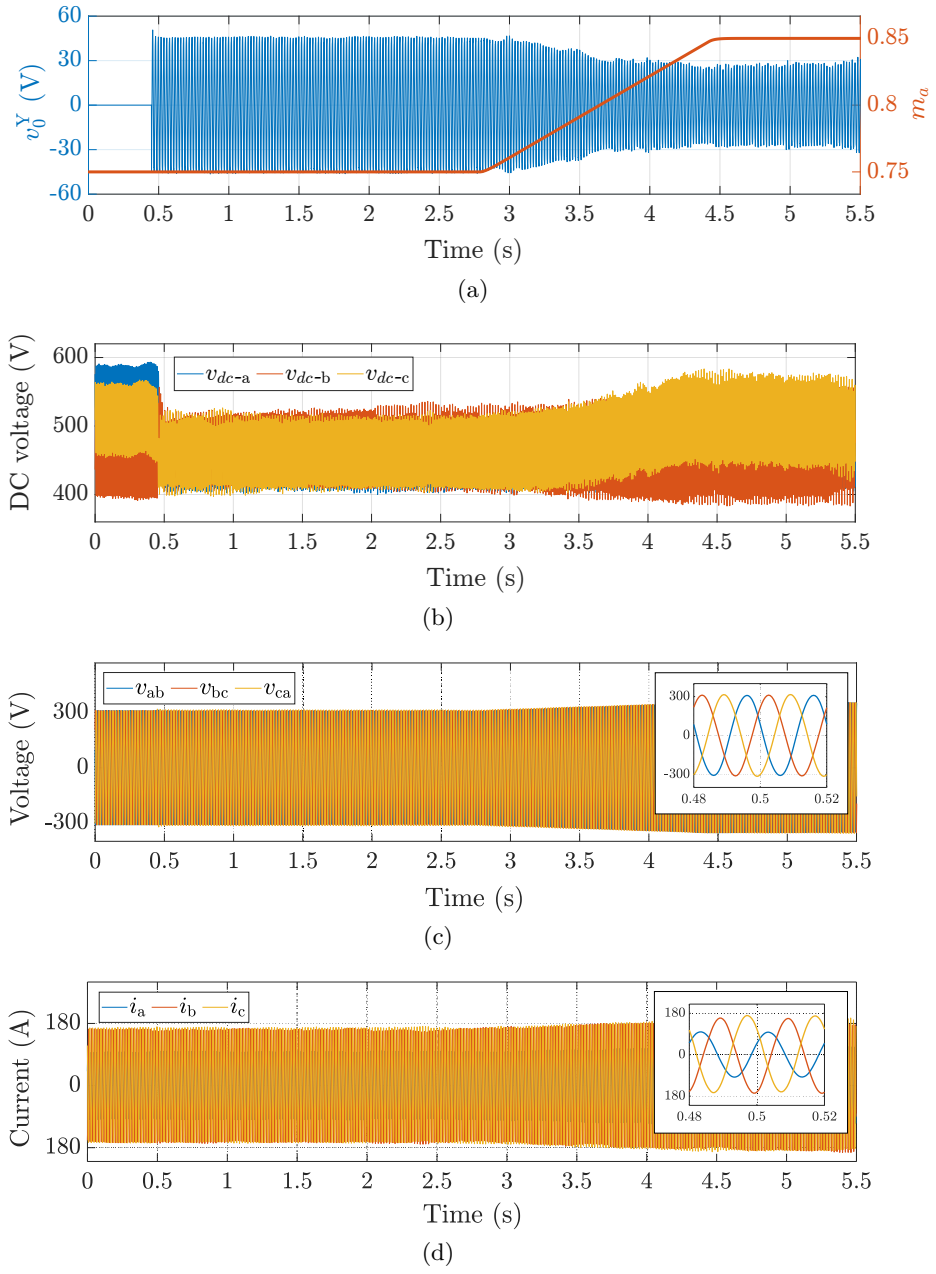

Fig. 4.12. Experimental Q^+ limits of the YCHB with $L_{load\text{-a}} = L_{load\text{-b}} = 3.2$ mH and $L_{load\text{-c}} = 7.5$ mH ($k_{ipn} = 0.31$, $\theta_{ipn} = 60°$).

A transition is made from an operating point where the converter does not exceed its Q^+ limit (green cross), to another point where it does (red cross), as Fig. 4.13 summarizes, thus validating the results obtained in Fig. 4.8. It can be seen that dc-link voltages begin to drift away when there is no available voltage for the injection of v_0^Y. When the operating limits of the converter are exceeded, the dc-link voltages would increase until the converter would stop due to overvoltage. Thus, for safety reasons, the injected v_0^Y is saturated once the limit is reached and not set to 0.

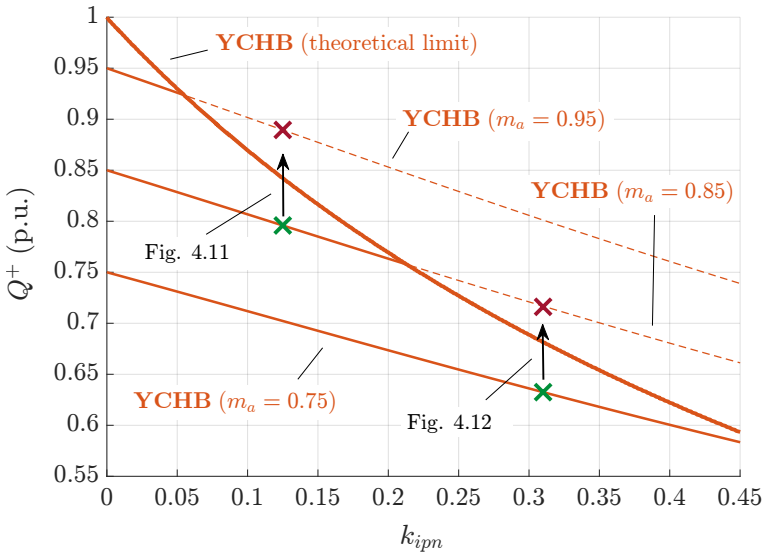

Fig. 4.13. Q^+ experimental operating transitions of Figs. 4.11 and 4.12 ($\theta_{ipn} = 60°$).

With regard to the DCHB configuration, Fig. 4.14 summarizes the I^+ transitions of the experiments illustrated in Figs. 4.15 and 4.16, which are analogous to the tests performed with the YCHB. On the one hand, $k_{ipn} = 0.38$ and $\theta_{ipn} = 0°$ are achieved in the experiment of Fig. 4.15 with $L_{load\text{-a}} = L_{load\text{-b}} = 3.2\,\text{mH}$, and $L_{load\text{-c}} = 10.7\,\text{mH}$. On the other hand, in the experiment of Fig. 4.16 $L_{load\text{-a}}$ and $L_{load\text{-b}}$ are 3.2 mH, while $L_{load\text{-c}}$ is 18.2 mH; thus generating a current unbalance of $k_{ipn} = 0.55$ and $\theta_{ipn} = 0°$.

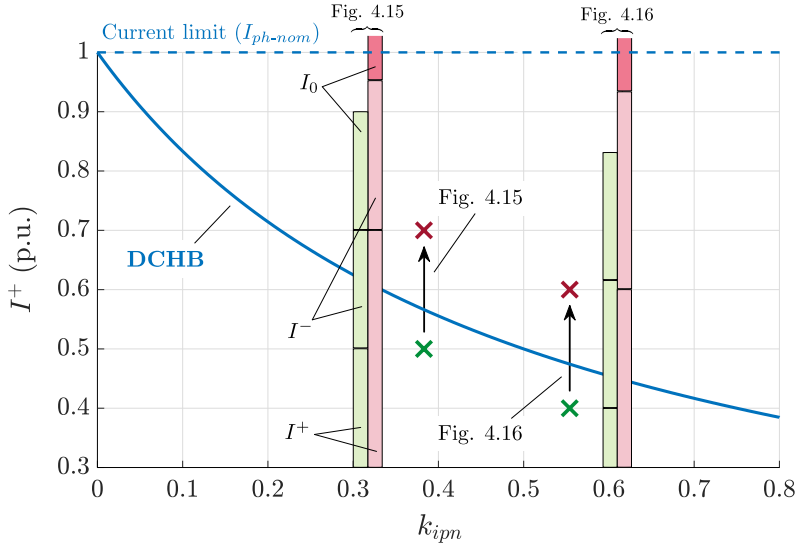

Fig. 4.14. I^+ experimental operating transitions of Figs. 4.15 and 4.16 ($\theta_{ipn} = 0°$). Solid bars represent the I^+, I^- and I_0 required in each point.

Analogous to the YCHB configuration, the injected instantaneous zero-sequence current (i_0) and the amplitude of the positive-sequence current phasor (I^+) are shown. Since the Q^+ de-rating of the delta configuration is only influenced by the de-rating of i^+ (see Fig. 4.7), the operating transitions are made by increasing the value of I^+; in Fig. 4.15 (a) I^+ goes from 0.5 to 0.7 p.u., while in Fig. 4.16 (a) is increased from 0.4 to 0.6. The injected zero-sequence voltage (v_0^Δ) that leads to the calculated reference i_0 is also served in Figs. 4.15 (b) and 4.16 (b), which is saturated once the limit is reached as in the star case. Figs. 4.15 (d) and 4.16 (d) show the output line-to-line voltages, which are not affected by the injected v_0^Δ. It can be seen in the load currents of Figs. 4.15 (e) and 4.16 (e) that

the injected i_0 circulates only inside the delta. As Fig. 4.14 depicts, which its I^+ per unit limit is equal to the Q^+ per unit limit of Fig. 4.8 (as explained in *subsection 4.2.3.2*), the current limit is exceeded due to the required i_0. As the converter is not able to inject this i_0, dc-link voltage balancing cannot be guaranteed, as Figs. 4.15 (c) and 4.16 (c) show.

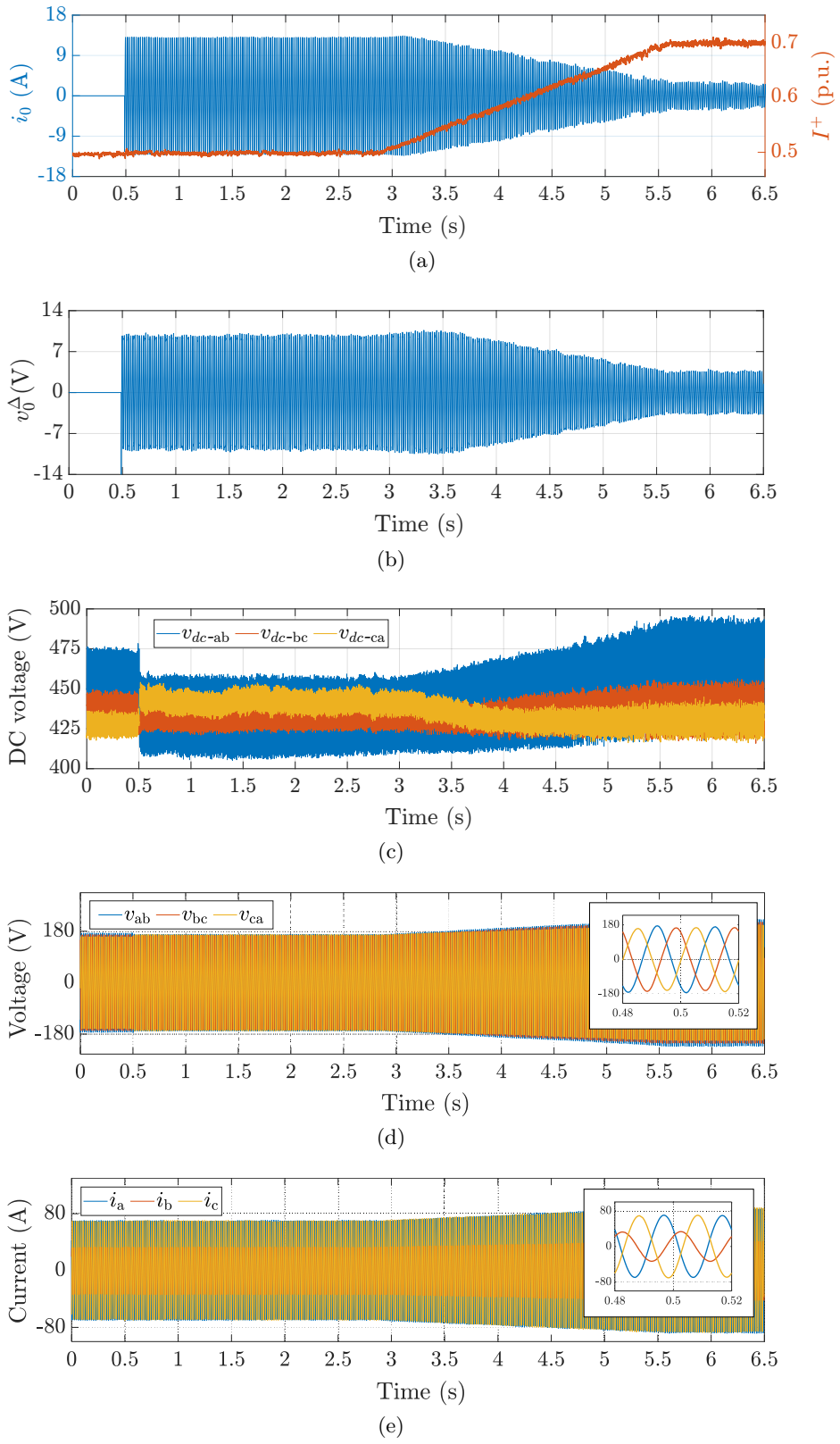

Fig. 4.15. Experimental Q^+ limits of the DCHB with $L_{load\text{-a}} = L_{load\text{-b}} = 3.2$ mH and $L_{load\text{-c}} = 10.7$ mH ($k_{ipn} = 0.38$, $\theta_{ipn} = 0°$).

The shown experimental results summarize twelve operating points in Figs. 4.11, 4.12, 4.15, and 4.16 under different k_{ipn} and θ_{ipn} values, as well as the transitions between them. It can be seen how the achieved results of both configurations meet the theoretical approach and validates the analysis.

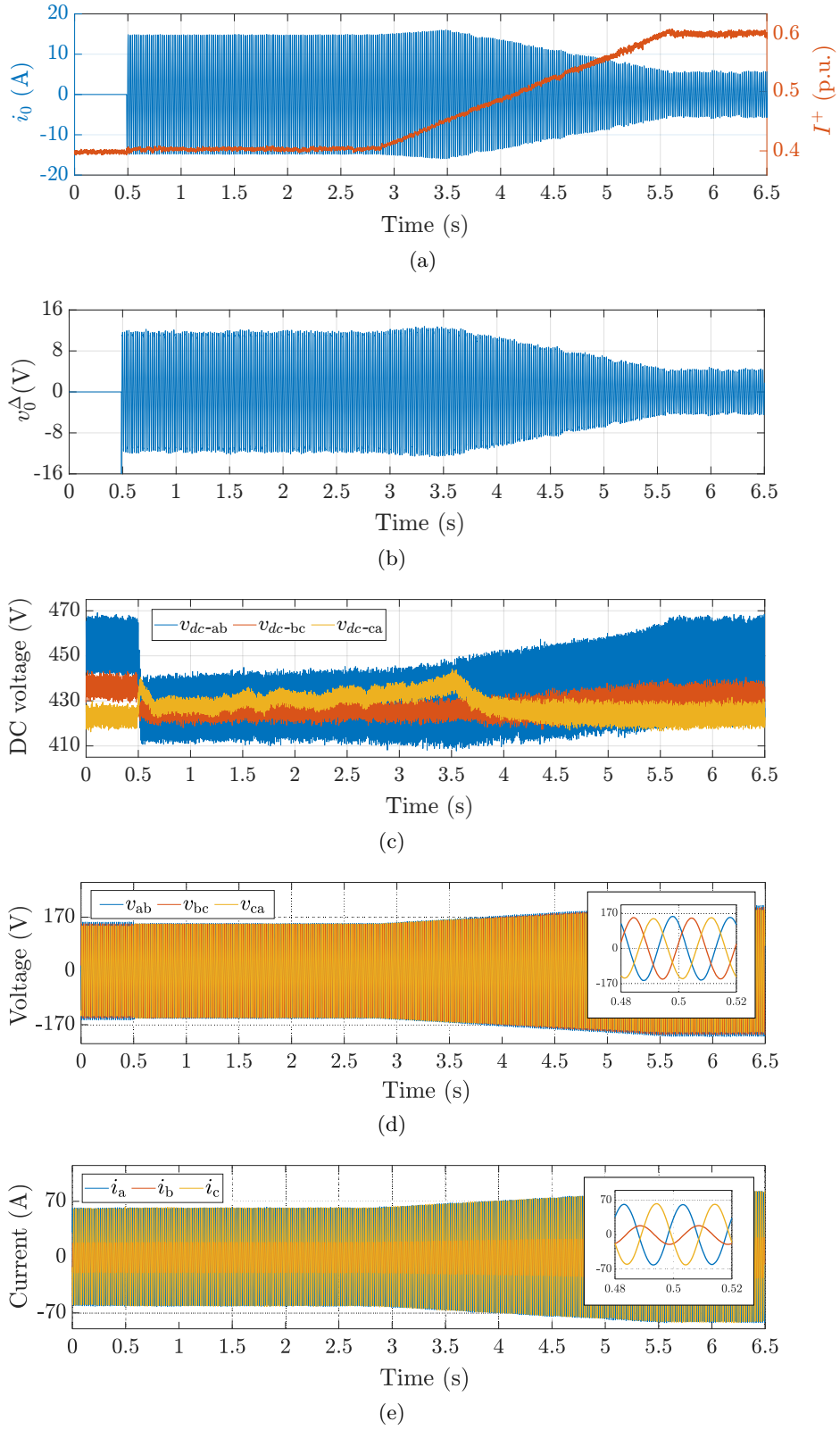

Fig. 4.16. Experimental Q^+ limits of the DCHB with $L_{load\text{-a}} = L_{load\text{-b}} = 3.2$ mH and $L_{load\text{-c}} = 18.2$ mH ($k_{ipn} = 0.55$, $\theta_{ipn} = 0°$).

4.3 SINGLE- AND THREE-PHASE DC-LINK VSC STRUCTURES UNDER NEGATIVE-SEQUENCE VOLTAGE AND/OR CURRENT

Negative-sequence voltage and/or current components in the ac side have an influence on the dc side of the VSC, especially when the dc-link has no energy source to feed it, such as in STATCOM application. Depending on the VSC structure using, the dc-link can be configured as single- or three-phase. The 3L NPC converter is an example of a common three-phase dc-link VSC topology, while each power cell is fed by single-phase dc-links in CHBs. For its part, the MMC is composed of both single- and three-phase dc-links. The aim of this section is to measure the influence of negative-sequence components in single- and three-phase configured dc-link VSCs. The analysis of *section 4.2* is extended by adding to the study the quantification of the Q^+ limits of the 3L NPC and the MMC for STATCOM application, operating under i^- as well as v^-. The analysis provided in this section led to publication [C2].

Subsection 3.3.1.1 and *section 4.2* have analyzed the effect of the average active power ($\bar{P}$) on the YCHB, the DCHB, and the MMC operating with negative-sequence components as STATCOM. However, the impact of the 2ω oscillating active power term ($\tilde{p}$) on VSCs under v^- and/or i^- has not been studied in depth.

4.3.1 Negative-Sequence Voltage and Current Effects on DC-Link Voltage Ripple

The oscillating active power term ($\tilde{p}$) has a zero average value and thus it does not represent any net energy exchange. However, as neglecting the inner losses of the converter the ac-side power should be equal to the dc-side power, $\tilde{p}$ is responsible of the second-order harmonic (2ω) oscillation in the dc-link of the VSC. This oscillation generates a voltage ripple across the dc-link capacitor voltages (Δv_{dc}). As can be seen in the per-phase instantaneous oscillating active power of (4.6), this effect depends on both the voltage and/or current unbalances, and also on the dc-link configuration of the VSC. In order to quantify the dc voltage ripple, its peak-to peak value (Δv_{dc}^{pp}) is used as an indicator.

$$\begin{aligned}\tilde{p}_{ph}(t) = &-\underbrace{\frac{V^+I^+}{2}\cos\left(2\omega t+\delta_v^++\theta_i^++k\frac{4\pi}{3}\right)}_{\tilde{p}_{ph}^{++}}-\underbrace{\frac{V^+I^-}{2}\cos\left(2\omega t+\delta_v^++\theta_i^-\right)}_{\tilde{p}_{ph}^{+-}}\\&-\underbrace{\frac{V^-I^+}{2}\cos\left(2\omega t+\delta_v^-+\theta_i^+\right)}_{\tilde{p}_{ph}^{-+}}-\underbrace{\frac{V^-I^-}{2}\cos\left(2\omega t+\delta_v^-+\theta_i^--k\frac{4\pi}{3}\right)}_{\tilde{p}_{ph}^{--}}\end{aligned} \tag{4.6}$$

When there is no cross-interaction between positive- and negative-sequence components (only $\tilde{p}_{ph}^{++}$ or $\tilde{p}_{ph}^{--}$ exist), the three-phase oscillating active power is zero; i.e., the sum of $\tilde{p}_{ph}^{++}$ or $\tilde{p}_{ph}^{--}$ in the three phases is zero ($\tilde{p}_{\mathrm{a}}+\tilde{p}_{\mathrm{b}}+\tilde{p}_{\mathrm{c}}=0$). Hence, VSC structures with a three-phase dc-link, such as the 3L NPC, do not experience any dc voltage ripple under balanced conditions (at least not as a result of the 2ω oscillation), regardless of the power factor (ϕ^+, ϕ^-) of the application. Nevertheless, while the presence of v^- and/or i^- increases, terms $\tilde{p}_{ph}^{+-}$ and/or $\tilde{p}_{ph}^{-+}$ arise in (4.6), which are common in the three phases. Thus, these terms do not cancel out when added together in the three phases, and are therefore responsible for creating a second-order harmonic voltage ripple in the three-phase

dc-link. Before knowing the mechanism that produces this dc-link voltage ripple, this effect has already been seen by simulation in *case study II* of *Chapter 2* (see Figs. 2.26 and 2.27).

Fig. 4.17 shows the evolution of the maximum Δv_{dc}^{pp} of a 3L NPC for STATCOM application as a function of k_{ipn} (at the worst θ_{ipn} case), and for different k_{vpn} scenarios. The analytical results have been compared with time-based simulations. It can be seen how both results are very similar; the difference is the dc voltage ripple caused by the switching harmonics generated due to the implemented modulation strategy, which has practically no weight compared to the dc voltage ripple caused by the cross-interaction between positive- and negative-sequence components. It is appreciated from Fig. 4.17 that the maximum Δv_{dc}^{pp} in a 3L NPC is given when uniquely $\tilde{p}_{ph}^{+-}$ or $\tilde{p}_{ph}^{-+}$ exist; that is, at operating points where all the voltage is positive-sequence ($k_{vpn} = 0$) and all the current negative ($k_{ipn} = 2$); as well as when all the voltage is negative-sequence ($k_{vpn} = 2$) and all the current positive ($k_{ipn} = 0$).

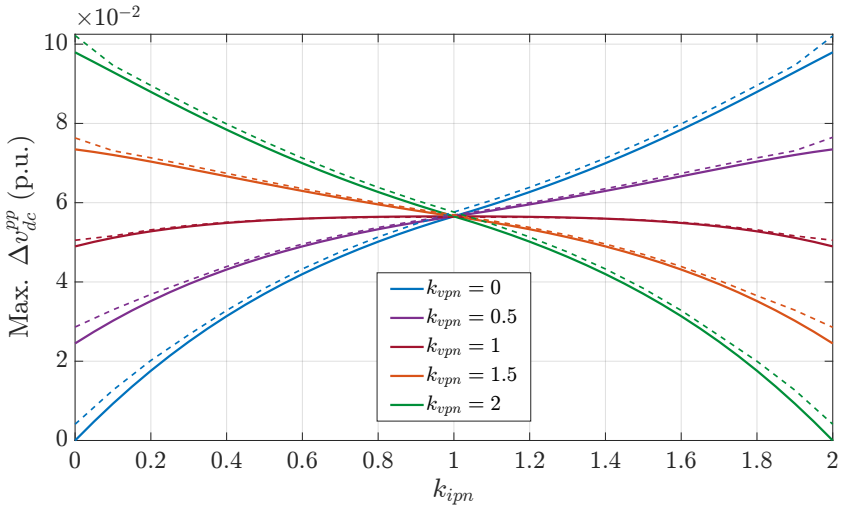

Fig. 4.17. Maximum dc-link voltage ripple peak-to-peak value of the 3L NPC STATCOM at rated voltage and current as a function of k_{ipn} for different k_{vpn} scenarios ($X_{C_{d_1}} = X_{C_{d_2}} = 0.13$ p.u.). Solid lines represent the analytical evolution, while dashed ones show the time-based simulation results.

Fig. 4.18 illustrates the evolution of the analytical maximum Δv_{dc}^{pp} in both the 3L NPC and the 5L NPC/HB structures for STATCOM application as a function of k_{ipn} and k_{vpn}, assuming the most restritive θ_{ipn}. The aforementioned conclusions can be clearly appreciated, and it can be concluded that the current and voltage unbalances are analogous in their impact on the 2ω dc voltage ripple of a three-phase dc-link VSC, such as the 3L NPC. In a real application, if Δv_{dc}^{pp} increases, a current de-rating can be applied in order to decrease it; this would imply the de-rating of the available Q^+ in the STATCOM, as it will be analyzed in *subsection 4.3.3*. The dc-link capacitance (C_d) can also be over-rated so as to reduce this 2ω dc voltage ripple.

Regarding single-phase dc-link VSC structures, Fig. 4.18 presents also the evolution of Δv_{dc}^{pp} in a 5L NPC/HB STATCOM; which its maximum value is constant regardless k_{ipn} and k_{vpn}. That is, at rated voltage and current values, the maximum $\tilde{p}_{ph}$ of any of the three phase clusters is constant for any unbalance depth and type. This is the reason why the effect of the oscillating term $\tilde{p}$ in CHBs has not been analyzed in *Chapter 3*. Indeed, the maximum Δv_{dc}^{pp} in a single-phase dc-link VSC coincides with the maximum value of an equivalent three-phase dc-link VSC (if the same C_d is considered per PEBB), as can be deducted from (4.6). This conclusion has already been drawn in the study by simulation of *subsection 2.4.2.4*.

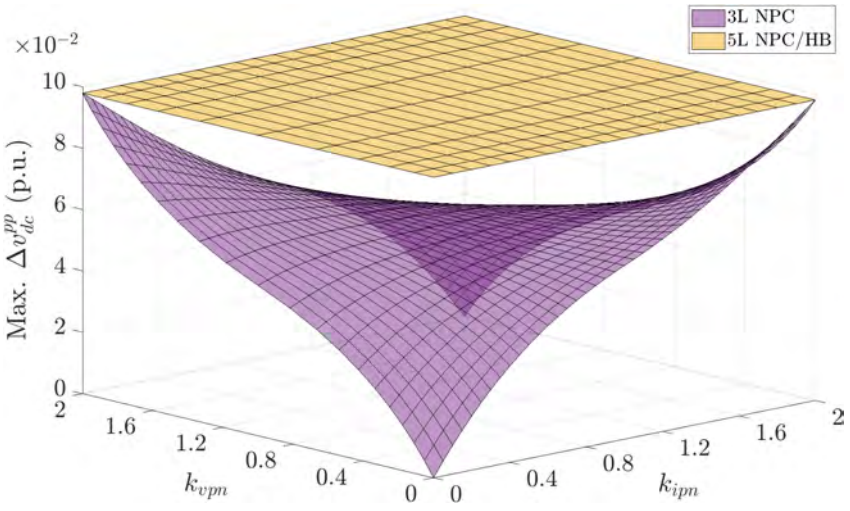

Fig. 4.18. Analytical maximum dc-link voltage ripple peak-to-peak value of 3L NPC and 5L NPC/HB STATCOMs at rated voltage and current as a function of k_{ipn} and k_{vpn}. Same dc-link capacitance is used per fundamental PEBB ($X_{C_{d\text{-}1\text{ph}}} = 2/3 \times X_{C_{d\text{-}3\text{ph}}}$).

Since there is no net energy exchange between the ac and the dc sides, the physical three-phase dc energy source can be avoided in the MMC for STATCOM application, as mentioned in *subsection 3.3.1.3*. That means that the sum of the circulating dc currents in the three phases naturally sums up to zero ($i_{dc} = i_{z\text{-a}} + i_{z\text{-b}} + i_{z\text{-c}} = 0$). It should be noted that the oscillating active power ($\tilde{p}$) makes that the circulating current presents naturally a 2ω component, regardless of whether there are negative-sequences (v^-, i^-) or not. If the 2ω circulating current is neglected, the conclusions drawn about the impact of the oscillating term $\tilde{p}$ in Δv_{dc}^{pp} for single-phase dc-link VSCs are applied to the MMC.

Summarizing, VSC STATCOMs with single-phase dc-links do not present any limitation so as to deal with $\tilde{p}$ under unbalanced conditions, while a current de-rating must be applied to structures with a three-phase dc-link in order to withstand or inject v^- and/or i^-. Identical conclusions from Fig. 4.18 would be drawn if any equivalent single- and three-phase dc-link VSC structures were compared.

4.3.2 Negative-Sequence Voltage and Current Effects on Average Active Power Distribution

As mentioned, the main aspect of the STATCOM application is that there is no need of any energy source, since, neglecting losses, the net active power exchange between the converter and the power grid is zero; i.e., $\bar{P}_{\text{a}} + \bar{P}_{\text{b}} + \bar{P}_{\text{c}} = 0$. From the per-phase instantaneous average active power of (4.7), it can be concluded that as long as there is no cross-interaction between positive- and negative-sequence components, the average active power which flows into each phase of the VSC STATCOM is also zero ($\bar{P}_{ph}^{++}, \bar{P}_{ph}^{--} = 0$).

$$\begin{aligned}\bar{P}_{ph} = &\underbrace{\frac{V^+I^+}{2}\cos\left(\delta_v^+ - \theta_i^+\right)}_{\bar{P}_{ph}^{++}} + \underbrace{\frac{V^-I^-}{2}\cos\left(\delta_v^- - \theta_i^-\right)}_{\bar{P}_{ph}^{--}} \\ &+ \underbrace{\frac{V^+I^-}{2}\cos\left(\delta_v^+ - \theta_i^- + k\frac{4\pi}{3}\right)}_{\bar{P}_{ph}^{+-}} + \underbrace{\frac{V^-I^+}{2}\cos\left(\delta_v^- - \theta_i^+ - k\frac{4\pi}{3}\right)}_{\bar{P}_{ph}^{-+}}\end{aligned} \tag{4.7}$$

However, under unbalanced current and/or voltage conditions terms $\bar{P}_{ph}^{+-}$ and/or $\bar{P}_{ph}^{-+}$ arise in (4.7), which are also different in each phase cluster. This means that each of the phases of the VSC might deliver or absorb an active power different from zero ($\bar{P}_{\mathrm{a}} \neq \bar{P}_{\mathrm{b}} \neq \bar{P}_{\mathrm{c}} \neq 0$).

Due to the fact that under unbalanced conditions the sum of $\bar{P}_{ph}^{+-}$ and/or $\bar{P}_{ph}^{-+}$ in the three phases is still zero ($\bar{P}_{\mathrm{a}} + \bar{P}_{\mathrm{b}} + \bar{P}_{\mathrm{c}} = 0$), structures with a three-phase dc-link, such as the 3L NPC, do not need any dc energy source for STATCOM application, whichever k_{vpn} and k_{ipn} are. That is the reason of removing the common three-phase dc-link in the MMC ($i_{dc} = 0$). In contrast, the phase clusters of single-phase dc-link VSC structures might deliver or absorb an active power different from zero ($\bar{P}_{\mathrm{a}} \neq \bar{P}_{\mathrm{b}} \neq \bar{P}_{\mathrm{c}} \neq 0$) under unbalanced operation, even in STATCOM applications. This can be seen in Fig. 4.19, which shows the evolution of the analytical maximum average active power in the three phase clusters ($\bar{P}_{ph}$) of a 5L NPC/HB topology for STATCOM application ($\phi^{+} = \pm 90°$), as a function of k_{ipn} (at the most restrictive θ_{ipn} case), and for different k_{vpn} values. As it is observed, the maximum $\bar{P}_{ph}$ is given when uniquely $\bar{P}_{ph}^{+-}$ or $\bar{P}_{ph}^{-+}$ exist; i.e., at $k_{vpn} = 0$ and $k_{ipn} = 2$, or at $k_{vpn} = 2$ and $k_{ipn} = 0$.

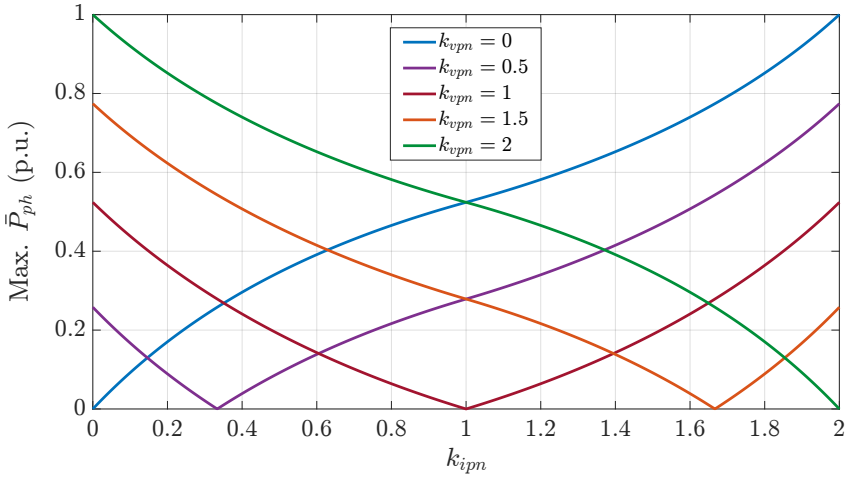

Fig. 4.19. Analytical maximum average active power of the 5L NPC/HB STATCOM at rated voltage and current as a function of k_{ipn} for different k_{vpn} scenarios.

For its part, Fig. 4.20 illustrates the evolution of the analytical maximum $\bar{P}_{ph}$ in the three phase clusters of the 5L NPC/HB STATCOM, and the three-phase average active power ($\bar{P}_{\mathrm{a}} + \bar{P}_{\mathrm{b}} + \bar{P}_{\mathrm{c}}$) in the 3L NPC STATCOM as a function of k_{ipn} and k_{vpn}. From both Figs. 4.19 and 4.20 can be deducted the current and voltage unbalances are analogous in their influence on the $\bar{P}_{ph}$ of a single-phase dc-link VSC. Besides, it can be seen that in three-phase dc-link structures the dc energy source is not needed for STATCOM application.

The lack of a common three-phase dc-link involves that countermeasures must be taken in order to correct the uneven active power distribution among the phase clusters in single-phase dc-link VSCs for STATCOM application. Otherwise, dc-link voltage balancing cannot be guaranteed when operating with negative-sequences, and dc voltages might drift away from their rated levels, as seen throughout the dissertation. As intercluster power balancing strategy, a fundamental-frequency zero-sequence voltage (v_0^{Y}) and current (i_0) are injected in the YCHB and DCHB, respectively. Both solutions have an impact on the power rating of the device, which have been quantified in *section 4.2*.

As studied in *subsection 3.3.1.3*, since terms $\bar{P}_{ph}^{+-}$ and $\bar{P}_{ph}^{-+}$ are cancelled out when added together in the three phase clusters of the MMC, the physical energy source connected to the common three-phase dc-link is also not needed to operate under v^{-} and/or i^{-} in STATCOM applications; i.e., $i_{dc} = 0$. However, the phase cluster active powers still differ from zero due to the cross-interaction between positive- and negative-sequence components.

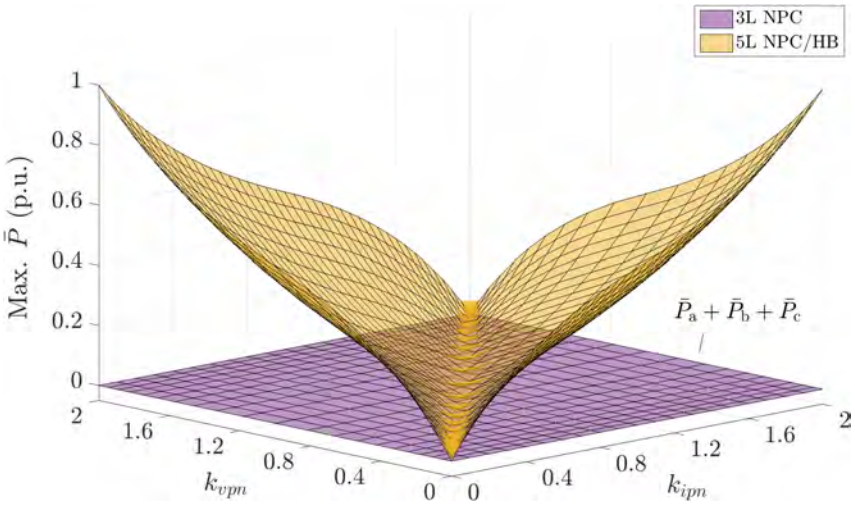

Fig. 4.20. Analytical maximum average active power of 3L NPC and 5L NPC/HB STATCOMs at rated voltage and current as a function of k_{ipn} and k_{vpn}.

In this scenario, as a result of the potential difference between the two sets of star-connected converters (V_{dc} in Fig. 2.14), a dc current circulates in each phase cluster of the MMC ($i_{z\text{-}ph}$). This current redistributes naturally the active power equally among the phase clusters, and maintains the charge of dc-link capacitors adjusted to the reference value. Nevertheless, this current, which recirculates in the dc side of the MMC, involves a reduction of the output ac current, with a consequent de-rating of the available Q^+.

In short, VSC structures with a common three-phase dc-link and without dc energy sources do not require any solution to deal with i^- and/or v^- for STATCOM due to the uneven active power distribution. On the contrary, single-phase dc-links of CHBs will have to absorb or deliver active power even at STATCOM application, so will require a solution which will have an impact on the available Q^+. Regarding the MMC, the circulation of a dc current under unbalanced conditions will also limit the Q^+ provided.

4.3.3 Reactive Power Limits

The presence of negative-sequence components (v^- and/or i^-) in STATCOM application has different effects depending on the dc-link configuration of the VSC. The countermeasures adopted so as to not exceeding the operational limits or remain connected to the PCC will have an impact on the power rating of the device. As explained above, from the STATCOM manufacturer dimensioning point of view, the reactive power is the indicative parameter to define the most suitable VSC structure for a certain scenario. Accordingly, this subsection quantifies and compares the Q^+ limits of the 3L NPC, YCHB, DCHB and MMC structures for STATCOM application operating with v^- and/or i^-.

If the 3L NPC and the MMC are added to the Q^+ limits of Fig. 4.8, as a function of k_{ipn}, at the most restrictive θ_{ipn}, and under balanced voltage conditions ($k_{vpn} = 0$), Fig. 4.21 is obtained. The theoretical maximum attainable Q^+ refers to the inner product between v^+ and i^+ at rated values. This limit is achieved with a three-phase dc-link VSC such as the 3L NPC, sized in such a way (C_d) that the dc voltage ripple peak to peak (Δv_{dc}^{pp}) does not exceed the limit value; which is given in $k_{vpn} = 0$ and $k_{ipn} = 2$, or in $k_{vpn} = 2$ and $k_{ipn} = 0$ (see Figs. 4.17 and Figs. 4.18). If the three-phase dc-link is sized with a lower capacitance ($C_d/2$ or $C_d/4$ with dashed lines in Fig. 4.21), there is a k_{ipn} point at which the Δv_{dc}^{pp} limit is reached, and hence a de-rating must be applied to the output ac current. As a result, the Q^+ limit begins to decrease (due to the reduction of i^+). This de-rating will be applied at lower k_{ipn} values as the dc-link capacitance is reduced.

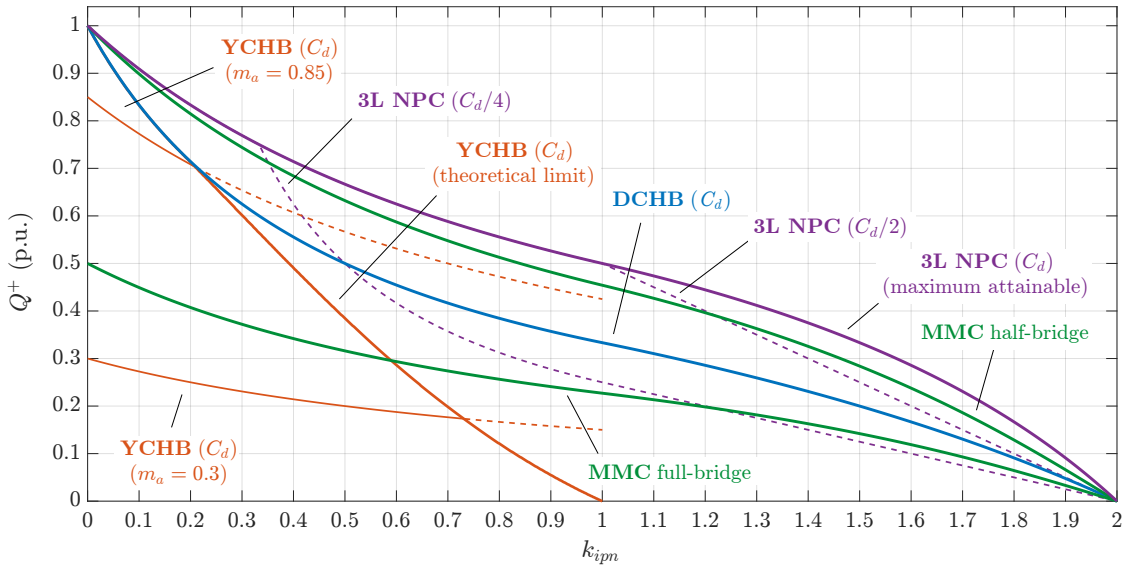

Fig. 4.21. Positive-sequence reactive power (Q^+) limits of YCHB (theoretical and real limits), DCHB, 3L NPC (for different C_d values), and MMC (with full- and half-bridge power cells) for STATCOM application as a function of k_{ipn} and for $k_{vpn} = 0$.

Both half-bridge and full-bridge configured MMC structures are shown in Fig. 4.21. The Q^+ limit of both configurations decrease when k_{ipn} increases due to the i^+ de-rating as a result of the increasing of the circulating dc current $i_{z\text{-}ph}$. That is to say, the difference between the maximum attainable Q^+ limit and the half-bridge MMC Q^+ limit is due to the dc current which circulates in each phase cluster of the MMC. Since the number of installed semiconductor devices is two times higher in the full-bridge than in the half-bridge, the Q^+ limit is reduced by half; to obtain the same output power, twice as many power electronic equipment is installed. However, the switching state redundancy and the fault tolerance are enhanced when using full-bridge power cells.

While in Fig. 4.21 there is no voltage unbalance ($k_{vpn} = 0$), in Fig. 4.22 (a), (b), and (c) the ratio k_{vpn} is set to 0.15, 0.3, and 0.45, respectively. It can be seen that as v^- increases, the YCHB can operate with higher k_{ipn} values. As mentioned, a remarcable drawback is that infinity V_0^{Y} is required in the operating point $k_{ipn} = 1$, regardless k_{vpn}. That means that beyond this point, the YCHB becomes uncontrollable in practical applications. It can be concluded that the capability of the YCHB STATCOM to operate under negative-sequences is strongly limited by the voltage rating of its phase clusters. Besides, Fig. 4.22 shows that the YCHB is more vulnerable to current unbalance than voltage unbalance.

As stated above, and in contrast with the YCHB, the DCHB does not present any limitation in terms of exceeding the rated voltage. That is why it can ensure the controllability of dc-link capacitor voltages guaranteeing the nominal ac voltage of the PCC up to $k_{ipn} = 2$. This is the major advantage of the delta over the star. However, the DCHB is more vulnerable to the voltage unbalance, as can be seen in Fig. 4.22. Moreover, it requires infinity I_0 in the operating point $k_{vpn} = 1$. At this singular point the DCHB becomes uncontrollable, and dc-link voltages would drift away; this is the only operating condition where the DCHB cannot operate. As demonstrated in [95], a duality exists between the voltage rating of the YCHB under unbalanced current conditions, and the current rating of the DCHB under unbalanced voltage conditions. It is noteworthy that the condition of singularity for the DCHB ($k_{vpn} = 1$) is less likely to occur in practice than the condition for the YCHB ($k_{ipn} = 1$), which makes the delta configuration more interesting for STATCOM applications and operation under negative-sequences.

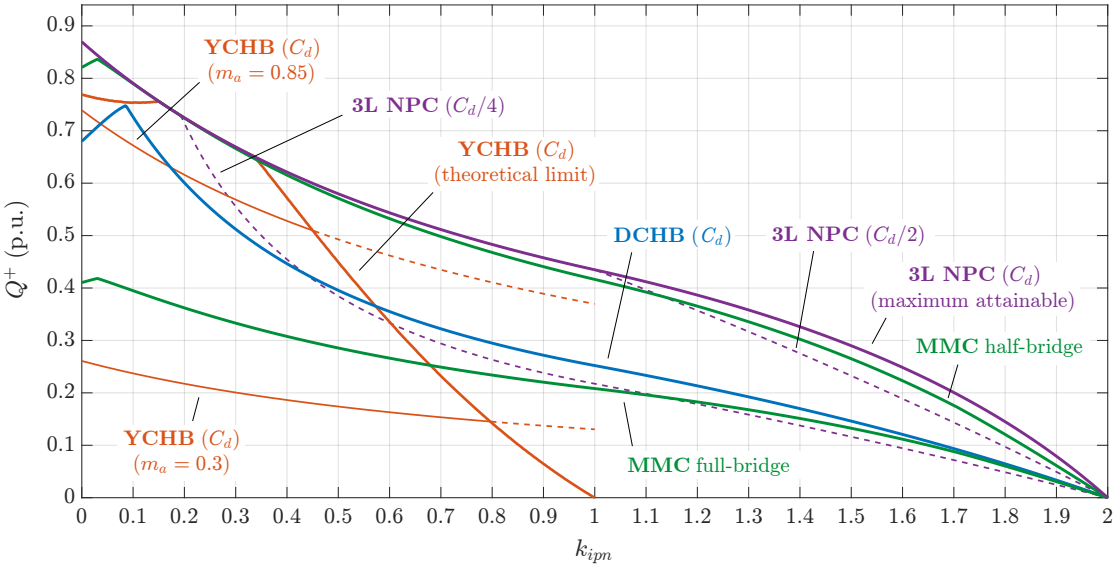

(a)

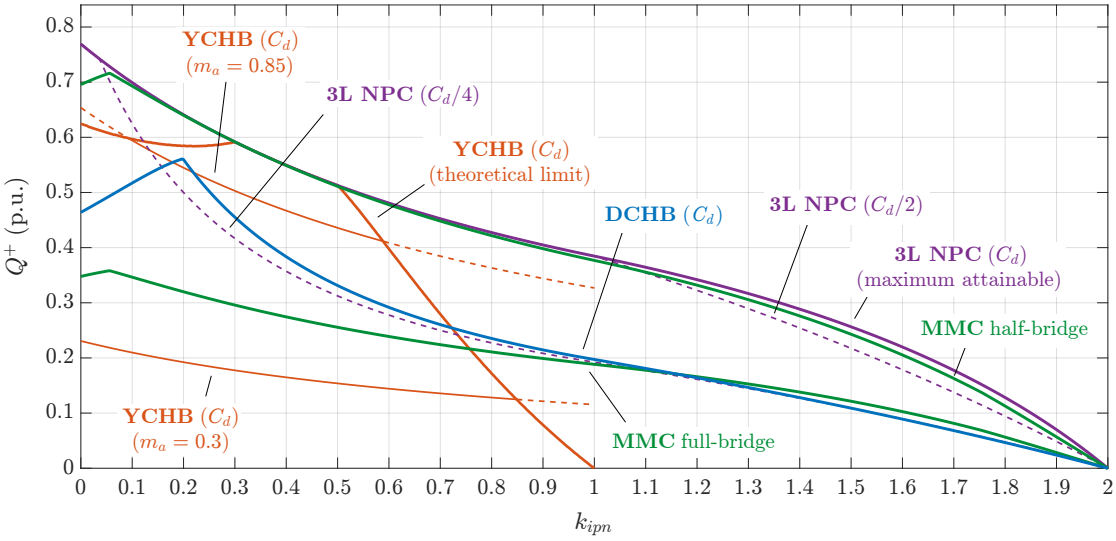

(b)

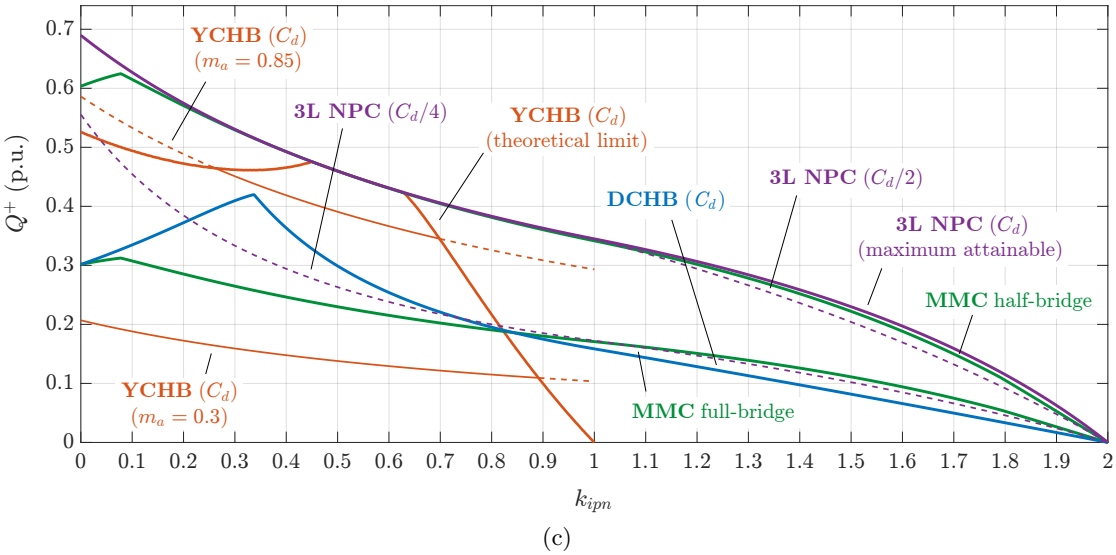

(c)

Fig. 4.22. Positive-sequence reactive power (Q^+) limits of YCHB (theoretical and real limits), DCHB, 3L NPC (for different C_d values), and MMC (with full- and half-bridge power cells) for STATCOM application as a function of k_{ipn}. (a) $k_{vpn} = 0.15$, (b) $k_{vpn} = 0.3$, and (c) $k_{vpn} = 0.45$.

4.4 CONCLUSIONS

When applications where no dc energy sources are needed, such as the STATCOM, are faced with unbalanced conditions, the cross-interaction between positive- and negative-sequence voltage and current components in the ac side have an influence on the dc side of the VSC. This chapter has evaluated this effect in different VSC topologies, which has permitted to quantify the available Q^+ and to compare the limitations presented by each of them.

Firstly, the YCHB and the DCHB configurations have been compared in a negative-sequence current withstanding scenario; being $v^- = 0$ in the terminals of the VSC-based STATCOM. In this particular scenario, the conclusions drawn have confirmed the DCHB as the preferable option to the YCHB for STATCOM application dealing with severe unbalanced current conditions. While the YCHB is strongly limited by the available dc-side voltage, the DCHB can stay connected to the PCC regardless of the i^- to withstand. It is worth mentioning that this study has been validated by experimental results in a real-scale set-up of a MV laboratory.

Secondly, the 3L NPC and the MMC have been included in the analysis, including also v^- in the comparison of the Q^+ limits. It has been demonstrated that the 3L NPC with a correctly dimensioned dc-link (C_d) can be the most interesting solution for STATCOM operating under unbalanced voltage and/or current conditions. However, it is not as easy as in cascaded/modular structures to reach high power – MV levels. The properly dimensioned half-bridge MMC can be the solution to this problem; the drawback of this is its control implementation. Regarding CHB configurations, the DCHB is still a very promising alternative, although under unbalanced voltage conditions the advantages over the YCHB are not so significant. It should also be noted that this last study could not be verified experimentally due to lack of resources.

After this study, it has been observed that the control implementation of the intercluster active power balancing strategy has not been studied extensively. Especially in the case of the DCHB, where small number of alternatives which deal with the zero-sequence current control loop can be found in the specialized literature. Besides, there is no source which analyzes the requirements that the regulator G in Fig. 4.6 has to fulfill considering the features of this particular system, nor which control method is the most appropriate. Accordingly, the next chapter analyzes and identifies the particularities of that system, in order to determine the requirements to be fulfilled by the implemented controller and hence be able to design it.

Chapter 5

ZERO-SEQUENCE CONTROLLER REQUIREMENTS AND COMPARISON FOR A DCHB STATCOM UNDER UNBALANCED OPERATION

Zero-sequence current needs to be injected to guarantee dc-link capacitor voltage balancing in the DCHB STATCOM when operating under unbalanced voltage and/or current conditions. The control loop of this zero-sequence current is analyzed in this chapter. The control loop of this zero-sequence current is analyzed in this chapter, in order to determine the requirements that the implemented controller must fulfill. Considering these requirements, appropriate transient response and stability margin indicators are defined to quantify and evaluate the performance of different controllers that could be employed —Proportional-Resonant controller (PR), PR controller with delay compensation (PR_d), and Vector Proportional-Integral controller (VPI) are proposed. Based on the defined indicators a comparison of the controllers is presented, and experimental results validate the analytical model of the controllers and their performance. This analysis resulted in publication [J3].

5.1 INTRODUCTION

In CHB-based STATCOMs operating with v^- and/or i^- the intercluster active power balancing strategy guarantees an equal active power distribution among phase clusters. In the YCHB, it is commonly addressed by injecting a zero-sequence voltage, while a zero-sequence current can be added in the case of the DCHB [95], [118]. As analyzed and quantified in *Chapter 4*, both have an impact on the power rating of the device, which will limit the capabilities of the STATCOM to provide Q^+ [56], [59]. Since the YCHB is strongly limited by the available dc-side voltage, the DCHB is the preferable option for STATCOM application dealing with unbalanced conditions [56], [59], [95], [96], [121].

References [56], [95], [96], [99], [118], [121], [136], [140], [141], [145], [161], [174], [193] present different alternatives to perform the intercluster power balancing in the DCHB, which require a controller to track the zero-sequence current (i_0^*). Studies [95], [96], [136], [161] have implemented a Proportional controller, and [145] a Proportional-Integral (PI) one. Nevertheless, these controllers cause a steady-state error when tracking alternating signals. In [56], [141], [174], [193] a Proportional-Resonant (PR) controller is used. This PR controller guarantees a zero steady-state error [194]–[196]. However, none of these references analyzes which are the requirements that the controller has to fulfill considering the features of this particular system, nor which control technique is the most adequate.

This chapter aims to analyze and identify the particularities of the zero-sequence current control loop in a DCHB STATCOM operating with v^- and/or i^-, in order to determine the most important requirements to be fulfilled by the implemented controller and thus be able to design it. Considering these requirements, appropriate transient response and stability margin indicators are defined to quantify and evaluate the performance of the controllers. Some resonant controllers which are suitable for this loop are compared; apart from the aforementioned PR controller, the PR with delay compensation ($\mathrm{PR_d}$) [197], [198], and the Vector Proportional-Integral (VPI) [199]–[201] are also considered. Both could also be suitable to track i_0^*, but have not been previously proposed for this application. Finally, the delta-configured real-scale experimental set-up of 100 kVA explained in *subsection 4.2.4* is used in order to validate the analytical model of the controllers and their performance.

5.2 CONTROLLERS FOR THE ZERO-SEQUENCE CURRENT LOOP

As mentioned in *section 4.2*, the equality of the three-phase dc-link voltages is guaranteed by the intercluster active power balancing control (see Fig. 5.1). The required i_0^* is calculated from (3.18) and (3.19) with the constant terms in (4.5), according to the power disturbances in each phase cluster ($\bar{P}^*_{dis\text{-}ph}$) generated by the intercluster dc voltage control. In order to redistribute the active power equally among phase clusters, a zero-sequence voltage ($v_0^{\Delta *}$) needs to be generated, which is added to the dual vector control output voltage references ($v^*_{\mathrm{ab}}, v^*_{\mathrm{bc}}, v^*_{\mathrm{ca}}$), and will lead to the calculated i_0^* reference [95].

Several studies have used the zero-sequence current injection in the DCHB STATCOM to operate with v^- and/or i^- [56], [95], [96], [99], [118], [121], [136], [141], [145], [161], [174], [193]. Some of these have used a proportional controller as G in Fig. 5.1 to track the fundamental-frequency reference i_0^* [95], [96], [136], [161], while in [145] a PI control is used. However, based on classical control theories [202], the closed-loop frequency response of a PI regulator shows that it is not possible to guarantee a zero steady-state error when controlling alternating signals; and even less with a proportional controller. In other words, there will be an unavoidable steady-state error in both the calculated amplitude I_0^* and the phase $\theta^*_{i_0}$. The impossibility to track properly i_0^* might make that the active power will

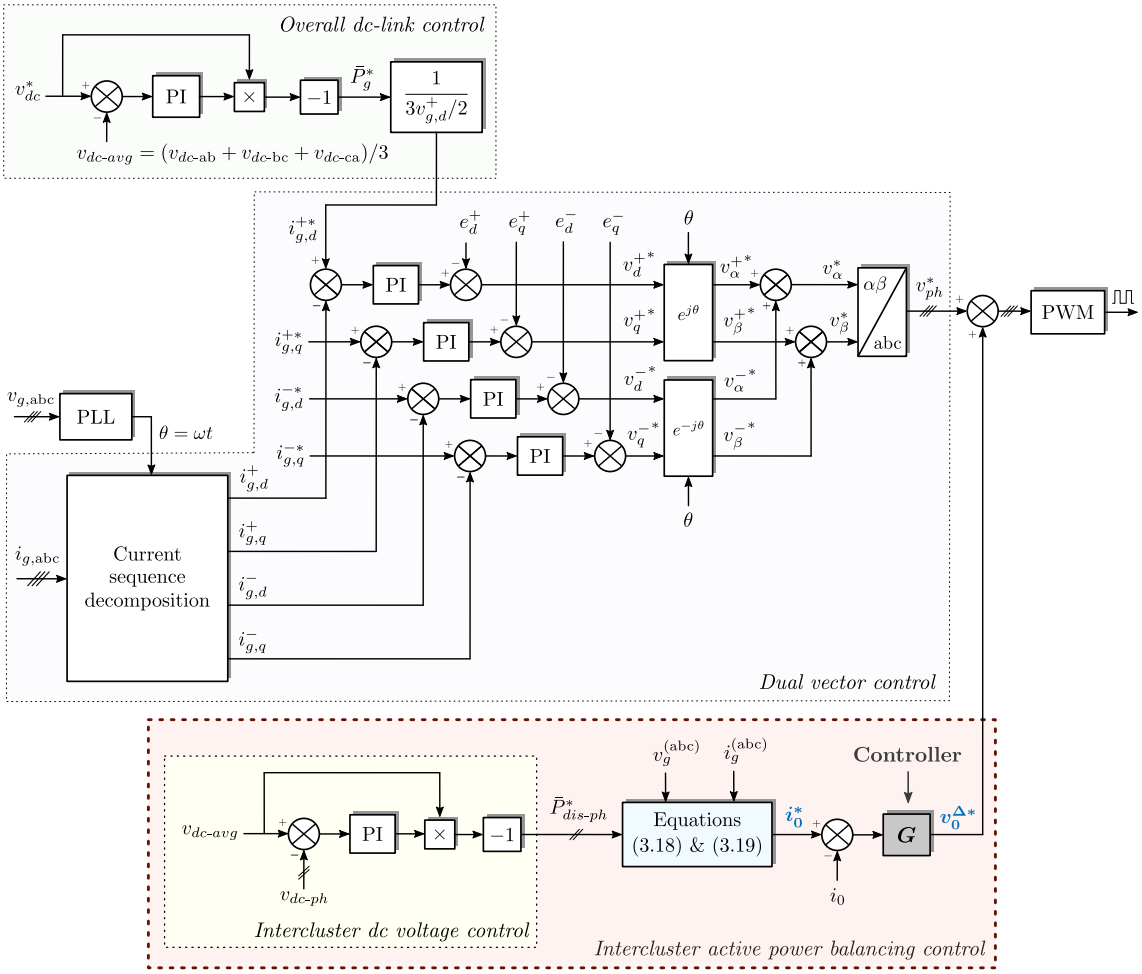

Fig. 5.1. Simplified block diagram of the overall control design of the DCHB STATCOM to operate with v^- and/or i^-.

not be redistributed equally among phase clusters, and it might lead to dc-link capacitor voltage drifting. Some studies have added a PR controller [56], [141], [174], [193], which is a better alternative than the previous ones since it is capable of tracking i_0^* with a zero steady-state error. As seen, small number of alternatives which deal with the zero-sequence current control loop of the DCHB STATCOM can be found in the specialized literature. Besides, there is no source which analyzes the requirements that the controller has to fulfill considering the features of this particular system, nor which control technique is the most appropriate.

Although the PI is one of the most established control techniques in many applications, its utilization to track sinusoidal signals is limited. PI controllers in stationary frame involve a considerable steady-state error, since they only guarantee a perfect tracking of the reference at 0 Hz [201]. Note that by implementing two independent PI controllers separetely at the same time, one for the amplitude I_0^* and one for the angle $\theta_{i_0}^*$, the reference i_0^* could be controlled with zero steady-state error. A resonant controller is equivalent to the latter, with an important saving of computational burden due to the reduction in the number of regulators [194]–[196]. Although the PR is the only resonant controller that has been used in the literature for the i_0 control loop in a DCHB [56], [141], [174], other controllers of this family such as the PR with delay compensation ($\mathrm{PR_d}$), and the Vector Proportional-Integral (VPI) are analyzed and compared in this chapter, which could be suitable for the system under study.

– *PR controller*
The s-domain transfer function of a PR controller can be expressed as [195], [196]

$$G_{\mathrm{PR}}(s) = K_p + \frac{K_i s}{s^2 + \omega_0^2} \tag{5.1}$$

being K_p and K_i the proportional and integral gains, and ω_0 the resonant angular frequency. $G_{\mathrm{PR}}(s)$ provides infinite gain in open-loop at the resonant frequency ($f_0 = \omega_0/2\pi$), and thus unity gain and zero phase-shift in closed-loop; this ensures zero steady-state error when tracking any signal pulsating at ω_0 [201].

– *PR controller with delay compensation*
In real systems, the computation or the implemented modulation scheme generate a delay which affects the system performance and might cause instability. Therefore, a delay compensation can be added to the PR controller in (5.1), whose resulting transfer function in the s domain can be expressed as [197]

$$G_{\mathrm{PR_d}}(s) = K_p + \frac{K_i\Big(s\cos(\phi) - \omega_0 \sin(\phi)\Big)}{s^2 + \omega_0^2} \tag{5.2}$$

where ϕ is the phase lead introduced in the vicinity of ω_0; i.e., the difference between the actual phase provided by the real controller at frequencies infinitely close to f_0 and that provided by $G_{\mathrm{PR}}(s)$. In order to compensate for n_{d} number of sampling periods, $\phi = n_{\mathrm{d}}\omega_0 T_s$ should be applied, being T_s the sampling period. Normally, $n_{\mathrm{d}} = 1.5 - 2$ is often considered [198], depending on the modulation technique used. The delay compensation becomes more crucial as ω_0 increases with respect to the sampling angular frequency (ω_s) [201]; e.g., in MV power converters which operate at low f_s.

– *VPI controller*
When employing resonant controllers, undesired peaks might appear around f_0 in closed-loop, mainly because of the terms of the plant not compensated by $G_{\mathrm{PR}}(s)$. This bad performance is aggravated when the frequency (f) deviates from its expected value (f_0) [201]. Lascu *et al.* proposed an alternative resonant regulator to PR ones, known as Vector Proportional-Integral (VPI) controller [199], [200]:

$$G_{\mathrm{VPI}}(s) = \frac{K_p s^2}{s^2 + \omega_0^2} + \frac{K_i s}{s^2 + \omega_0^2} \tag{5.3}$$

The aim of this regulator is the cancellation of the pole of any plant with the form of $G_{\mathrm{PL}}(s) = 1/(L_f s + R_f)$, being L_f and R_f the inductance and its resistive value. Note that this is the form of the plant of the zero-sequence current control loop under study. The plant pole cancellation is achieved by maintaining the relationship $K_i/K_p = R_f/L_f$, obtaining

$$G_{\mathrm{VPI}}(s) = \frac{K_h s(L_f s + R_f)}{s^2 + \omega_0^2} \tag{5.4}$$

where $K_h = K_p/L_f$. By doing so, and neglecting the effects of the computational delay or the modulation, the plant pole is cancelled by one of the zeros of the VPI regulator, resulting in the following simplified open-loop transfer function [201]:

$$G_{\mathrm{VPI}}(s)\, G_{\mathrm{PL}}(s) = \frac{K_h s}{s^2 + \omega_0^2} \tag{5.5}$$

In practice, due to system non-idealities and the effect of the temperature, the estimation of the plant (L_f and R_f) is not straightforward. As a consequence, and accompanied with unavoidable calculation errors, the plant pole cancellation is complicated in practical applications. However, it has been proven that the non-cancellation of the plant pole have little influence on the stability margins, transient response, and parameter tuning of the VPI controller [200], [203]. Besides, the fact that the zero-sequence plant is not as variable as the grid-equivalent, makes the VPI an interesting alternative, which its utilization has not been proposed for the system under study.

Fig. 5.2 (a) shows the closed-loop s-domain pole-zero map of each resonant controller and a LR plant $G_{\mathrm{PL}}(s)$, whose transfer functions are shown in Table 5.1. Both the PR and $\mathrm{PR_d}$ have a complex conjugate pole pair $p_1{-}p_2$, a complex conjugate zero pair $z_1{-}z_2$, and a real pole p_3. For its part, the plant pole cancellation causes the VPI to have one pole and one zero less. As can be seen, the complex conjugate pole pair of the VPI has greater damping ratio ($\zeta \uparrow$) than the PR and $\mathrm{PR_d}$ ones, which makes the VPI have a much damper and less oscillating response than common regulators. Regarding the $\mathrm{PR_d}$, Fig. 5.2 (a) shows that the position of the poles and zeros is similar with respect to the PR when tracking fundamental-frequency signals.

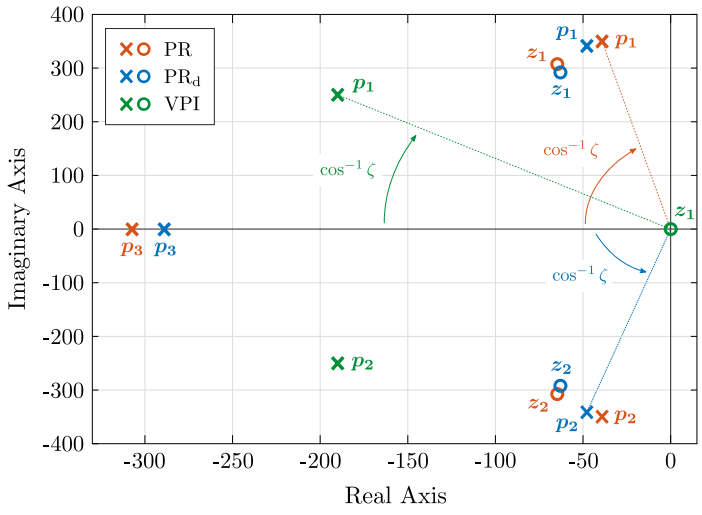

(a)

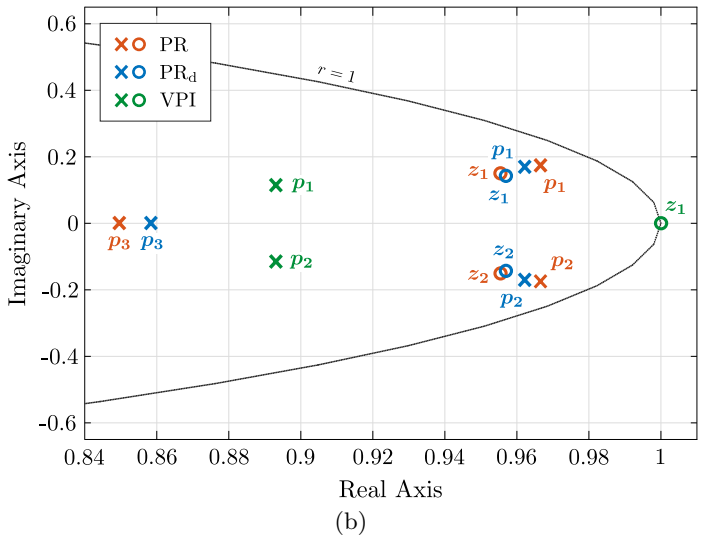

(b)

Fig. 5.2. Closed-loop (C_L) pole-zero map of each controller tuned at $\omega_0 = 50\,\mathrm{Hz}$. (a) s-domain, and (b) z-domain with ZOH technique. K_p and K_i are 0.95 and 123 for the PR and $\mathrm{PR_d}$, and 0.95 and 5.7 for the VPI. L_f and R_f of the plant are 2.5 mH and 15 mΩ, respectively, while T_s is 500 μs.

Table 5.1. Closed-loop s-domain transfer functions of each resonant controller.

	$C_{\mathrm{L}}(s) = \dfrac{G(s)\,G_{\mathrm{PL}}(s)}{1+G(s)\,G_{\mathrm{PL}}(s)}$
PR	$\dfrac{K_p s^2 + K_i s + K_p\omega_0^2}{L_f s^3 + (R_f+K_p)s^2 + (L_f\omega_0^2 + K_i)s + (R_f+K_p)\omega_0^2}$
PR$_\mathrm{d}$	$\dfrac{K_p s^2 + K_i s\cos\phi + K_p\omega_0^2 - K_i\omega_0\sin\phi}{L_f s^3 + (R_f+K_p)s^2 + (L_f\omega_0^2 + K_i\cos\phi)s + (R_f+K_p)\omega_0^2 - K_i\omega_0\sin\phi}$
VPI	$\dfrac{K_p s^2 + K_i s}{L_f s^3 + (R_f+K_p)s^2 + (L_f\omega_0^2 + K_i)s + R_f\omega_0^2} \xrightarrow{K_i/K_p = R_f/L_f} \dfrac{K_h s}{s^2 + K_h s + \omega_0^2}$

Both $G_{\mathrm{PR_d}}(s)$ and $G_{\mathrm{VPI}}(s)$ permit to reduce anomalous peaks in the closed-loop frequency response with respect to $G_{\mathrm{PR}}(s)$, providing higher stability margins [201]. An important advantage of $G_{\mathrm{VPI}}(s)$ is that it offers more damped response than $G_{\mathrm{PR}}(s)$ and $G_{\mathrm{PR_d}}(s)$ [204], [205]. Besides, $G_{\mathrm{VPI}}(s)$ only requires the delay compensation for very high-order harmonics [200], being in these cases $G_{\mathrm{PR_d}}(s)$ a preferable option [203].

Any controller expressed in the s domain has to be discretized to the z domain to be implemented in digital devices. Due to their selectivity and hence the dependance on the accuracy at ω_0 [201], resonant controllers are especially sensitive to the discretization process. Inaccuracies such as displacement of poles, or influence on the delay compensation effectivity, might result in significant loss of performance, especially for tracking high frequency signals; the non-infinite gain at the expected frequency does not assure zero steady-state error, and might compromise stability. That is the reason why the VPI is often optimized by a combination of the most adequate discrete-time implementations for each resonant term in (5.3). Nevertheless, it has been proven that the discretization method has no influence when tracking fundamental-frequency (such as i_0^*) and low-order harmonic references. Consequently, although it is not the most popular method in digital controller design since it has many drawbacks [203], for simplicity and for the comparison to be fair, the regulators have been discretized with the same method: Zero-Order Hold (ZOH). The three resonant controllers under study share the z-domain transfer function in (5.6), each of them having different coefficients in the numerator, collected in Table 5.2.

$$G(z) = \frac{a_0 + a_1 z^{-1} + a_2 z^{-2}}{1 - 2z^{-1}\cos(\omega_0 T_s) + z^{-2}} \tag{5.6}$$

Fig. 5.2 (b) also shows the closed-loop z-domain pole-zero map of each resonant controller and the plant $G_{\mathrm{PL}}(z)$, using the ZOH method and a 500 μs sampling period (T_s).

Table 5.2. Numerator coefficients of the z-domain transfer functions of the resonant controllers using the ZOH method.

	a_0	a_1	a_2
PR	K_p	$\dfrac{K_i}{\omega_0}\sin(\omega_0 T_s) - 2K_p\cos(\omega_0 T_s)$	$K_p - \dfrac{K_i}{\omega_0}\sin(\omega_0 T_s)$
PR$_\mathrm{d}$	K_p	$\dfrac{K_i}{\omega_0}\Big(\sin(\omega_0 T_s + \phi) - \sin\phi\Big) - 2K_p\cos(\omega_0 T_s)$	$K_p - \dfrac{K_i}{\omega_0}\Big(\sin(\omega_0 T_s - \phi) + \sin\phi\Big)$
VPI	K_p	$\dfrac{K_i}{\omega_0}\sin(\omega_0 T_s) - K_p\Big(\cos(\omega_0 T_s) + 1\Big)$	$K_p\cos(\omega_0 T_s) - \dfrac{K_i}{\omega_0}\sin(\omega_0 T_s)$

5.3 SYSTEM REQUIREMENTS

5.3.1 System Description

The z-domain closed-loop diagram of this particular system is shown in Fig. 5.3, which is based on the experimental set-up of *section 5.5*.

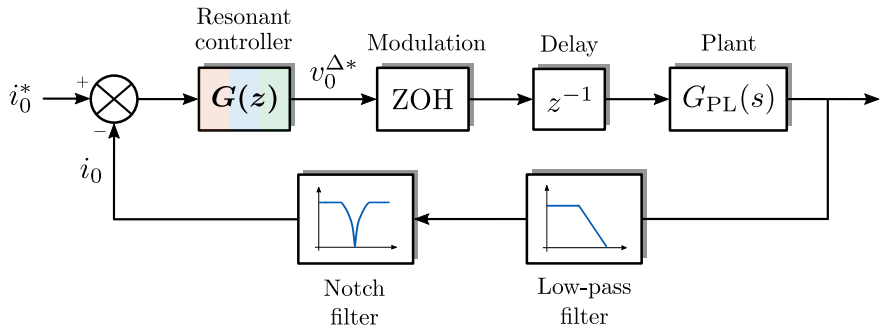

Fig. 5.3. Block diagram of the zero-sequence current control loop model.

The system analytical model is composed of the following blocks:

– $G(z)$ represents the discrete-domain resonant controller (either PR, $\mathrm{PR_d}$ or VPI controllers), which tracks the reference i_0^*, tuned at $\omega_0 = \omega$.

– A ZOH block models the used Space Vector Modulation (SVM).

– z^{-1} models the one sample computational delay.

– The zero-sequence LR plant inside the delta. Its s-domain transfer function is derived as follows, assuming the same L_f and R_f in the three phase clusters:

$$\begin{aligned} 3v_0(t) = 3L_f\frac{di_0(t)}{dt} + 3R_f i_0(t) \;\; \rightarrow \;\; v_0 = L_f i_0 s + R_f i_0 \\ G_{\mathrm{PL}}(s) = \frac{i_0}{v_0} = \frac{1}{L_f s + R_f} \end{aligned} \tag{5.7}$$

By discretizing the plant also with the ZOH method, the effect of the used SVM is already considered; i.e., a half of a sample delay [201], [206].

– The measured three-phase currents are filtered by a first-order low-pass filter, being ω_c the cut-off frequency:

$$H_{\mathrm{lpf}}(s) = \frac{1}{s + \omega_c} \tag{5.8}$$

– In order to guarantee that both upper and lower switches in the power cell leg never conduct simultaneously, dead times are introduced, especially in high power converters such as the one in this study. These dead times might generate a zero-sequence third-order harmonic (3ω) component [207]–[209], which can circulate within the delta-connected clusters. As a consequence, the 3ω component will appear in the zero-sequence current measurement added to the fundamental one. Fig. 5.4 shows the simulated zero-sequence current measurement in the experimental set-up of *section 5.5* with 7.5 μs dead times introduced, in which the weight of 3ω can be clearly appreciated. With the aim of preventing this component from being coupled with the controller response (so that does not affect the assumed active power distribution in the

calculation of i_0^*), the system must be able to attenuate it. The specialized literature makes no mention about this problem in DCHB STATCOMs, but the authors have experimentally verified that this 3ω component might generate instabilities in the control loop. Thus, the author recommends adding a notch filter tuned at $\omega_n = 3\omega$ to the measured zero-sequence current (see Fig. 5.3). The s-domain transfer function of the notch filter can be expressed as

$$H_{\text{notch}}(s) = \frac{s^2 + \omega_n^2}{s^2 + 2\zeta\omega_n s + \omega_n^2} \tag{5.9}$$

being ω_n the notch frequency, and ζ the damping ratio. It should be noted that the notch filter has been discretized using the *Tustin's Trapezoid* method, since it is with this technique that the frequency response most similar to that of the filter in the s domain is achieved [203].

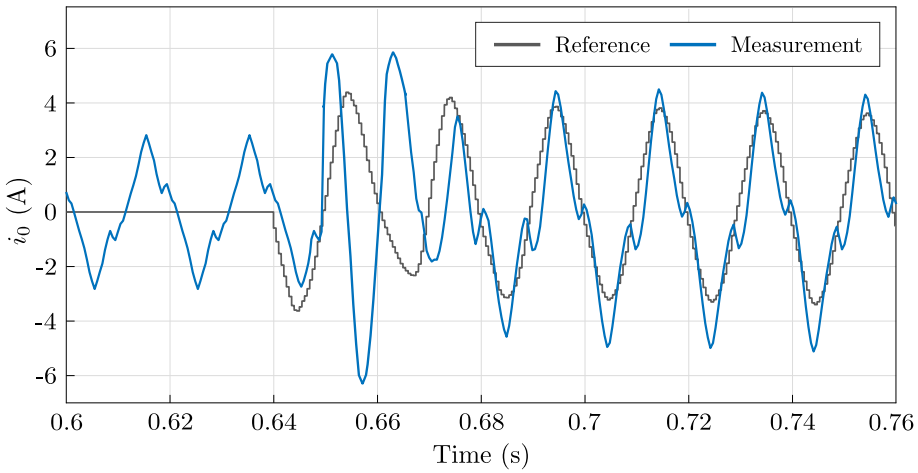

Fig. 5.4. Presence of the 3ω component in the simulated zero-sequence current measurement due to the introduced 7.5 μs dead times.

5.3.2 Requirements and Indicators

Considering the particularities of the closed-loop system model of Fig. 5.3, the aim is to identify the most important requirements to be fulfilled by the implemented controller. This requirements are quantified and evaluated by means of some indicators, which are obtained through the system time response, frequency response Bode diagrams, and z-domain pole-zero map analysis. Then, controllers will be compared based on these indicators.

5.3.2.1 *Speed of response*

Converter inner loops like the one under study have to be fast enough for the outer loops to be effective. This system requires the controller to be fast so that the dc-link voltages do not drift away from their reference value. The indicator used to measure the system speed of response is the settling time (t_{set}), which corresponds to the time needed to reach the final value of the reference. The position of the poles and zeros determines the transient response of the system. t_{set} is determined by the pole with the biggest module in the z domain, not having a zero nearby that tends to cancel its effect; this is called *dominant pole*. The dominant pole presents the smallest decay rate (λ) at the time-domain response, being A the residue and $Ae^{-\lambda t}$ the exponentially decaying component corresponding to that pole. Its time constant (τ) is determined by the pole location as

$$\tau = \frac{1}{\lambda} = \frac{-T_s}{\ln r} \tag{5.10}$$

where r is the module of the dominant pole, and t_{set} corresponds to 3τ. Thus, dominant poles will be the ones whose effect needs more time to be extinguished during transients (slowly decaying components); i.e., the bigger the module of the dominant pole ($r \uparrow$), the slower the system ($t_{\text{set}} \uparrow$). The transient response can be optimized by making poles fast ($\lambda \uparrow$ and $r \downarrow$), and by placing them next to zeros that cancel their effect ($A \downarrow$) [204].

Dominant poles are also the ones that are closer to the instability limit circle ($r = 1$ in the z-domain pole-zero map). Therefore, by setting the dominant poles within a desired module (keeping $r < 1$ to guarantee the stability), in addition to defining t_{set}, the stability margin is also determined [210]. The dominant pole corresponds to the closed-loop

$$C_{\text{L}}(z) = \frac{G(z)\, z^{-1}\, G_{\text{PL}}(z)}{1 + D_{\text{L}}(z)} \tag{5.11}$$

being the direct-loop the following:

$$D_{\text{L}}(z) = G(z)\, z^{-1}\, G_{\text{PL}}(z)\, H_{\text{lpf}}(z)\, H_{\text{notch}}(z) \tag{5.12}$$

5.3.2.2 *Third-order harmonic attenuation*

As mentioned, the zero-sequence control loop under study is vulnerable to the 3ω component in the zero-sequence current measurement, especially in high power applications. The added z-domain notch filter will attenuate this component, but it will not eliminate it completely, so one of the main requirements of the resonant controller is to mitigate it as much as possible. The indicator to quantify this requirement is the magnitude at 3ω of the system direct-loop $D_{\text{L}}(z)$ frequency response.

5.3.2.3 *Overshoot or peak value during transients*

High i_0 overshoot values could lead the current exceeding the rated level of semiconductor devices. The overshoot for an alternating signal input depends also on the phase of the reference at the instant when the transient occurs [211], being the zero-crossing of i_0^* the most favorable case (min. overshoot), and the peak-crossing the most unfavorable (max. overshoot). Both cases are distinguished, which are obtained calculating the system time

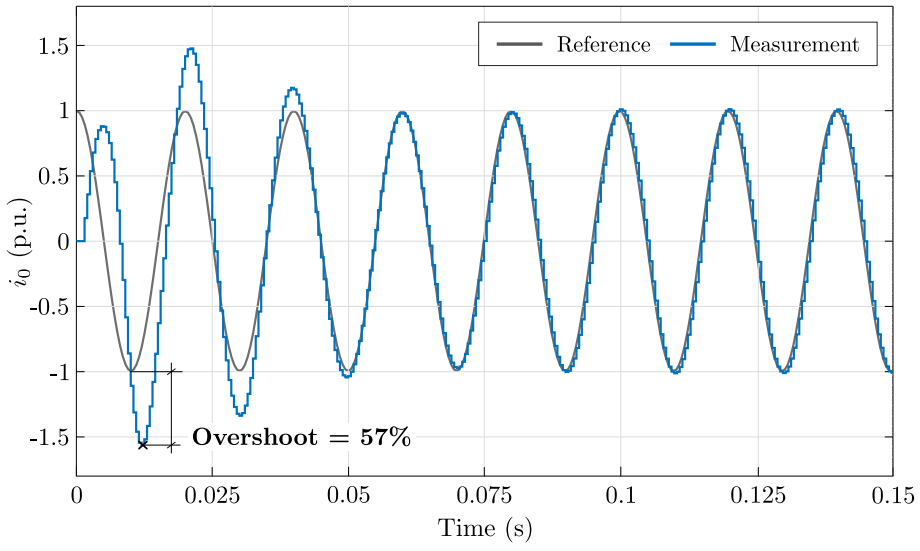

Fig. 5.5. Reference peak-crossing overshoot calculation.

response maximum amplitude with respect to the reference amplitude, as the example in Fig. 5.5 shows.

5.3.2.4 *Robustness in the face of the uncertainty of plant parameters*

It is important for a system to remain stable even if the parameters of the plant vary. This work proposes the use of a single indicator to evaluate the stability margin (robustness) of the system in the face of the uncertainty of L_f and R_f [210], [212]. The uncertainty refers to the deviation of this parameters with respect to the nominal values used to design the controller. The indicator to measure the robustness proposed by the authors is the sensitivity, which quantifies the percentage of the closed-loop systems with unstable poles ($r > 1$) obtained for a certain deviation of the plant parameters (see example of Fig. 5.6). For the calculation of the sensitivity, a deviation of $\pm 20\%$ with an increment of 2% has been considered for L_f, and -50% to $+100\%$ with an increment of 10% for R_f (see Table 5.4). A sweep of all these values (338 systems in total) allows quantifying how many of these are unstable systems.

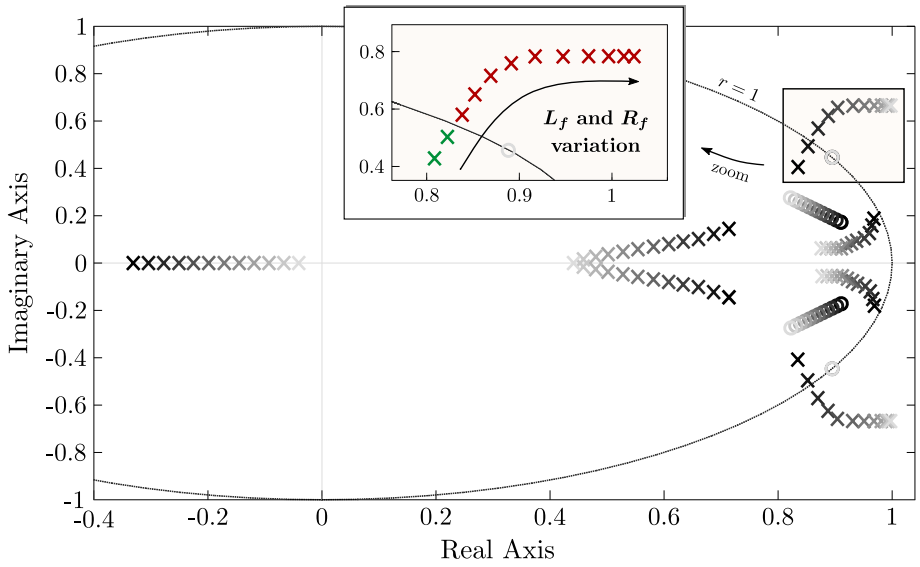

Fig. 5.6. Sensitivity to become unstable due to poles displacement in the face of plant parameters (L_f and R_f) variation. In this example where 10 systems are unstable (red poles) and 2 systems stable (green poles), the sensitivity is $10/(10+2) = 83.\hat{3}\%$.

5.3.3 Indicator Normalization

In order to compare controllers, the calculated indicators should be normalized. The base values are chosen considering the elements and characteristics of the system; in this case, the experimental set-up used in *section 5.5* to validate the theoretical study. The proposed criteria for calculating the base values are the following:

- t_{set} is normalized to three times the time constant of the plant ($3\tau_f = 3L_f/R_f$).
- The base value of the amplification of the 3ω component is set to 0.2 p.u. This value has been chosen empirically because the authors have experimentally verified that above this value this system might present stability problems.
- Assuming the capacity to withstand transitory overloads in an air-cooled VSC, both 0- and peak-crossing overshoot values are normalized to 50%. This value can be increased with water-cooled power converters.

– The values of the sensitivity are normalized to 50%.

Considering these criteria, the base values used are collected in Table 5.4.

5.3.4 Multi-Objective Controller Parameter Selection

In this work, the tuning of the controllers is carried out based on the defined indicators. To choose a suitable combination of the parameters K_p and K_i in each controller, as a first step, the stability of the system is analyzed in order to identify the range of values in which the system is stable. Within this valid range of values, a sweep of K_p and K_i is performed, and the normalized values of the defined indicators are calculated at each point.

The proposed multi-objective controller parameter selection method is based on giving a weight to each indicator, and finds a certain combination of K_p and K_i depending on the criteria used to fulfill the requirements of the system. That is, the values of K_p and K_i which obtain the minimum of the sum of all indicators with the corresponding weighting.

5.4 CONTROLLER COMPARISON

An important feature of MV STATCOMs is that they operate at relatively low switching frequencies (around 1 kHz), where the w_s/w ratio is not so large. However, $G_{\mathrm{PR_d}}(s)$ and $G_{\mathrm{VPI}}(s)$ present more advantages with respect to $G_{\mathrm{PR}}(s)$ as the ratio w_s/w_0 increases [201], so quantifying how much better they are for the system under study is a fair approach; even more considering the lack of studies which compare them.

The comparison between PR, $\mathrm{PR_d}$ and VPI controllers in the system under study is presented by means of spider charts in Fig. 5.4. In these, the values of the indicators of each controller are shown for six different tuning criteria. First, controllers are compared in the so-called *balanced tuning*, where the same priority (weighting) is given to all the indicators; i.e., a weight of 20% for each indicator. The other five tuning criteria prioritize the minimization of one indicator; e.g., aim a fast transient response ($t_{\mathrm{set}} \downarrow$), or a great stability margin (sensitivity $\downarrow$). In this case, the highest weighting is given to the target indicator: 98%, and 0.5% to the other four indicators.

As the aim is to minimize the indicators, the controller with the smallest area is the most suitable. Note that each spider chart should be analyzed separately, since the scaling of the axes is different in each of them. Table 5.3 collects the K_p and K_i corresponding to

Table 5.3. K_p and K_i values of the controllers for each tuning criteria in the system under study.

Tuning criteria	PR	$\mathrm{PR_d}$	VPI
Fig. 5.4 (a) **Balanced tuning**	$K_p = 0.95$ $K_i = 124$	$K_p = 0.95$ $K_i = 122$	$K_p = 0.45$ $K_i = 2.7$
Fig. 5.4 (b) $\boldsymbol{t_{\mathrm{set}} \downarrow}$	$K_p = 1.35$ $K_i = 252$	$K_p = 1.25$ $K_i = 223$	$K_p = 1$ $K_i = 6$
Fig. 5.4 (c) **3ω amplification** $\downarrow$	$K_p = 0.5$ $K_i = 19$	$K_p = 0.35$ $K_i = 36$	$K_p = 0.05$ $K_i = 0.3$
Fig. 5.4 (d) **0-crossing ov.** $\downarrow$	$K_p = 1.35$ $K_i = 32$	$K_p = 1.2$ $K_i = 11$	$K_p = 0.65$ $K_i = 3.9$
Fig. 5.4 (e) **Peak-crossing ov.** $\downarrow$	$K_p = 1.05$ $K_i = 21$	$K_p = 0.95$ $K_i = 29$	$K_p = 0.05$ $K_i = 0.3$
Fig. 5.4 (f) **Sensitivity** $\downarrow$	$K_p = 1.4$ $K_i = 322$	$K_p = 1$ $K_i = 321$	$K_p = 1.4$ $K_i = 8.4$

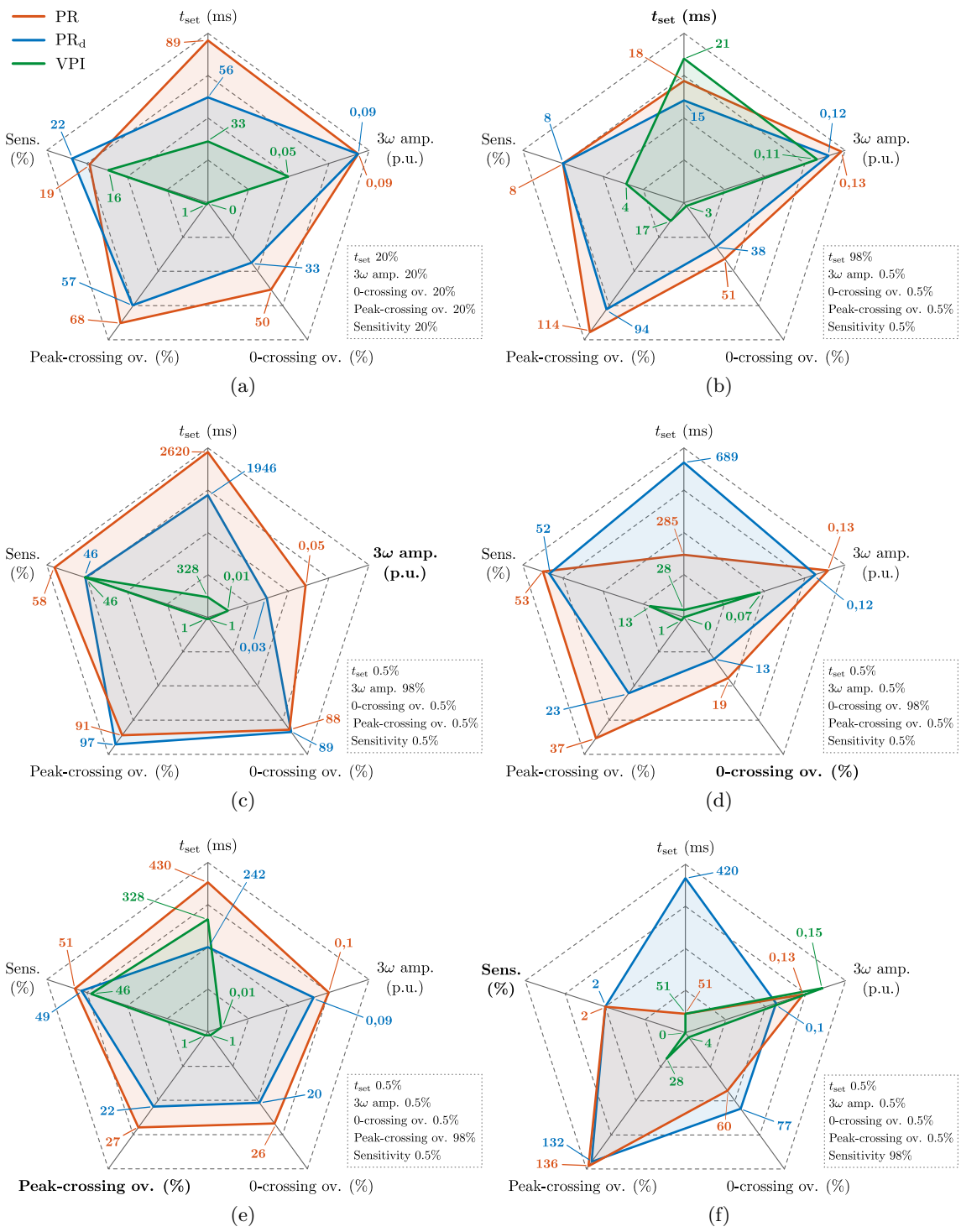

Fig. 5.7. Comparison spider charts of the PR, PR_d and VPI controllers for different tuning criteria. (a) Balanced tuning, which gives the same priority to minimize all the indicators, (b) priorizing a fast transient response ($t_{set}\downarrow$), (c) priorizing the 3ω attenuation (amplification $\downarrow$), (d) priorizing the input zero-crossing overshoot minimization, (e) priorizing the input peak-crossing overshoot minimization, and (f) priorizing the robustness of the system in the face of the uncertainty of L_f and R_f (sensitivity $\downarrow$). The weighting of each tuning criteria is also given.

each tuning criteria. It can be seen that in the VPI the relationship between K_i and K_p is always the same in order to guarantee the plant pole cancellation ($K_i/K_p = R_f/L_f = 6$). Table 5.4 shows the values of the parameters of the system in which the comparison is made, assuming the elements and characteristics of the experimental set-up used in *section 5.5* to validate the theoretical study.

Table 5.4. Parameters of the system under study.

Parameter	**Value**
Sampling period (T_s)	500 μs
Fundamental and resonant frequency ($f_0 = f$)	50 Hz
Inductive filter (L_f)	2.5 mH
Deviation	$\pm$20%
Resistance (R_f)	15 mΩ
Deviation	-50% to $+100\%$
Filter cut-off frequency (f_c)	1 kHz
Notch frequency ($f_n = 3f$)	150 Hz
Notch damping (ζ)	$1/4\pi$
Dominant pole max. time constant (τ)	3.5 s
Compensated sampling periods in the PR$_\mathrm{d}$ (n_d)	1.5
Normalization of the indicators	
Settling time (t_set)	$3\tau_f = 500$ ms
3ω amplification	0.2 p.u.
Overshoot (0- and peak-crossing)	50%
Sensitivity	50%

The results show that giving almost all the weight to one indicator can be prejudicial to other indicators. The most appropriate performance is therefore obtained with the balanced tuning in Fig. (a) (first column in Table 5.3). It can be seen how the VPI obtains the lowest values in each of the indicators.

The time response of the balanced tuning of each regulator for a reference zero-crossing input is presented in Fig. 5.8. The fastest transient response (lowest t_set) corresponds to the VPI, followed by the PR$_\mathrm{d}$, and the PR. This can also be deduced in the pole-zero map of the balanced tuning in Fig. 5.9, where the dominant pole pair $p_3{-}p_4$ of the VPI has the smallest module (r), and the dominant pole pair $p_1{-}p_2$ of the PR the biggest, the latter having therefore the slowest time response (biggest t_set). Note that the complex pole pair $p_1{-}p_2$ belongs to the original poles of each controller, shown in Figs. 5.2 (a) and (b).

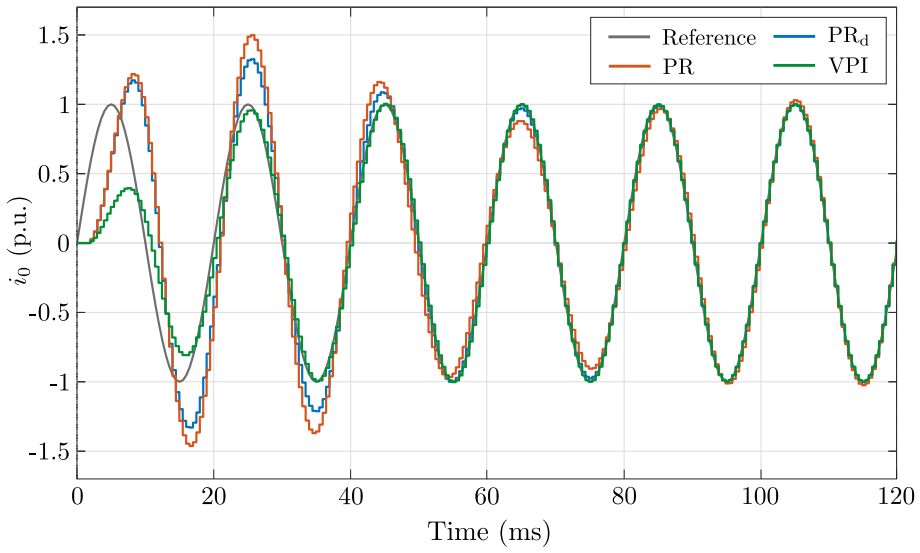

Fig. 5.8. Time response with reference zero-crossing input of the balanced tuning of the PR, PR$_\mathrm{d}$ and VPI controllers in Fig. 5.4 (a).

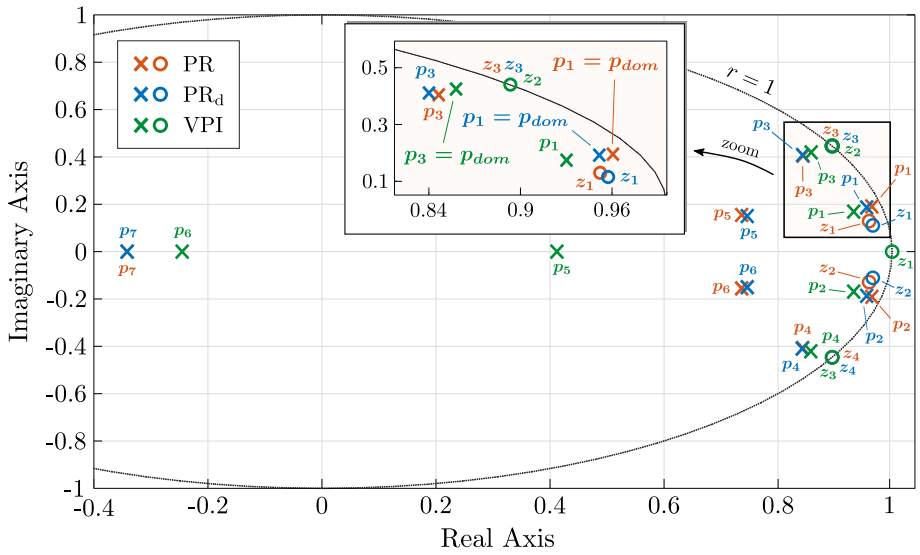

Fig. 5.9. Closed-loop (C_L) z-domain pole-zero map of the balanced tuning of the PR, PR$_d$ and VPI controllers in Fig. 5.4 (a).

In terms of the overshoot, Fig. 5.8 shows that the PR has the highest value, somewhat greater than the PR$_d$, for both reference zero- and peak-crossing inputs. It should be emphasized that the VPI has practically no overshoot, regardless of how it is tuned. This characteristic of the VPI can be explained by the position of the poles in Fig. 5.2. The overshoot of a system depends essentially on the damping ratio (ζ) of its complex conjugate pole pairs, which are responsible of the oscillatory component in the time-domain response (a decaying sinusoid); greater ζ, less overshoot. From Fig. 5.2 (a), the high ζ of the original pole pair $p_1{-}p_2$ results in the VPI having no overshoot; that is, the decaying sinusoid component corresponding to this pole pair has hardly any oscillation. For its part, the original pole pairs $p_1{-}p_2$ of the PR and PR$_d$ have a very low damping ($\zeta << 1$), which causes the PR and PR$_d$ to have high overshoot, being that their major disadvantage.

This characteristics of the resonant controllers under study can also be understood by means of Fig. 5.10, which shows the time response of the s-domain closed-loop original poles of the PR and VPI controllers of Fig. 5.2. As can be seen, the decaying sinusoidal

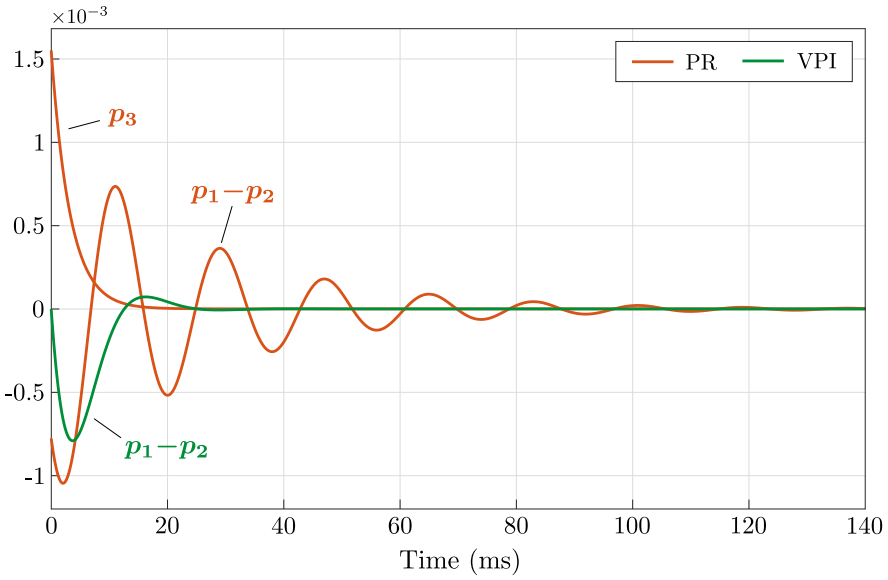

Fig. 5.10. Time response of the s-domain closed-loop (C_L) original poles of the PR and VPI controllers in Fig. 5.2 (a).

component, with the form of $A_{12}e^{-t}\sin(2t+\alpha)$, produced by the original conjugate pole pair $p_1{-}p_2$ of the PR controller oscillates much more than that of the VPI. As the original conjugate pole pairs $p_1{-}p_2$ are the dominant ones in each controller, are also the ones that most influence the overall homogenous time respone; the greater their oscillation, the greater the overshoot. For its part, Fig. 5.10 also shows that the real pole p_3 of the PR controller decays rapidly with the form of $A_3e^{-\lambda t}$, as explained in *subsection 5.3.2*.

Regarding the attenuation of the 3ω component, it is calculated by the direct-loop $D_{\mathrm{L}}(z)$ Bode diagram, shown in Fig. 5.11 for the balanced tuning case of Fig. 5.4 (a). As this frequency response shows, the three systems offer a very high gain at the ω to which they have been tuned (ω_0), and very low gain around the notch frequency (ω_n). The system based on the VPI has the lowest gain at 3ω, and thus the smallest amplification of this harmonic component. The gain at any frequency in the direct-loop of any of the three systems is proportional to the tuning parameter K_p; so the lower K_p, the higher the attenuation at 3ω, as Table 5.3 confirms. The VPI is also the most robust controller in the face of the uncertainty of L_f and R_f in the balanced tuning, as well as in the rest of the tuning criteria.

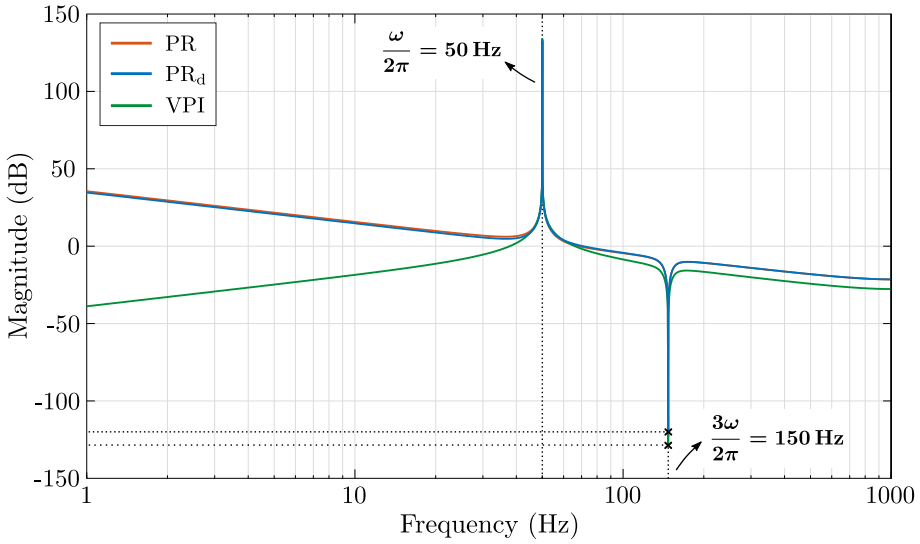

Fig. 5.11. Direct-loop (D_L) z-domain Bode diagram of the balanced tuning of the PR, $\mathrm{PR_d}$ and VPI controllers in Fig. 5.4 (a).

In the spider chart of Fig. 5.4 (b) the minimization of t_{set} is prioritized, where the $\mathrm{PR_d}$ controller achieves the fastest time response. As curiosity, note that with the tuning by which a fast response is prioritized, the VPI is the slowest controller. When the attenuation of 3ω is the main objective, in Fig. 5.4 (c), the VPI controller offers the lowest gain to this component, and the PR the biggest. However, this tuning criteria forces the system to be very slow and very sensitive to the uncertainty of the plant parameters, in addition to the excessive overshoot values in the PR and the $\mathrm{PR_d}$ controllers. Moving to the overshoot, if the reduction of this indicator is prioritized, $\mathrm{PR_d}$ seems to be a better option than the PR, as Figs. 5.4 (d) and (e) show. Finally, when the aim of the tuning is to maximize the stability margin, the VPI is the least sensitive regulator. Nevertheless, as Fig. 5.4 (f) shows, its high K_p makes the VPI controller the one which attenuates the 3ω component the least.

Summarizing, in general, the VPI controller is the most interesting regulator for the system under study, due to its fast time response, robustness, 3ω attenuation, and, above all, almost no overshoot. Regarding the improvement obtained with the $\mathrm{PR_d}$ with respect to the PR, note that it is not noticeable for the fundamental-frequency zero-sequence current control loop of a DCHB STATCOM operating under unbalanced conditions.

5.5 EXPERIMENTAL RESULTS

With the aim of validating the system analytical model and the performance of the resonant controllers studied in this chapter for the i_0 loop of the DCHB STATCOM under unbalanced conditions, the delta configuration of the real-scale experimental set-up of *subsection 4.2.4* is used (see Figs. 4.9 and 4.10 (b), and Table 4.1).

As explained, by an open-loop scalar voltage/frequency regulation, the 500 V – 100 kVA 5L NPC/HB converter used synthesizes positive-sequence voltage (v^+), and connected to single-phase unbalanced passive inductive loads ($L_{load\text{-}ph}$) to emulate a STATCOM scenario without net energy exchange (other than active power losses), i^- circulation is generated through the delta-connected phase clusters of the converter. For these tests, 3.2 mH and 7.5 mH loads are combined so as to generate different unbalanced current scenarios, which will request the injection of i_0. Single-phase inductances of 2.5 mH are used as a filter inside the delta (L_f), and a LCR meter is employed to measure the resistive value of them, as Fig. 5.12 shows. These inductances form the plant of the zero-sequence loop with their resistive values (rounding, $R_f = 15\,\text{m}\Omega$ is considered). The switching scheme used is the multilevel SVM with a switching frequency of 1 kHz.

Fig. 5.12. Measurement of the plant parameters L_f and R_f by a LCR meter.

In order to validate the theoretical analysis, a step change of the voltage reference ($V_{ll\text{-}rms}$) modifies the reference i_0^* to be injected according (3.18) and (3.19); this will allow to analyze and compare the transient response of each controller studied. Firstly, the analytical model of the system (i.e., the system z-domain transfer function) is validated with the measured i_0 in the experimental prototype for the PR, PR_d and VPI. For that purpose, the PI of the intercluster dc voltage control (see Fig. 5.1) has been tuned in the same way for all the tests so that it does not affect the conclusions (see Table 5.5).

Table 5.5. Intercluster dc voltage control PI tuning.

Parameter	**Value**
Proportional gain (K_p')	0.006
Integral gain (K_i')	0.02

In the first tests, $L_{load\text{-a}}$ and $L_{load\text{-b}}$ are 3.2 mH, while $L_{load\text{-c}}$ is 18.2 mH; i.e., $k_{ipn} = 0.55$ and $\theta_{ipn} = 0°$. Fig. 5.13 (a) shows the dc-link voltages in each phase cluster ($v_{dc\text{-ab}}, v_{dc\text{-bc}}, v_{dc\text{-ca}}$), which begin to drift away when i_0^* is modified by means of increasing $V_{ll\text{-}rms}$ from 50 V to 150 V. Without the DFE, at least one of the dc capacitors would discharge. The voltage reference is changed at a particular phase so that i_0^* changes at its zero-crossing. It can be seen how the intercluster active power balancing control adjusts the

dc-link voltages in each phase cluster to the reference value. Since i_0 circulates only inside the DCHB, its injection does not affect the output three-phase unbalanced load currents (i_a, i_b, i_c), which are shown in Fig. 5.13 (b). The resonant controller used in this test is

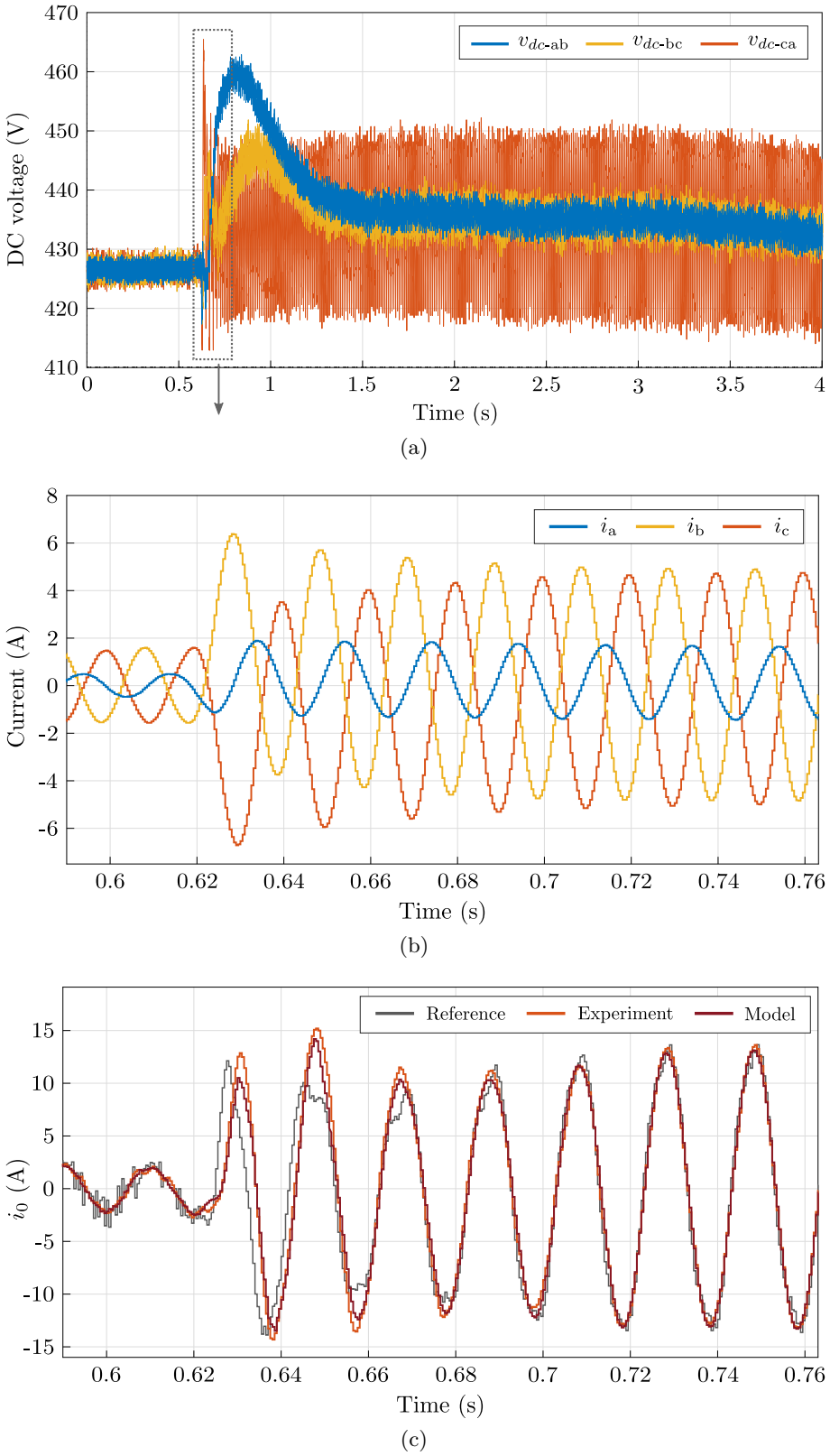

Fig. 5.13. PR controller with reference 0-crossing change in its balanced tuning. $V_{ll\text{-}rms}$ is increased from 50 V to 150 V. $L_{load\text{-a}} = L_{load\text{-b}} = 3.2$ mH, and $L_{load\text{-c}} = 18.2$ mH ($k_{ipn} = 0.55$, $\theta_{ipn} = 0°$). (a) DC-link voltage in each phase cluster, (b) load currents, and (c) i_0 reference, measurement and analytical model.

the PR, and Fig. 5.13 (c) shows the zero-sequence current reference, the corresponding response of the analytical model, and the test measurement. The balanced tuning of Fig. 5.4 (a) and the first column of Table 5.3 is used in this experiment. Figs. 5.14 and 5.15 show the transient response of the same experiment using the PR_d and the VPI, respectively.

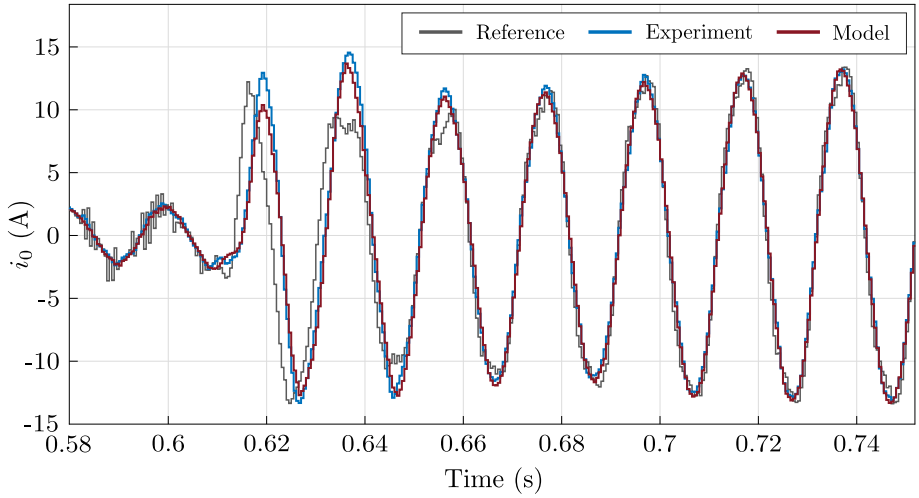

Fig. 5.14. i_0 reference, measurement and analytical model of the PR_d controller with reference 0-crossing change in its balanced tuning. $V_{ll\text{-}rms}$ is increased from 50 V to 150 V. $L_{load\text{-a}} = L_{load\text{-b}} = 3.2\,\text{mH}$, and $L_{load\text{-c}} = 18.2\,\text{mH}$ ($k_{ipn} = 0.55$, $\theta_{ipn} = 0°$).

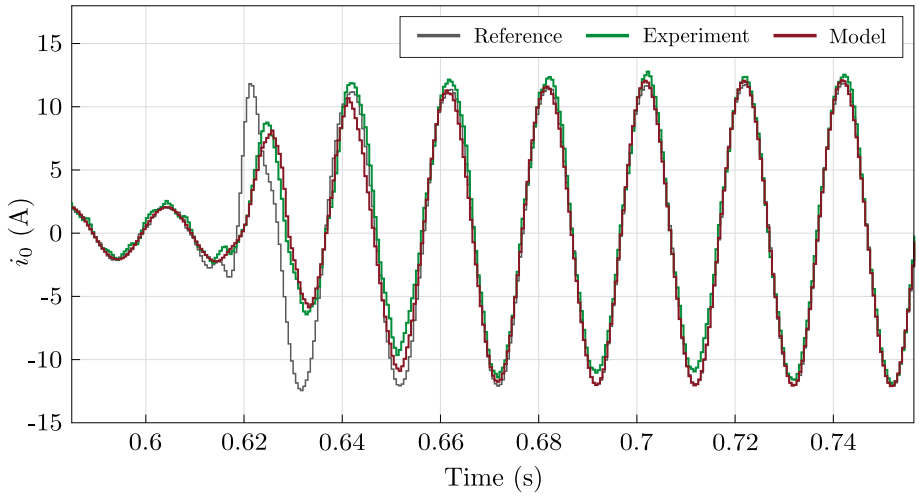

Fig. 5.15. i_0 reference, measurement and analytical model of the VPI controller with reference 0-crossing change in its balanced tuning. $V_{ll\text{-}rms}$ is increased from 50 V to 150 V. $L_{load\text{-a}} = L_{load\text{-b}} = 3.2\,\text{mH}$, and $L_{load\text{-c}} = 18.2\,\text{mH}$ ($k_{ipn} = 0.55$, $\theta_{ipn} = 0°$).

The experiments in Figs. 5.13, 5.14, and 5.15 show that the analytical model response and the zero-sequence current measurement match well, which completely validates the analytical model (see Fig. 5.3), as well as the conclusions of the comparison. Regarding the performance of the controllers, it is difficult to evaluate the settling time (t_{set}) of the transient response of each one, and it is even more difficult considering that i_0^* is different in each experiment; it depends on the other control loops of the converter, and varies until the three dc-link voltages are equalized. However, it can be seen how the three systems respond relatively fast. What is noteworthy is the overshoot, which is almost null with the VPI compared to the PR and PR_d, where the overshoots are about $40 - 50\%$; values close to those obtained in Fig. 5.4 (a).

Once the analytical model has been validated, Figs. 5.16 and 5.17 show two other test scenarios, tuned also with the balanced tuning, but with a reference peak-crossing disturbance. On the one hand, in Fig. 5.16 the voltage reference $V_{ll\text{-}rms}$ change is modified,

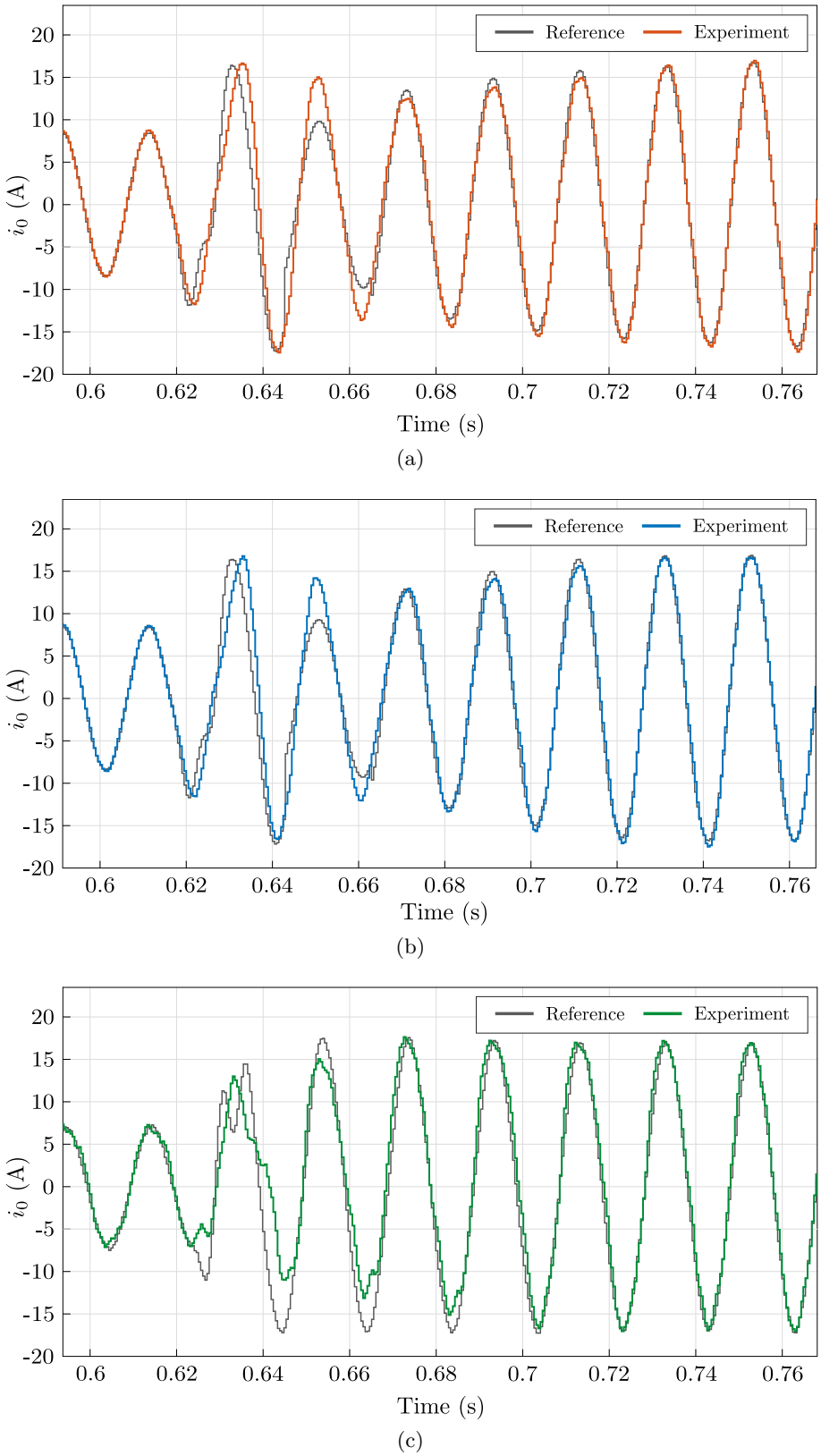

Fig. 5.16. i_0 reference and measurement with reference peak-crossing change in the balanced tuning. $V_{ll\text{-}rms}$ is increased from 100 V to 200 V. $L_{load\text{-a}} = L_{load\text{-b}} = 3.2$ mH, and $L_{load\text{-c}} = 18.2$ mH ($k_{ipn} = 0.55$, $\theta_{ipn} = 0°$). (a) PR, (b) PR_d, and (c) VPI.

where it goes from 100 V to 200 V. On the other hand, a different current unbalance is generated in the experiments of Fig. 5.17; $L_{load\text{-a}}$ is 3.2 mH, while $L_{load\text{-b}}$ and $L_{load\text{-c}}$ are 10.7 mH ($k_{ipn} = 0.27$ and $\theta_{ipn} = 0°$). $V_{ll\text{-}rms}$ goes from 100 V to 250 V in this case. Both

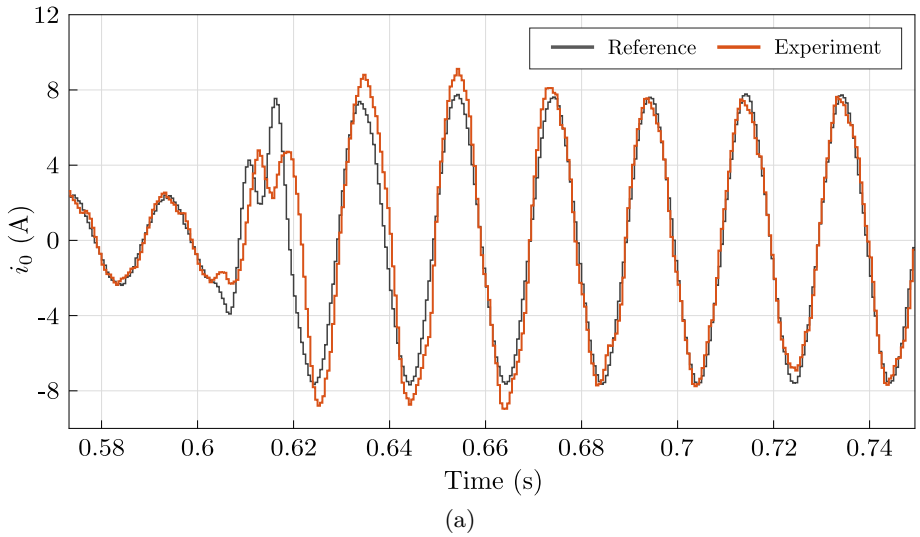

(a)

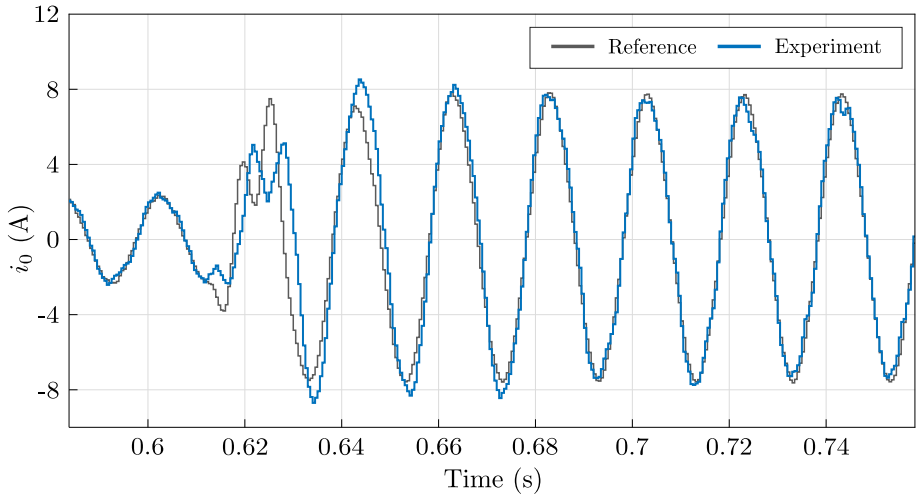

(b)

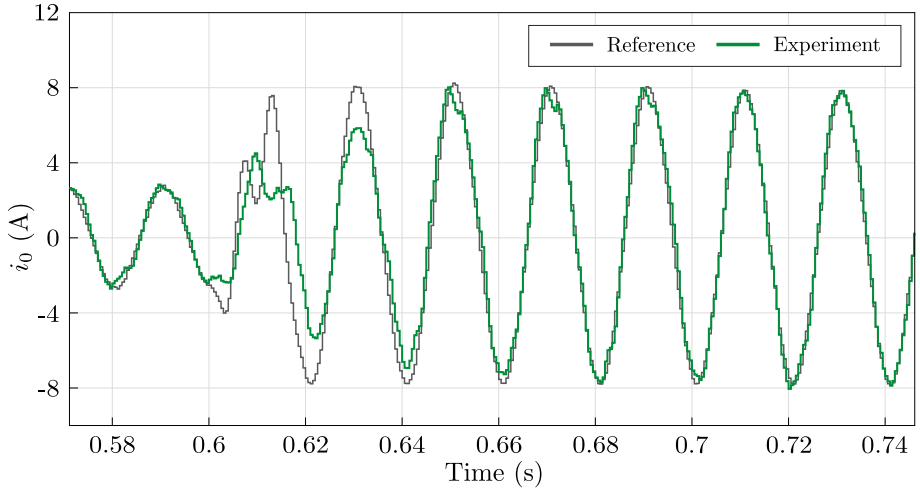

(c)

Fig. 5.17. i_0 reference and measurement with reference peak-crossing change in the balanced tuning. $V_{ll\text{-}rms}$ is increased from 100 V to 250 V. $L_{load\text{-a}} = 3.2$ mH, and $L_{load\text{-b}} = L_{load\text{-c}} = 10.7$ mH ($k_{ipn} = 0.27$, $\theta_{ipn} = 0°$). (a) PR, (b) PR_d, and (c) VPI.

tests confirm the advantage of the VPI controllers over the PR and PR_d: more damped response with no overshoot. Besides, in these experiments it can be seen how the VPI is faster as it reaches the final value earlier. As for the PR_d controller, it can be said that its behavior and dynamic response are not advantageous in this application since they are very similar to the PR.

The shown experimental results collect nine tests in Figs. 5.13 to 5.17. It can be seen how the achieved results meet the theoretical approach.

5.6 CONCLUSIONS

The DCHB converter is a suitable alternative for STATCOM applications operating with v^- and/or i^-. However, a zero-sequence current (i_0) needs to be injected in this situation to redistribute equally the active power among phase clusters and to guarantee dc-link capacitor voltage balancing. This chapter has identifed the particularities of this i_0 control loop, with the aim of determining the requirements to be fulfilled by the implemented controller.

Note that in high power applications such as the one in this study, the addition of the proposed notch filter attenuates the 3ω component in the measured i_0, thus solving a serious problem caused by dead times, which could affect very negatively the assumed intercluster active power redistribution.

Based on the identified requirements, appropriate indicators have been defined to quantify and evaluate the performance of some controllers which are suitable for this loop —PR, PR_d and VPI are proposed. The used multi-objective controller parameter selection method have allowed to tune the controllers using different criteria which prioritize the defined indicators, and a comparison of the controllers has been presented.

The carried out comparison confirms the VPI as the preferable option to the PR and PR_d due to its fast time response, robustness, 3ω attenuation, and especially, no overshoot. The VPI, with very few exceptions, improves all the indicators of the other two controllers with the six tuning criteria analyzed. Regarding the need of a delay compensation, the improvements of the PR_d with respect to the PR are not appreciable in this scenario where a fundamental-frequency signal needs to be tracked. The comparison presented has been supported by experimental results which completely validate the analytical model of the three resonant controllers and their performance.

The experimental analysis also validates that the defined indicators are valid to quantify the behavior of the controllers for the system under study. However, some more could be defined and included in the comparison. For instance, analogous to the sensitivity to become unstable in the face of the uncertainty of the plant parameters, the variation of the other indicators —t_{set}, 3ω amplification, and zero- and peak-crossing overshoots— due to the uncertainty of R_f and L_f could be also quantified and considered for tuning. However, more indicators would mean higher computational cost.

Finally, it should also be mentioned that apart from the STATCOM application, the conclusions drawn can be extrapolated to any other unbalanced scenario in which a DCHB is used; i.e., the unequal active power generation in a large-scale PV power plant, or the uneven active power distribution in BESS [55], analyzed in *Chapter 3*.

Chapter 6

CONCLUSIONS AND FUTURE LINES

This chapter collects an overview of the main conclusions and most important remarks of this doctoral thesis, discussing the degree of accomplishment of the specific objectives defined. Future lines that arise from this thesis and some ideas for further work are also suggested.

6.1 CONCLUSIONS

Traditional power systems are evolving due to the rapid increment in the energy consumption, the concern about climate change, and the high dependency on imported energy. This has accelerated the progressive integration of distributed RES, which has changed electrical power system functioning, emphasizing on system regulation and control. The non-dispatchable nature of RES results in many grid factors requiring greater flexibility to accommodate the changes in generation. Besides, RES often use inverters to connect to the grid instead of synchronous generators, and thus, as non-conventional variable generation sources are introduced in the system, actual transmission and distribution grids become power electronic converter-dominated.

Throughout this PhD dissertation, some of the most important advantages of multilevel VSCs based on modular structures for the converter-dominated grid have been remarked; especially their scalable attributes that make it easier to reach MV levels and high power ratings. FACTS devices and in particular the STATCOM play a crucial role in this new power grid paradigm, and the converters employed for these applications have to face increasingly demanding operating requirements. Unbalanced operation is one of these new requirements, where v^- and/or i^- appear at the converter terminals. Grid codes did not demand power converters to face these operating conditions before, and thus, specific designs need to be carried out in order to adapt them to these new challenging scenarios. VSC topologies which behave properly under balanced conditions, might cease to be so interesting depending on the application demands.

In this framework, the main objective of this doctoral thesis has been to facilitate the power converter manufacturer to compare and select the most appropriate VSC topology for each operating requirement that will be demanded to the converter; focusing mainly on the STATCOM application, employing multilevel VSCs based on modular structures, and operating under unbalanced voltage and/or current conditions.

Chapter 2 has presented a methodology which facilitates the evaluation of different VSC structures. The proposed methodology allows studying the converter features and limitations under any required operating requirement, enabling the user to compare, select, or design the most suitable configuration. An n-dimensional database is generated, and the presented results analysis tool extracts from the database the measured parameters. Following a data post-processing, provides valuable information to determine which VSC structure is the most appropriate, or which suits better the specific operating requirement. After identifying the operating scenario of a demanded application, the designer can analyze the results in a simple way without carrying out any extra simulation. This methodology has been published in the form of conference paper [**C1**].

Focusing on the STATCOM application under unbalanced conditions —object of research of this doctoral thesis—, a case study analyzed in order to demonstrate the potential of the methodology and the results analysis tool concludes that, for STATCOM application, the CHB presents higher dc-link voltage ripple than the 3L NPC under unbalanced current conditions. However, the CHB sees the same maximum dc voltage ripple regardless of the ratio k_{ipn}. So, in terms of dc-link voltage ripple, CHBs dimensioned to operate under balanced conditions can operate also with unbalanced currents. Nevertheless, it has been observed that they present also certain drawbacks, which might limit the maximum power that the converter could deliver in this application. More indicators other than the dc-link voltage ripple should be studied and added to the methodology in order to analyze the behavior of VSCs in the face of unbalanced conditions for STATCOM.

The overview provided also in *Chapter 2* about multilevel VSC topologies concludes that those based on modular structures —these include mainly the CHB and the MMC— are the most promising alternatives for the power electronic converter-based grid that

demands higher voltage and power equipment. An increase in voltage results in lower power losses than an increase in current, and therefore it is more efficient to connect single-phase power cells in cascade than to parallelize three-phase VSCs such as the 3L NPC. Cascaded structures make it easier the direct grid connection, avoiding the bulky step-up transformer.

However, modular structures present some drawbacks, since they require single-phase dc-links which are isolated from each other. This means that for applications where active power (P) is exchanged, it is also necessary for all energy sources to be isolated from each other. In STATCOM applications, where only reactive power (Q) is exchanged between the VSC and the grid, the above drawback disappears, which makes the CHB or the MMC very well-positioned alternatives for this application.

With the aim of meeting [**O2**], [**O3**], and [**O4**], a comprehensive literature review about the problems that the unbalanced operation in different applications suppose for multilevel VSCs based on modular structures has been provided in *Chapter 3*. Among these applications, the STATCOM under v^- and/or i^-, the unequal power generation in PV plants, and the uneven power distribution in BESS have been distinguished, classifying the proposed intercluster active power balancing strategies. An equivalency between the three analyzed applications has been observed, as well as an equivalency between the intercluster balancing applied to the YCHB, DCHB, and MMC. All these reflections have led to the publication of a journal review [**J1**].

From this review it has been concluded that there is no source which clearly evaluates, quantifies, and fairly compares the capabilities of CHB configurations and the MMC for STATCOM application operating under the same unbalanced voltage and/or current conditions. Since normally the aim of the STATCOM is to provide Q^+, from the manufacturer point of view, the limit of this indicator is the indicative parameter to compare and select the most suitable VSC structure to operate with v^- and/or i^-.

The most interesting outcome has been that when applications without dc energy sources such as the STATCOM are faced with unbalanced conditions, the cross-interaction $v^+ - i^-$ and/or $v^- - i^+$ in the ac side have an influence on the dc side of the VSC. This effect was already seen by simulation in *case study II* of *Chapter 2*. In *Chapter 4* the analytical equations have been obtained in order evaluate the effect in the dc side of these cross-interactions. These equations have permitted to quantify the available Q^+ and to compare the limits of each VSC topology.

Firstly, the YCHB and the DCHB configurations have been compared in a very particular scenario —negative-sequence current withstanding scenario—, in which real-scale experimental results in a MV laboratory have been obtained. This study has confirmed the DCHB as the preferable option to the YCHB for STATCOM application dealing with severe unbalanced current conditions. While the YCHB is strongly limited by the available dc-side voltage, the DCHB can stay connected to the PCC regardless of the i^- to withstand. It is worth noting that this contribution has been published as journal paper [**J2**].

From the review provided in *Chapter 3* it has also been concluded that apart from CHBs and the MMC, any evaluation about the operation of three-phase dc-link VSC structures such as the 3L NPC for STATCOM application operating with v^- and/or i^- has not been reported before. Thus, in the second part of *Chapter 4*, both the 3L NPC and the MMC have been incorported to the analysis, including also v^- in the comparison of the Q^+ limits. The conclusions drawn have demonstrated that the 3L NPC with a correctly dimensioned dc-link is the most attractive solution for STATCOM under unbalanced voltage and/or current conditions. Nevertheless, it is not as easy as in cascaded/modular structures to reach high power – MV levels. That is why the properly sized half-bridge MMC can be the solution to this problem. Regarding CHB configurations, the DCHB is still a very well positioned alternative, although under unbalanced voltage conditions the advantages over the YCHB are not so significant. The lack of resources has made it impossible to

obtain experimental results of the 3L NPC and the MMC topologies, as well as of the operation under unbalanced voltage conditions. This study has been published in the form of conference paper [**C2**].

A further observation has been that the control implementations of the intercluster active power balancing strategies have not been studied extensively before. Especially in the case of the DCHB, where only a small number of papers which deal with the i_0 control loop can be found in the specialized literature.

Chapter 5 has identifed the particularities of this i_0 control loop, with the aim of determining the requirements to be fulfilled by the implemented controller. Based on the identified requirements, appropriate indicators have been defined to quantify and evaluate the performance of some controllers which are suitable for this loop —PR, PR_d and VPI. The used multi-objective controller parameter selection method have allowed to tune the controllers using different criteria which prioritize the defined indicators, and a comparison of the controllers has been presented.

The carried out analysis has confirmed the VPI as the preferable option to the PR and the PR_d due to its fast time response, robustness, 3ω attenuation, and especially, no overshoot. With regard to the necessity of a delay compensation, it has been concluded that the improvements of the PR_d with respect to the PR are not very appreciable in this scenario where a fundamental-frequency signal needs to be tracked. The analytical model of the three resonant controllers and their performance have been successfully verified by experimental results. Besides, the experimental analysis also validates that the defined indicators are valid to quantify the behavior of the controllers for the system under study. This contribution has been submitted to be considered for publication as journal paper [**J3**]. An important remark is that the conclusions drawn are valid for other unbalanced scenarios in which the DCHB configuration is used, such as the unequal active power generation in large-scale PV plants, or the uneven active power distribution in BESS. Another point worth mentioning is that the utilization of the proposed notch filter in the measured zero-sequence current attenuates the 3ω component, and therefore could solve serious problems caused by the introduced dead times, which do not allow to redistribute the active power properly among the delta-connected phase clusters; a situation that is aggravated in high power applications.

Degree of Accomplishment of the Partial Objectives

[O1] Develop a methodology which provides valuable information that allows the converter manufacturer to compare and select the most appropriate VSC topology for any required application.

The methodology presented in *Chapter 2* allows studying the converter features and limitations under any operating requirement that will be demanded to the converter, enabling the user to compare, select, or develop the most appropriate VSC configuration. The methodology has been integrated into a software-based results analysis tool, which for the moment incorporates limited operating points and indicators. Even so, the case studies analyzed have validated the proposed methodology. Thus, taking into account that it would be necessary to enrich the tool with more content —more operating variables/dimensions and indicators—, we can say that the objective has been partially fulfilled.

[O2] Study and compare the limitations of Cascaded H-Bridge STATCOMs in star and delta configurations to withstand negative-sequence current.

Section 4.2 has analyzed and compared the Q^+ limits of YCHB and DCHB STATCOMs to withstand i^-. By means of the presented systematic procedure, the available Q^+ of

each CHB STATCOM configuration is quantified depending on the ratio k_{ipn} at converter terminals. Experimental results obtained from a real-scale set-up in a MV laboratory have validated the theoretical analysis. Therefore, this objective has been completely achieved.

[O3] Study and compare the limitations of single-phase dc-link and three-phase dc-link VSC topologies for STATCOM application operating under unbalanced voltage and/or current conditions.

Section 4.3 has extended the analysis of *section 4.2* by including also the MMC and the 3L NPC topology to the study, as well as by adding also v^- in converter terminals. The effects of the average active power term ($\bar{P}$) and the 2ω oscillating active power term ($\tilde{p}$) as a result of v^- and/or i^- have been evaluated in each VSC topology, which has permitted to quantify the Q^+ limits of each one. This objective has been partially fulfilled, since some studies still need to be verified experimentally.

[O4] Analyze the control implementation of star- and delta-connected Cascaded H-Bridge configurations to operate under unbalanced conditions.

In *section 4.2*, the overall control designs of the YCHB and DCHB STATCOMs to operate under v^- and/or i^- have been studied, so this objective has been achieved. As the intercluster active power balancing strategy corresponding to the DCHB has not been deeply studied in the specialized literature, we have gone one step further. *Chapter 5* has identifed the particularities of the i_0 control loop in the DCHB STATCOM, with the aim of determining the requirements to be fulfilled by the implemented controller. A comparison of the PR, PR_d and VPI controllers has been presented. Experimental results have validated the analytical model of the controllers and their performance.

6.2 FUTURE LINES

One of the most important conclusions of this doctoral thesis is that there are still several fields that require further investigation. Thus, this section mentions some of the most interesting research paths that we have identified in the course of this project. The main opportunities for further work could be:

- The methodology proposed in *section 2.4* to evaluate converter structures based on 3L NPC PEBBs can be applied for any converter topology or PEBB connection structure; even for structures other than VSC-based. The study can also be extended with more operating point dimensions/variables and more indicators that the user considers important to be analyzed. For instance, if a database of different type of switching semiconductor devices is added, other indicators such as the number of switches needed, the conduction losses, or the switching losses could be analyzed. Another example, if the most suitable cooling system needs to be selected, other indicators such as the maximum current could also be evaluated.

- If the STATCOM application in the presence of unbalanced conditions has to be studied, the analytical calculation of the positive-sequence reactive power (Q^+) could also be included in the methodology as another indicator to be considered. In this case, the calculation of the injected zero-sequence voltage for the YCHB (v_0^Y) or zero-sequence current (i_0) for the DCHB need to be added as well. Also the circulating dc current in the MMC ($i_{z\text{-}ph}$) needs to be assumed, or the derivation of the dc-link voltage ripple (Δv_{dc}) in the case of three-phase configured dc-link topologies such as the 3L NPC.

– Besides, in applications where the VSC-based STATCOM is asked to inject v^- and/or i^-, the limit of the negative-sequence reactive power (Q^-) could also be another interesting indicator to analyze.

– The analytical deduction of the dc-link voltage ripple produced by the harmonics corresponding to the modulation technique might be another point to be further studied, which has been calculated by simulation in this dissertation.

– As concluded in the literature review of *Chapter 3*, the injection of novel zero-sequence components proposed for the intercluster power balancing in PV plants can be considered another interesting open point in order to increase the STATCOM available Q^+.

– Regarding large-scale PV integration, mostly CHB configurations have been studied in the specialized literature. The possible extension to the MMC topology has not been analyzed in depth, which might be a promising research topic. As new grid codes demand unbalanced voltage and/or currents in the PCC, in order to support an asymmetrical grid fault or LVRT, the author of this PhD thesis considers the analysis of unbalanced PV power generation during unbalanced PCC conditions a key research topic for the future power grid. Also, the hybridization of PV and BESS for that purpose.

– The utilization of multilevel VSCs based on modular structures for BESS has not been so widely covered as STATCOM or PV applications. While large-scale PV power integration aims to maximize the active power extraction, BESS applications need to supply/absorb active power depending on the application demands. It is remarkable that the DCHB configuration, which is a competitive solution for other unbalanced scenarios, has not been examined for BESS. Moreover, even some references about the MMC have been found, the employment of this structure has not been completely justified in the specialized literature.

– When analyzing the Q^+ limits of different VSC topologies, experimental results have only been obtained in a negative-sequence current withstanding scenario, and only for two specific configurations: YCHB and DCHB. In this sense, being able to obtain experimental results including also the negative-sequence voltage at the converter terminals is a short term future line. Furthermore, if resources permit, obtaining experimental results with a MMC and a 3L NPC would be also a great approach.

– Concerning the comparison of the performance of the resonant regulators in *Chapter 5*, this has been carried out taking into account specific indicators. The comparison could be further completed if more indicators are added to the analysis, such as the variation of t_{set}, 3ω amplification, and zero- and peak-crossing overshoots in the face of the uncertainty of the plant parameters R_f and L_f.

– An important note to keep in mind is that this PhD thesis has focused only on the internal control loops of the converter. Therefore, a continuation of this study would be to analyze the higher control loops of the VSC for STATCOM application operating under unbalanced power grid conditions. That is, not only to study the control loops so that the converter can operate under unbalanced conditions, but also so that the converter can act and compensate for the unbalance. For that purpose, the regulators employed could be compared and designed by means of the multi-objective tuning method presented in *Chapter 5*, which is useful to analyze any control loop.

– Among the internal control loops of the converter, it should also be noted that this doctoral thesis has only focused on the *intercluster active power balancing* of

the YCHB and the DCHB configurations. The carried out studies could be further completed by modeling the system including also the *dual vector control* and the *overall dc-link voltage control*, as well as the *intracluster active power balancing control*. This would allow to properly tune the control loops taking into account how they interact with each other.

– Another novel approach might be the translation of the requirements that different grid codes demand in the PCC —such as LVRT— to the converter terminals. That is, to be able to translate the action required by the corresponding grid code to positive- and negative-sequence voltage and currents at the converter terminals. This work would then make it easier to select the appropriate topology and design it correctly according to the requirements of the power grid.

BIBLIOGRAPHY

[1] J. Blunden and T. Boyer, "State of the Climate in 2020", *Bull. Am. Meteorol. Soc.*, vol. 102, no. 8, pp. 1–475, 2021.

[2] European Statistical Office, *Energy, Transport and Environment Statistics*. 2019.

[3] International Energy Agency, *World Energy Outlook 2021*. 2021.

[4] M. H. Nehrir, C. Wang, K. Strunz *et al.*, "A review of hybrid renewable/alternative energy systems for electric power generation: Configurations, control, and applications", *IEEE Trans. Sustain. Energy*, vol. 2, no. 4, pp. 392–403, 2011.

[5] J. M. Carrasco, L. G. Franquelo, J. T. Bialasiewicz *et al.*, "Power-electronic systems for the grid integration of renewable energy sources: a survey", *IEEE Trans. Ind. Electron.*, vol. 53, no. 4, pp. 1002–1016, 2006.

[6] F. Blaabjerg, R. Teodorescu, M. Liserre and A. V. Timbus, "Overview of control and grid synchronization for distributed power generation systems", *IEEE Trans. Ind. Electron.*, vol. 53, no. 5, pp. 1398–1409, 2006.

[7] International Renewable Energy Agency, *Global Energy Transformation: A Roadmap to 2050*. 2019.

[8] United Nations, *The Paris Agreement*. 2015.

[9] H. Abu-Rub, M. Malinowski and K. Al-Haddad, *Power Electronics for Renewable Energy Systems, Transportation and Industrial Application*. Wiley-IEEE Press, 2014.

[10] N. Mararakanye and B. Bekker, "Renewable energy integration impacts within the context of generator type, penetration level and grid characteristics", *Renew. Sustain. Energy Rev.*, vol. 108, pp. 441–451, 2019.

[11] B. Kroposki, B. Johnson, Y. Zhang *et al.*, "Achieving a 100% renewable grid: operating electric power systems with extremely high levels of variable renewable energy", *IEEE Power Energy Mag.*, vol. 15, no. 2, pp. 61–73, 2017.

[12] F. Blaabjerg, Z. Chen and S. B. Kjaer, "Power electronics as efficient interface in dispersed power generation systems", *IEEE Trans. Power Electron.*, vol. 19, no. 5, pp. 1184–1194, 2004.

[13] A. Ulbig, T. S. Borsche and G. Andersson, "Impact of low rotational inertia on power system stability and operation", in *19th IFAC World Congr.*, vol. 47, 2014, pp. 7290–7297.

[14] W. Cole and A. W. Frazier, "Impacts of increasing penetration of renewable energy on the operation of the power sector", *Electr. J.*, vol. 31, no. 10, pp. 24–31, 2018.

[15] J. P. Barton and D. Infield, "Energy storage and its use with intermittent renewable energy", *IEEE Trans. Energy Convers.*, vol. 19, no. 2, pp. 441–448, 2004.

[16] P. Breeze, *Power System Energy Storage Technologies*, 1st ed. Elsevier Ltd, 2018.

[17] H. Akagi, Y. Kanazawa and A. Nabae, "Instantaneous reactive power compensators comprising switching devices without energy storage components", *IEEE Trans. Ind. Appl.*, vol. IA-20, no. 3, pp. 625–630, 1984.

[18] P. Rao, M. L. Crow and Z. Yang, "STATCOM control for power system voltage control applications", *IEEE Trans. Power Deliv.*, vol. 15, no. 4, pp. 1311–1317, 2000.

[19] D. Soto and T. C. Green, "A comparison of high-power converter topologies for the implementation of FACTS controllers", *IEEE Trans. Ind. Electron.*, vol. 49, no. 5, pp. 1072–1080, 2002.

[20] M. Molinas, J. A. Suul and T. Undeland, "Low voltage ride through of wind farms with cage generators: STATCOM versus SVC", *IEEE Trans. Power Electron.*, vol. 23, no. 3, pp. 1104–1117, 2008.

[21] H. P. Mohammadi and M. T. Bina, "A transformerless medium-voltage STATCOM topology based on extended modular multilevel converters", *IEEE Trans. Power Electron.*, vol. 26, no. 5, pp. 1534–1545, 2011.

[22] A. Balikci and E. Akpinar, "A multilevel converter with reduced number of switches in STATCOM for load balancing", *Electr. Power Syst. Res.*, vol. 123, pp. 164–173, 2015.

[23] S. N. Duarte, F. T. Ghetti, P. M. de Almeida and P. G. Barbosa, "Zero-sequence voltage compensation of a distribution network through a four-wire modular multilevel static synchronous compensator", *Int. J. Electr. Power Energy Syst.*, vol. 109, pp. 57–72, 2019.

[24] K. R. Padiyar and A. M. Kulkarni, "Modeling and Analysis of FACTS and HVDC Controllers", in *Dyn. Control Electr. Transm. Microgrids*, Wiley-IEEE Press, 2019, pp. 145–194.

[25] J. Rabkowski, D. Peftitsis and H.-P. Nee, "Silicon carbide power transistors: A new era in power electronics is initiated", *IEEE Ind. Electron. Mag.*, vol. 6, no. 2, pp. 17–26, 2012.

[26] S. Bernet, "Recent developments of high power converters for industry and traction applications", *IEEE Trans. Power Electron.*, vol. 15, no. 6, pp. 1102–1117, 2000.

[27] B. K. Bose, "Power electronics and motor drives recent progress and perspective", *IEEE Trans. Ind. Electron.*, vol. 56, no. 2, pp. 581–588, 2009.

[28] J.-S. Lai and F. Z. Peng, "Multilevel converters – A new breed of power converters", *IEEE Trans. Ind. Appl.*, vol. 32, no. 3, pp. 509–517, 1996.

[29] J. Rodriguez, S. Bernet, B. Wu, J. O. Pontt and S. Kouro, "Multilevel voltage-source-converter topologies for industrial medium-voltage drives", *IEEE Trans. Ind. Electron.*, vol. 54, no. 6, pp. 2930–2945, 2007.

[30] L. G. Franquelo, J. Rodriguez, J. I. Leon, S. Kouro, R. Portillo and M. Á. M. Prats, "The age of multilevel converters arrives", *IEEE Ind. Electron. Mag.*, vol. 2, no. 2, pp. 28–39, 2008.

[31] J. Rodriguez, L. G. Franquelo, K. Samir *et al.*, "Multilevel converters: an enabling technology for high-power applications", *Proc. IEEE*, vol. 97, no. 11, pp. 1786–1817, 2009.

[32] H. Abu-Rub, J. Holtz, J. Rodriguez and G. Baoming, "Medium-voltage multilevel converters: state of the art, challenges, and requirements in industrial applications", *IEEE Trans. Ind. Electron.*, vol. 57, no. 8, pp. 2581–2596, 2010.

[33] S. Kouro, M. Malinowski, K. Gopakumar *et al.*, "Recent advances and industrial applications of multilevel converters", *IEEE Trans. Ind. Electron.*, vol. 57, no. 8, pp. 2553–2580, 2010.

[34] S. Kouro, J. Rodriguez, B. Wu, S. Bernet and M. A. Perez, "Powering the future of industry: High-power adjustable speed drive topologies", *IEEE Ind. Appl. Mag.*, vol. 18, no. 4, pp. 26–39, 2012.

[35] N. S. Hasan, N. Rosmin, D. A. A. Osman and A. H. Musta'amal Jamal, "Reviews on multilevel converter and modulation techniques", *Renew. Sustain. Energy Rev.*, vol. 80, pp. 163–174, 2017.

[36] B. Wu, *High-Power Converters and AC Drives*, 2nd ed. Wiley-IEEE Press, 2017.

[37] IEEE Std 1547-2018, *IEEE Standard for Interconnection and Interoperability of Distributed Energy Resources with Associated Electric Power Systems Interfaces*, 2018.

[38] L. M. Tolbert and F. Z. Peng, "Multilevel converters as a utility interface for renewable energy systems", in *2000 Power Eng. Soc. Summer Meet.*, vol. 2, 2000, pp. 1271–1274.

[39] M. Malinowski, K. Gopakumar, J. Rodriguez and M. A. Perez, "A survey on cascaded multilevel inverters", *IEEE Trans. Ind. Electron.*, vol. 57, no. 7, pp. 2197–2206, 2010.

[40] H. Akagi, "Classification, terminology, and application of the modular multilevel cascade converter (MMCC)", *IEEE Trans. Power Electron.*, vol. 26, no. 11, pp. 3119–3130, 2011.

[41] E. Villanueva, P. Correa, J. Rodriguez and M. Pacas, "Control of a single-phase cascaded H-bridge multilevel inverter for grid-connected photovoltaic systems", *IEEE Trans. Ind. Electron.*, vol. 56, no. 11, pp. 4399–4406, 2009.

[42] S. Kouro, B. Wu, Á. Moya, E. Villanueva, P. Correa and J. Rodríguez, "Control of a cascaded H-bridge multilevel converter for grid connection of photovoltaic systems", in *IECON 2009 – 35th Annu. Conf. IEEE Ind. Electron. Soc.*, 2009, pp. 3976–3982.

[43] A. I. Elsanabary, G. Konstantinou, S. Mekhilef, C. D. Townsend, M. Seyedmahmoudian and A. Stojcevski, "Medium voltage large-scale grid-connected photovoltaic systems using cascaded H-bridge and modular multilevel converters: A review", *IEEE Access*, vol. 8, pp. 223 686–223 699, 2020.

[44] L. Maharjan, S. Inoue and H. Akagi, "State-of-charge (SOC)-balancing control of a battery energy storage system based on a cascade PWM converter", *IEEE Trans. Power Electron.*, vol. 24, no. 6, pp. 1628–1636, 2009.

[45] G. Wang, G. Konstantinou, C. D. Townsend *et al.*, "A review of power electronics for grid connection of utility-scale battery energy storage systems", *IEEE Trans. Sustain. Energy*, vol. 7, no. 4, pp. 1778–1790, 2016.

[46] S. K. Chaudhary, A. F. Cupertino, R. Teodorescu and J. R. Svensson, "Benchmarking of modular multilevel converter topologies for ES-STATCOM realization", *Energies*, vol. 13, no. 13, pp. 1–22, 2020.

[47] M. Zubiaga, A. Sanchez-Ruiz, E. Olea, E. Unamuno, A. Bilbao and J. Arza, "Power capability boundaries for an inverter providing multiple grid support services", *Energies*, vol. 13, no. 17, pp. 1–14, 2020.

[48] Y. Yang, F. Blaabjerg and H. Wang, "Low-voltage ride-through of single-phase transformerless photovoltaic inverters", *IEEE Trans. Ind. Appl.*, vol. 50, no. 3, pp. 1942–1952, 2014.

[49] IEC 61000-2-4, *Electromagnetic compatibility (EMC) – Part 2-4: Environment - Compatibility levels in industrial plants for low-frequency conducted disturbances*, 2004.

[50] ANSI C84.1, *Electric Power Systems Voltage Ratings (60 Hz)*, 2020.

[51] Verband der Elektrotechnik Elektronik Informationstechnik (VDE), *Technical Connection Rules for High-Voltage (VDE-AR-N 4120)*, 2018.

[52] T. Tanaka, K. Ma, H. Wang and F. Blaabjerg, "Asymmetrical reactive power capability of modular multilevel cascade converter based STATCOMs for offshore wind farm", *IEEE Trans. Power Electron.*, vol. 34, no. 6, pp. 5147–5164, 2019.

[53] H. Akagi, S. Inoue and T. Yoshii, "Control and performance of a transformerless cascade PWM STATCOM with star configuration", *IEEE Trans. Ind. Appl.*, vol. 43, no. 4, pp. 1041–1049, 2007.

[54] Q. Song and W. Liu, "Control of a cascade STATCOM with star configuration under unbalanced conditions", *IEEE Trans. Power Electron.*, vol. 24, no. 1, pp. 45–58, 2009.

[55] I. Marzo, A. Sanchez-Ruiz, J. A. Barrena, G. Abad and I. Muguruza, "Power balancing in cascaded H-bridge and modular multilevel converters under unbalanced operation: A review", *IEEE Access*, vol. 9, pp. 110 525–110 543, 2021.

[56] I. Marzo, J. A. Barrena, A. Sanchez-Ruiz, G. Abad, H. Fernandez-Rebolleda and I. Muguruza, "Reactive power limits of cascaded H-bridge STATCOMs in star and delta configuration under negative-sequence current withstanding", *Int. J. Electr. Power Energy Syst.*, vol. 142, p. 108 267, 2022.

[57] I. Marzo, I. Muguruza, J. A. Barrena, A. Sanchez-Ruiz, G. Abad and H. Fernandez-Rebolleda, "Zero-sequence controller requirements and comparison for a delta-CHB STATCOM under unbalanced operation", *Submitt. to Int. J. Electr. Power Energy Syst.*, 2022.

[58] I. Marzo, J. A. Barrena and A. Sanchez-Ruiz, "Methodology to evaluate converter structures based on 3L NPC PEBBs", in *IECON 2020 – 46th Annu. Conf. IEEE Ind. Electron. Soc.*, 2020, pp. 4107–4114.

[59] I. Marzo, J. A. Barrena, A. Sanchez-Ruiz, G. Abad and I. Muguruza, "Reactive power limits of single-phase and three-phase dc-link VSC STATCOMs under negative-sequence voltage and current", in *IECON 2021 – 47th Annu. Conf. IEEE Ind. Electron. Soc.*, 2021, pp. 1–8.

[60] S. Schröder, P. Tenca, T. Geyer *et al.*, "Modular high-power shunt-interleaved drive system: a realization up to 35 MW for oil and gas applications", *IEEE Trans. Ind. Appl.*, vol. 46, no. 2, pp. 821–830, 2010.

[61] A. Laka, J. A. Barrena, J. Chivite-Zabalza and M. Á. Rodríguez, "Analysis and improved operation of a PEBB-based voltage-source converter for FACTS applications", *IEEE Trans. Power Deliv.*, vol. 28, no. 3, pp. 1330–1338, 2013.

[62] J. Chivite-Zabalza, M. Á. R. Vidal, P. Izurza-Moreno, G. Calvo and D. Madariaga, "A large-power voltage source converter for FACTS applications combining three-level neutral-point-clamped power electronic building blocks", *IEEE Trans. Ind. Electron.*, vol. 60, no. 11, pp. 4759–4772, 2013.

[63] D. G. Holmes and T. A. Lipo, *Pulse Width Modulation for Power Converters: Principles and Practice*. Wiley-IEEE Press, 2003.

[64] M. Mazuela, I. Baraia, A. Sanchez-Ruiz, I. Echeverria, I. Torre and I. Atutxa, "Simple voltage balancing method to protect series-connected devices experimentally verified in a 5L-MPC converter", *IEEE Trans. Ind. Electron.*, vol. 65, no. 5, pp. 3699–3707, 2018.

[65] J. I. Leon, S. Kouro, L. G. Franquelo, J. Rodriguez and B. Wu, "The essential role and the continuous evolution of modulation techniques for voltage-source inverters in the past, present, and future power electronics", *IEEE Trans. Ind. Electron.*, vol. 63, no. 5, pp. 2688–2701, 2016.

[66] R. Rojas, T. Ohnishi and T. Suzuki, "An improved voltage vector control method for neutral-point-clamped inverters", *IEEE Trans. Power Electron.*, vol. 10, no. 6, pp. 666–672, 1995.

[67] Y.-W. Lee, B.-S. Suh and D.-S. Hyun, "A novel PWM scheme for a three-level voltage source inverter with GTO thyristors", *IEEE Trans. Ind. Appl.*, vol. 32, no. 2, pp. 260–268, 1996.

[68] D. Zhou, "A self-balancing space vector switching modulator for three-level motor drives", *IEEE Trans. Power Electron.*, vol. 17, no. 6, pp. 1024–1031, 2002.

[69] A. Nabae, I. Takahashi and H. Akagi, "A new neutral-point-clamped PWM inverter", *IEEE Trans. Ind. Appl.*, vol. IA-17, no. 5, pp. 518–523, 1981.

[70] P. W. Hammond, "Medium voltage PWM drive and method", *U.S. Pat. 5.625.545*, no. 19, pp. 1–21, 1997.

[71] P. W. Hammond, "A new approach to enhance power quality for medium voltage AC drives", *IEEE Trans. Ind. Appl.*, vol. 33, no. 1, pp. 202–208, 1997.

[72] A. Lesnicar and R. Marquardt, "An innovative modular multilevel converter topology suitable for a wide power range", in *2003 IEEE Bol. PowerTech Conf.*, 2003, pp. 1–6.

[73] S. Allebrod, R. Hamerski and R. Marquardt, "New transformerless, scalable modular multilevel converters for HVDC-transmission", in *IEEE Power Electron. Spec. Conf.*, 2008, pp. 174–179.

[74] R. Marquardt, "Modular multilevel converter: an universal concept for HVDC-networks and extended DC-bus-applications", in *2010 Int. Power Electron. Conf. - ECCE Asia*, 2010, pp. 502–507.

[75] A. Nami, J. Liang, F. Dijkhuizen and G. D. Demetriades, "Modular multilevel converters for HVDC applications: Review on converter cells and functionalities", *IEEE Trans. Power Electron.*, vol. 30, no. 1, pp. 18–36, 2015.

[76] S. Du, A. Dekka, B. Wu and N. Zargari, *Modular Multilevel Converters: Analysis, Control, and Applications*. Wiley-IEEE Press, 2018.

[77] M. A. Perez, S. Bernet, J. Rodriguez, S. Kouro and R. Lizana, "Circuit topologies, modeling, control schemes, and applications of modular multilevel converters", *IEEE Trans. Power Electron.*, vol. 30, no. 1, pp. 4–17, 2015.

[78] D. Krug, S. Bernet and S. S. Fazel, "Comparison of 2.3 kV medium-voltage multilevel converters for industrial medium-voltage drives", *IEEE Trans. Ind. Electron.*, vol. 54, no. 6, pp. 2979–2992, 2007.

[79] S. S. Fazel, S. Bernet, D. Krug and K. Jalili, "Design and comparison of 4-kV neutral-point-clamped, flying-capacitor, and series-connected H-bridge multilevel converters", *IEEE Trans. Ind. Appl.*, vol. 43, no. 4, pp. 1032–1040, 2007.

[80] A. Sanchez-Ruiz, M. Mazuela, S. Alvarez, G. Abad and I. Baraia, "Medium voltage-high power converter topologies comparison procedure, for a 6.6 kV drive application using 4.5 kV IGBT modules", *IEEE Trans. Ind. Electron.*, vol. 59, no. 3, pp. 1462–1476, 2012.

[81] A. Sanchez-Ruiz, G. Abad, I. Echeverria, I. Torre and I. Atutxa, "Continuous phase-shifted selective harmonic elimination and DC-link voltage balance solution for H-bridge multilevel configurations, applied to 5L HNPC", *IEEE Trans. Power Electron.*, vol. 32, no. 4, pp. 2533–2545, 2017.

[82] B. W. Williams, *Power Electronics. Devices, Drivers and Applications*. Macmillan, 1987.

[83] P. Hu, J. M. Guerrero and Z. He, "Design and analysis of a transformerless STATCOM based on hybrid cascaded multilevel converter", *Int. J. Electr. Power Energy Syst.*, vol. 104, pp. 694–704, 2019.

[84] Y. Cheng, C. Qian, M. L. Crow, S. Pekarek and S. Atcitty, "A comparison of diode-clamped and cascaded multilevel converters for a STATCOM with energy storage", *IEEE Trans. Ind. Electron.*, vol. 53, no. 5, pp. 1512–1521, 2006.

[85] L. Gyugyi, "Reactive power generation and control by thyristor circuits", in *IEEE Power Electron. Spec. Conf.*, 1976, pp. 174–184.

[86] Y. Sumi, Y. Harumoto, T. Hasegawa, M. Yano, K. Ikeda and T. Matsuura, "New static var control using force-commutated inverters", *IEEE Trans. Power Appar. Syst.*, vol. PAS-100, no. 9, pp. 4216–4224, 1981.

[87] S. Rivera, B. Wu, S. Kouro, H. Wang and D. Zhang, "Cascaded H-bridge multilevel converter topology and three-phase balance control for large scale photovoltaic systems", in *2012 3rd IEEE Int. Symp. Power Electron. Distrib. Gener. Syst.*, 2012, pp. 690–697.

[88] J. Pou, S. Ceballos, G. Konstantinou, V. G. Agelidis, R. Picas and J. Zaragoza, "Circulating current injection methods based on instantaneous information for the modular multilevel converter", *IEEE Trans. Ind. Electron.*, vol. 62, no. 2, pp. 777–788, 2015.

[89] M. Vasiladiotis, N. Cherix and A. Rufer, "Impact of grid asymmetries on the operation and capacitive energy storage design of modular multilevel converters", *IEEE Trans. Ind. Electron.*, vol. 62, no. 11, pp. 6697–6707, 2015.

[90] H. Akagi, E. H. Watanabe and M. Aredes, *Instantaneous Power Theory and Applications for Power Conditioning*. Wiley-IEEE Press, 2007.

[91] J. A. Barrena, L. Marroyo, M. A. Rodriguez Vidal and J. R. Torrealday Apraiz, "Individual voltage balancing strategy for PWM cascaded H-bridge converter-based STATCOM", *IEEE Trans. Ind. Electron.*, vol. 55, no. 1, pp. 21–29, 2008.

[92] J. Li, G. Konstantinou, S. Member, H. R. Wickramasinghe and J. Pou, "Operation and control methods of modular multilevel converters in unbalanced AC grids: A review", *IEEE J. Emerg. Sel. Top. Power Electron.*, vol. 7, no. 2, pp. 1258–1271, 2019.

[93] Y. Yu, G. Konstantinou, B. Hredzak and V. G. Agelidis, "Power balance of cascaded H-bridge multilevel converters for large-scale photovoltaic integration", *IEEE Trans. Power Electron.*, vol. 31, no. 1, pp. 292–303, 2016.

[94] Y. Yang, P. Enjeti, F. Blaabjerg and H. Wang, "Wide-scale adoption of photovoltaic energy: Grid code modifications are explored in the distribution grid", *IEEE Ind. Appl. Mag.*, vol. 21, no. 5, pp. 21–31, 2015.

[95] E. Behrouzian and M. Bongiorno, "Investigation of negative-sequence injection capability of cascaded H-bridge converters in star and delta configuration", *IEEE Trans. Power Electron.*, vol. 32, no. 2, pp. 1675–1683, 2017.

[96] O. J. K. Oghorada and L. Zhang, "Unbalanced and reactive load compensation using an MMCC-based STATCOM with third-harmonic injection", *IEEE Trans. Ind. Electron.*, vol. 66, no. 4, pp. 2891–2902, 2019.

[97] F. Z. Peng and J. Wang, "A universal STATCOM with delta-connected cascade multilevel inverter", in *IEEE Annu. Power Electron. Spec. Conf.*, vol. 5, 2004, pp. 3529–3533.

[98] P.-H. Wu, H.-C. Chen, Y.-T. Chang and P.-T. Cheng, "Delta-connected cascaded H-bridge converter application in unbalanced load compensation", *IEEE Trans. Ind. Appl.*, vol. 53, no. 2, pp. 1254–1262, 2017.

[99] Z. He, F. Ma, Q. Xu *et al.*, "Reactive power strategy of cascaded delta-connected STATCOM under asymmetrical voltage conditions", *IEEE J. Emerg. Sel. Top. Power Electron.*, vol. 5, no. 2, pp. 784–795, 2017.

[100] P.-H. Wu, Y.-T. Chen and P.-T. Cheng, "The delta-connected cascaded H-bridge converter application in distributed energy resources and fault ride through capability analysis", *IEEE Trans. Ind. Appl.*, vol. 53, no. 5, pp. 4665–4672, 2017.

[101] Y. Peng, Y. Li, K. Y. Lee *et al.*, "Coordinated control strategy of PMSG and cascaded H-bridge STATCOM in dispersed wind farm for suppressing unbalanced grid voltage", *IEEE Trans. Sustain. Energy*, vol. 12, no. 1, pp. 349–359, 2021.

[102] Z. Liu, B. Liu, S. Duan and Y. Kang, "A novel DC capacitor voltage balance control method for cascade multilevel STATCOM", *IEEE Trans. Power Electron.*, vol. 27, no. 1, pp. 14–27, 2012.

[103] F. Z. Peng, J.-S. Lai, J. W. McKeever and J. VanCoevering, "A multilevel voltage-source inverter with separate DC sources for static VAr generation", *IEEE Trans. Ind. Appl.*, vol. 32, no. 5, pp. 1130–1138, 1996.

[104] F. Z. Peng and J.-S. Lai, "Dynamic performance and control of a static VAr generator using cascade multilevel inverters", *IEEE Trans. Ind. Appl.*, vol. 33, no. 3, pp. 748–755, 1997.

[105] Y. Liang and C. O. Nwankpa, "A new type of STATCOM based on cascading voltage-source inverters with phase-shifted unipolar SPWM", *IEEE Trans. Ind. Appl.*, vol. 35, no. 5, pp. 1118–1123, 1999.

[106] S. Sirisukprasert, A. Q. Huang and J.-S. Lai, "Modeling, analysis and control of cascaded-multilevel converter-based STATCOM", in *2003 IEEE Power Eng. Soc. Gen. Meet.*, 2003, pp. 2561–2568.

[107] C. K. Lee, J. S. K. Leung, S. Y. R. Hui and H. S.-H. Chung, "Circuit-level comparison of STATCOM technologies", *IEEE Trans. Power Electron.*, vol. 18, no. 4, pp. 1084–1092, 2003.

[108] C. Hochgraf and R. H. Lasseter, "Statcom controls for operation with unbalanced voltages", *IEEE Trans. Power Deliv.*, vol. 13, no. 2, pp. 538–544, 1998.

[109] C. A. C. Cavaliere, E. H. Watanabe and M. Aredes, "Multi-pulse STATCOM operation under unbalanced voltages", in *2002 IEEE Power Eng. Soc. Winter Meet.*, vol. 1, 2002, pp. 567–572.

[110] N. I. A. Wahab, N. Mariun, A. Mohamed and M. Mohamad, "Response of D-STATCOM under unbalanced voltage condition caused by SLG fault", in *Student Conf. Res. Dev. (SCOReD 2003)*, 2003, pp. 395–400.

[111] G. Escobar, A. M. Stankovic and P. Mataveli, "An adaptive controller in stationary reference frame for D-Statcom in unbalanced operation", *IEEE Trans. Power Electron.*, vol. 51, no. 2, pp. 401–409, 2004.

[112] L. Xu, B. R. Andersen and P. Cartwright, "VSC transmission operating under unbalanced AC conditions - Analysis and control design", *IEEE Trans. Power Deliv.*, vol. 20, no. 1, pp. 427–434, 2005.

[113] Y. Liu and F. L. Luo, "Trinary hybrid multilevel inverter used in STATCOM with unbalanced voltages", in *IEE Proc. – Electr. Power Appl.*, vol. 152, 2005, pp. 1203–1222.

[114] B. Blažič and I. Papič, "Improved D-Statcom control for operation with unbalanced currents and voltages", *IEEE Trans. Power Deliv.*, vol. 21, no. 1, pp. 225–233, 2006.

[115] K. Fujii, U. Schwarzer and R. W. De Doncker, "Comparison of hard-switched multi-level inverter topologies for STATCOM by loss-implemented simulation and cost estimation", in *2005 IEEE 36th Power Electron. Spec. Conf.*, 2005, pp. 340–346.

[116] K. Fujii, R. W. De Doncker and S. Konishi, "A novel DC-link voltage control of PWM-switched cascade cell multi-level inverter applied to STATCOM", in *Fourtieth IAS Annu. Meet. Conf. Rec. 2005 Ind. Appl. Conf.*, 2005, pp. 961–967.

[117] N. Hatano and T. Ise, "A configuration and control method of cascade H-bridge STATCOM", in *2008 IEEE Power Energy Soc. Gen. Meet. - Convers. Deliv. Electr. Energy 21st Century*, vol. 1, 2008, pp. 1–8.

[118] R. E. Betz, T. Summers and T. Furney, "Symmetry compensation using a H-bridge multilevel STATCOM with zero sequence injection", in *41st IAS Annu. Meet. Conf. Rec. 2006 Ind. Appl. Conf.*, 2006, pp. 1724–1731.

[119] R. E. Betz and T. Summers, "Using a cascaded H-bridge STATCOM for rebalancing unbalanced voltages", in *7th Int. Conf. Power Electron.*, 2007, pp. 1–6.

[120] T. Summers, R. E. Betz and G. Mirzaeva, "Phase leg voltage balancing of a cascaded H-bridge converter based STATCOM using zero-sequence injection", in *2009 13th Eur. Conf. Power Electron. Appl.*, 2009, pp. 1–10.

[121] O. J. K. Oghorada and L. Zhang, "Analysis of star and delta connected modular multilevel cascaded converter-based STATCOM for load unbalanced compensation", *Int. J. Electr. Power Energy Syst.*, vol. 95, pp. 341–352, 2018.

[122] N. Hatano and T. Ise, "Control scheme of cascaded H-bridge STATCOM using zero-sequence voltage and negative-sequence current", *IEEE Trans. Power Deliv.*, vol. 25, no. 2, pp. 543–550, 2010.

[123] Y. Shi, B. Liu, Y. Shi and S. Duan, "Individual phase current control based on optimal zero-sequence current separation for a star-connected cascade STATCOM under unbalanced conditions", *IEEE Trans. Power Electron.*, vol. 31, no. 3, pp. 2099–2110, 2016.

[124] H.-C. Chen, P.-H. Wu, C.-T. Lee, C.-W. Wang, C.-H. Yang and P.-T. Cheng, "A flexible DC voltage balancing control based on the power flow management for star-connected cascaded H-bridge converter", *IEEE Trans. Ind. Appl.*, vol. 52, no. 6, pp. 4946–4954, 2016.

[125] D. Lu, J. Zhu, J. Wang, J. Yao, S. Wang and H. Hu, "A simple zero-sequence-voltage-based cluster voltage balancing control and the negative sequence current compensation region identification for star-connected cascaded h-bridge STATCOM", *IEEE Trans. Power Electron.*, vol. 33, no. 10, pp. 8376–8387, 2018.

[126] W. Liu, X. Zhao, Q. Song and X. Zhang, "Research on unbalance load compensation by cascaded STATCOM with star configuration", in *IECON 2012 - 38th Annu. Conf. IEEE Ind. Electron. Soc.*, 2012, pp. 734–738.

[127] K. Sano and M. Takasaki, "A transformerless D-STATCOM based on a multivoltage cascade converter requiring no DC sources", *IEEE Trans. Power Electron.*, vol. 27, no. 6, pp. 2783–2795, 2012.

[128] L. Tan, S. Wang, P. Wang *et al.*, "High performance controller with effective voltage balance regulation for a cascade STATCOM with star configuration under unbalanced conditions", in *EPE 2013 - 15th Eur. Conf. Power Electron. Appl.*, 2013.

[129] M. Zhang and Q. Wang, "Implementation of a cascade D-STATCOM under unbalanced conditions", in *2014 Int. Power Electron. Appl. Conf. Expo.*, 2014.

[130] C.-T. Lee, B.-S. Wang, S.-W. Chen *et al.*, "Average power balancing control of a STATCOM based on the cascaded H-bridge PWM converter with star configuration", *IEEE Trans. Ind. Appl.*, vol. 50, no. 6, pp. 3893–3901, 2014.

[131] J. I. Yutaka Ota, Y. Shibano, N. Niimura and H. Akagi, "A phase-shifted-PWM D-STATCOM using a modular multilevel cascade converter (SSBC) - Part I: Modeling, analysis, and design of current control", *IEEE Trans. Ind. Appl.*, vol. 51, no. 1, pp. 279–288, 2015.

[132] J. I. Yutaka Ota, Y. Shibano and H. Akagi, "A phase-shifted PWM D-STATCOM using a modular multilevel cascade converter (SSBC) - Part II: Zero-voltage-ride-through capability", *IEEE Trans. Ind. Appl.*, vol. 51, no. 1, pp. 289–296, 2015.

[133] H.-C. Chen, P.-H. Wu, C.-T. Lee, C.-W. Wang, C.-H. Yang and P.-T. Cheng, "Zero-sequence voltage injection for DC capacitor voltage balancing control of the star-connected cascaded H-Bridge PWM converter under unbalanced grid", *IEEE Trans. Ind. Appl.*, vol. 51, no. 6, pp. 4584–4594, 2015.

[134] O. J. K. Oghorada and L. Zhang, "Control of a modular multi-level converter STATCOM for low voltage ride-through condition", in *IECON 2016 – 42nd Annu. Conf. IEEE Ind. Electron. Soc.*, 2016, pp. 3691–3696.

[135] Y. Neyshabouri, S. K. Chaudhary, R. Teodorescu, R. Sajadi and H. Iman-Eini, "Improving the reactive current compensation capability of cascaded H-bridge based STATCOM under unbalanced grid voltage", *IEEE J. Emerg. Sel. Top. Power Electron.*, vol. 8, no. 2, pp. 1466–1476, 2020.

[136] M. Hagiwara, R. Maeda and H. Akagi, "Negative-sequence reactive-power control by a PWM STATCOM based on a modular multilevel cascade converter (MMCC-SDBC)", *IEEE Trans. Ind. Appl.*, vol. 48, no. 2, pp. 720–729, 2012.

[137] S. Du, J. Liu, J. Lin and Y. He, "Control strategy study of STATCOM based on cascaded PWM H-bridge converter with delta configuration", in *Proc. 7th Int. Power Electron. Motion Control Conf.*, 2012, pp. 345–350.

[138] S. Du, J. Liu, J. Lin and Y. He, "A novel DC voltage control method for STATCOM based on hybrid multilevel H-bridge converter", *IEEE Trans. Power Electron.*, vol. 28, no. 1, pp. 101–111, 2013.

[139] M. Nieves, J. M. Maza, J. M. Mauricio, R. Teodorescu, M. Bongiorno and P. Rodriguez, "Enhanced control strategy for MMC-based STATCOM for unbalanced load compensation", in *2014 16th Eur. Conf. Power Electron. Appl.*, 2014, pp. 1–10.

[140] H. Huang, L. Zhang, O. J. Oghorada and M. Mao, "A delta-connected MMCC-based active power conditioner for unbalanced load compensation and harmonic elimination", *Int. J. Electr. Power Energy Syst.*, vol. 118, p. 105 811, 2020.

[141] S. Ouyang, J. Liu and H. Chen, "Arm current stress reduction technique for a delta-connected solid state transformer using zero-sequence current injection", *IEEE Trans. Power Electron.*, vol. 36, no. 11, pp. 12 234–12 250, 2021.

[142] E. Behrouzian, M. Bongiorno and H. Z. De La Parra, "Investigation of negative sequence injection capability in H-bridge multilevel STATCOM", in *2014 16th Eur. Conf. Power Electron. Appl.*, 2014, pp. 1–10.

[143] D. Basic, M. Geske and S. Schroeder, "Limitations of the H-bridge multilevel STATCOMs in compensation of current imbalance", in *EPE 2015 – 17th Eur. Conf. Power Electron. Appl.*, 2015, pp. 1–10.

[144] U. Hameed, H. Sadiq, H. A. Khalid, M. U. Khan and M. Ali, "Investigation of zero sequence injection method for balancing of multi-level cascaded-H bridge inverter", in *2018 Int. Conf. Comput. Electron. Electr. Eng. ICE Cube 2018*, IEEE, 2018, pp. 1–6.

[145] R. Luo, Y. He and J. Liu, "Research on the unbalanced compensation of delta-connected cascaded H-bridge multilevel SVG", *IEEE Trans. Ind. Electron.*, vol. 65, no. 11, pp. 3439–3444, 2018.

[146] J.-J. Jung, J.-H. Lee, S.-K. Sul, G. T. Son and Y.-H. Chung, "DC capacitor voltage balancing control for delta-connected cascaded H-bridge STATCOM considering unbalanced grid and load conditions", *IEEE Trans. Power Electron.*, vol. 33, no. 6, pp. 4726–4735, 2018.

[147] G. Liang, H. D. Tafti, G. G. Farivar *et al.*, "Analytical derivation of intersubmodule active power disparity limits in modular multilevel converter-based battery energy storage systems", *IEEE Trans. Power Electron.*, vol. 36, no. 3, pp. 2864–2874, 2021.

[148] G. A. Reddy and A. Shukla, "Circulating current optimization control of MMC", *IEEE Trans. Ind. Electron.*, vol. 68, no. 4, pp. 2798–2811, 2021.

[149] M. Hagiwara and H. Akagi, "Control and experiment of pulsewidth-modulated modular multilevel converters", *IEEE Trans. Power Electron.*, vol. 24, no. 7, pp. 1737–1746, 2009.

[150] M. Hagiwara, R. Maeda and H. Akagi, "Theoretical analysis and control of the modular multilevel cascade converter based on double-star chopper-cells (MMCC-DSCC)", in *2010 Int. Power Electron. Conf. - ECCE Asia*, 2010, pp. 2029–2036.

[151] M. Hagiwara, R. Maeda and H. Akagi, "Negative-sequence reactive-power control by the modular multilevel cascade converter based on double-star chopper-cells (MMCC-DSCC)", in *2010 IEEE Energy Convers. Congr. Expo.*, 2010, pp. 3949–3954.

[152] S. Du and J. Liu, "A brief comparison of series-connected modular topology in STATCOM application", in *2013 IEEE ECCE Asia Downunder*, 2013, pp. 456–460.

[153] J.-W. Moon, C.-S. Kim, J.-W. Park, D.-W. Kang and J.-M. Kim, "Circulating current control in MMC under the unbalanced voltage", *IEEE Trans. Power Deliv.*, vol. 28, no. 3, pp. 1952–1959, 2013.

[154] S. Li, X. Wang, Z. Yao, T. Li and Z. Peng, "Circulating current suppressing strategy for MMC-HVDC based on nonideal proportional resonant controllers under unbalanced grid conditions", *IEEE Trans. Power Electron.*, vol. 30, no. 1, pp. 387–397, 2015.

[155] J.-W. Moon, J.-W. Park, D.-W. Kang and J.-M. Kim, "A control method of HVDC-modular multilevel converter based on arm current under the unbalanced voltage condition", *IEEE Trans. Power Deliv.*, vol. 30, no. 2, pp. 529–536, 2015.

[156] C. Xu, K. Dai, X. Chen and Y. Kang, "Unbalanced PCC voltage regulation with positive- and negative-sequence compensation tactics for MMC-DSTATCOM", *IET Power Electron.*, vol. 9, no. 15, pp. 2846–2858, 2016.

[157] Y. Liang, J. Liu, T. Zhang and Q. Yang, "Arm current control strategy for MMC-HVDC under unbalanced conditions", *IEEE Trans. Power Deliv.*, vol. 32, no. 1, pp. 125–134, 2017.

[158] J. Wang, J. Liang, C. Wang and X. Dong, "Circulating current suppression for MMC-HVDC under unbalanced grid conditions", *IEEE Trans. Ind. Appl.*, vol. 53, no. 4, pp. 3250–3259, 2017.

[159] G. Tsolaridis, E. Kontos, S. K. Chaudhary, P. Bauer and R. Teodorescu, "Internal balance during low-voltage-ride-through of the modular multilevel converter STATCOM", *Energies*, vol. 10, no. 7, pp. 1–18, 2017.

[160] Z. Ou, G. Wang and L. Zhang, "Modular multilevel converter control strategy based on arm current control under unbalanced grid condition", *IEEE Trans. Power Electron.*, vol. 33, no. 5, pp. 3826–3836, 2018.

[161] A. F. Cupertino, J. V. M. Farias, H. A. Pereira, S. I. Seleme and R. Teodorescu, "Comparison of DSCC and SDBC modular multilevel converters for STATCOM application during negative sequence compensation", *IEEE Trans. Ind. Electron.*, vol. 66, no. 3, pp. 2302–2312, 2019.

[162] V. Sridhar and S. Umashankar, "A comprehensive review on CHB MLI based PV inverter and feasibility study of CHB MLI based PV-STATCOM", *Renew. Sustain. Energy Rev.*, vol. 78, pp. 138–156, 2017.

[163] J. Chavarria, D. Biel, F. Guinjoan, C. Meza and J. J. Negroni, "Energy-balance control of PV cascaded multilevel grid-connected inverters under level-shifted and phase-shifted PWMs", *IEEE Trans. Ind. Electron.*, vol. 60, no. 1, pp. 98–111, 2013.

[164] C. D. Townsend, T. Summers and R. E. Betz, "Control and modulation scheme for a cascaded H-bridge multi-level converter in large scale photovoltaic systems", in *2012 IEEE Energy Convers. Congr. Expo.*, 2012, pp. 3707–3714.

[165] Y. Yu, G. Konstantinou, B. Hredzak and V. G. Agelidis, "Optimal zero sequence injection in multilevel cascaded H-bridge converter under unbalanced photovoltaic power generation", in *2014 Int. Power Electron. Conf. (IPEC Hiroshima 2014 - ECCE ASIA)*, 2014, pp. 1458–1465.

[166] Y. Yu, G. Konstantinou, C. D. Townsend and V. G. Agelidis, "Comparison of zero-sequence injection methods in cascaded H-bridge multilevel converters for large-scale photovoltaic integration", *IET Renew. Power Gener.*, vol. 11, no. 5, pp. 603–613, 2017.

[167] R. P. Aguilera, P. Acuna, Y. Yu *et al.*, "Predictive control of cascaded H-bridge converters under unbalanced power generation", *IEEE Trans. Ind. Electron.*, vol. 64, no. 1, pp. 4–13, 2017.

[168] H. D. Tafti, C. D. Townsend, J. Pou, A. I. Maswood, G. Konstantinou and P. Acuna, "Flexible control of photovoltaic grid-connected cascaded H-bridge converters during unbalanced voltage sags", *IEEE Trans. Ind. Electron.*, vol. 65, no. 8, pp. 6229–6238, 2018.

[169] C. D. Townsend, Y. Yu, G. Konstantinou and V. G. Agelidis, "Cascaded H-bridge multilevel PV topology for alleviation of per-phase power imbalances and reduction of second harmonic voltage ripple", *IEEE Trans. Power Electron.*, vol. 31, no. 8, pp. 5574–5586, 2016.

[170] B. Xiao, L. Hang, J. Mei, C. Riley, L. M. Tolbert and B. Ozpineci, "Modular cascaded H-bridge multilevel PV inverter with distributed MPPT for grid-connected applications", *IEEE Trans. Ind. Appl.*, vol. 51, no. 2, pp. 1722–1731, 2015.

[171] P. Sochor and H. Akagi, "Theoretical comparison in energy-balancing capability between star- and delta-configured modular multilevel cascade inverters for utility-scale photovoltaic systems", *IEEE Trans. Power Electron.*, vol. 31, no. 3, pp. 1980–1992, 2016.

[172] Y. Yu, G. Konstantinou, B. Hredzak and V. G. Agelidis, "Power balance optimization of cascaded H-bridge multilevel converters for large-scale photovoltaic integration", *IEEE Trans. Power Electron.*, vol. 31, no. 2, pp. 1108–1120, 2016.

[173] Y. Yu, G. Konstantinou, B. Hredzak and V. G. Agelidis, "On extending the energy balancing limit of multilevel cascaded H-bridge converters for large-scale photovoltaic farms", in *2013 Australas. Univ. Power Eng. Conf.*, 2013, pp. 1–6.

[174] Y. Yu, G. Konstantinou, C. D. Townsend, R. P. Aguilera and V. G. Agelidis, "Delta-connected cascaded H-bridge multilevel converters for large-scale photovoltaic grid integration", *IEEE Trans. Ind. Electron.*, vol. 64, no. 11, pp. 8877–8886, 2017.

[175] P. Sochor and H. Akagi, "Energy-balancing control of a delta-configured modular multilevel cascade inverter for utility-scale photovoltaic systems", in *2015 IEEE Energy Convers. Congr. Expo.*, 2015, pp. 4706–4713.

[176] Y. Yu, G. Konstantinou, C. D. Townsend, R. P. Aguilera, B. Hredzak and V. G. Agelidis, "Delta-connected cascaded H-bridge multilevel photovoltaic converters", in *IECON 2015 – 41st Annu. Conf. IEEE Ind. Electron. Soc.*, 2015, pp. 2229–2234.

[177] C. Qian and M. L. Crow, "A cascaded converter-based StatCom with energy storage", in *2002 IEEE Power Eng. Soc. Winter Meet.*, vol. 1, 2002, pp. 544–549.

[178] L. Baruschka and A. Mertens, "Comparison of cascaded H-bridge and modular multilevel converters for BESS application", in *2011 IEEE Energy Convers. Congr. Expo.*, 2011, pp. 909–916.

[179] M. Schroeder, S. Henninger, J. Jaeger, A. Rašić, H. Rubenbauer and H. Leu, "Integration of batteries into a modular multilevel converter", in *EPE 2013 – 15th Eur. Conf. Power Electron. Appl.*, 2013, pp. 1–12.

[180] T. Soong and P. W. Lehn, "Evaluation of emerging modular multilevel converters for BESS applications", *IEEE Trans. Power Deliv.*, vol. 29, no. 5, pp. 2086–2094, 2014.

[181] W. Cao, Y. Xu, Y. Han and B. Ren, "Comparison of cascaded multilevel and modular multilevel converters with energy storage system", in *2016 IEEE 11th Conf. Ind. Electron. Appl.*, 2016, pp. 290–294.

[182] E. Chatzinikolaou and D. J. Rogers, "A comparison of grid-connected battery energy storage system designs", *IEEE Trans. Power Electron.*, vol. 32, no. 9, pp. 6913–6923, 2017.

[183] L. Maharjan, T. Yamagishi and H. Akagi, "Active-power control of individual converter cells for a battery energy storage system based on a multilevel cascade PWM converter", *IEEE Trans. Power Electron.*, vol. 27, no. 3, pp. 1099–1107, 2012.

[184] L. Maharjan, S. Inoue and H. Akagi, "A transformerless energy storage system based on a cascade multilevel PWM converter with star configuration", *IEEE Trans. Ind. Appl.*, vol. 44, no. 5, pp. 1621–1630, 2008.

[185] L. Maharjan, T. Yamagishi and H. Akagi, "Discussions on a battery energy storage system based on a cascade PWM converter with star configuration", in *2010 Int. Power Electron. Conf. - ECCE Asia*, 2010, pp. 2043–2049.

[186] N. Kawakami, S. Ota, H. Kon *et al.*, "Development of a 500-kW modular multilevel cascade converter for battery energy storage systems", *IEEE Trans. Ind. Appl.*, vol. 50, no. 6, pp. 3902–3910, 2014.

[187] N. Li, F. Gao, T. Hao, Z. Ma and C. Zhang, "SOH balancing control method for the MMC battery energy storage system", *IEEE Trans. Ind. Electron.*, vol. 65, no. 8, pp. 6581–6591, 2018.

[188] A. F. Cupertino, W. C. S. Amorim, H. A. Pereira, S. I. Seleme Junior, S. K. Chaudhary and R. Teodorescu, "High performance simulation models for ES-STATCOM based on modular multilevel converters", *IEEE Trans. Energy Convers.*, vol. 35, no. 1, pp. 474–483, 2020.

[189] L. Zhang, F. Gao and N. Li, "Control strategy of MMC battery energy storage system under asymmetrical grid voltage condition", *Chinese J. Electr. Eng.*, vol. 2, no. 2, pp. 76 –83, 2016.

[190] Q. Chen, R. Li and X. Cai, "Analysis and fault control of hybrid modular multilevel converter with integrated battery energy storage system", *IEEE J. Emerg. Sel. Top. Power Electron.*, vol. 5, no. 1, pp. 64–78, 2017.

[191] T. Soong and P. W. Lehn, "Internal power flow of a modular multilevel converter with distributed energy resources", *IEEE J. Emerg. Sel. Top. Power Electron.*, vol. 2, no. 4, pp. 1127–1138, 2014.

[192] G. Abad, *Power Electronics and Electric Drives for Traction Applications*. John Wiley & Sons, 2017.

[193] D. d. C. Mendonça, J. M. Soares Callegari, A. F. Cupertino, H. A. Pereira, S. I. Seleme Junior and R. Teodorescu, "Delta-CHB STATCOM with reduced energy storage requirements based on third harmonic injection", in *2021 Brazilian Power Electron. Conf.*, 2021, pp. 1–7.

[194] X. Yuan, W. Merk, H. Stemmler and J. Allmeling, "Stationary-frame generalized integrators for current control of active power filters with zero steady-state error for current harmonics of concern under unbalanced and distorted operating conditions", *IEEE Trans. Ind. Appl.*, vol. 38, no. 2, pp. 523–532, 2002.

[195] D. N. Zmood, D. G. Holmes and G. H. Bode, "Frequency-domain analysis of three-phase linear current regulators", *IEEE Trans. Ind. Appl.*, vol. 37, no. 2, pp. 601–610, 2001.

[196] D. N. Zmood and D. G. Holmes, "Stationary frame current regulation of PWM inverters with zero steady-state error", *IEEE Trans. Power Electron.*, vol. 18, no. 3, pp. 814–822, 2003.

[197] R. Bojoi, G. Griva, V. Bostan, M. Guerriero, F. Farina and F. Profumo, "Current control strategy for power conditioners using sinusoidal signal integrators in synchronous reference frame", *IEEE Trans. Power Electron.*, vol. 20, no. 6, pp. 1402–1412, 2005.

[198] L. R. Limongi, R. Bojoi, G. Griva and A. Tenconi, "Digital current-control schemes", *IEEE Ind. Electron. Mag.*, vol. 3, no. 1, pp. 20–31, 2009.

[199] C. Lascu, L. Asiminoaei, I. Boldea and F. Blaabjerg, "High performance current controller for selective harmonic compensation in active power filters", *IEEE Trans. Power Electron.*, vol. 22, no. 5, pp. 1826–1835, 2007.

[200] C. Lascu, L. Asiminoaei, I. Boldea and F. Blaabjerg, "Frequency response analysis of current controllers for selective harmonic compensation in active power filters", *IEEE Trans. Ind. Electron.*, vol. 56, no. 2, pp. 337–347, 2009.

[201] A. G. Yepes, F. D. Freijedo, Ó. López and J. Doval-Gandoy, "High-performance digital resonant controllers implemented with two integrators", *IEEE Trans. Power Electron.*, vol. 26, no. 2, pp. 563–576, 2011.

[202] K. Ogata, *Modern Control Engineering*, 5th ed. Pearson, 2010.

[203] A. G. Yepes, F. D. Freijedo, J. Doval-Gandoy, S. Lopez, J. Malvar and P. Fernandez-Comesana, "Effects of discretization methods on the performance of resonant controllers", *IEEE Trans. Power Electron.*, vol. 25, no. 7, pp. 1692–1712, 2010.

[204] A. Vidal, F. D. Freijedo, A. G. Yepes, J. Malvar, Ó. López and J. Doval-Gandoy, "Transient response evaluation of stationary-frame resonant current controllers for grid-connected applications", *IET Power Electron.*, vol. 7, no. 7, pp. 1714–1724, 2014.

[205] A. G. Yepes, F. D. Freijedo, Ó. López and J. Doval-Gandoy, "Analysis and design of resonant current controllers for voltage-source converters by means of nyquist diagrams and sensitivity function", *IEEE Trans. Ind. Electron.*, vol. 58, no. 11, pp. 5231–5250, 2011.

[206] A. Vidal, F. D. Freijedo, A. G. Yepes *et al.*, "Assessment and optimization of the transient response of proportional-resonant current controllers for distributed power generation systems", *IEEE Trans. Ind. Electron.*, vol. 60, no. 4, pp. 1367–1383, 2013.

[207] J.-W. Choi and S.-K. Sul, "Inverter output voltage synthesis using novel dead time compensation", *IEEE Trans. Power Electron.*, vol. 11, no. 2, pp. 221 –227, 1996.

[208] A. R. Muñoz and T. A. Lipo, "On-line dead-time compensation technique for open-loop PWM-VSI drives", *IEEE Trans. Power Electron.*, vol. 14, no. 4, pp. 683–689, 1999.

[209] C. M. Wu, W.-H. Lau and H. S.-H. Chung, "Analytical technique for calculating the output harmonics of an H-bridge inverter with dead time", *IEEE Trans. Circuits Syst. I Fundam. Theory Appl.*, vol. 46, no. 5, pp. 617–627, 1999.

[210] G. Abad, A. Sanchez-Ruiz, J. J. Valera-García and A. Milikua, "Analysis and design guidelines for current control loops of grid-connected converters based on mathematical models", *Energies*, vol. 13, pp. 1–47, 2020.

[211] H. Yi, F. Zhuo and F. Wang, "Analysis about overshoot peaks appearing in the current loop with resonant controller", *IEEE J. Emerg. Sel. Top. Power Electron.*, vol. 4, no. 1, pp. 26–36, 2016.

[212] A. E. Ariffin and N. Munro, "Robust control analysis of a gas-turbine aeroengine", *IEEE Trans. Control Syst. Technol.*, vol. 5, no. 2, pp. 178–188, 1997.